

# Dynamic Bridge Substructure Evaluation and Monitoring

PUBLICATION NO. FHWA-RD-03-089

SEPTEMBER 2005



U.S. Department of Transportation  
**Federal Highway Administration**

Research, Development, and Technology  
Turner-Fairbank Highway Research Center  
6300 Georgetown Pike  
McLean, VA 22101-2296

## **FOREWORD**

This research project was performed to investigate the possibility that, by measuring the dynamic response characteristics of a bridge substructure, it might be possible to determine the condition and safety of the substructure and identify its foundation type (shallow or deep). Determining bridge foundation conditions with this approach may be applied to quantify losses in foundation stiffness caused by earthquakes, scour, and impact events. Identifying bridge foundation type may be used to estimate bridge stability and vulnerability under dead and live load ratings, particularly for unknown bridge foundations. Of several protocols evaluated, Hilbert-Huang Transforms (HHT) showed the most promise for structural damage diagnosis. Further work using the HHT method is recommended. The results of this study will be of interest to geotechnologists and others who are involved in nondestructive bridge condition assessment.

Steven B. Chase, Ph.D.  
Acting Director, Office of  
Infrastructure Research and  
Development

### **Notice**

This document is disseminated under the sponsorship of the U.S. Department of Transportation in the interest of information exchange. The U.S. Government assumes no liability for the use of the information contained in this document. This report does not constitute a standard, specification, or regulation.

The U.S. Government does not endorse products or manufacturers. Trademarks or manufacturers' names appear in this report only because they are considered essential to the objective of the document.

### **Quality Assurance Statement**

The Federal Highway Administration (FHWA) provides high-quality information to serve Government, industry, and the public in a manner that promotes public understanding. Standards and policies are used to ensure and maximize the quality, objectivity, utility, and integrity of its information. FHWA periodically reviews quality issues and adjusts its programs and processes to ensure continuous quality improvement.

**Technical Documentation Page**

1. Report No  FHWA-RD-03-089	2. Government Accession No.  NA	3. Recipient's Catalog No.  N/A	
4. Title and Subtitle  Dynamic Bridge Substructure Evaluation and Monitoring		5. Report Date September 2005  6. Performing Organization Code N/A	
7. Author(s)  Larry D. Olson, P.E.  9. Performing Organization Name and Address  Olson Engineering, Inc. 5191 Ward Road Ste. #1 Wheat Ridge, CO 80033		8. Performing Organization Report No. N/A	
		10. Work Unit No. (TRAI) N/A	
		11. Contract or Grant No. DTFH61-96-C-00030	
		13. Type of Report and Period Covered Final Report 1995–2003	
12. Sponsoring Agency Name and Address Office of Infrastructure Research and Development Federal Highway Administration 6300 Georgetown Pike McLean, VA 22101		14. Sponsoring Agency Code HRDI-01	
15. Supplementary Notes Contracting Officer's Technical Representative (COTR): Michael Adams, HRDI-06			
16. Abstract This research project was funded to investigate the possibility that, by measuring and modeling the dynamic response characteristics of a bridge substructure, it might be possible to determine the condition and safety of the substructure and identify its foundation type (shallow or deep). Determination of bridge foundation conditions with this approach may be applied to quantify losses in foundation stiffness caused by earthquakes, scour, and impact events. Identification of bridge foundation type may be employed to estimate bridge stability and vulnerability under dead and live load ratings, particularly for unknown bridge foundations.			
17. Key Words Bridge Foundation, Hubert-Huang Transform, Scour, Nondestructive Testing, Bridge Substructure, Unknown Bridge Foundations, Bridge Condition Assessment, Earthquakes	18. Distribution Statement No restrictions. This document is available to the Public through the National Technical Information Service, Springfield, VA 22161		
19. Security Classif. (of this report)  Unclassified	20. Security Classif. (of this page)  Unclassified	21. No. of Pages  216	22. Price

# SI\* (MODERN METRIC) CONVERSION FACTORS

## APPROXIMATE CONVERSIONS TO SI UNITS

Symbol	When You Know	Multiply By	To Find	Symbol
<b>LENGTH</b>				
in	inches	25.4	millimeters	mm
ft	feet	0.305	meters	m
yd	yards	0.914	meters	m
mi	miles	1.61	kilometers	km
<b>AREA</b>				
in <sup>2</sup>	square inches	645.2	square millimeters	mm <sup>2</sup>
ft <sup>2</sup>	square feet	0.093	square meters	m <sup>2</sup>
yd <sup>2</sup>	square yard	0.836	square meters	m <sup>2</sup>
ac	acres	0.405	hectares	ha
mi <sup>2</sup>	square miles	2.59	square kilometers	km <sup>2</sup>
<b>VOLUME</b>				
fl oz	fluid ounces	29.57	milliliters	mL
gal	gallons	3.785	liters	L
ft <sup>3</sup>	cubic feet	0.028	cubic meters	m <sup>3</sup>
yd <sup>3</sup>	cubic yards	0.765	cubic meters	m <sup>3</sup>
NOTE: volumes greater than 1000 L shall be shown in m <sup>3</sup>				
<b>MASS</b>				
oz	ounces	28.35	grams	g
lb	pounds	0.454	kilograms	kg
T	short tons (2000 lb)	0.907	megagrams (or "metric ton")	Mg (or "t")
<b>TEMPERATURE (exact degrees)</b>				
°F	Fahrenheit	5 (F-32)/9 or (F-32)/1.8	Celsius	°C
<b>ILLUMINATION</b>				
fc	foot-candles	10.76	lux	lx
fl	foot-Lamberts	3.426	candela/m <sup>2</sup>	cd/m <sup>2</sup>
<b>FORCE and PRESSURE or STRESS</b>				
lbf	poundforce	4.45	newtons	N
lbf/in <sup>2</sup>	poundforce per square inch	6.89	kilopascals	kPa

## APPROXIMATE CONVERSIONS FROM SI UNITS

Symbol	When You Know	Multiply By	To Find	Symbol
<b>LENGTH</b>				
mm	millimeters	0.039	inches	in
m	meters	3.28	feet	ft
m	meters	1.09	yards	yd
km	kilometers	0.621	miles	mi
<b>AREA</b>				
mm <sup>2</sup>	square millimeters	0.0016	square inches	in <sup>2</sup>
m <sup>2</sup>	square meters	10.764	square feet	ft <sup>2</sup>
m <sup>2</sup>	square meters	1.195	square yards	yd <sup>2</sup>
ha	hectares	2.47	acres	ac
km <sup>2</sup>	square kilometers	0.386	square miles	mi <sup>2</sup>
<b>VOLUME</b>				
mL	milliliters	0.034	fluid ounces	fl oz
L	liters	0.264	gallons	gal
m <sup>3</sup>	cubic meters	35.314	cubic feet	ft <sup>3</sup>
m <sup>3</sup>	cubic meters	1.307	cubic yards	yd <sup>3</sup>
<b>MASS</b>				
g	grams	0.035	ounces	oz
kg	kilograms	2.202	pounds	lb
Mg (or "t")	megagrams (or "metric ton")	1.103	short tons (2000 lb)	T
<b>TEMPERATURE (exact degrees)</b>				
°C	Celsius	1.8C+32	Fahrenheit	°F
<b>ILLUMINATION</b>				
lx	lux	0.0929	foot-candles	fc
cd/m <sup>2</sup>	candela/m <sup>2</sup>	0.2919	foot-Lamberts	fl
<b>FORCE and PRESSURE or STRESS</b>				
N	newtons	0.225	poundforce	lbf
kPa	kilopascals	0.145	poundforce per square inch	lbf/in <sup>2</sup>

\*SI is the symbol for the International System of Units. Appropriate rounding should be made to comply with Section 4 of ASTM E380.  
(Revised March 2003)

# TABLE OF CONTENTS

<b>CHAPTER 1. INTRODUCTION .....</b>	<b>1</b>
<b>CHAPTER 2. PROJECT SCOPE AND LITERATURE REVIEW .....</b>	<b>3</b>
<b>BACKGROUND .....</b>	<b>3</b>
<b>RESEARCH SCOPE .....</b>	<b>3</b>
<b>PROJECT BACKGROUND AND REVIEW .....</b>	<b>5</b>
<b>Damage Risks to Bridge Substructures .....</b>	<b>6</b>
<b>Related Work for Bridge Substructure Condition Evaluation.....</b>	<b>7</b>
<b>Related Work for Bridge Superstructure Condition Evaluation .....</b>	<b>9</b>
<b>Bridge Structural Parameter Identification Work.....</b>	<b>10</b>
<b>Uncertainty in Structural Parameter Identification.....</b>	<b>15</b>
<b>Damage Indices .....</b>	<b>16</b>
<b>Bridge Management Systems.....</b>	<b>17</b>
<b>The Role of Bridge Substructure Condition in Bridge Management Systems.....</b>	<b>19</b>
<b>CHAPTER 3. DESCRIPTION OF MODAL VIBRATION TEST BRIDGES.....</b>	<b>21</b>
<b>INTRODUCTION.....</b>	<b>21</b>
<b>TRINITY RIVER RELIEF BRIDGE.....</b>	<b>21</b>
<b>WOODVILLE ROAD BRIDGE .....</b>	<b>26</b>
<b>OLD RELIANCE ROAD BRIDGE .....</b>	<b>28</b>
<b>CHAPTER 4. MODAL TEST PROGRAM FOR BRIDGE SUBSTRUCTURES .....</b>	<b>31</b>
<b>INTRODUCTION.....</b>	<b>31</b>
<b>DYNAMIC TESTING INSTRUMENTATION.....</b>	<b>31</b>
<b>Vibroseis Truck.....</b>	<b>31</b>

Seismic Accelerometers .....	33
Dynamic Signal Analyzer Data Acquisition System .....	35
<b>FIELD MODAL VIBRATION TEST PROCEDURES .....</b>	<b>36</b>
Field Test Program for Trinity River Relief Bridge Bents .....	38
Field Test Program for Woodville Road Bridge .....	50
Field Test Program for Old Reliance Road Bridge .....	53
<b>CHAPTER 5. MODAL VIBRATION DATA PROCESSING AND ANALYSES .....</b>	<b>55</b>
<b>INTRODUCTION.....</b>	<b>55</b>
<b>EXAMPLE MODAL VIBRATION FIELD DATA RESULTS .....</b>	<b>55</b>
Time-Domain Data, Bents of Structure 4, Trinity River Relief Bridge.....	55
Frequency-Domain Data, Bent 2 of Structure 4, Trinity River Relief Bridge .....	60
Transfer Function Results, Bents of Structure 4, Trinity River Relief Bridge .....	62
<b>MODAL VIBRATION DATA PROCESSING.....</b>	<b>66</b>
Curve-Fitting of DP420 Field Modal Vibration Data.....	66
Mode Shape Determination Using PCMODAL.....	68
<b>SOUND VERSUS SIMULATED SCOUR AND EARTHQUAKE DAMAGE RESULTS, TRINITY RIVER RELIEF BRIDGE.....</b>	<b>69</b>
Flexibility Transfer Function Results for Bents 2 and 12 .....	70
Modal Curve-Fitting Results for Bent 12 .....	85
<b>SHALLOW VERSUS DEEP FOUNDATION IDENTIFICATION RESULTS—WOODVILLE AND OLD RELIANCE BRIDGES.....</b>	<b>95</b>
<b>CHAPTER 6. STRUCTURAL MODELING AND PARAMETER ESTIMATION.....</b>	<b>99</b>
<b>INTRODUCTION.....</b>	<b>99</b>
<b>3-D ANSYS MODEL .....</b>	<b>99</b>
Descriptions of 3-D FEM Modeling.....	100

<b>Results of 3-D FEM Modeling .....</b>	<b>102</b>
<b>2-D ANSYS MODELS.....</b>	<b>103</b>
<b>Rayleigh-Ritz Method.....</b>	<b>104</b>
<b>Description of 2-D FEM Modeling .....</b>	<b>106</b>
<b>Results of 2-D FEM Modeling .....</b>	<b>106</b>
<b>PARAMETER ESTIMATION WITH PARIS PROGRAM .....</b>	<b>107</b>
<b>Error Functions in PARIS .....</b>	<b>108</b>
<b>Minimization of Modal Error Functions in PARIS.....</b>	<b>109</b>
<b>PARAMETER ESTIMATION USING SIMULATED FIELD DATA .....</b>	<b>110</b>
<b>Feasibility Study for Bridge Foundation Stiffness Estimation (Stage 1).....</b>	<b>111</b>
<b>Feasibility Study for Bridge Foundation Stiffness Estimation with Unknown Beam and Column Parameters (Stage 2).....</b>	<b>112</b>
<b>Effect of Measurement Errors (Stage 3).....</b>	<b>113</b>
<b>Effect of Modeling Errors (Stage 4) .....</b>	<b>118</b>
<b>PARAMETER ESTIMATION USING REAL FIELD DATA .....</b>	<b>120</b>
<b>Variations of Mode Shapes Extracted from Real Field Data .....</b>	<b>120</b>
<b>PARIS Runs Using Real Field Data for Bent 2 .....</b>	<b>120</b>
<b>PARIS Runs Using Real Field Data for Bent 12 .....</b>	<b>122</b>
<b>CHAPTER 7. USING THE HILBERT-HUANG TRANSFORM FOR SUBSTRUCTURE DAMAGE EVALUATION.....</b>	<b>125</b>
<b>BACKGROUND .....</b>	<b>125</b>
<b>CURRENT APPROACHES IN NONDESTRUCTIVE CONDITION ASSESSMENT</b>	<b>126</b>
<b>CURRENT VIBRATION-BASED SIGNATURE-RECOGNITION TECHNIQUES...</b>	<b>127</b>
<b>Experimental Vibration Data Processing Analysis Approaches .....</b>	<b>127</b>
<b>Signature of Damaged Structural Members .....</b>	<b>128</b>
<b>LIMITATIONS OF MODAL VIBRATION APPROACH FOR BENT 12 .....</b>	<b>129</b>

Review of Field Test Conditions for Structure 4 of the Trinity River Relief Bridge..	129
Fourier and Wavelet Analysis Limitations for Dynamic Properties of Bent 12 .....	131
<b>HILBERT-HUANG TRANSFORM ANALYSES OF VIBRATION DATA FROM BENTS 12 AND 2.....</b>	<b>137</b>
Fundamentals of HHT Method.....	137
Hilbert Spectral Analysis .....	138
HHT Analysis of Data from Bent 12 .....	139
HHT Analysis of Data from Bent 2 .....	156
Force Excitation Normalized HHT Spectra for Bent 12 .....	160
Model-Based Validation for Bent 12 .....	164
<b>SUMMARY OF HILBERT-HUANG TRANSFORM RESULTS .....</b>	<b>173</b>
<b>CHAPTER 8. INTEGRATION OF DYNAMIC TESTING RESULTS TO BRIDGE MANAGEMENT SYSTEMS.....</b>	<b>175</b>
INTRODUCTION.....	175
THE ROLE OF NDE IN A BMS.....	176
THE ROLE OF DYNAMIC TESTING RESULTS IN A BMS .....	177
INTEGRATION OF DYNAMIC TESTING RESULTS INTO A BMS.....	179
Experimentation.....	179
Evaluation of NDE Methods .....	180
Developing Data-Collection Strategy .....	180
SUMMARY .....	180
<b>CHAPTER 9. CONCLUSIONS AND RECOMMENDATIONS.....</b>	<b>183</b>
FIELD MODAL VIBRATION DYNAMIC TESTING FOR DAMAGE.....	183
FIELD MODAL VIBRATION DYNAMIC TESTING FOR SHALLOW VERSUS DEEP FOUNDATION DETERMINATION .....	183
STRUCTURAL MODELING AND PARAMETER ESTIMATION .....	184

<b>HILBERT-HUANG TRANSFORM FOR EVALUATION OF BRIDGE SUBSTRUCTURE DAMAGE.....</b>	<b>184</b>
<b>IMPLEMENTING DYNAMIC TESTING RESULTS IN BRIDGE MANAGEMENT SYSTEMS.....</b>	<b>186</b>
<b>RECOMMENDATIONS FOR RESEARCH.....</b>	<b>186</b>
<b>REFERENCES .....</b>	<b>187</b>
<b>BIBLIOGRAPHY .....</b>	<b>203</b>

## LIST OF FIGURES

Figure 1. Diagram. Parameter identification system excitation and output options.....	11
Figure 2. Diagram. Structural parameter-identification system tree.....	12
Figure 3. Photo. Relief structure 4 of the Trinity River Relief Bridge with the Vibroseis truck over bent 2. ....	22
Figure 4. Photo. Excessive differential settlements on relief structure 4, Trinity River Relief Bridge. ....	22
Figure 5. Diagram. Geometric details of bent 2, structure 4, of the Trinity River Relief Bridge.	24
Figure 6. Diagram. SASW method. ....	25
Figure 7. Photo. SASW tests at bent 12, structure 4, Trinity River Relief Bridge. ....	25
Figure 8. Photo. Western pier of the southwestern span of the Woodville Road Bridge. ....	27
Figure 9. Photo. Vibroseis truck over the east pier, Old Reliance Bridge.....	29
Figure 10. Photo. Vibroseis truck over Woodville Road Bridge pier.....	32
Figure 11. Photo. Vertical vibrator mechanism of Vibroseis truck. ....	33
Figure 12. Photo. Seismic accelerometer and power supply unit. ....	34
Figure 13. Photo. DP420 dynamic signal analyzer in portable PC.....	35
Figure 14. Photo. Drilling concrete holes to mount seismic accelerometers on bent 2 of structure 4, Trinity River Relief Bridge.....	37
Figure 15. Photo. Seismic accelerometers on blocks bolted to piles of bent 2 of structure 4, Trinity River Relief Bridge. ....	37
Figure 16. Photo. One-hundred-pound vibrator with dynamic load cell on bent 2. ....	39
Figure 17. Photo. Twelve-pound impulse sledge hammer with soft gray rubber tip.....	40
Figure 18. Photo. Closeup of the vibrator frame of the Vibroseis truck.....	41
Figure 19. Photo. Dual-wheel depressions in asphalt overlay on deck over bent 2. ....	41
Figure 20. Diagram. Loading points and accelerometer receiver locations on bents 2 and 12, Trinity River Relief Bridge. ....	42
Figure 21. Photo. Vibroseis single-point-plate loading system. ....	43
Figure 22. Photo. Demolition of structure 4, Trinity River Relief Bridge.....	44
Figure 23. Photo. Backhoe excavation at bent 12, Trinity River Relief Bridge. ....	45
Figure 24. Photo. Ground water in excavation of bent 2, Trinity River Relief Bridge. ....	45
Figure 25. Photo. Pile of bent 2 just after excavation. ....	46
Figure 26. Photo. Piles of bent 12 just after excavation. ....	46
Figure 27. Photo. Shearing of pile of bent 2. ....	47
Figure 28. Photo. Shearing of pile of bent 12. ....	47
Figure 29. Photo. Sheared south pile of bent 2 with ground water seepage. ....	48
Figure 30. Photo. Bent and broken rebars of south column of bent 2. ....	48
Figure 31. Photo. Sheared south pile of bent 12. ....	49
Figure 32. Photo. Rebars of south column of bent 12. ....	49
Figure 33. Photo. Vibroseis truck over west pier of Woodville Road Bridge.....	50
Figure 34. Diagram. Woodville Road Bridge, loading points and accelerometer receiver locations. ....	51
Figure 35. Photo. Accelerometers on column and beam cap of west pier, Woodville Road Bridge. ....	52
Figure 36. Photo. Biaxial accelerometer mount with vertical and horizontal accelerometers, west pier, Woodville Road Bridge. ....	52

Figure 37. Photo. Vertical accelerometer at base of column of west pier, Woodville Road Bridge. ....	53
Figure 38. Photo. Horizontal accelerometer on side of column of west pier, Woodville Road Bridge. ....	53
Figure 39. Diagram. Old Reliance Road Bridge, loading points and accelerometer receiver locations. ....	54
Figure 40. Diagram. Node locations on bent 2. ....	56
Figure 41. Diagram. Node locations on bent 12. ....	57
Figure 42. Graph. Vibroseis at node 8 of bent 2. ....	58
Figure 43. Graph. Vertical accelerometer at node 27 of bent 2. ....	59
Figure 44. Graph. Horizontal accelerometer at node 27 of bent 2. ....	59
Figure 45. Graph. Vertical accelerometer at node 24 of bent 2. ....	60
Figure 46. Graphs. Average spectra of figures 42 through 45 for bent 2. ....	61
Figure 47. Equation. Accelerance TF. ....	62
Figure 48. Equation. Mobility TF. ....	62
Figure 49. Equation. Flexibility TF. ....	62
Figure 50. Graphs. Accelerance TF for figures 42 through 45 for bent 2. ....	63
Figure 51. Graphs. Flexibility TFs with coherences for figures 42 through 50 for bent 2. ....	64
Figure 52. Graphs. Bent 12 flexibility TFs with coherences for test configuration identical to bent 2. ....	65
Figure 53. Graph. Curve-fit for accelerance TF, bent 2, node 27V/node 8V. ....	67
Figure 54. Graph. Curve-fit for accelerance TF, bent 2, node 27H/node 8V. ....	67
Figure 55. Graph. Curve-fit for accelerance TF, bent 2, node 24V/node 8V. ....	68
Figure 56. Diagram. First mode shape, frequency, and damping for bent 2. ....	69
Figure 57. Diagram. Node points and geometry of bent 2. ....	70
Figure 58. Diagram. Node points and geometry of bent 12. ....	71
Figure 59. Graph. Bent 12 flexibility TFs at node 2 for intact (i), excavated (e), and broken (n) piles. ....	72
Figure 60. Graph. Bent 12 flexibility TFs at node 4 for intact (i), excavated (e), and broken (n) piles. ....	73
Figure 61. Graph. Bent 12 flexibility TFs at nodes 6, 10, and 11 for the intact pile. ....	74
Figure 62. Graph. Bent 12 flexibility TFs for node 8/node 2 for intact (i), excavated (e), and broken (n) piles. ....	75
Figure 63. Graph. Bent 12 flexibility TFs for node 9/node 4 for intact (i), excavated (e), and broken (n) piles. ....	76
Figure 64. Graph. Bent 12 flexibility TFs for node 10/node 4 for intact (i), excavated (e), and broken (n) piles. ....	77
Figure 65. Graph. Bent 12 flexibility TFs for node 11/node 6 for intact (i) and excavated (e) piles. ....	78
Figure 66. Graph. Bent 2 flexibility TFs at node 2 for intact (i), excavated (e), and broken (n) piles. ....	79
Figure 67. Graph. Bent 2 flexibility TFs at node 4 for intact (i), excavated (e), and broken (n) piles. ....	80
Figure 68. Graph. Bent 2 flexibility TFs at node 6 for intact (i) and excavated (e) piles. ....	81
Figure 69. Graph. Bent 2 flexibility TFs for node 8/node 2 for intact (i), excavated (e), and broken (n) piles. ....	82

Figure 70. Graph. Bent 2 flexibility TFs for node 9/node 2 for intact (i), excavated (e), and broken (n) piles. ....	83
Figure 71. Graph. Bent 2 flexibility TFs for node 10/node 6 for intact (i) and excavated (e) piles. ....	84
Figure 72. Graph. Bent 2 flexibility TFs for node 11/node 6 for intact (i) and excavated (e) piles. ....	85
Figure 73. Diagram. Bent 12, Mode 1 Vertical, node 4 (center) loading, frequency and damping. ....	87
Figure 74. Diagram. Bent 12, Mode 1 Vertical, node 4 (center) loading, magnitude and phase. ....	87
Figure 75. Diagram. Bent 12, Mode 1 Vertical, loading at nodes 2 and 4, frequency and damping. ....	88
Figure 76. Diagram. Bent 12, Mode 1 Vertical, loading at nodes 2 and 4, magnitude and phase. ....	88
Figure 77. Diagram. Bent 12, Mode 2 Vertical, node 4 (center) loading, frequency and damping. ....	90
Figure 78. Diagram. Bent 12, Mode 2 Vertical, node 4 (center) loading, magnitude and phase. ....	90
Figure 79. Diagram. Bent 12, Mode 2 Vertical, loading at nodes 2 and 4, frequency and damping. ....	91
Figure 80. Diagram. Bent 12, Mode 2 Vertical, loading at nodes 2 and 4, magnitude and phase. ....	91
Figure 81. Diagram. Bent 12, Mode 2 Horizontal, node 4 (center) loading, frequency and damping. ....	93
Figure 82. Diagram. Bent 12, Mode 2 Horizontal, node 4 (center) loading, magnitude and phase. ....	93
Figure 83. Diagram. Bent 12, Mode 2 Horizontal, loading at nodes 2 and 4, frequency and damping. ....	94
Figure 84. Diagram. Bent 12, Mode 2 Horizontal, loading at nodes 2 and 4, magnitude and phase. ....	94
Figure 85. Graph. Woodville and Old Reliance Bridges, flexibility TFs, node 9/node 17. ....	96
Figure 86. Graph. Woodville and Old Reliance Bridges, flexibility TFs, node 9/node 18. ....	97
Figure 87. Equation. $K_{SSS}$ . ....	100
Figure 88. Equation. $M_{SSS}$ . ....	100
Figure 89. Equation. $K_{SSS}$ (3-by-3 matrix). ....	104
Figure 90. Equation. $M_{SSS}$ (3-by-3 matrix). ....	104
Figure 91. Equation. $KE_{max}$ (distributed properties). ....	105
Figure 92. Equation. $SE_{max}$ (distributed properties). ....	105
Figure 93. Equation. $KE_{max}$ (lumped properties). ....	105
Figure 94. Equation. $SE_{max}$ (lumped properties). ....	105
Figure 95. Equation. $\alpha_n$ . ....	106
Figure 96. Equation. Matrix K times vector $\Phi$ . ....	108
Figure 97. Equation. Matrix K times vector $\Phi$ (partitioned). ....	108
Figure 98. Equation. Stiffness-based residual modal error function. ....	109
Figure 99. Equation. Flexibility-based residual modal error function. ....	109
Figure 100. Equation. Error function approximation. ....	110

Figure 101. Equation. Objective function $J$ .	110
Figure 102. Equation. Change in parameter vector.	110
Figure 103. Equation. Parameter iteration.	110
Figure 104. Equation. Resonant frequency with artificial errors.	113
Figure 105. Equation. Mode shape with artificial errors.	113
Figure 106. Equation. Grand mean percentage error.	114
Figure 107. Equation. Grand standard deviation percentage error.	114
Figure 108. Equation. Percentage error.	115
Figure 109. Diagram. Vibration tests of bent 12 of the Trinity River Relief Bridge.	131
Figure 110. Graphs. (a) Vibroseis chirp forcing function in poundforce at center of bent 2. (b) Accelerometer 15 response in inches/seconds squared.	132
Figure 111. Graphs. Fourier spectra (F.S.) of figure 110 data.	133
Figure 112. Graphs. Morlet (graph b) and Db5 (graph c) wavelet spectra of the forcing function (graph a).	135
Figure 113. Graphs. Accelerance TFs for intact, excavated, and broken pile states.	136
Figure 114. Equation. $X(t)$ .	138
Figure 115. Equation. $Z(t)$ .	138
Figure 116. Equation. $X(t)$ in Hilbert transform form.	138
Figure 117. Equation. $X(t)$ in Fourier series representation.	139
Figure 118. Graph. HHT spectrum of forcing function, bent 12, intact state.	141
Figure 119. Graph. HHT spectrum of vibration, accelerometer 15, bent 12, intact state.	142
Figure 120. Graphs. EMD with the eight IMF components of vibration, accelerometer 15, bent 12, intact state.	143
Figure 121. Graphs. Fourier spectra of IMF components in figure 120.	144
Figure 122. Graph. HHT spectrum of first IMF component of vibration, accelerometer 15, bent 12, intact state.	145
Figure 123. Graph. HHT spectrum of second IMF component of vibration, accelerometer 15, bent 12, intact state.	145
Figure 124. Graph. HHT spectrum of vibration, accelerometer 15, bent 12, intact state.	146
Figure 125. Graph. HHT spectrum of vibration, accelerometer 15, bent 12, excavated state.	147
Figure 126. Graph. HHT spectrum of vibration, accelerometer 15, bent 12, broken state.	148
Figure 127. Graph. HHT spectrum of vibration, accelerometer 13, bent 12, intact state.	150
Figure 128. Graph. HHT spectrum of vibration, accelerometer 13, bent 12, excavated state.	151
Figure 129. Graph. HHT spectrum of vibration, accelerometer 13, bent 12, broken state.	152
Figure 130. Graph. HHT spectrum, second component of vibration, accelerometer 15, bent 12, intact state.	153
Figure 131. Graph. HHT spectrum, second component of vibration, accelerometer 13, bent 12, intact state.	153
Figure 132. Graph. HHT spectrum, second component of vibration, accelerometer 15, bent 12, excavated state.	154
Figure 133. Graph. HHT spectrum, second component of vibration, accelerometer 13, bent 12, excavated state.	154
Figure 134. Graph. HHT spectrum, second component of vibration, accelerometer 15, bent 12, broken state.	155
Figure 135. Graph. HHT spectrum, second component of vibration, accelerometer 13, bent 12, broken state.	155

Figure 136. Diagram. Locations of accelerometers 9 and 11 on bent 2. ....	156
Figure 137. Graph. HHT spectrum of vibration, accelerometer 11, bent 2, intact state. ....	157
Figure 138. Graph. HHT spectrum of vibration, accelerometer 11, bent 2, excavated state. ....	157
Figure 139. Graph. HHT spectrum of vibration, accelerometer 11, bent 2, broken state. ....	158
Figure 140. Graph. HHT spectrum of vibration, accelerometer 9, bent 2, intact state. ....	158
Figure 141. Graph. HHT spectrum of vibration, accelerometer 9, bent 2, excavated state. ....	159
Figure 142. Graph. HHT spectrum of vibration, accelerometer 9, bent 2, broken state. ....	159
Figure 143. Graph. Normalized HHT spectrum of vibration, accelerometer 15, bent 12, intact state. ....	161
Figure 144. Graph. Amplitude of force applied to bent 12, intact state. ....	161
Figure 145. Graph. Normalized HHT spectrum of vibration, accelerometer 15, bent 12, excavated state. ....	162
Figure 146. Graph. Amplitude of force applied to bent 12, excavated state. ....	162
Figure 147. Graph. Normalized HHT spectrum of vibration, accelerometer 15, bent 12, broken state. ....	163
Figure 148. Graph. Amplitude of force applied to bent 12, broken state. ....	163
Figure 149. Equation. Damping matrix $[C]$ . ....	164
Figure 150. Diagram. ANSYS model for bent 12. ....	165
Figure 151. Graph. HHT spectra of vibration of 2-D FEM, node 37, bent 12, intact state, $d = 0$ . ....	168
Figure 152. Graph. HHT spectra of vibration of 2-D FEM, node 37, bent 12, intact state, $d = 0.00198$ . ....	168
Figure 153. Graph. HHT spectra of vibration of 2-D FEM, node 37, bent 12, intact state, $d = 0.05305$ . ....	168
Figure 154. Graph. Spectra of marginal amplitude, node 37, bent 12, intact state, $d = 0$ . ....	169
Figure 155. Graph. Spectra of marginal amplitude, node 37, bent 12, intact state, $d = 0.00198$ . ....	169
Figure 156. Graph. Spectra of marginal amplitude, node 37, bent 12, intact state, $d = 0.05305$ . ....	169
Figure 157. Graph. HHT spectra of vibration of 2-D FEM, $d = 0.003979$ , bent 12, broken state, node 37. ....	171
Figure 158. Graph. HHT spectra of vibration of 2-D FEM, $d = 0.003979$ , bent 12, broken state, node 53. ....	171
Figure 159. Graph. Spectra of marginal amplitude, $d = 0.003979$ , bent 12, broken state, node 37. ....	172
Figure 160. Graph. Spectra of marginal amplitude, $d = 0.003979$ , bent 12, broken state, node 53. ....	172
Figure 161. Graph. Hypothetical probability density functions for percent change in vertical stiffness. ....	179

## LIST OF TABLES

Table 1. Shear wave velocity profile results from the Trinity River Relief Bridge site. ....	26
Table 2. Shear wave velocity profile results from the Woodville Road Bridge site. ....	28
Table 3. Shear wave velocity profile results from the Old Reliance Road Bridge site. ....	30
Table 4. First 15 resonant frequencies in hertz for 3-D ANSYS FEM models. ....	102
Table 5. Feasibility study for bridge foundation stiffness estimations. ....	111
Table 6. Bridge foundation stiffness estimations with unknown concrete beam and column moments of inertia. ....	113
Table 7. Effects of measurement errors (stiffness-based modal error function) using one-mode simulated field data. ....	116
Table 8. Effects of measurement errors (flexibility-based modal error function) using one-mode simulated field data. ....	117
Table 9. Effects of modeling errors for the most measurement error tolerance case (center loading). ....	119
Table 10. Initial and resulting $K_{yy}$ in PARIS runs with real field data for bent 2. ....	121
Table 11. Resonant frequencies from 2-D ANSYS models and real field data for the center-loading cases of bent 2 with an alpha of 1.056. ....	121
Table 12. Initial and resulting $K_{yy}$ in PARIS runs with real field data for bent 12. ....	122
Table 13. Resonant frequencies from 2-D ANSYS models and real field data for the side-loading cases of bent 12 with an alpha of 1.035. ....	122
Table 14. Resonant frequencies from 2-D ANSYS models and real field data for the center-loading cases of bent 12 with an alpha of 1.055. ....	123
Table 15. Comparison of fundamental natural frequencies of a column in three states. ....	149
Table 16. Fundamental natural frequencies of bent 12. ....	166
Table 17. Hypothetical integrated condition state for reinforced concrete substructure. ....	176
Table 18. Integrated condition states for a reinforced concrete element, modified from Hearn and Shim. ....	177
Table 19. Hypothetical thresholds for action. ....	178



## CHAPTER 1. INTRODUCTION

This research project, “Dynamic Bridge Substructure Evaluation and Monitoring,” was sponsored by the Federal Highway Administration (FHWA) under contract number DTFH61-96-C-00030. The research was funded to investigate the possibility that by measuring and modeling the dynamic response characteristics of a bridge substructure, one could determine the condition and safety of the substructure and identify its foundation type (shallow or deep). Determination of bridge foundation conditions with this approach may be applied to quantify losses in foundation stiffness caused by earthquake, scour, and impact events. Identification of bridge foundation type may be employed to estimate bridge stability and vulnerability under dead and live load ratings, particularly for unknown bridge foundations.

Chapter 2 introduces the research project scope and presents the results of a literature review of related topics. Chapter 3 describes the bridges in Texas that were selected for modal vibration tests during the research. Three bridges and four substructures were selected to provide footing (shallow), pile cap on piles (deep), and piles (deep) foundation types to investigate the type of foundation. Chapter 4 presents the modal vibration testing program, looking at instrumentation and field test procedures used to measure the vibration responses of the bridges. Of particular interest is that selected piles of two bridge bents were able to be tested in a sound, undamaged state initially, and then as selected piles were first excavated and ultimately broken, to simulate scour and earthquake damage events, respectively. Chapter 5 details modal vibration data processing and analyses performed on the four tested bridge substructures for the three bridges. Example time, frequency spectra, and modal transfer function (TF) data are presented for the bridge substructures and sound, excavated, and broken pile states. The TFs were found to show increased flexibility (lower stiffness) for substructures as they were excavated and ultimately broken. However, comparisons of modal TF data for two similar bridges and substructures with shallow and deep (footing and pile cap on piles) foundations did not show promise for only experimental data indicating shallow versus deep bridge foundations. The possibility of determining substructure damage or foundation type, or both, using structural modeling and structural parameter estimation techniques to obtain so-called super-spring elements was extensively researched as discussed in chapter 6. Unfortunately, the outcome of the structural parameter estimation analyses was that the damage states could not be predicted reliably, nor could the foundation type be determined.

As a consequence of this inability of theoretical approaches to identify either damage or substructure foundation type while experimental data showed the effects of the damage, the completion of the research was delayed while a new analysis technique for identifying instantaneous, brief changes in frequency associated with nonlinear responses of structures to damage was investigated. This technique is known as the Hilbert-Huang Transform (HHT), and the results of these analyses of the modal vibration test data are presented in chapter 7 for the two bent substructures that were tested in sound (undamaged), excavated, and broken pile states. The HHT method was found to have considerable promise for identifying expected but brief changes in frequency associated with nonlinear responses that are masked by the dominant linear responses of otherwise sound structures in traditional modal vibration testing and analysis. Chapter 8 presents a preliminary discussion of the potential for integrating modal vibration

testing and HHT analyses into bridge management systems in the future. Chapter 9 presents the conclusions of the research and recommendations for future research on the HHT method.

## **CHAPTER 2. PROJECT SCOPE AND LITERATURE REVIEW**

### **BACKGROUND**

This FHWA research project, “Dynamic Bridge Substructure Evaluation and Monitoring” was proposed and funded in 1995 to investigate the possibility that by measuring and modeling the dynamic response characteristics of a bridge substructure, one could determine the condition and safety of the substructure and identify its foundation type (shallow or deep). Determination of bridge foundation conditions may be applied to quantify losses in foundation stiffness caused by earthquake, scour, and impact events. Identification of bridge foundation type may be employed to estimate bridge stability and vulnerability under dead and live load ratings, particularly for unknown bridge foundations. The dynamic evaluation and monitoring results eventually may be integrated into current and proposed bridge management system (BMS) databases to provide baseline data for comparison of bridge substructures after catastrophic events.

Accurate information on a bridge substructure is an essential part of implementing a cost effective and safety-conscious bridge management program. For bridge piers and abutments, scour can quickly reduce the load capacities of foundations, and ground motions induced by earthquakes can produce ground-coupled resonance, liquefaction of soils, and loss of soil support. Therefore, it is very important that bridge foundation vulnerability to seismic and scour events be assessed or monitored, or both, cost-effectively so that catastrophic failures can be prevented and corrective repairs can be carried out in a timely fashion. Furthermore, more than 100,000 bridges over water in the United States have what is known as “unknown foundations,”<sup>(1)</sup> which means their vulnerability to scour cannot be calculated by normal hydraulic and geotechnical analysis procedures.

As a potential approach to address this problem of foundation condition and type, dynamic testing is a powerful tool for bridge superstructure and substructure condition assessment and system identification in both global and local element levels. A moderate amount of work has been done over the past 25 years in bridge vibration measurements and comparisons of dynamic field data and analytical predictions, as well as in an attempt to relate dynamic testing results to potential deterioration of a bridge.<sup>(2)</sup> However, most of the work emphasized dynamic testing and analysis of bridge superstructures with little or no consideration given to bridge substructures and their foundations.<sup>(3)</sup> The National Cooperative Highway Research Program (NCHRP) Project 21-5 demonstrated promise for a complete bridge substructure nondestructive evaluation (NDE) method based on dynamic testing of bridge substructures.<sup>(4)</sup> However, funds were limited for research on this new method in the NCHRP research on NDE methods to determine unknown bridge foundation depths for bridge scour safety analyses; thus, only the initial feasibility of the approach could be evaluated before this report.

### **RESEARCH SCOPE**

The objectives of this project were to backcalculate bridge foundation dynamic stiffness and identify bridge foundation type using dynamic measurements of a bridge substructure, and to monitor bridge substructure conditions over time by repeating dynamic tests at preselected time intervals or after the occurrence of a natural event such as an earthquake or flood. The project

objectives were met by performing field vibration tests before and after simulated earthquake and scour damage to actual bridge foundations, modal analysis, finite element modeling (FEM), structural parameter estimation, and a new dynamic response system identification technique known as the HHT.<sup>(5)</sup>

Chapter 3 discusses the details of four bridge bents in three bridges with different foundation conditions and types that were field tested in Texas during 1996 and 1997. All four bridge bents were first tested in their existing, undamaged states. Because one of the bridges was demolished during the field research, two bents could be tested in an undamaged state, and then in a simulated scour state, and finally in a simulated earthquake damage state. The simulated foundation damage conditions were meant to represent the effects of scour and earthquake events on bridge foundations, and the selected foundation types are representative of typical highway bridge foundation configurations in the United States.

Chapter 4 discusses the dynamic testing of the four bridge substructures including instrumentation, test procedures, and data processing used in the field modal vibration tests of the four bridge bents. A specially modified large, truck-mounted geophysical vibrator (a Vibroseis) owned by the Geotechnical Engineering Center of the University of Texas at Austin was used primarily as the vibration source.<sup>(6)</sup> The Vibroseis consists of a large truck with a gross weight of about 22,246 kilograms (kg) (49,000 pounds (lb)) with a servo-hydraulic vibrator mounted on it. Vertical dynamic forces up to 31,780 kg (70,000 lb) over a frequency range from 1 to 120 hertz (Hz) may be produced with the Vibroseis. Seismic accelerometers were attached to various locations on the tested bridge bents to record bridge dynamic responses under forced vibrations. A personal computer (PC)-based four-channel dynamic signal analyzer served as the central vibration control and measurement unit.

Chapter 5 presents the experimental findings in terms of foundation condition and type identification. Dynamic characteristics of each bridge substructure such as natural frequency, damping ratio, and mode shape were extracted from the field data and interpreted by modal analysis techniques.

Chapter 6 discusses the results of modeling and structural parameter estimation and system identification techniques that were used to produce engineering information such as lateral, vertical, and rotational resistance of the bridge foundations. In terms of theoretical analysis, three-dimensional (3-D) FEMs for all four tested bridge bents were accomplished by using a commercial software package. The 3-D FEMs consist of super-soil-structural elements that can represent the bridge foundation conditions and types. Based on the 3-D FEMs, two-dimensional (2-D) FEMs for the four tested bridge bents were established because the current structural parameter estimation and system identification program used in this project is available for 2-D models only.

Chapter 7 discusses the HHT and results of its application to the two bents that were tested in undamaged, simulated flood, and simulated earthquake states. The HHT method is designed to identify instantaneously at points in time the reduction in natural frequency associated with local damage from otherwise linearly elastic response data for the rest of a structure that are often unidentifiable in conventional modal testing and analysis.

Chapter 8 explores the possibility of incorporating the dynamic bridge substructure testing and analysis results into BMS. This step will be taken in the future to provide practical benefits to departments of transportation (DOT) and the public with research in improved safety and reduced risk of bridge substructure failure.

Chapter 9 presents the findings and conclusions resulting from this research. Recommendations for future research are also discussed.

## **PROJECT BACKGROUND AND REVIEW**

The highway transportation system is the largest and perhaps most important subsystem in the transportation infrastructure of the United States. It helps sustain commerce in almost every sector of our national economy and is used daily for both pleasure and necessity by almost every citizen. Maintaining this system at a high performance level is vital for public safety, societal well-being, and economic productivity and growth. Bridges comprise significant and critical discrete links in the highway transportation subsystem. An estimate made in 1995 was that about 45 percent of the bridge inventory was deficient due to either structural or traffic inadequacy, or both.<sup>(7)</sup> In 2004, when measured by deck area adjusted for average daily traffic, 29.8 percent of national highway system bridges and 31.5 percent of non-national highway system bridges were deficient.<sup>(8)</sup>

Clearly, the job of managing and maintaining the transportation infrastructure represents a significant challenge, especially considering the difficulties in generating the level of additional funds necessary to finance these activities. At present, the principal information available to bridge owners comes from FHWA's National Bridge Inspection Program, which was put in place in 1967 in response to the collapse of the Silver Bridge spanning the Ohio River between Gallipolis, OH, and Point Pleasant, WV. In the intervening 2 decades, many State DOTs initiated and accomplished significant improvements in inspection, rating, and management operations of highway bridges; however, according to FHWA, a fundamental weakness in bridge management systems has been the reliance on visual inspection and subjective condition assessment.<sup>(7)</sup> Thus, these inspections cannot evaluate damage in the absence of visible symptoms such as concrete deck deterioration under asphalt overlay, corrosion of reinforcement, and scour. Moreover, data analysis is based on characterizations that typically do not incorporate the mechanisms significantly influencing actual bridge behavior. Current practices in evaluating serviceability, fatigue, and ultimate limit capacity of a bridge are accomplished only with significant uncertainty; thus, their effectiveness in management decisionmaking is greatly reduced. Without more accurate information on bridge superstructure and substructure, bridge owners cannot decide where, when, and how to spend limited resources efficiently.

The objective of this research project is to produce a dynamic bridge substructure evaluation and monitoring system that can provide more accurate information on the condition, type, and vulnerability of bridge piers and abutments that cannot be obtained by normal visual surveys. Dynamic testing plays a key role in this bridge substructure evaluation and monitoring system.

Although many researchers have studied dynamic behavior of highway bridges, it is still difficult to understand fully all parameters that affect vibration measurements. Cantieni explained the difficulties encountered when he conducted an experiment on a bridge to study the dynamic

behavior of highway bridges under the passage of heavy vehicles.<sup>(9)</sup> During the literature search, the current researchers realized that most experiments and theoretical studies previously performed were related to dynamic behavior of a bridge superstructure, and little had been done on dynamic behavior of a bridge substructure. The following sections summarize the key issues for bridge substructure condition assessment and relate this assessment to the proposed bridge evaluation and monitoring system.

### **Damage Risks to Bridge Substructures**

Typically, a bridge abutment is designed to resist lateral movement and overturning created by soil pressure and settlement resulting from dead and live loads. The bridge abutment and its connection to the footing must resist moments and shear forces, and the footing must provide resistance to vertical, lateral, and overturning forces. Live loads add slightly to the vertical dead loads, but they also add to the resistance to overturning and sliding. Therefore, the bridge superstructure usually controls the load ratings. A bridge abutment condition rating is governed by three factors: (1) the presence of excessive soil pressure caused by poor drainage, (2) the condition of the abutment structure, and (3) the dimension and type of foundation (shallow, deep, or combined such as footing, pile, or pile cap on pile).

A bridge pier is designed to resist vertical settlement resulting from dead and live loads, and lateral movement and rotation caused by temperature change, friction, wind, water, and seismic loads. The bridge pier and its connection to the footing must resist moments, shear, and compressive forces. The footing must resist lateral, vertical, and rotational movements. The bridge pier condition rating is governed by the condition of the pier structure and the dimension and type of footing (shallow, deep, or combined).

The most common cause of bridge failure is from floods when scour causes failure of bridge piers and abutments.<sup>(10)</sup> Scour occurs progressively as supporting material under a footing is removed during flood events and is replaced with material that has little or no bearing capacity. During the spring floods of 1987, 17 bridges in New York and New England were damaged and destroyed by flood scour action. In 1985, floods destroyed 73 bridges in Pennsylvania, Virginia, and West Virginia. A national study of 383 bridge failures caused by catastrophic floods showed that 25 percent involved pier damage and 72 percent involved abutment damage.<sup>(11)</sup> More than 85,000 bridges in the United States are vulnerable to scour; bridge foundation conditions for another 104,000 cannot be determined.<sup>(1)</sup> Devices have been developed for monitoring scour events.<sup>(12,13)</sup> These devices could be tied in with the proposed dynamic substructure monitoring system to correlate the bridge pier and foundation response with the potential occurrence of scour.

Substructure damage during earthquakes generally consists of foundation elements broken in shear, or loss of soil support, or both, caused by liquefaction. Rapid, nondestructive identification of such hidden substructure damage after an earthquake would increase public safety.

Barge and ship collisions with bridges are common worldwide, and can represent a significant cause of damage to bridge substructure.<sup>(14)</sup> From 1981 to 1990, 2,418 bridges in the United States alone were hit by commercial marine vessels. Most did not involve fatalities but may have resulted in damage that could have been monitored and reported.<sup>(15)</sup> Although damage to

substructures can be similar to that from an earthquake, impact damage primarily affects the bridge substructure and there is a comparatively low risk of reduced soil support.

Loss of capacity in bridge piers and abutments can occur either over a period of time resulting from alkali-silica reaction, freeze-thaw damage, corrosion of reinforcement, and unconstrained thermal movements, or because of sudden floods, earthquake, or vessel impact.<sup>(16)</sup> The long-term damage conditions can be evaluated using a variety of local tests including impact-echo, ground-penetrating radar, and corrosion-potential measurements. However, damage caused by floods, earthquake, and vessel impact is more difficult to evaluate locally for buried portions of bridge substructures, and thus global bridge evaluation and monitoring methods are more suitable (as was researched in this project).

### **Related Work for Bridge Substructure Condition Evaluation**

Raghavendrchar and Aktan successfully conducted a multireference impact testing on a reinforced concrete slab bridge.<sup>(17)</sup> This pilot study demonstrated that a multireference impact testing could serve as the main experimental component for comprehensive structural identification of large constructed facilities. If an accurate measure of flexibility (displacement divided by force as a function of frequency, that is, the inverse of stiffness) is to be obtained directly from the experimental data, demanding standards are required for modal testing designs. Aktan and Helmicki performed a study to explore the issues and advancement of knowledge in instrumented monitoring of a full-scale bridge.<sup>(18)</sup> When impact testing may not be the appropriate method (such as for buildings, large bridges, large facilities with complex geometry, or structures subjected to lateral loads), forced-excitation modal testing using larger vibrators may be required.<sup>(19)</sup>

Warren and Malvar used a falling weight deflectometer to assess structural conditions of reinforced concrete piers.<sup>(20)</sup> By comparing the deflected shapes from the FEM and testing results, the local stiffness and soft areas of the piers were determined. The FEMs of the piers were generated from the design data and drawings using a commercial software package called Automatic Dynamic Incremental Nonlinear Analysis (ADINA™). The differences between a rating of ideal and actual testing data were resolved by the systematic changes of the stiffness parameters based on matching dynamic responses of the FEMs to the measured data. This method was demonstrated on a real bridge with timber piles in New Jersey. Because the bridge geometry was well known, it was deemed sufficient to identify the effective stiffness of the piers and damaged areas.

To investigate the seismic vulnerability of bridge piers, the Washington State DOT studied lateral load responses of a full-scale reinforced concrete bridge.<sup>(21)</sup> This study addressed concerns that the design of pier columns in the 1950s and 1960s was not adequate to sustain displacements during earthquakes. A three-span highway bridge was pulled transversely using a jacking arrangement and cables that produced a load equal to 65 percent of the weight of the bridge. The overall movement was 7.62 millimeters (mm) (0.3 inches), and very little damage was detected. This study concluded that the pier design was adequate for earthquakes.

Pierce and Dowding reported on a long-term monitoring method for concrete bridge piers using Time Domain Reflectometry (TDR).<sup>(22)</sup> This method focused on the determination of internal

cracking and large local deformations caused by earthquakes. To use the method, coaxial TDR cables must be embedded in the concrete during construction or retrofitting. The cables were placed in critical areas such as the column/base connection. The cables were selected as either extension sensitive or shear sensitive. If localized extension or shear occurred along the length of any cable, it could be identified as a reflector using the TDR external electronics.

A bridge abutment generally is designed to resist backfill soil pressures; however, for a rigid frame abutment, the thermal deck expansion causes backfill pressures that are far in excess of the active soil pressures used in design.<sup>(23)</sup> In addition, bridge skew results in a large horizontal gradient of the backfill pressures, producing local backfill pressures that could exceed the capacity of the abutment walls. A software program, BASSIN, was developed in 1996 at the University of California, Berkeley, CA, for dynamic analysis of a bridge-abutment-backfill system that is subjected to traveling seismic waves. BASSIN can compute 3-D dynamic responses of an arbitrarily configured bridge-abutment-backfill system induced by compressional, vertical shear, horizontal shear, and surface waves (planar P-, SV-, SH- or R-waves, respectively) with arbitrary wavelength, amplitude, and direction of incidence.

During the North American Workshop on Instrumentation and Vibration Analysis of Highway Bridges in 1995, researchers and practitioners agreed that instrumentation is a viable tool for bridge inspection. In fact, many State DOTs (such as Connecticut, Florida, and New York) have used instrumentation in their bridge inspection programs. The California DOT (Caltrans) has an extensive instrumentation program that involves monitoring seismic excitations and foundation systems. Practicing bridge engineers recognized the need to evaluate and formalize the use of structural identification and instrumentation for bridge inspection.

Hussein et al. reported the use of compression waves for investigating single pile length and integrity, settlement, and scour.<sup>(24)</sup> Finno and Prommer studied the impulse response (IR) method for inaccessible drilled shafts under pile caps.<sup>(25)</sup> Several drilled shafts connected together with concrete grade beams were tested using the nondestructive IR method. Based on the field data, it was found that shaft heads that were more rigid (because of larger or several grade-beam connections) exhibited greater signal attenuation, and become more difficult to evaluate. Chen and Kim used transverse waves as a means for investigating pier conditions and local defects.<sup>(26)</sup> This so-called “bending wave” method involved the measurements of the velocity dispersion curve of the transverse waves propagated down from the top of a pier. The dispersion of the directly arrived wave was used to assess local damages, while the dispersion of the reflected waves from the pier bottom was used to assess overall pier conditions. The method proved most suitable to short piles in softer soils.<sup>(27)</sup>

The previously mentioned NCHRP 21-5 research study for determination of unknown subsurface bridge foundations was conceived to evaluate and develop NDE methods and equipment that allowed the determination of subsurface bridge foundation depths and other characteristics where such information is unavailable, unknown, or uncertain.<sup>(4)</sup> Out of approximately 580,000 highway bridges in the National Bridge Inventory, a large number of older non-Federal-aid bridges, and, to a lesser extent, Federal-aid bridges have no design or as-built bridge plans. Consequently, little or no information is available to document the type, depth, geometry, or materials incorporated in their foundations. The study evaluated many existing and new NDE methods including five acoustic methods (sonic echo and impulse response, bending wave,

ultraseismic, parallel seismic, and borehole sonic), one modal vibration method (dynamic foundation response), and one electromagnetic (borehole and surface ground penetrating radar) method. A follow-on phase II study focused on researching and developing equipment, field techniques, and analysis methods for the surface-based ultraseismic and borehole-based parallel seismic methods.<sup>(27)</sup> These two methods showed the most promise for immediate application to the determination of unknown foundation depths for the most substructures.

Recent research was done on Interstate 15 (I-15) bridges in the Salt Lake City, UT, area on dynamic testing for condition assessment of bridge bents.<sup>(28)</sup> The research used seven forced vibration tests with horizontal excitation. Modeling and experimental modal vibration test results were compared in terms of mode shapes and frequencies. Both damaged and repaired substructure states could be used to identify the condition of the structure at each state. The estimated location and intensity of the damage or retrofit also was identified.

### **Related Work for Bridge Superstructure Condition Evaluation**

Bridge superstructure condition evaluation research programs generally have focused on two primary areas: ultimate load tests and dynamic tests. An excellent reference on dynamic testing for modal vibration measurement and analysis is given by Ewins.<sup>(29)</sup> For the ultimate load tests, the bridges that were slated for removal from service were tested to failure.<sup>(30,31,32)</sup> These studies generally provided some insight on the ultimate load capacity and mechanisms of failure that could be used in the future. On the other hand, laboratory and field studies to evaluate dynamic properties of bridges and relate them to condition assessments have been reported extensively in past years.<sup>(33)</sup>

Salane et al. reported dynamic tests of a bridge for detecting structural deterioration caused by girder fatigue cracks.<sup>(34)</sup> A concrete deck on steel girders was loaded with an electrohydraulic actuator system up to 465,000 load cycles. Accelerometers were used to determine damping ratios, frequency contents, and impedance at various stages during the loading. The testing results indicated increases in damping ratios with cycles of loading, presumably caused by cracking, and a decrease in amplitude at resonant frequencies, as well as a 20 percent to 40 percent change in computed stiffness coefficients.

Cawley and Adams related changes of successive mode frequencies to the existence and location of structural deterioration in beams.<sup>(35)</sup> Manning, DeWolf et al., Huston et al., and Gregory et al. reported various full-scale bridge dynamic tests, showing that dynamic characteristics may be revealed using vibratory shakers, impact hammers, and traffic and wind loads. (See references 36, 37, 38, and 39.) Gregory et al. and DeWolf et al. demonstrated a relationship between dynamic testing results and structural deterioration.<sup>(39,37)</sup> Sensitivity of dynamic characteristics to deterioration was shown to depend on the particular modes being observed. Manning suggested that a more localized dynamic analysis might be advantageous because serious loss of strength of a single member may occur before it can be observed on the entire structure.

Mazurek and DeWolf showed in field tests that ambient traffic loads could be used as a basis for an automated monitoring scheme based on changes in vibration signatures.<sup>(40)</sup> They also showed in laboratory tests that changes in support condition and crack development affect natural frequencies and modal amplitudes. Changes in modal frequency were up to 30 percent for

changes in support condition and up to 10 percent for cracking. These laboratory results encouraged further field investigations.

Biswas et al. reported a component evaluation technique based on dynamic responses to a hammer impact on the component of interest.<sup>(41)</sup> Results were confirmed with laboratory models, but field verification was limited and did not produce conclusive results.

Woodward et al. conducted dynamic tests for a full-scale bridge subject to artificially induced fatigue cracking (vertical cuts) in a main girder.<sup>(32)</sup> Preliminary field test results showed that the changes in dynamic characteristics due to the damage were detected, but only when the maximum amount of damage was inflicted. Salawu and Williams reported a study of the forced vibrations of a bridge before and after repair.<sup>(42)</sup> The test results demonstrated the changes in natural frequency induced by the repair; however, the magnitude of the changes is quite small, on the order of 2 percent.

The principle of continuous monitoring of bridge dynamic characteristics has been implemented experimentally by the New York State DOT.<sup>(43)</sup> The system, called the Remote Bridge Monitoring System, is based on measuring dynamic motion (using accelerometers) as well as strain and rotation (using inclinometers). The sensors are hardwired to an onsite data acquisition system, and the acquired data are transmitted to the central office by telephone wire and modem. A threshold accelerometer signal level is used to trigger data collection and a warning alarm to announce significant changes in modal frequencies. Dynamic response data collected to date show some scatter in the modal frequency measurement, in which significant changes on the order of 5 percent to 10 percent might be obscured.

It is possible to conclude from the above studies that further work is needed to relate dynamic properties to component deterioration; however, simpler interpretations for vibration measurements have not been reported in the literature. For example, dynamic measurements can be used to evaluate the distribution of loading in axially loaded members such as cables and truss diagonal braces. The natural frequency of such axially loaded members is highly sensitive to the magnitude of the axial load. Baumgartner and Waubke showed how frequency measurements in tension hangers under traffic loading relate to the end fixity of the hangers.<sup>(44)</sup>

### **Bridge Structural Parameter Identification Work**

The objective of structural parameter identification is to obtain an understanding of the critical mechanisms of flexibility, energy dissipation, and inertia. 3-D kinematics, resistance mechanisms (load paths), and critical structure region studies (with respect to stress, strength, and stiffness) are essential to reliably assess and identify the available supplies of strength, stiffness, stability, hardening, and energy dissipation in a structure. Structural parameter identification consists of two subactivities—experimental testing results and parameter identification.

Structural parameter identification is the art of reconciling an analytical model of a structure with experimental data using optimization. The identified parameters should be useful for structural condition assessment in the geometric space. The principle behind structural parameter identification is not new, but, in recent years, increased computational capability has resulted in

significant progress in algorithm development and experimental data processing. (See references 45, 46, 47, 48, and 49.) Doebling et al. summarized current damage identification methods using measured vibration data; however, none of the papers cited discussed parameter identification or bridge foundation condition assessment.<sup>(50)</sup>

As a minimum input, structural parameter identifications require some structural response measurements to static or dynamic loads. Figure 1 shows typical excitations and outputs of a parameter identification system. Structural responses to controlled or operating excitations are combined within the parameter identification system to produce either structural modal estimates or structural element parameter estimates. When controlled excitations are used, the excitation information can be added in the parameter identifications; however, a more practical approach is to perform structural parameter identifications with unknown operating excitations.

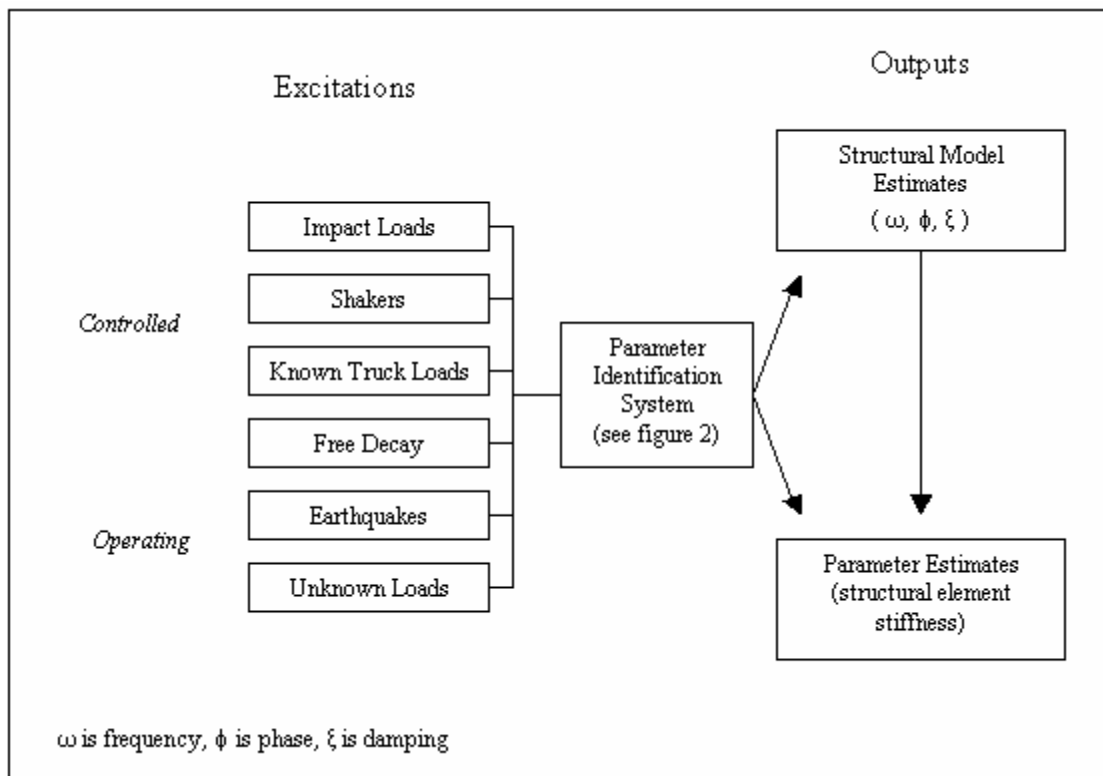


Figure 1. Diagram. Parameter identification system excitation and output options.

Figure 2 shows that structural parameter identification can be classified into problems with and without mathematical models. Then the mathematical models are subdivided into static and dynamic models. The static model is further divided into displacement and rotational measurements and strain measurements. The dynamic model is divided into time domain and frequency domain. Structural parameter identification with no mathematical models is subdivided into neural network, signal processing, pattern recognition, and expert systems.

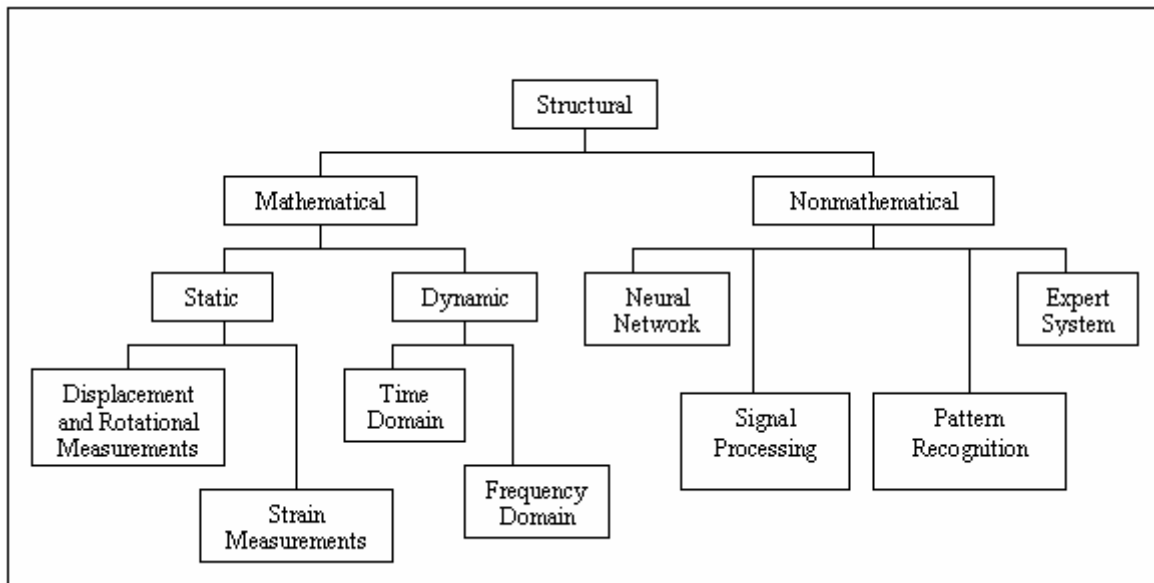


Figure 2. Diagram. Structural parameter-identification system tree.

### ***Parameter Identification with a Mathematical Model***

If a mathematical model exists, or it is possible to make reasonable assumptions about structural connectivity and general properties, an FEM is useful. An optimization-based method can be used to adjust FEM parameters so that the differences between the analytical and experimental data are minimized. Major differences between the FEM and experimental results are classified as damage. At present, most of the static or dynamic FEM excitations are limited to producing linear-elastic responses of a structure regardless of any damage that structural components might have experienced.

**Static Testing:** Static testing is based on measured deformations induced by static loads. Comparatively little research has been performed using static loads, although static testing is analytically and computationally simpler than dynamic testing. Static testing can be easily applied on bridges using stationary truck loads or lateral pullback forces. Either displacements and rotations measurements or strains measurement can be determined. The displacements and rotations measurements can be used easily in FEM parameter estimation algorithms; however, static testing has limited general applications because most practical excitations are dynamic in nature.

Sanayei and Nelson proposed parameter estimations using static displacements and rotations measured at a subset of degrees of freedom (DOF).<sup>(51)</sup> Sanayei and Onipede expanded this work to estimate parameters with static loads applied at one subset of DOFs and displacements measured at another.<sup>(52)</sup> In both studies, structural element stiffness was successfully estimated including element failures in stable structures. Hajela and Soeiro successfully developed

parameter estimations using simulated static deflections and vibration modes.<sup>(53)</sup> Banan and Hjelmstad<sup>(54)</sup> and Banan et al.<sup>(55,56)</sup> estimated stiffness parameters using incomplete sets of static load and displacement measurements. Bruno formulated a parameter identification technique to locate and characterize loose joints of a deployable space truss using actuator-induced static loading and unloading.<sup>(57)</sup>

Strains on a structural element are caused by both bending and axial deformations; therefore, strain measurements can capture structural element behavior, as well. Warren and Malvar monitored temperature strains and strains caused by slow-moving cranes on naval piers.<sup>(58)</sup> Sanayei and Salehnik developed parameter estimations for linear-elastic structures, using static strains and preserving structural connectivity.<sup>(59)</sup> Numerical simulations on truss and frame structures demonstrated the ability to identify all or a portion of structural cross-sectional properties including element failures.

**Dynamic Testing:** Most previous experiments have been done with dynamic excitations. Parameter estimations can be performed in either time or frequency domain to obtain structural parameters with identified or measured modal properties.

Directly using dynamic testing data in the time domain prevents further contamination resulting from data processing. Ibrahim and Mikulcik developed the algorithm that uses free vibration response of a structure to determine its modal parameters.<sup>(60)</sup> Ibrahim and Pappa applied this technique to large modal testing.<sup>(61)</sup> Seibold and Fritzen applied the Extended Kalman Filter technique to a nonlinear system and estimated unknown states and parameters simultaneously.<sup>(62)</sup> The Extended Kalman Filter technique might show poor convergence because of poor initial estimates or inaccurate assumptions regarding noise. A filter can be tuned to reduce the problems. Hjelmstad et al.<sup>(63)</sup> developed a robust time-domain estimator using velocities and displacements derived from the measured accelerations. This method can accommodate structural responses sampled incompletely in time, state, and space, and it is applicable to complex structural systems. Ghanem and Shinozuka evaluated four of the most popular methods for time domain parameter estimations with experimental data in a laboratory.<sup>(48)</sup> Based on the expertise required for each method and the quality of the estimated results, the method of recursive least squares with exponential memory was found to be the most promising.<sup>(64)</sup>

Dynamic testing data in the frequency domain is more compact than that in the time domain, and it more readily reveals structural modal properties. Earlier work by Baruch,<sup>(65)</sup> Berman and Nagy,<sup>(66)</sup> Chen et al.,<sup>(67)</sup> Collins et al.,<sup>(68)</sup> and Kabe<sup>(69)</sup> has laid the groundwork for more recent applications. Beck and Jennings estimated optimal modal parameters using a minimized output-error function and earthquake ground motion.<sup>(70)</sup> Because of noise and limited test locations, only dominant modes were identified. Natke and Yao developed a damage-detection method based on multiple data sets where each set was obtained from different locations on a structure.<sup>(71)</sup> Stubbs and Osegueda developed a theory using changes in modal properties in beams, plates, and shells to detect damage.<sup>(72)</sup> The validity was demonstrated with cantilevered specimens with known damage.<sup>(73)</sup> This theory was refined and applied to offshore structures by Kim and Stubbs.<sup>(74)</sup> Dascotte was able to successfully update structural models using modal properties.<sup>(75)</sup> Smith and Beattie developed a method for optimal estimation of model parameters using inconsistent modal test data for large space structures.<sup>(76)</sup> Chen and Lurie used active members instead of external forces to induce vibrations and measured displacement responses.<sup>(77)</sup> Modal parameters were

identified with equal or better accuracy than with conventional excitation tests. Fritzen and Zhu measured TFs by exciting mechanical models with broadband impulse spectrums, and the FEMs of the real structures were updated successfully.<sup>(78)</sup> Gornshteyn used selected frequencies and incomplete mode shape measurements for optimal parameter estimation at the structural element level.<sup>(79)</sup> Aktan et al.<sup>(3)</sup> successfully correlated the FEM and bridge load rating for a three-span continuous bridge using modal test data. Banan and Hjelmstad developed a method with sparsely sampled data in space, time, and state.<sup>(54)</sup> Liu minimized the norm of the modal force error to obtain the elemental properties of a truss structure.<sup>(80)</sup> Olson et al. performed modal testing on a bridge with unknown foundations.<sup>(4)</sup> Capabilities of modal testing to identify the unknown foundation characteristics were not confirmed. Farrar et al. studied the I-40 bridge over the Rio Grande River in Albuquerque, NM, with both FEM and experimental data.<sup>(81)</sup> The researchers concluded that the analytical and measured resonant frequencies or modal shapes were not sensitive to the damage through the plate girder.

Strains do not relate to mode shapes directly, but Yao et al.<sup>(82)</sup> developed a damage-detection method using vibration signature analysis and the concept of “strain mode shapes.”<sup>(83)</sup> Strain measurements were found to be more sensitive to local damage and better at identifying damage than were displacement measurements.

### ***Parameter Identification without a Mathematical Model***

Parameter identification can be performed without a mathematical model in terms of the measured input and output, and the underlying mechanics can be treated as a black box. These methods are neural network, signal processing, pattern recognition, and expert system.

Ignoring the underlying mechanics involved with a problem, a neural network attempts to match a predefined pattern. Wu et al. performed a feasibility study to explore the use of neural networks in structural damage assessment.<sup>(84)</sup> Successful application requires that the neural network be trained to identify both damaged and undamaged structural behavior. Case studies at a three-story shear frame showed promising results. Masri et al. trained neural networks to predict the response of a damped Duffing oscillator.<sup>(85)</sup> The neural network successfully predicted the response of this nonlinear oscillator for both deterministic and stochastic excitations; however, significant issues must be resolved before neural networks can be applied to complex structures.

Signal processing produces structural modal properties from the experimental data; however, it is difficult, if not impossible, to identify the specific location of the damage without a mathematical model. Shinozuka et al. used the autoregressive moving average (ARMA) model to simulate multivariate random processes and prescribed correlation function matrices.<sup>(86)</sup> Unlike the Fast Fourier Transform (FFT) method, the analysis using the ARMA representation is not limited to computer memory availability. Signal processing can be used to extract the structural modal properties, which can then be used as input to a parameter-estimation system to identify structural element properties.

Kim and Stubbs used hypothesis testing and statistical pattern recognition for damage location.<sup>(74)</sup> They demonstrated the proposed algorithm to locate and estimate the severity of damage on a 41-member simplified jacket-type offshore platform. Stubbs et al. verified this algorithm on an instrumented multispan bridge located in New Mexico.<sup>(87)</sup> The damage was

located accurately with three modes of vibration and no prior knowledge of the bridge material properties. This algorithm requires a mathematical model to identify the mode shapes; however, the damage location scheme is performed with pattern recognition and does not require a mathematical model.

An expert system can use both quantitative and qualitative data to assess the severity of damage in a structure. Because an expert system relies on expert judgment, it may not be possible to locate damage that is not apparent from a visual inspection. Ross et al. quantified the linguistic variables used to describe damage as fuzzy sets.<sup>(88)</sup> The fuzzy set, numerical data, and rules comprise the knowledge base for the expert system. The proposed bridge substructure evaluation and monitoring system will not use an expert system, so more examples are not provided.

Huang et al. recently developed the HHT, a technique for applying time domain data that makes it possible to analyze vibration data and determine the resonant frequencies of systems instantaneously by location throughout a time domain record for nonlinear, nonstationary systems.<sup>(5)</sup> In other words, the HHT method helps determine short-duration changes in the system response frequencies that indicate the lower frequency resonance associated with damage to a structural member. This technique promises to be more sensitive to short-term changes through lower frequency, nonlinear responses when a moving or varied excitation force is most actively exciting and closest to a damaged member. Thus, the masking of lower frequency responses associated with damage to a single member is better analyzed using the HHT approach. This comparatively new technique, applied late in this research, is discussed in chapter 7.

### **Uncertainty in Structural Parameter Identification**

The purpose of structural parameter identification is to use measured data to determine the best-guess values of preselected unknown parameters. Uncertainty in structural parameter identification results from inherent errors and noise in the measured data, modeling errors, and some techniques that inherently estimate a biased parameter.

Regardless of the type of testing data used for parameter identification, sensors are subject to measurement noise. In the presence of noisy measurements (input error), the parameter identification algorithm will produce results different than those with noise-free simulated input data. The difference between the estimated parameters and true values (output error) is evaluated to determine the effect of input errors for a specific subset of measurements. It is economical to use as few inputs (applied forces and measured responses) as necessary, but each set of inputs has its own input-output error relationship; some sets of measurements are more sensitive to errors than others.<sup>(89,90)</sup> Therefore, designing a practical parameter identification system requires a careful selection of sensor locations to produce meaningful results at minimum cost. Because sensor location selection has a large effect on input-output errors, the most promising subset of measurements must be selected.

Hafka and Adelman proposed two integer program methods for selecting actuator locations to correct surface distortions of an orbiting spacecraft.<sup>(91)</sup> DeLorenzo proposed an improved version of the heuristic method, published in 1990.<sup>(92)</sup> DeLorenzo's sensor and actuator configuration was used for control of large space structures. Hajela and Soeiro proposed the idea of dominant

displacements for both static and dynamic testing, indicating that certain forces and responses are more representative of the structural system.<sup>(53)</sup> They also showed that errors are more prevalent when loading does not result in an equal stress distribution in each of the structural elements. In a related paper, they showed through the experimental results that a uniform stress loading produces excellent results.<sup>(93)</sup> Kammer developed the method of effective independence for sensor location selection for on-orbit modal identification.<sup>(94)</sup> A method developed by Holnicki-Szulc et al. was based on the progressive collapse analogy for optimal locations of actuators controlling the selected vibration modes.<sup>(95)</sup> Lim determined that damage is most easily detected for the elements that are fully participating in load bearing and contain the most energy.<sup>(96)</sup> Damage in such elements appears in the parameter estimation results. If there is a systemwide change in the estimated parameters, individual element damage cannot be isolated. Sanayei et al. studied the effect of measurement noise on the parameter estimates, and the researchers proposed a heuristic best-in-worst-out method for the preselection of static forces and displacement measurements based on error sensitivity analysis.<sup>(97)</sup> Sanayei and Saletnik applied the method to static strain measurements.<sup>(98)</sup>

Uncertainty in modeling and algorithms is inevitable, and further study in performing successful parameter identifications is needed. Brown developed a parameter identification procedure to estimate structural model parameters using measured responses and expert judgment.<sup>(99)</sup> Fuzzy updating was used to supply subjective information when numerical measurements were unavailable. Beck proposed a statistical system identification procedure that used averaged response measurements to estimate the structural model parameters.<sup>(100)</sup> Gangadharan et al. proposed a probabilistic system-identification method to infer structural model parameters of flexible joints.<sup>(101)</sup>

## **Damage Indices**

A measure of damage or a damage index is required to make a rehabilitation decision. This information helps interpret the stiffness changes the parameter estimation procedures identified. A damage index, often normalized to a fixed scale for structural integrity, is an essential criterion in the damage assessment process.

Most damage indices available have been developed from research in the earthquake engineering community. During an earthquake, a structure is expected to experience inelastic response; consequently, it is possible to measure factors such as ductility and dissipated energy. Researchers Newmark and Rosenblueth,<sup>(102)</sup> Bertero and Bresler,<sup>(103)</sup> Banon and Veneziano,<sup>(104)</sup> Park and Ang,<sup>(105)</sup> Stephens and Yao,<sup>(106)</sup> Yao and Munse,<sup>(107)</sup> and Chung et al.<sup>(108)</sup> developed damage indices based on ductility ratios, cumulative damage, and component damage. Because of the redundancy of engineered structures, the damage estimate obtained for a simple structural element does not necessarily correspond to the damage sustained by the structural system. Bertero and Bresler,<sup>(103)</sup> Park and Ang,<sup>(105)</sup> DiPasquale et al.,<sup>(109)</sup> Pandey and Barai,<sup>(110)</sup> and other researchers have expanded their element damage indices to structural system damage indices with the use of weighting functions. Chung et al. discussed the importance of understanding the use of a structural damage index in its derivation.<sup>(108)</sup> To determine the integrity of a full structural system, the local damage indices for each element in the structural system can be combined with a Monte Carlo analysis to determine the probability of a structure's failure.

Nondestructive bridge condition assessment is performed either by visual inspection or with controlled or operating excitation, and it requires elastic structural responses. In a bridge management system, engineers commonly conduct visual inspections to assign a damage index to a bridge. Similarly, structural identification results must be interpreted on a comparable scale in a bridge management system. Aktan et al. related bridge damages to the incremental increase of structural flexibility.<sup>(3)</sup> Farrar and Cone determined that damage to a bridge superstructure must be significant before the global dynamic properties are affected.<sup>(111)</sup> Mayes applied the structural translation and rotation error-checking algorithm to locate the damage on a complex bridge that crosses the Rio Grande River in New Mexico.<sup>(112)</sup> Stubbs et al. located the damage in the same Rio Grande bridge by successfully using the first few dynamic modes, a baseline structure, and pattern recognition.<sup>(87)</sup>

Not much research has been done on bridge foundation identification and condition assessment. Reese and Stokoe performed a study on what instrumentation should be used for pile axial load tests.<sup>(113)</sup> Richart and Whitman conducted a study that compared experimental and theoretical results for a model footing foundation.<sup>(114)</sup> They found that footings on a semi-infinite elastic plane might be modeled as a mass-spring-dash pot system. Samtani et al. found that 2-D stress elastic-plastic finite element analysis underestimates the pier resistance to ship impact because it does not account for the wedging resistance in the plane strain analysis and the side friction on the out-of-plane sides of the caissons.<sup>(115)</sup> They presented a methodology that helps extrapolate 2-D models to account for 3-D effects. Further research is needed in this area.

In addition to the efforts outlined above, the interest in instrumentation to monitor the health and condition of structures is not limited to the civil infrastructure research community. In fact, research has been underway in areas such as aerospace, mechanical, electrical, computer, and systems engineering. Certain elements of this research form reasonably mature fields on their own, such as Norman et al.,<sup>(116)</sup> Pau,<sup>(117)</sup> Patton et al.,<sup>(118)</sup> and Willsky.<sup>(119)</sup> Therefore, it is logical and potentially advantageous to approach instrumented bridge health and condition monitoring from an interdisciplinary point of view.

A damage index provides information about the state of a structure when the index was measured. Long-term structural deterioration is defined as the change in value of structural parameters at incremental stages during the design life of a structure. Such changes in structural parameters can be represented as time-dependent damage indices. Damage accumulates and reaches a certain level such that the structure becomes deficient. Structural deterioration models can be used to predict the change in structural parameters or damage indices considering the intended structural loads, environmental conditions, maintenance practices, and historical data.

### **Bridge Management Systems**

In the past 2 decades, the relationships between bridge conditions and rehabilitation decisions have begun to be formalized in the form of BMSs. A BMS is an integrated collection of the following elements:

- Organizational roles.
- Procedures.
- Data.

- Analytical tools.
- Computer programs.
- Support services.

BMSs can be used to accomplish the following tasks:

- Determine bridge needs.
- Optimize funding allocation and project scheduling with budget constraints.
- Develop persuasive funding requests.
- Perform what-if analyses and policy analysis.
- Monitor bridge condition.

BMSs can be used to answer the following example questions:

- What is the history of the bridge and what is its condition?
- What are the implications of project decisions?
- What are the project priorities and schedules?
- What is the project budget and what are the tradeoffs?
- What is the cost of alternative standards?
- What is the value of preventive maintenance?

As new types of data are generated and the relationships between structural condition and vulnerability to natural hazards are better understood, BMSs can assist in preservation and improvement decisions during the lives of bridges.

The current managerial focus for a BMS requires the ability to plan and forecast maintenance needs or rehabilitation procedures. The two most widely known BMSs, Pontis<sup>®(120)</sup> and BRIDGIT<sup>©</sup>, are described in Czepiel<sup>(121)</sup> and Egri et al.<sup>(2)</sup> The history of bridge management is also described in Czepiel.<sup>(121)</sup> The next three paragraphs briefly review changes and advances in three areas: the aging bridge inventory, regulations, and technical advances. Examples illustrate the need for BMSs and their capabilities.

### ***Aging Bridge Inventory***

Although the condition of the Nation's bridges gradually improved over the period from 1992 to 2004, the percent of deck area on deficient bridges still exceeds the targets, which in 2004 were 26.4 percent for national highway system bridges and 28.8 percent for non-national highway system bridges.<sup>(122)</sup> Meanwhile, highway travel grows annually, and financial resources are highly constrained at all levels of government. The 50th anniversary of the interstate highway system will be observed in 2006. The system is aging, and bridge owners have expressed concern about problems caused by age, fatigue, impact, and the environment. These issues have encouraged many States to pursue the development of BMSs as a systematic method for managing some of the problems.

### ***Regulatory Constraints***

The Intermodal Surface Transportation Efficiency Act (ISTEA) of 1991 required States to develop and use BMSs.<sup>(123)</sup> The requirements were detailed in an interim final rule effective January 3, 1993.<sup>(124)</sup> The rule was issued as interim “because of concerns about the data burden that states, metropolitan planning organizations (MPO), and local agencies may have.”<sup>(125)</sup> Based on comments and reports from many agencies of burdensome experiences, ISTEA, as of November 1995, did not mandate BMSs; however, FHWA encourages agencies to implement the systems and required States to report on progress by October 1996.<sup>(123)</sup> The spirit of ISTEA is evident as numerous States continue to pursue BMS development.

### ***Technical Advances***

Several technical advances are likely to have significant effect on state-of-the-art BMSs. These advances range from faster, larger, more portable, and more flexible computer systems, to new data collection technologies and sensors for data acquisition. In addition, advances in software, graphical user interfaces, and multimedia technologies facilitate integration of BMSs into organizations.

### **The Role of Bridge Substructure Condition in Bridge Management Systems**

In a BMS, the role of bridge substructure condition varies with the specific implementation. In the National Bridge Inventory, bridge substructures have an overall rating based on visual inspection. Each State should maintain, at a minimum, a history of bridge substructure condition rated visually.

Beyond the National Bridge Inventory rating, Pontis provides bridge substructure as a default element category definition; specific elements can constitute a condition. Elements can be user defined or drawn from a list of default element definitions that include piers, pier walls, and abutments of various materials (concrete, reinforced concrete, masonry, and timber). Condition states and actions for each element are also provided. For example, a reinforced concrete submerged pile (element 227) in condition state 3 (exposed steel) would require cleaning and patching (action item 41). Pontis also allows users to define condition units as parts of the same element that are in different environments and may have different conditions.<sup>(126)</sup>

BRIDGIT is similar to Pontis in inventory and condition rating. Additional user-defined data items can be added to the inventory and condition information is included as a percentage of a particular element in a given condition state. BRIDGIT appears to offer some additional flexibility in bridge-specific condition data such as load rating. The limits of this flexibility warrant further exploration.

In general, visual inspection is the widely used means for including condition data in a BMS.<sup>(121)</sup> This has several disadvantages. First, it is qualitative, and ratings generally do not exhibit a high degree of consistency or repeatability. Second, the rating reflects an aggregate measure of condition. For example, microscopic flaws can be catastrophic, but they will never be reflected in the rating. Third, the ratings are not closely related to the cause of the problem or the response. Finally, the rating accuracy is unknown.

While there is clearly a role for improving and enhancing the status of bridges in this country through better NDE and its integration with BMSs, several issues must be addressed.

A dynamic bridge substructure evaluation and monitoring system is just one aspect of nondestructive testing appropriate for bridges. How valuable is this information compared with other NDE methods? Answering this question requires consideration of the cost of NDE.<sup>(127)</sup>

Because BMSs currently include only visual condition data, the value of multiple sources of data needs to be explored. NDE data might not substitute for visual condition ratings, but could complement, reinforce, or support visual condition rating data.

Much of the work on dynamic bridge evaluation is in search of a specific type of defect. No systematic attempts have been undertaken to analyze dynamic testing data in terms of the effect on bridge life cycle costs, the opportunities to reduce the probability of such defects in similar bridges, and the effectiveness of remedial strategies.

The influence of low probability, high impact catastrophic events on bridge life cycle costs need to be considered. Bridge engineers have been successful at avoiding catastrophic failure but the cost must be accounted for.<sup>(128)</sup> The burdens of data collection and analysis also should be explored.<sup>(128)</sup>

The opportunities to improve BMSs using a dynamic bridge substructure evaluation and monitoring system lie in the following areas:

- Monitoring.
- Measuring vulnerability to scour, seismic events, and impacts such as vehicles, boats, ice, flood debris.
- Integration into a BMS of problem-specific inspection and condition data.
- Determination of optimal inspection frequencies.

Recent work on structural reliability, data needs for a BMS, and expert systems such as RETAIN, an expert system for retaining wall rehabilitation, may provide some insight into opportunities to integrate into BMSs in use or under development a dynamic bridge substructure evaluation and monitoring system.<sup>(129, 130, 131)</sup>

## **CHAPTER 3. DESCRIPTION OF MODAL VIBRATION TEST BRIDGES**

### **INTRODUCTION**

In this project, four bents of three east Texas highway bridges were tested with modal vibration. The Trinity River Relief Bridge Number 4, located on old U.S. Highway 90 east of Houston near Liberty, TX, was a common type of flat concrete slab bridge built in the 1920s. The Texas DOT (TxDOT) was in the process of demolishing and replacing the bridge because of excessive differential settlements, which provided an excellent opportunity to investigate the bridge substructure's response to the effects of simulated scour and seismic events through dynamic modal vibration. After testing the initially sound pile bent substructures, the testing was accomplished by intentionally excavating soil from around selected piles to simulate scour, and then breaking piles and piles with footing foundations to simulate earthquake damage.

Two newer prestressed concrete slab-on-girder bridges that cross Texas State Highway 6 near College Station and Bryan, TX, also were included in the research. The Woodville Road Bridge and the Old Reliance Road Bridge are typical of 1960s bridge construction in the United States based on of the American Association of State Highway Officials (AASHO) standard 1965 specifications. These two bridges are similar in structural design except for different foundation types. The Woodville Road Bridge has a concrete spread footing; the Old Reliance Road Bridge has steel piles below a concrete pile cap. Thus, testing for this project included both an old and two newer bridges and shallow and deep foundations. The following section discusses bridge details for the three test bridges.

### **TRINITY RIVER RELIEF BRIDGE**

The Trinity River Relief Bridge, located on U.S. Highway 90 just west of Liberty, TX, was built in the 1920s. It consisted of four bridge structures. For this testing, a Vibroseis truck belonging to the Geotechnical Engineering Center of the University of Texas at Austin was used to excite the bridge substructures with vertical vibration force. Bents 2 and 12 of the western-most relief structure 4 were selected for dynamic testing. Figure 3 shows the Vibroseis truck over bent 2. At the time of these field tests, the bridge structure was being demolished and replaced because of excessive differential settlements of the concrete pile foundations, as shown in figure 4.



Figure 3. Photo. Relief structure 4 of the Trinity River Relief Bridge with the Vibroseis truck over bent 2.



Figure 4. Photo. Excessive differential settlements on relief structure 4, Trinity River Relief Bridge.

Relief structure 4 had a 6.1-meter (m) (20-foot (ft))-wide roadway. The structure consisted of 151 reinforced concrete slab panels directly supported by 66 concrete pile bents with spans of 5.49 m (18 ft). The nominal thickness of these concrete slab panels was 0.41 m (1.34 ft). The concrete slabs were reinforced with number 7 steel bars at a spacing of 1.53 m (5.02 ft) in the longitudinal direction and number 4 steel bars at a spacing of less than 0.61 m (2 ft) in the transverse direction. The concrete panels had one fixed end and a free expansion end, resulting in both fixed and roller connections sitting on each intermediate bridge bent. The asphalt topping had been removed to the concrete slab level at the time of the field tests.

Bents 2 and 12 were tested because they had the same superstructures with different foundation types. Bent 2 was the second pile bent to the east from the west abutment of relief structure 4. Bent 2 was composed of a concrete beam cap supported by four concrete piles with a concrete strip footing that had been added at ground level in an attempt to minimize further differential settlement. The beam cap on top of the 7.63-m (25-ft)-long piles was 7.17 m (23.52 ft) by 0.61 m (2 ft) by 0.737 m (2.42 ft) (length by width by height) while the pile/columns had a cross section of 0.356 m (1.17 ft) by 0.356 m (1.17 ft). The beam cap was reinforced longitudinally with seven number 7 steel bars, while there were number 4 steel stirrups at spacing of 0.458 m (1.5 ft) in the transverse direction. The concrete pile/columns spanned 1.93 m (6.33 ft) symmetrically. Each pile/column had four number 8 steel bars at four corners of its cross section with number 2 steel hoops at variable spacing from 5.08 to 15.24 centimeters (cm) (2 to 6 inches) along the column. The pile/column length between the top of the concrete strip footing and the bottom of the concrete beam cap was 2.21 m (7.25 ft). A 7.08 m (23.22 ft) by 1.22 m (4 ft) by 0.61 m (2 ft) (length by width by thickness) concrete strip footing surrounded the four concrete piles. No concrete reinforcing details were available for the concrete strip footing. Below the concrete strip footing, the four concrete piles continued. The concrete piles had a 0.356-m by 0.356-m (14-inch by 14-inch) square cross section at the top by the beam and tapered to 0.203-m by 0.203-m (8-inch by 8-inch) square cross section at the pile tip. The details of bent 2 are illustrated in figure 5. (Figure 5 reflects the excavation of the piles that is described in chapter 4, and it does not show the concrete footing that was just below ground level.) The embedded length of the concrete piles was 4.80 m (15.74 ft) from the bottom of the concrete strip footing to the concrete pile tips for a total pile/column length of 7.63 m (25 ft).

Bent 12 was the twelfth pile bent to the east from the west abutment of relief structure 4. Bent 12 had the same structural components as bent 2, except there was no concrete strip footing at ground level. As a result, the exposed pile/column length between the ground level and the bottom of the beam cap was 2.14 m (7 ft), and the embedded length of the concrete piles was 5.49 m (18 ft) from ground level to the pile tips—a total length of 7.63 m (25 ft).

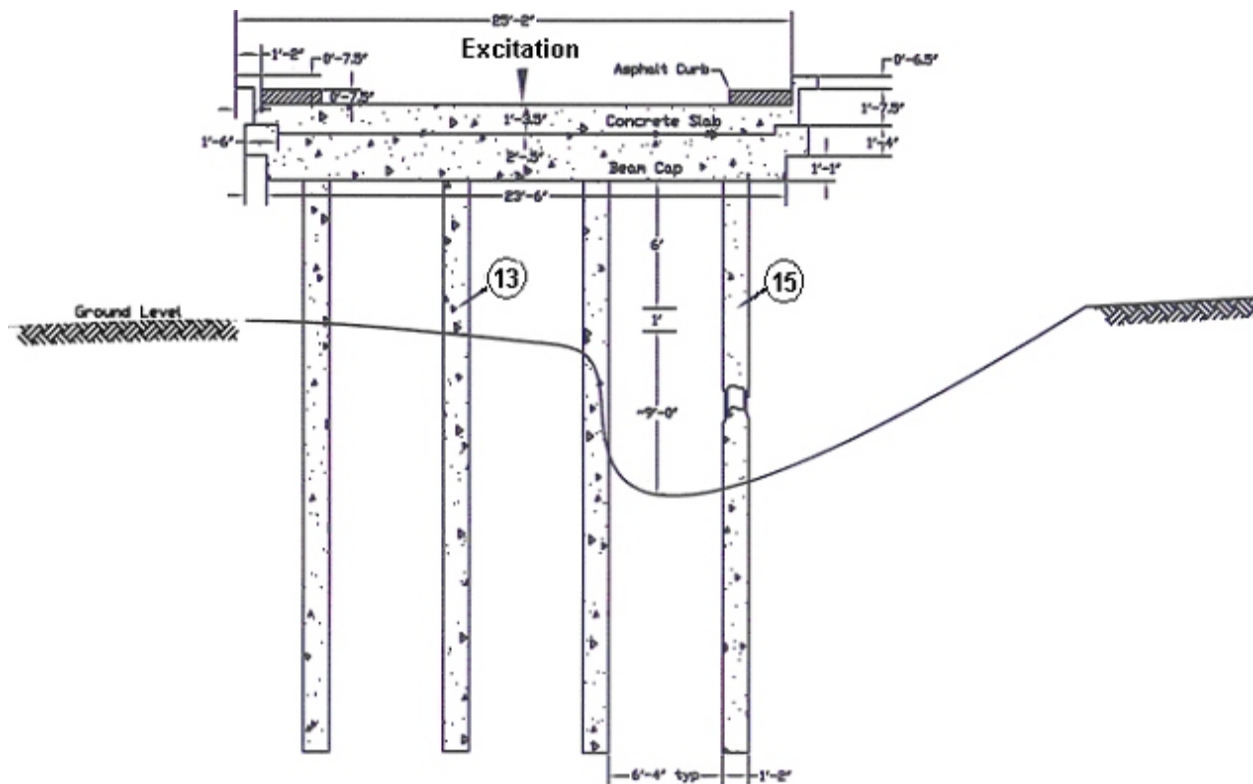


Figure 5. Diagram. Geometric details of bent 2, structure 4, of the Trinity River Relief Bridge.

Construction design details for the mid-1920s bridge called for steel in tension to be designed for a working stress of 110,240 kilopascals (kPa) (16,000 poundforce per square inch (lbf/inch<sup>2</sup>, or psi) while concrete in compression was designed to have a working stress of 4,479 kPa (650 psi). The concrete mixture designs were 1:2:4 with maximum aggregate of 2.54 cm (1 inch) for beam caps and slabs and 1:2:3 with maximum aggregate of 1.905 cm (0.75 inch) for columns and piles. The concrete of bents 2 and 12 showed little deterioration after more than 70 years of service, and only minor cracks and honeycombing were observed at the time of field tests.

Field ultrasonic pulse velocity (UPV) tests on bent 12 for this project revealed an average pulse velocity of 4,148 meters per second (m/s) (13,600 feet per second (ft/s)). Assuming normal weight concrete, about 2,323 kilograms per cubic meter (kg/m<sup>3</sup>) (145 pounds per cubic foot (lb/ft<sup>3</sup>)), and a Poisson's ratio of 0.25, this velocity corresponds to a Young's modulus of 33.07 E+6 kPa (4.8 E+6 psi). See the UPV method in the American Concrete Institute (ACI) Manual of Concrete Practice.<sup>(132)</sup>

The seismic properties of the subsurface soils of all three bridges were investigated with the spectral analysis of surface wave (SASW) method at the time of field tests for this project. The seismic velocity data were used in dynamic modeling studies. The method is illustrated in figure 6, and a photo of the testing is shown in figure 7. The ACI Manual of Concrete Practice also gives details on the SASW method.<sup>(132)</sup>

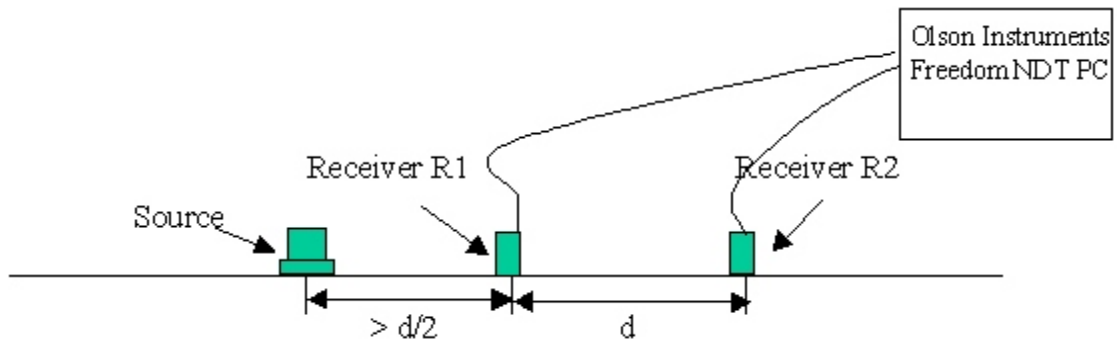


Figure 6. Diagram. SASW method.



Figure 7. Photo. SASW tests at bent 12, structure 4, Trinity River Relief Bridge.

SASW tests involve measuring the variation of surface wave velocity versus wavelength (the dispersion curve) without drilling borings. The SASW experimental results were theoretically matched using the WinSASW software of the Geotechnical Engineering Center of the University of Texas at Austin. The soil layer thickness and shear and compression wave velocity profiles were determined from this theoretical matching for use in modeling of the bents. The SASW results indicated that the shear wave velocity profile consists of four soil layers with shear wave velocities varying from 76.25 m/s (250 ft/s) to 244 m/s (800 ft/s). Based on the SASW results and assumed values of Poisson’s ratio and density for the clay soils, the shear wave velocity profile was determined. The results are shown in table 1.

Table 1. Shear wave velocity profile results from the Trinity River Relief Bridge site.

<b>Soil Shear Wave Velocity from WinSASW Model (m/s (ft/s))</b>	<b>Layer Thicknesses from Ground Level with Increasing Depth (m (ft))</b>	<b>Unit Weight (kg/m<sup>3</sup> (lb/ft<sup>3</sup>))</b>	<b>Assumed Value of Poisson’s Ratio</b>
76.2 (250)	1.8 (6)	1762 (110)	0.35
121.9 (400)	2.4 (8)	1842 (115)	0.35
213.4 (700)	2.4 (8)	1922 (120)	0.30
243.8 (800)	3.0 (10)	1922 (120)	0.30

## **WOODVILLE ROAD BRIDGE**

Woodville Road Bridge crosses Texas State Highway 6 between College Station and Bryan in Brazos County, TX. Built in the 1960s, it consists of four bridge spans with an equal span length of 24.4 m (80 ft). The first intermediate bent from the southwest end of the bridge, illustrated in figure 8, was selected for dynamic testing. At the time of field tests, this four-lane bridge carried two lanes eastbound and two lanes westbound over State Highway 6.

The Woodville Road Bridge has a 7.93-m (26-ft)-wide roadway; its superstructure consists of a 16.51-cm (6.5-inch)-thick reinforced concrete slab supported by four prestressed concrete I girders for each span. The spacing between two adjacent girders at each span is 2.24 m (7.35 ft). For each span, the reinforced concrete slab is constructed compositely with the four prestressed concrete girders, but four span composites of the slab and the girders are separated from each other at the three intermediate bents. The prestressed concrete girders are 1.07 m (3.5 ft) high and 0.560 m (1.84 ft) wide with a 20.32-cm (8-inch)-wide web and two 19.05-cm (7.5-inch)-thick flanges. There are two end diaphragms and two interior diaphragms for each span. The interior diaphragms are posing at one-third points of the spans. The prestressed concrete girders are resting directly on the beam caps through polystyrene bearing pads. The extension of the girder ends into the beam caps is 0.267 m (10.5 inches); therefore, the connections between the bents and the girders can be modeled as pinned ends.



Figure 8. Photo. Western pier of the southwestern span of the Woodville Road Bridge.

The tested bent is composed of a reinforced concrete beam cap supported by two concrete columns with two concrete spread footings at approximate 1.83 m (6 ft) below the ground level. The concrete beam cap is 7.7 m (25.5 ft) by 0.839 m (2.75 ft) by 0.839 m (2.75 ft) (length by width by height); the two concrete columns have a cross section 0.763 m (2.5 ft) in diameter. The concrete beam cap is reinforced longitudinally with four number 11, eight number 10, two number 9, and two number 5 steel bars; there are number 5 steel stirrups at variable spaces from 12.7 cm (5 inches) to 0.407 m (1.33 ft) in the transverse direction. The two concrete pier columns are spaced 4.88 m (16 ft) apart. Each concrete column has eight number 9 steel bars in the vertical direction with a number 3 spiral at a 15.24-cm (6-inch) pitch along the concrete column. Each concrete column extends at least 0.686 m (2.25 ft) into the concrete beam cap, creating a fixed connection between the concrete column and the concrete beam cap. The concrete column length between the top of the concrete spread footing and the bottom of the concrete beam cap is 6.38 m (20.93 ft), but the distance between the bottom of the concrete beam cap and ground level is about 4.58 m (15 ft). The column axial design load is 128,936 kg (284,000 lb) per column. The concrete spread footings are 2.14 m (7 ft) by 2.14 m (7 ft) square reinforced concrete with a thickness of 0.763 m (2.5 ft). For each concrete spread footing, there are seven number 9 steel bars in each direction on the bottom. Eight number 9 steel bars extend 0.864 m (2.83 ft) from the concrete footing bottom into the concrete column. These dowels are bent to 90 degrees and extend 0.43 m (1.42 ft) horizontally away from the concrete columns. As a result, the concrete spread footing can be considered as having a fixed connection with the concrete columns.

This bridge was designed according to AASHO 1965 standard specifications and interim revisions. All concrete was designed to be Class C; however, no field measurements for construction material properties were conducted for this bridge.

The soil layer profiles at the Woodville Road Bridge were investigated by the SASW method at the time of field tests for this project. Based on the SASW results and assumed values of the Poisson’s ratio and density for the clay to sand soils, the shear wave velocity profile was determined as shown in table 2. The SASW results indicated that the shear velocity profile consisted of five soil layers with the shear wave velocities of soil varying from 122 m/s (400 ft/s) to 366 m/s (1,200 ft/s).

Table 2. Shear wave velocity profile results from the Woodville Road Bridge site.

<b>Soil Shear Wave Velocity from WinSASW Model (m/s (ft/s))</b>	<b>Layer Thicknesses from Ground Level with Increasing Depth (m (ft))</b>	<b>Unit Weight (kg/m<sup>3</sup> (lb/ft<sup>3</sup>))</b>	<b>Assumed Value of Poisson’s Ratio</b>
137.2 (450)	0.6 (2)	1602 (100)	0.35
243.8 (800)	2.4 (8)	1842 (115)	0.35
121.9 (400)	2.4 (8)	1602 (100)	0.35
274.3 (900)	6.1 (20)	1922 (120)	0.30
365.8 (1,200)	6.1 (20)	2002 (125)	0.28

### **OLD RELIANCE ROAD BRIDGE**

The Old Reliance Road Bridge is similar to the Woodville Road Bridge except that Old Reliance has steel pilings under the intermediate bents below concrete pile caps. This bridge is also located on State Highway 6 between College Station and Bryan in Brazos County, TX. This 7.93-m (26-ft)-wide bridge, built in the 1960s, consists of four bridge spans. Two end spans are 18.3 m (60 ft) long; the two center spans are 30.5 m (100 ft) long. The first intermediate bent from the northeast end of the bridge was selected for dynamic testing. At the time of field tests, this four-lane bridge carried two lanes eastbound and two lanes westbound over State Highway 6. The bridge is shown in figure 9.



Figure 9. Photo. Vibroseis truck over the east pier, Old Reliance Bridge.

The bridge superstructure consists of a 16.51-cm (6.5-inch)-thick reinforced concrete slab supported by four prestressed concrete girders for each span. The spacing between two adjacent girders at each span is 2.26 m (7.41 ft). The abutments and intermediate bents are skewed by 15 degrees from being transverse to the traffic direction. For each span, the reinforced concrete slab is constructed compositely with the four prestressed concrete girders, but the four span sections of the slab and the girders are separated from each other by joints at the three intermediate bents. The prestressed concrete girders are 1.37 m (4.5 ft) high and 0.381 m (1.25 ft) wide. Two end diaphragms for each span are parallel to the abutments and the intermediate bents, but the interior diaphragms for each span are perpendicular to the roadway; they have a 15-degree skew to the abutments and the intermediate bents. The two interior diaphragms for the 18.3-m (60-ft) end spans are at the one-third points of the spans, while the three interior diaphragms for the 30.5-m (100-ft) center spans are at the one-quarter points of the spans. The prestressed concrete girders are resting directly on the concrete beam caps through polystyrene bearing pads. The extension of the prestressed concrete girder ends into the concrete beam caps is 26.7 cm (10.5 inches); therefore, the connections between the intermediate bents and the prestressed concrete girders can be modeled as pinned ends.

The tested bent is composed of a reinforced concrete beam cap supported by two concrete columns with deep foundations. The concrete beam cap is 8.08 m (26.5 ft) by 0.839 m (2.75 ft) by 0.839 m (2.75 ft) (length by width by height), while the two concrete columns have a 0.763-m

(2.5-ft)-diameter cross section. The concrete beam cap of the Old Reliance Road Bridge has the same structural design as that of the Woodville Road Bridge except that the concrete pier columns are supported by concrete pile caps on 10 steel pilings per column. The concrete column length between the top of the concrete footing and the bottom of the concrete beam cap is 5.82 m (19.1 ft), but the distance between the bottom of the concrete beam cap and the ground level is about 4.73 m (15.5 ft). The nominal designed column axial loading is 128,936 kg (284,000 lb) per column. The concrete pile caps are 1.98 m (6.5 ft) by 2.23 m (7.5 ft) T-shaped (in plan view) reinforced concrete with a thickness of 0.763 m (2.5 ft). Eight number 9 steel bars extend 0.864 m (2.83 ft) from the concrete footing bottom into the concrete column; therefore, the concrete pile caps can be considered as having a fixed connection with the concrete columns. The steel pilings underneath the concrete footings are HP (bearing piles) 12 by 53 piles with varying lengths from 6.1 m (20 ft) to 7.47 m (24.5 ft). The properties of the HP 12 by 53 steel piles can be found in the American Institute of Steel Construction, Inc., manual.<sup>(133)</sup>

This bridge was designed according to AASHTO 1965 standard specifications and interim revisions. All concrete was designed to be Class C.

The soil layer profiles at the Old Reliance Road Bridge were investigated by the SASW method at the time of field tests in this project. Based on the SASW results and assumed values of the Poisson’s ratio and density for the clay to sand soils, the shear wave velocity profile was determined, as shown in table 3. The SASW results indicated that six shear wave velocity profile layers existed with the shear wave velocities of soil varying from 91.5 m/s (300 ft/s) to 518.5 m/s (1,700 ft/s).

Table 3. Shear wave velocity profile results from the Old Reliance Road Bridge site.

<b>Soil Shear Wave Velocity from WinSASW Model (m/s (ft/s))</b>	<b>Layer Thicknesses from Ground Level with Increasing Depth (m (ft))</b>	<b>Unit Weight (kg/m<sup>3</sup> (lb/ft<sup>3</sup>))</b>	<b>Assumed Value of Poisson’s Ratio</b>
121.9 (400)	0.6 (2)	1602 (100)	0.35
91.5 (300)	0.6 (2)	160 (10)	0.35
365.8 (1,200)	0.6 (2)	1922 (120)	0.30
213.4 (700)	6.1 (20)	1762 (110)	0.33
457.5 (1,500)	6.1 (20)	1922 (120)	0.28
518.5 (1,700)	6.1 (20)	2002 (125)	0.27

## **CHAPTER 4. MODAL TEST PROGRAM FOR BRIDGE SUBSTRUCTURES**

### **INTRODUCTION**

The Trinity River Relief Bridge was initially tested on November 19, 20, and 21, 1996, and retested on September 4, 5, and 6, 1997. The first field tests on this bridge were performed to better understand the frequency ranges involved and help in the selection of the appropriate sources and receivers. During the process of demolishing and replacing this bridge, the second field tests were performed for three foundation conditions on bent 12 (piles only) and bent 2 (piles through strip footing). The three foundation test conditions were forced vibration measurements with existing, undamaged bridge bent conditions; forced vibration measurements with the surrounding soil excavated and two piles partially exposed in each bent; and forced vibration measurements with two piles excavated and one outside pile broken in each bent. The Woodville Road Bridge (footing) was tested on May 13 and 14, 1997, and the Old Reliance Road Bridge (pile cap footing on H-piles) was tested on May 15, 1997. This chapter discusses the dynamic testing instrumentation and field test procedures.

### **DYNAMIC TESTING INSTRUMENTATION**

The modal vibration tests were conducted primarily using a geophysical vibrator truck (Vibroiseis) to excite the bridge bents from the bridge deck level. Limited tests were also done from the bridge decks using small vibrator and impulse sledge hammer energy sources. The vibration responses of the bridges were measured with seismic accelerometer transducers. All data were recorded on a PC-based dynamic signal analyzer. The following sections discuss the Vibroseis source, accelerometer transducers, and dynamic signal analyzer recording equipment.

#### **Vibroseis Truck**

The Vibroseis truck, shown in figure 10, was used as the primary dynamic source in this project. It is a large (gross weight of about 22,246 kg (49,000 lb)) truck with a servo-hydraulic vibrator mounted on it. The vibrator has a 3,405-kg (7,500-lb) reaction mass that is capable of generating vertical dynamic forces above 311,500 newtons (N) (70,000 poundforce (lbf)) over a frequency range from 1 Hz to 120 Hz. The type of dynamic loading functions can be steady state (frequency range from 5 Hz to 100 Hz), swept frequency, random noise, or transient. The vibrator has a loading frame with single or dual points in contact with the structure being tested.

The vibrator is separated from the truck through a system of air springs, shown in figure 11. The dead weight of the vibrator itself, including the reaction mass and the load frame system, is about 9,080 kg (20,000 lb); however, a static holddown force ranging up to 218,050 N (49,000 lbf) can be applied at the loading points by adjusting the hydraulic pressure control. This static holddown force provides the base reaction for generating dynamic forces at the desired levels. Typical dynamic peak-to-peak forces ranged from 2,225 to 151,300 N (500 to 34,000 lbf) in the up-and-down vertical excitation direction. As the resonance of the loading system is about 12 Hz, this results in the generation of even higher force output levels around this frequency.



Figure 10. Photo. Vibroseis truck over Woodville Road Bridge pier.

The separation between the vibrator and the truck implies that the gross mass of the truck excluding the mass of the vibrator is part of the tested bridge; but, the vibrator itself adds an additional DOF to the tested bridge. It is important to note out that the reaction mass and servo-hydraulic system, rather than the gross weight of the truck, controls the static and dynamic force outputs. The dynamic force output actually comes from the inertial force created by the reaction mass moving at the excitation driving frequencies from the dynamic signal analyzer.



Figure 11. Photo. Vertical vibrator mechanism of Vibroseis truck.

### **Seismic Accelerometers**

Model 393C seismic accelerometers were selected to be the vibration response transducers because of their excellent response over the excitation frequency range of 3 Hz to about 80 Hz. This sensitive quartz accelerometer contains a built-in microelectronic amplifier that converts high impedance voltage signals from the quartz crystals to a low impedance (less than 100 ohm) voltage, imparting the ability to drive long coaxial cables (hundreds of meters/feet) for remote monitoring with no appreciable degradations of sensitivity and resolution. The internal amplifier is protected against blowout from excessive mechanical shocks up to 100 G.

The Model 393C seismic accelerometer uses a 0.454-kg (1-lb) stainless steel mass coupled to a sensitive quartz element with a design to minimize transverse vibration coupling effects (maximum transverse sensitivity less than 5 percent to excitations along the measurement axis). The seismic accelerometer has a nominal sensitivity of 1.0 volt per G (1 G equals  $9.8 \text{ m/s}^2$ ) (386

inches/s<sup>2</sup>). The seismic accelerometer has a discharge time constant of 20 seconds (s), nominally. This gives a low frequency cutoff (−3 decibels (dB)) of 0.08 Hz. The 5 percent down response frequency ranges from 0.025 Hz to 800 Hz and the output (for ±2.5 volts) ranges ±2.5 G with resolution of 0.0001 G. The seismic accelerometer has its resonant frequency in excess of 3,500 Hz, and it works well in the temperature range of from −73.3 °C (−100 °F) to 93.3 °C (200 °F).

The seismic accelerometer is designed for ground-isolated operation. The mounting stud port is electrically isolated from case ground so that the seismic accelerometer can be mounted to a surface, with or without the mounting base, by using an insulating tape. The accelerometer can be mounted in any direction such as upright, horizontal, or inverted. The accelerometer is connected to a power unit by a coaxial cable or a regular twisted pair cable during field tests. Battery-powered units were used in the field because of their low inherent noise. The noise from the accelerometer is broadband; therefore, selective frequency filtering can help increase resolution. The accelerometer and power supply unit used in this project are shown in figure 12.

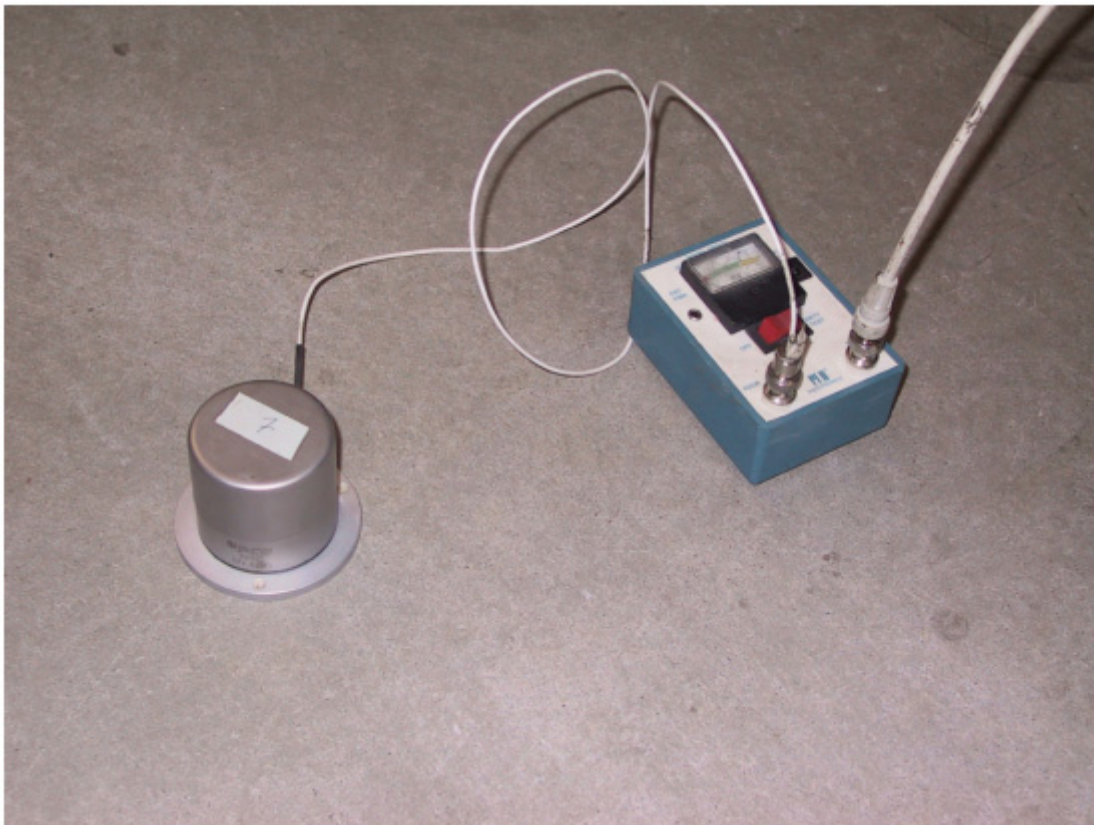


Figure 12. Photo. Seismic accelerometer and power supply unit.

## Dynamic Signal Analyzer Data Acquisition System

A portable field computer with two Data Physics SignalCalc™ DP420™ multichannel signal analyzer cards, shown in figure 13, was used as the data acquisition system for this project. The four-channel system has four input and four output channels. The DP420 hardware configuration consists of two FFT signal processor boards, four analog input/analog output (AIAO) modules, two interface pods and one synchronizing daisy chain cable. The accompanying FFT analyzer software controls the vibrator driving operations, and it collects up to four channels of time-domain test data. The DP420 also allowed for field processing of the time-domain data into modal transfer-function frequency-domain results.

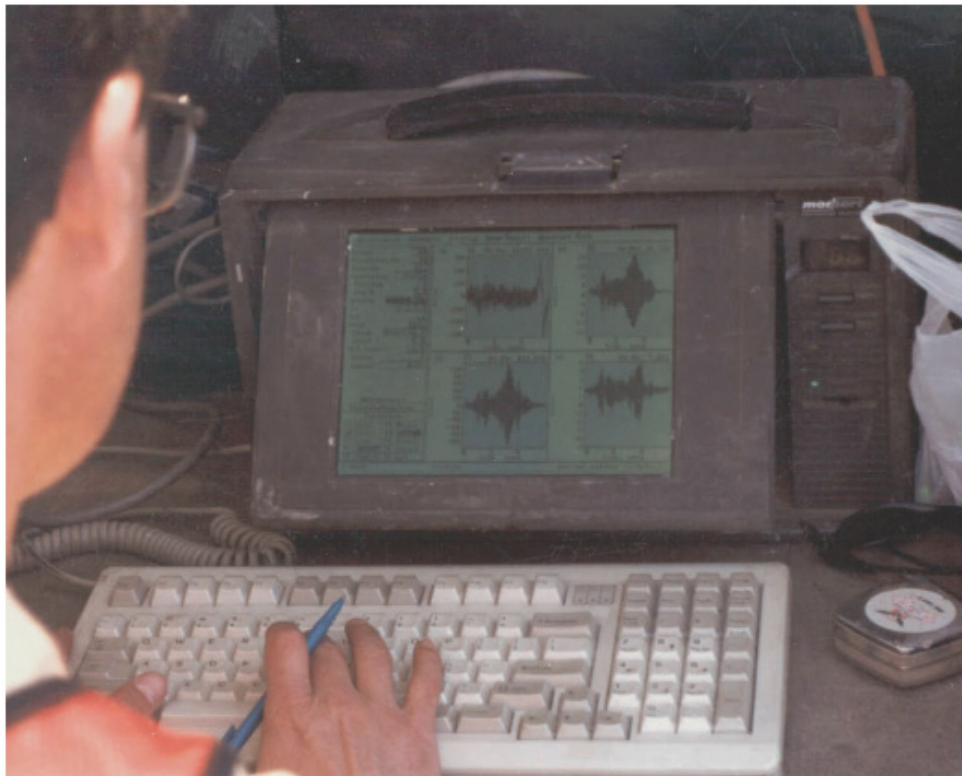


Figure 13. Photo. DP420 dynamic signal analyzer in portable PC.

The channel assignments of the DP420 generally were kept the same throughout this project. Input channel 1 was always connected to the Vibroseis load cell vibrator. The rest of input channels 2, 3, and 4 were always connected to the seismic accelerometers as the response channels. Output channel 1 functioned as the excitation driving and control channel; it was directly connected to the control unit of the vibrator. The field computer was linked with the vibrator and the seismic accelerometers by lead cables as long as 30.5 m (100 ft).

The test and processed data in the time and frequency domains were recorded and saved in the field on the hard drive of the field computer, depending on the FFT analyzer software setups. Later in the office, these field test data were recalled and saved with different file names because the commercial software used for modal analysis in this project requires the test data to be in the

frequency domain with specified data formats. The field test procedures are discussed in the next section.

## **FIELD MODAL VIBRATION TEST PROCEDURES**

In general, the Vibroseis truck was placed on the top of the bridge deck over the concrete beam cap of each of the three tested bridges. After the truck was moved to a designated loading location, the vibrator was released and separated from the truck. At this time, the air springs were the only connection between the truck and the vibrator. A load cell was then placed between the vibrator and the bridge slab. Next, the weight of the truck was lifted up by hydraulic cylinders on the truck. As a result, the static holddown force was applied to the vibrator through the air springs, which provided the base reaction for generating dynamic forces at the desired levels. After the reaction load of the truck was in place, the load-cell reading was reset to be zero before dynamic testing began. Therefore, the recorded excitation force that was applied and measured through the load cell was the actual dynamic force that was directly applied to the tested bridge bents.

The load cell force was recorded on channel 1 of the DP420 analyzer along with the seismic accelerometer outputs in time on channels 2, 3, and 4. The DP420 then calculated the linear frequency response functions, also known as TFs, of the tested bridge bents for acceleration, velocity, and displacement, divided by the excitation force as a function of frequency.

The seismic accelerometers were attached to aluminum triaxial mounting blocks that were bolted with concrete anchors to the columns and beams of the tested bridge bents. The installation of the concrete anchors was accomplished by drilling small holes at the designated locations and setting concrete anchors into the drilled holes as shown in figure 14. The seismic accelerometers were mounted upright on the tops of the aluminum blocks for the vertical response measurements and attached horizontally to the sides of the aluminum blocks for the horizontal response measurements (see figure 15).



Figure 14. Photo. Drilling concrete holes to mount seismic accelerometers on bent 2 of structure 4, Trinity River Relief Bridge.



Figure 15. Photo. Seismic accelerometers on blocks bolted to piles of bent 2 of structure 4, Trinity River Relief Bridge.

The DP420 was connected with the vibrator and the seismic accelerometers by coaxial cables. Battery-powered power units were used as the power supply and amplifier units for the load cell and the seismic accelerometers. Because each power unit conditioned one input channel, four units were used.

In addition, the vibrator excitation frequency was controlled by the DP420 output channel 1 of the analog signal interfaces. The maximum input voltage of the DP420 analyzer channels was 10 volts. The Vibroseis typically was swept by a chirp pulse (increasing frequency sine wave) from the DP420 from a frequency of 3 Hz to about 80 Hz for 5 to 6 cycles. The loads applied to the bridge bents ranged from 44,500 N (10,000 lbf) to 445,000 N (100,000 lbf) of peak-to-peak force. Most loads were between 89,000 and 178,000 N (20,000 and 40,000 lbf) of peak-to-peak force to minimize nonlinear excitation effects on the soil-pile system.

### **Field Test Program for Trinity River Relief Bridge Bents**

Two series of field tests were conducted at the Trinity River Relief Bridge. The first test series was done to work out field test procedures and gather initial data. The second series was done before and during controlled damage to the two tested bents of the bridge as bridge demolition was proceeding.

#### ***Initial Trinity River Relief Bridge Bents 2 and 12 Tests***

In the first tests on the bridge in November 1996, bents 2 and 12, located east of the west abutment of bridge structure 4, were selected for testing. The primary purposes of the first field tests were to better understand the frequency ranges involved and select the dynamic sources and receivers. Several dynamic excitation sources and receivers were evaluated, including a 1.36-kg (3-lb) instrumented impulse hammer, a 5.45-kg (12-lb) impulse drop hammer, a 45.4-kg (100-lb) vibrator, the Vibroseis truck, and different types of PCB accelerometers.

The DP420 initially was set to be from 0 to 320 Hz and 500 spectral lines, which resulted in a frequency resolution of 0.64 Hz. Most of the testing was done within a frequency range of 0 to 80 Hz and 500 spectral lines for improved frequency resolution of 0.16 Hz. Five impulse hammer impacts or chirped vibrator excitation forces were applied on the bridge deck slab at about the one-third points of the beams between the four piles. The corresponding acceleration responses of the bridge bents were averaged and saved in the field computer for each test configuration. The PCB accelerometer receivers were installed at either the bottom of the beam cap or on the northern/southern sides of the concrete piles/columns.

A 1.36-kg (3-lb) instrumented impulse hammer (built-in force transducer) with a black or gray tip was used on bent 2 at first. Higher dynamic forces with higher frequencies can be generated from the hard plastic black tip than from the soft rubber gray tip because of the differences in both tip hardness and associated impact-contact time. Next, a 45.4-kg (100-lb) vibrator, shown in figure 16, was applied to the same loading point on the bridge deck as it was for the 1.36-kg (3-lb) hammer, which was 0.305-m (1-ft) north of the northern pile of bent 2. A 5.45-kg (12-lb) impulse hammer, shown in figure 17, was used at different loading locations on bent 12. The field data from these relatively small hammers and vibrator showed that not enough energy was generated to vibrate the bridge bents at the desired lower frequencies of down to a few Hz. For

these sources, the useable frequency ranges were above 50 Hz to 200 Hz, according to the coherence of the TFs. Coherence is related to signal-to-noise ratio: A value of 1.0 indicates the response resulted from the input; good data have coherences of 0.9 to 1.0; however, the frequencies of interest in this modal testing needed to be as low as 3 Hz and up to 100 Hz, which indicated that a large vibrator such as the Vibroseis, with low frequency output, was essential for the research. The Vibroseis is shown in chapter 3, figure 3.

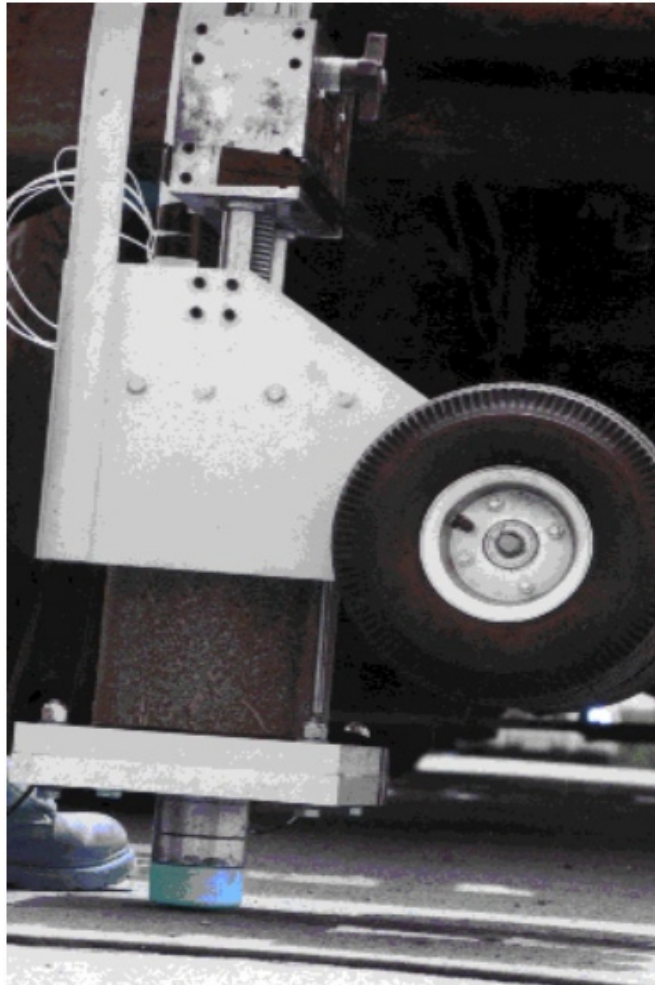


Figure 16. Photo. One-hundred-pound vibrator with dynamic load cell on bent 2.



Figure 17. Photo. Twelve-pound impulse sledge hammer with soft gray rubber tip.

Consequently, the Vibroseis truck with a dual-wheel loading pattern system, see figures 18 and 19, was used on bents 2 and 12 for all of the field tests. The truck, facing east, was placed at three loading locations at the midpoints between adjacent piles on the top of the bridge deck. The dynamic forces from the Vibroseis were swept from 2 Hz to 92 Hz with a chirp pulse from the DP420 and varied in magnitude from 124,600 N (28,000 lbf) to 623,000 N (140,000 lbf) peak-to-peak (upward to downward forces) to determine the force levels at which the bridge responses changed from linear to nonlinear for the bents. The results of these tests showed that force levels less than 178,000 N (40,000 lbf) peak-to-peak were still linear.

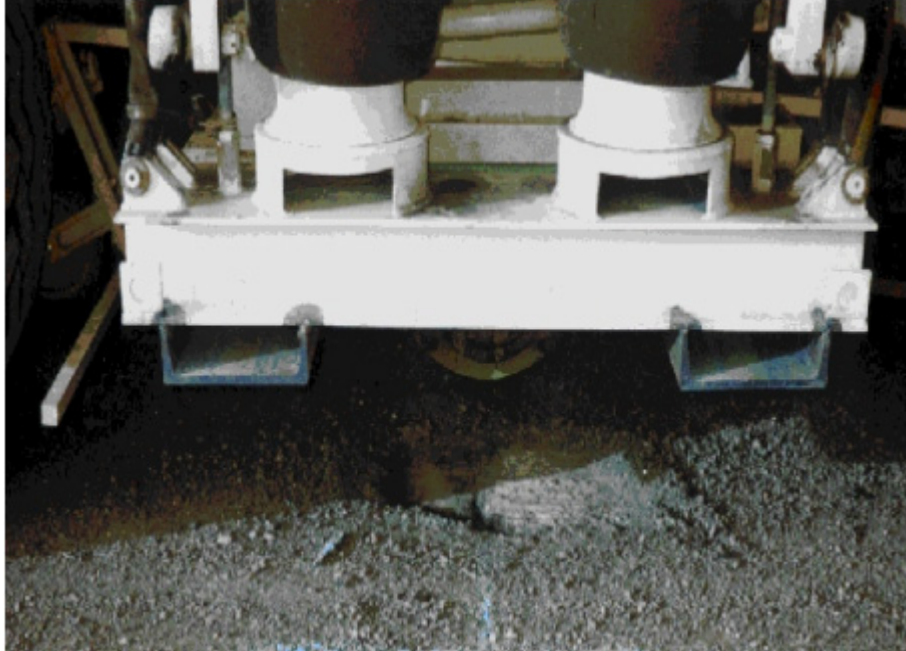


Figure 18. Photo. Closeup of the vibrator frame of the Vibroseis truck.



Figure 19. Photo. Dual-wheel depressions in asphalt overlay on deck over bent 2.

### ***Final Trinity River Relief Bridge Bent 2 and 12 Tests***

The final field tests were conducted on the Trinity River Relief Bridge in September 1997, before and during the bridge demolition operations. The Vibroseis loading and receiver locations tested on bents 2 and 12 were labeled the same, and the nodes were located as shown in figure 20. The Vibroseis truck with a single-point-plate loading pattern system was used as the sole dynamic excitation source at this time, and it was positioned on top of the deck at nodes 2, 4, and 6 for modal tests. The accelerometer receivers were positioned in a biaxial arrangement (vertical and in-plane horizontal accelerometers at each node during the testing) on the underside of the beam cap at nodes 2, 4, and 6, and on the pile (column) sides at nodes 8 through 15 (north) through 15 (south).

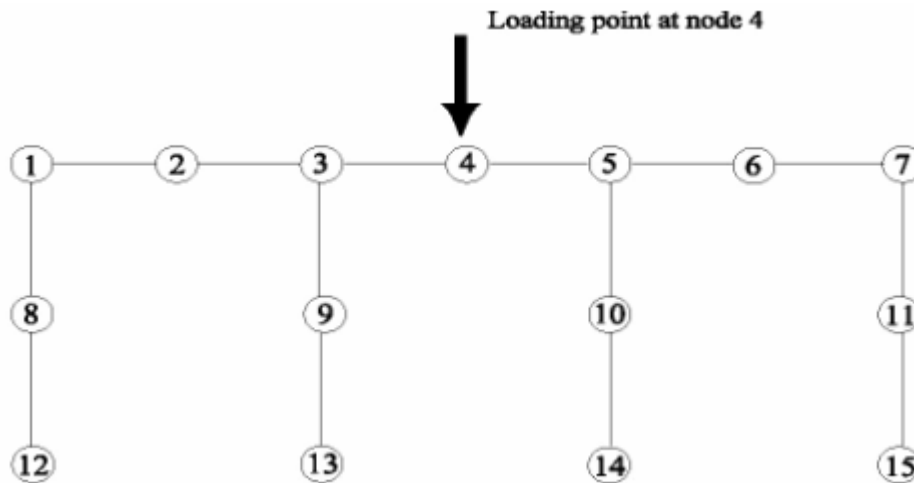


Figure 20. Diagram. Loading points and accelerometer receiver locations on bents 2 and 12, Trinity River Relief Bridge.

A round steel plate 0.305 m (1 ft) in diameter and 2.54 cm (1 inch) thick was placed between the bridge deck and the Beowulf load cell as shown in figure 21. The DP420 data recording setup ranged up to 80 Hz with 500 lines, resulting in a frequency resolution of 0.16 Hz. Five chirp pulses generated vertical vibration forces at frequencies from 1 Hz to 76 Hz. The corresponding dynamic responses of the tested bridge bents were averaged and all data saved in the field computer for each excitation test series. The magnitudes of the output forces from the Vibroseis were controlled at two levels of around 89,000 N (20,000 lbf) and 178,000 N (40,000 lbf) peak-to-peak so that the tested bridge bents behaved linearly. The seismic accelerometer receivers were installed at either the western/eastern sides of the beam caps or the western/eastern sides of the concrete piles/columns.

Field tests of bents 2 and 12 were conducted for three bent conditions: (1) existing, undamaged bridge bents, (2) with the surrounding soil excavated so that the two southern piles were partially exposed for each bent (scour simulation), and (3) with the two southern piles excavated and the most southern pile sheared or broken (earthquake damage simulation). For the first 2 cases, 3 dynamic loading and 11 receiver locations were used for each bridge bent. Only 2 dynamic

loading and 10 receiver locations were used for the third case because of safety concerns about placing the Vibroseis directly over the damaged piles at node 6.



Figure 21. Photo. Vibroseis single-point-plate loading system.

As shown in figure 21, the single-point-plate loading system was used exclusively in the final tests. This allowed for point loading of the bridge deck and cap beam at the three loading points (nodes 2, 4, and 6). This load setup better matched the theoretical modeling of the bridge responses than did the dual-wheel two-point loading used initially.

The excavation and damage to the piles were performed by the general contractor on the project. The equipment was onsite for demolition of the bridge, as shown in figure 22.



Figure 22. Photo. Demolition of structure 4, Trinity River Relief Bridge.

For settlement and safety concerns, the settlements of undamaged piles that supported bents 2 and 12 were monitored during the field tests with strings strung between adjacent bents and marks on a pile of each bent. A final settlement of 0.397 cm (0.16 inch) was measured for the south pile and column of bent 2 after the Vibroseis truck had been operated on the south side of bent 2 for about 1 hour. Bent 12 showed a slightly smaller settlement of about 0.318 cm (0.125 inch).

After the field tests were completed for the case of existing, undamaged bridge conditions, 3.05-m (10-ft)-deep excavations were dug completely around the most southern piles of bents 2 and 12 using a backhoe, shown in figure 23. Ground water eventually came into the excavation of bent 2 just below the strip footing, shown in figure 24.



Figure 23. Photo. Backhoe excavation at bent 12, Trinity River Relief Bridge.



Figure 24. Photo. Ground water in excavation of bent 2, Trinity River Relief Bridge.

The excavations extended to the center-south piles, resulting in the upper 2.75 m (9 ft) around the center-south piles being exposed on the south, east, and west pile sides, with soil still against the north sides of the piles, as shown in figures 25 and 26 for bents 2 and 12, respectively. After the excavations were completed, the field modal vibration tests were then performed for the two southern-most piles that were being excavated at each bent.



Figure 25. Photo. Pile of bent 2 just after excavation.



Figure 26. Photo. Piles of bent 12 just after excavation.

Finally, the south piles or columns of bents 2 and 12 were sheared or broken using a vibrating breaker point on a backhoe (figures 27 and 28).



Figure 27. Photo. Shearing of pile of bent 2.



Figure 28. Photo. Shearing of pile of bent 12.

Because the seepage of ground water into the excavation around bent 2 resulted in a water level near the bottom of the strip footing (see figure 29), the south column/pile of bent 2 was sheared just above the strip footing at ground level. Four number 8 steel rebars of the south column/pile of bent 2 were exposed; one was completely broken, as shown in figure 30.



Figure 29. Photo. Sheared south pile of bent 2 with ground water seepage.



Figure 30. Photo. Bent and broken rebars of south column of bent 2.

Because no seepage of ground water occurred around bent 12 after excavation, the south column/pile of bent 12 was sheared at about 2.44 m (8 ft) below the pile beam cap. Four number 8 steel rebars of the south pile of bent 12 were exposed, but none was broken even after 0.305 m (1 ft) of the entire concrete cross section of the pile was removed, as shown in figures 31 and 32. The field tests under conditions of the south piles sheared after excavation were performed at the center and northern loading locations (nodes 2 and 4) for each bridge bent to accommodate safety concerns about positioning the truck over the damaged piles.



Figure 31. Photo. Sheared south pile of bent 12.



Figure 32. Photo. Rebars of south column of bent 12.

## Field Test Program for Woodville Road Bridge

The dynamic field tests on the west pier of the Woodville Road Bridge (figure 33) were performed in May 1997. Figure 34 shows the dynamic loading and accelerometer receiver locations. The Vibroseis truck with a dual-wheel loading pattern system that was used in the first field test on the Trinity River Relief Bridge was the dynamic excitation source. The Vibroseis truck was placed at two outside lane locations on top of the bridge deck approximately over the north and south columns. No center loading position was possible because of the need to maintain traffic on the bridge.



Figure 33. Photo. Vibroseis truck over west pier of Woodville Road Bridge.

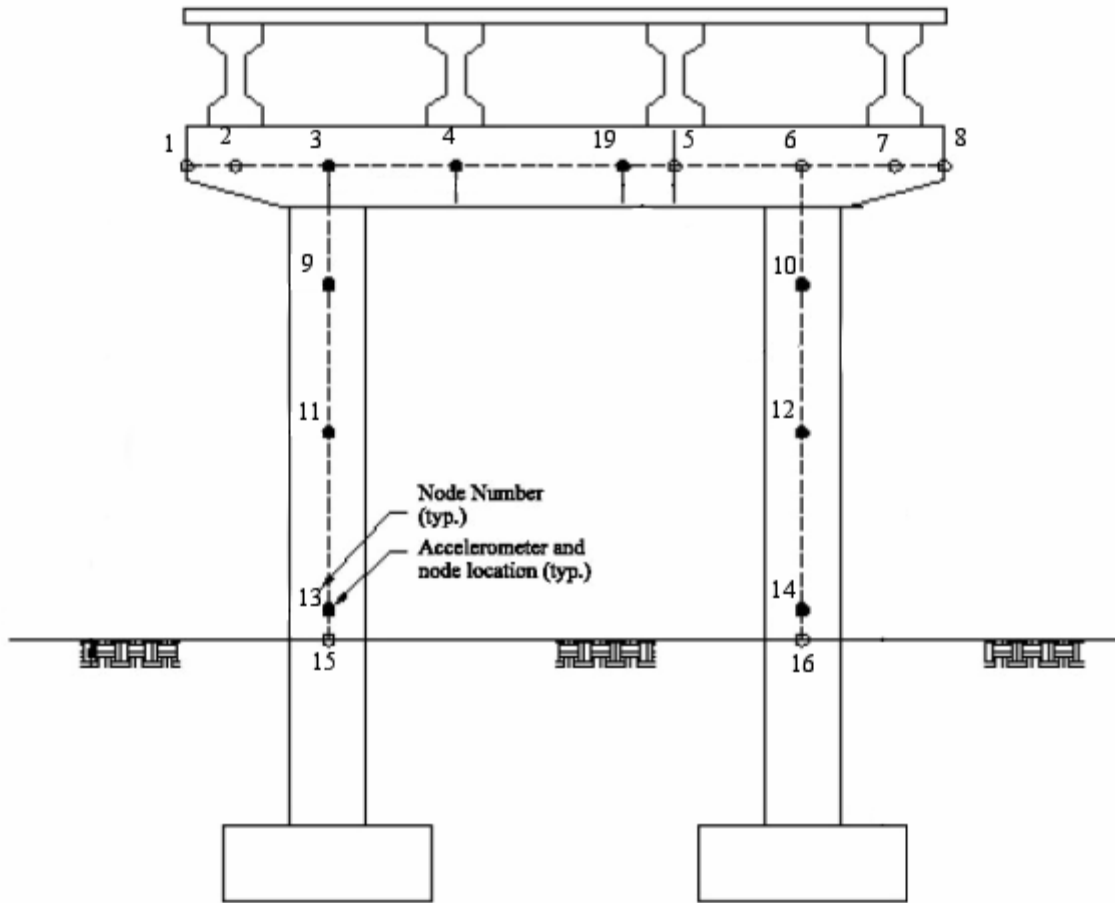


Figure 34. Diagram. Woodville Road Bridge, loading points and accelerometer receiver locations.

The seismic accelerometer receivers were installed on the west sides of the concrete beam cap and two concrete columns of the west pier as shown in figures 35, 36, 37, and 38. The DP420 setup was set to be 80 Hz and 500 spectral lines, resulting in the frequency resolution of 0.16 Hz. Six to 20 chirp forces from 1 Hz to 80 Hz and corresponding dynamic responses of the bridge bents were averaged and saved in the field for each test run. The magnitudes of the output forces from the Vibroseis were set to be at two levels of around 89,000 N (20,000 lbf) and 178,000 N (40,000 lbf) to verify that the tested bridge bents behaved in a linearly elastic fashion.



Figure 35. Photo. Accelerometers on column and beam cap of west pier, Woodville Road Bridge.



Figure 36. Photo. Biaxial accelerometer mount with vertical and horizontal accelerometers, west pier, Woodville Road Bridge.



Figure 37. Photo. Vertical accelerometer at base of column of west pier, Woodville Road Bridge.



Figure 38. Photo. Horizontal accelerometer on side of column of west pier, Woodville Road Bridge.

### **Field Test Program for Old Reliance Road Bridge**

The Old Reliance Road Bridge was tested with the same test equipment and test setups as the Woodville Road Bridge. Again, only two dynamic loading locations were available in the outside lanes at the top of the bridge deck because of the need to maintain traffic on the bridge. The seismic accelerometer receivers were installed on the east sides of the concrete beam cap and north and south columns of the east pier. Figure 39 shows the dynamic loading and receiver locations on the Old Reliance Road Bridge.

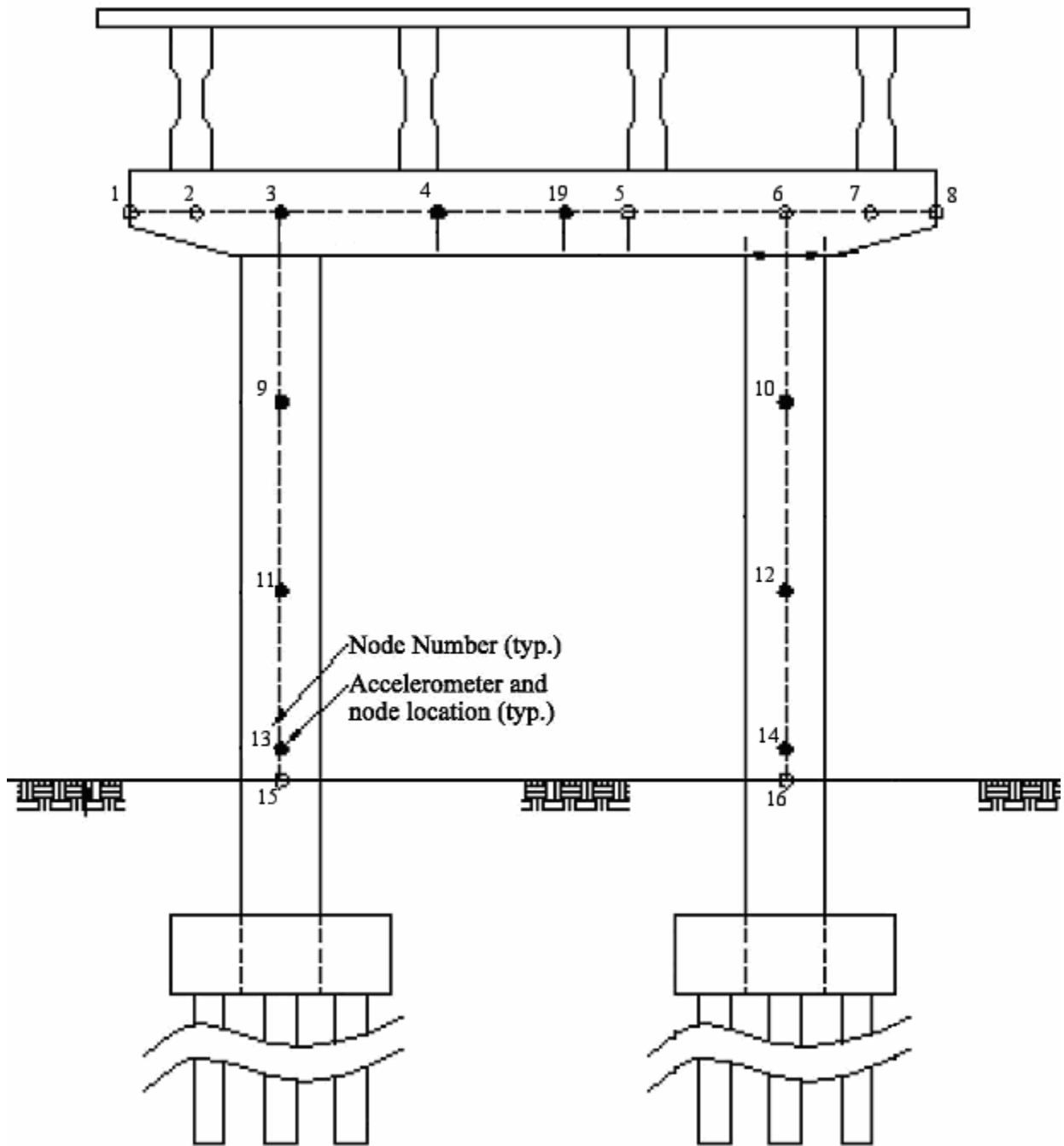


Figure 39. Diagram. Old Reliance Road Bridge, loading points and accelerometer receiver locations.

## CHAPTER 5. MODAL VIBRATION DATA PROCESSING AND ANALYSES

### INTRODUCTION

The process of obtaining and processing the modal vibration test data from the bridge substructures involved two steps. The first was to acquire the data in the field with various source and receiver locations using the DP420 signal analyzer as discussed in chapter 4. Example results of this field data from the DP420 appear in the following section. The second step was to combine all data from the various and multiple source and receiver combinations and perform a modal analysis of each bridge substructure for each test condition. The modal analysis procedures that provided frequency, damping, and mode shape data for the substructures are discussed in the third section of the chapter, followed in the fourth section by comparisons of dynamic bridge responses for the undamaged, excavated, and sheared pile cases for bents 2 and 12. The purpose of the comparisons is to evaluate the potential of the flexibility TF data (inverse of stiffness) to indicate sound, scoured, and broken pile foundations directly while in the field. The concluding section examines the flexibility TF results to determine if there was a direct field indication of shallow versus deep foundations for the Old Reliance versus Woodville bridges.

### EXAMPLE MODAL VIBRATION FIELD DATA RESULTS

The initial field test geometry and nodes used on bents 2 and 12 of structure 4 of the Trinity River Relief Bridge are shown in figures 40 and 41, respectively. In the initial tests, vibration measurements were not performed at all node locations above ground because symmetry was assumed in the responses of the bents. In the final tests, vibration measurements were performed at all selected node locations for each bridge substructure. Because only three data acquisition channels were connected to the seismic accelerometer receivers for each dynamic loading along with the chirped sine-excitation-force input from the Vibroseis load cell, the repeatability of dynamic loading and the resultant responses were very important. The excitation and response data were found to be very repeatable, and in the final analyses, at least 14 TF measurements were used to extract the modal shapes for each test series performed on each bridge substructure. The following discussions provide examples of the data gathered and processed in the field using the DP420 signal analyzer. The examples include the time, spectral, and TF data gathered from one test on bent 2 (piles plus footing).

#### **Time-Domain Data, Bents of Structure 4, Trinity River Relief Bridge**

In the initial tests of bent 2, accelerometers were placed at nodes 24, 25, 6, 26, 7, and 8. (Node 8 was on top of the deck over the beam; all other receiver locations were on the pile sides or bottom of the beam, as shown in figure 40.) The geometry for initial tests of bent 12, shown in figure 41, is similar to bent 2. The following paragraphs discuss example time-domain data results for bent 2.

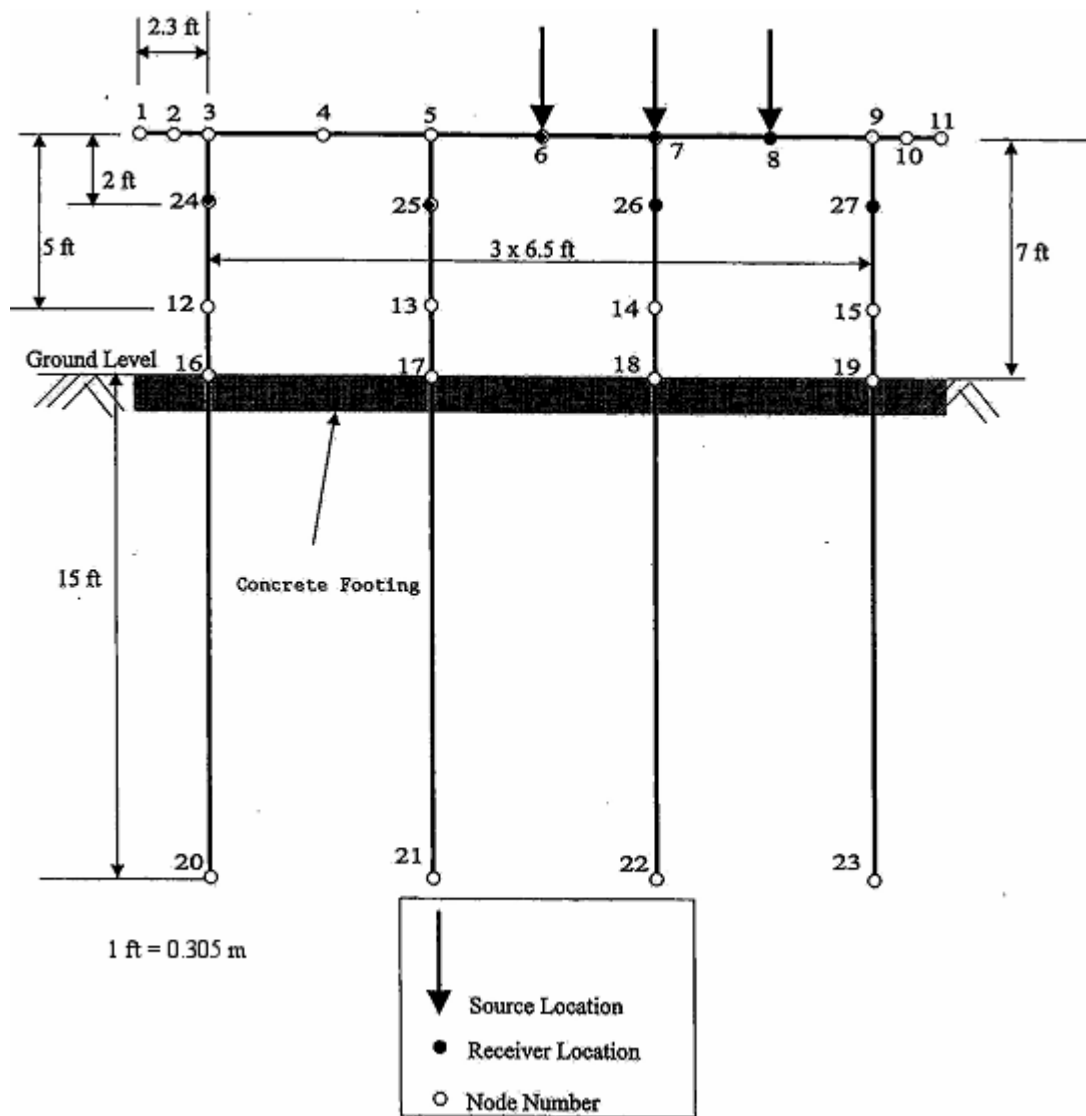


Figure 40. Diagram. Node locations on bent 2.

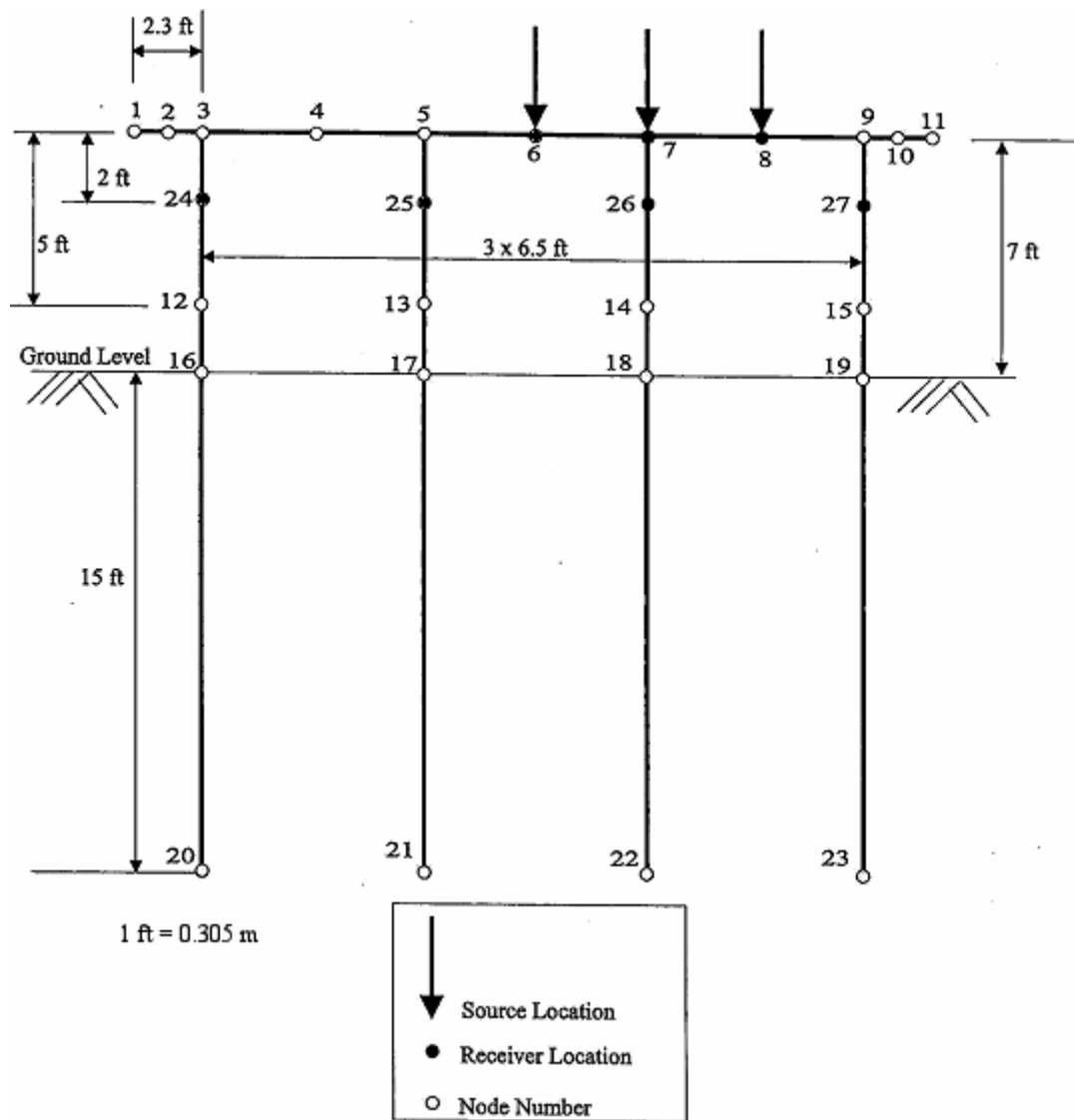


Figure 41. Diagram. Node locations on bent 12.

For initial tests of bent 2, the Vibroseis was centered over nodes 6, 7, and 8 on top of the deck over the beam. The Vibroseis was excited by a chirp sine pulse from 3 Hz up to about 80 Hz for 5 to 6 cycles for averaging. Excitation loads ranged from 44,500 N (10,000 lbf) to more than 445,000 N (100,000 lbf) peak-to-peak. The Vibroseis induced nonlinear responses in the piles for loads greater than 178,000 N (40,000 lbf) peak-to-peak, and the piles were visibly moving up and down at these higher loading forces. Because it was desirable to keep the responses of the bridge linear, modal analyses were performed largely of test series where the Vibroseis chirped force was kept below about 178,000 N (40,000 lbf) peak-to-peak.

Example bent 2 time-domain data records are shown in figure 42 for the forcing function of the Vibroseis at node 8, and the corresponding acceleration responses are shown in figures 43, 44,

and 45 for a vertical accelerometer at node 27V (north pile), a horizontal accelerometer at node 27H, and a vertical accelerometer at node 24V (south pile), respectively. Figure 42 shows an example plot of the Vibroseis excitation load force in poundforce versus time in seconds for about 6 s of data from a single chirp pulse. The excitation force ranged from peak-to-peak values of about 26,700 N (6,000 lbf) at 3 Hz near time 0 s to a maximum of about 124,600 N (28,000 lbf) at 0.5 s. A second peak loading force occurred at about 2.5 s with a value of about 80,100 N (18,000 lbf) peak-to-peak. The increase in the sinusoidal chirped frequency of excitation from 3 Hz at the start of the chirp pulse at about 0 s to near 80 Hz is readily apparent with increasing time in figure 42.

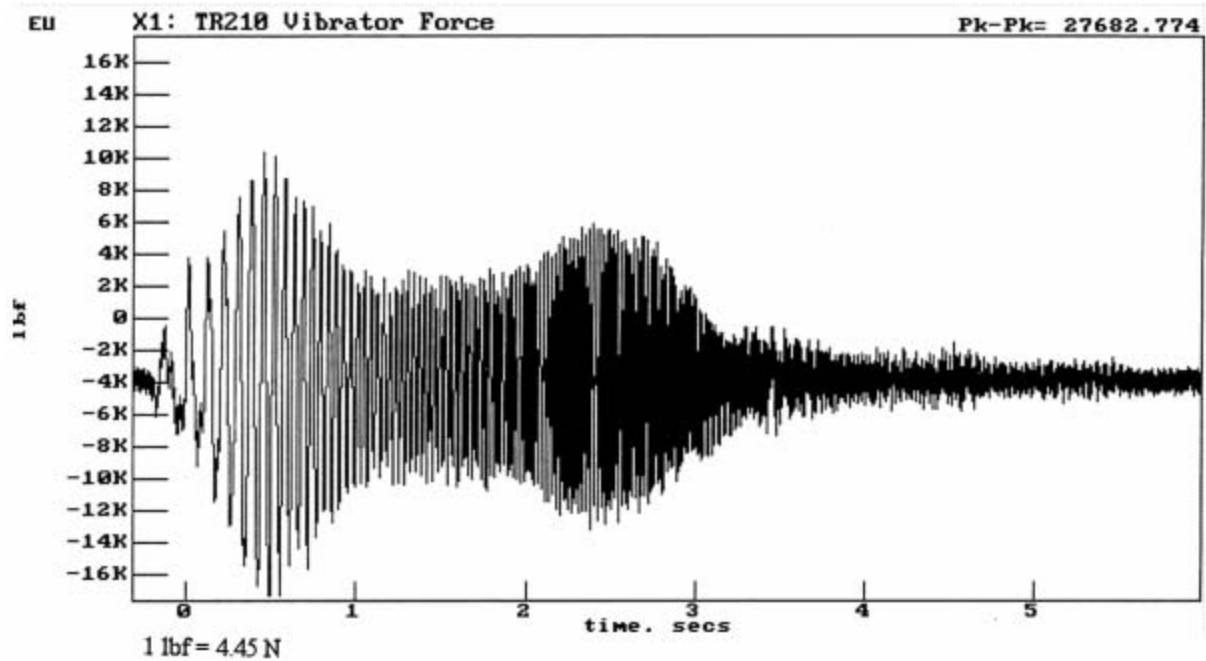


Figure 42. Graph. Vibroseis at node 8 of bent 2.

Figures 43, 44, and 45 show the calibrated acceleration responses of the seismic accelerometers in units of inches/s<sup>2</sup> versus time (1 unit of gravitational acceleration = 1 G = 386 inches/s<sup>2</sup> or 9.8 m/s<sup>2</sup>). Review of the accelerometer responses in figures 43, 44, and 45 shows the largest accelerations were measured by the vertical accelerometer of node 27, which is expected because it is most directly below the excitation force at node 8. In addition, figures 43, 44, and 45 show an increase in responses at the approximate times that the excitation force increased. The peak acceleration for the three accelerometers of about 0.4 G, or 4.06 m/s<sup>2</sup> (160 inches/s<sup>2</sup>) peak-to-peak was measured at node 27V, and it occurred at about 0.5 s and 2.5 s (figure 43). These peak acceleration times agree with the peak excitation force results of figure 42. These peak forces and accelerations are attributed to resonances in the Vibroseis that magnified the excitation force.

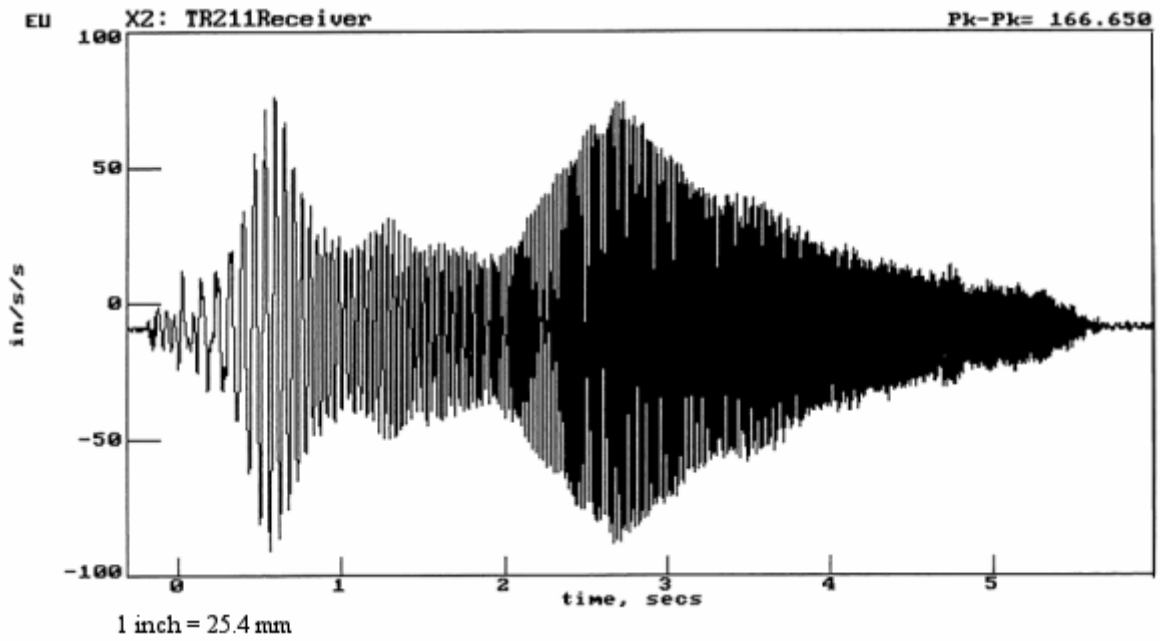


Figure 43. Graph. Vertical accelerometer at node 27 of bent 2.

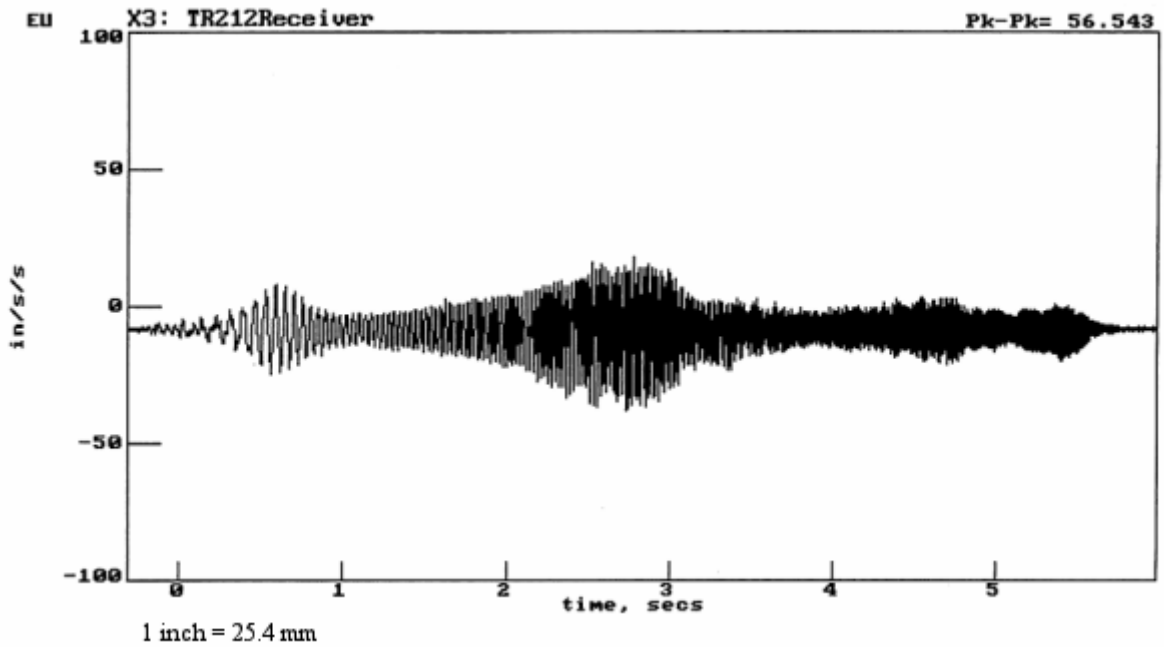


Figure 44. Graph. Horizontal accelerometer at node 27 of bent 2.

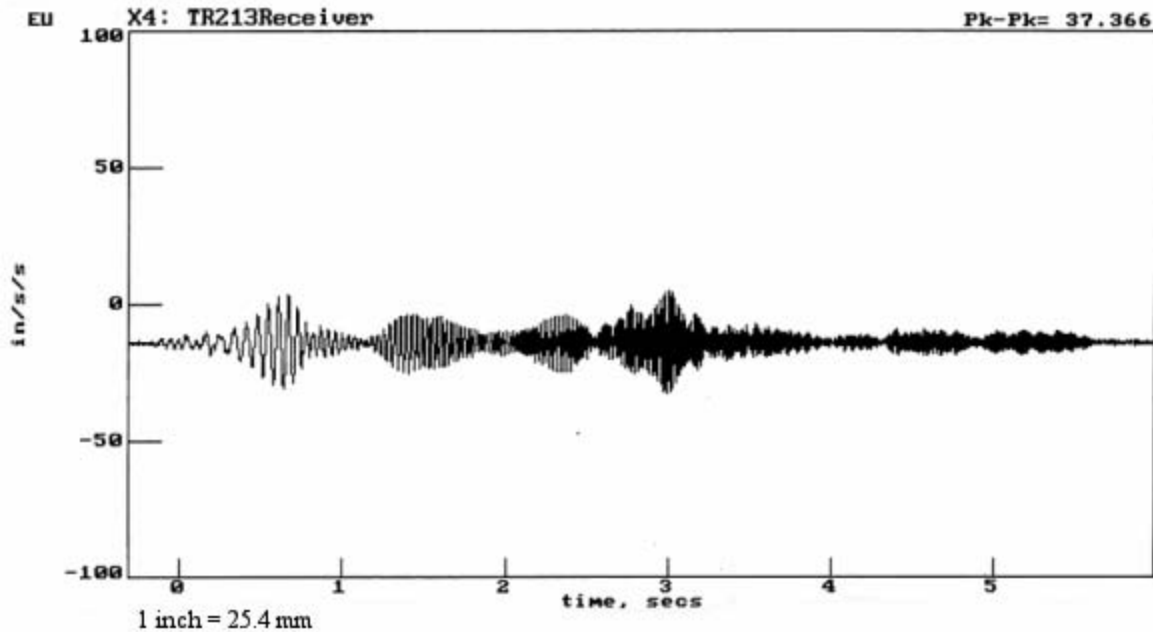


Figure 45. Graph. Vertical accelerometer at node 24 of bent 2.

### Frequency-Domain Data, Bent 2 of Structure 4, Trinity River Relief Bridge

The average linear frequency spectra calculated by the DP420 for the time-domain data test series of figures 42 through 45 are presented in figure 46 for bent 2. The vertical scales of the plots in figure 46 are the spectral amplitude in force or acceleration units, and the horizontal scale is the frequency in Hz from 0 to 55 Hz. Review of the force frequency spectrum (G11 in figure 46) shows peak excitation forces at about 14 Hz and 47 Hz that correspond to the time-domain peak excitation forces discussed previously.

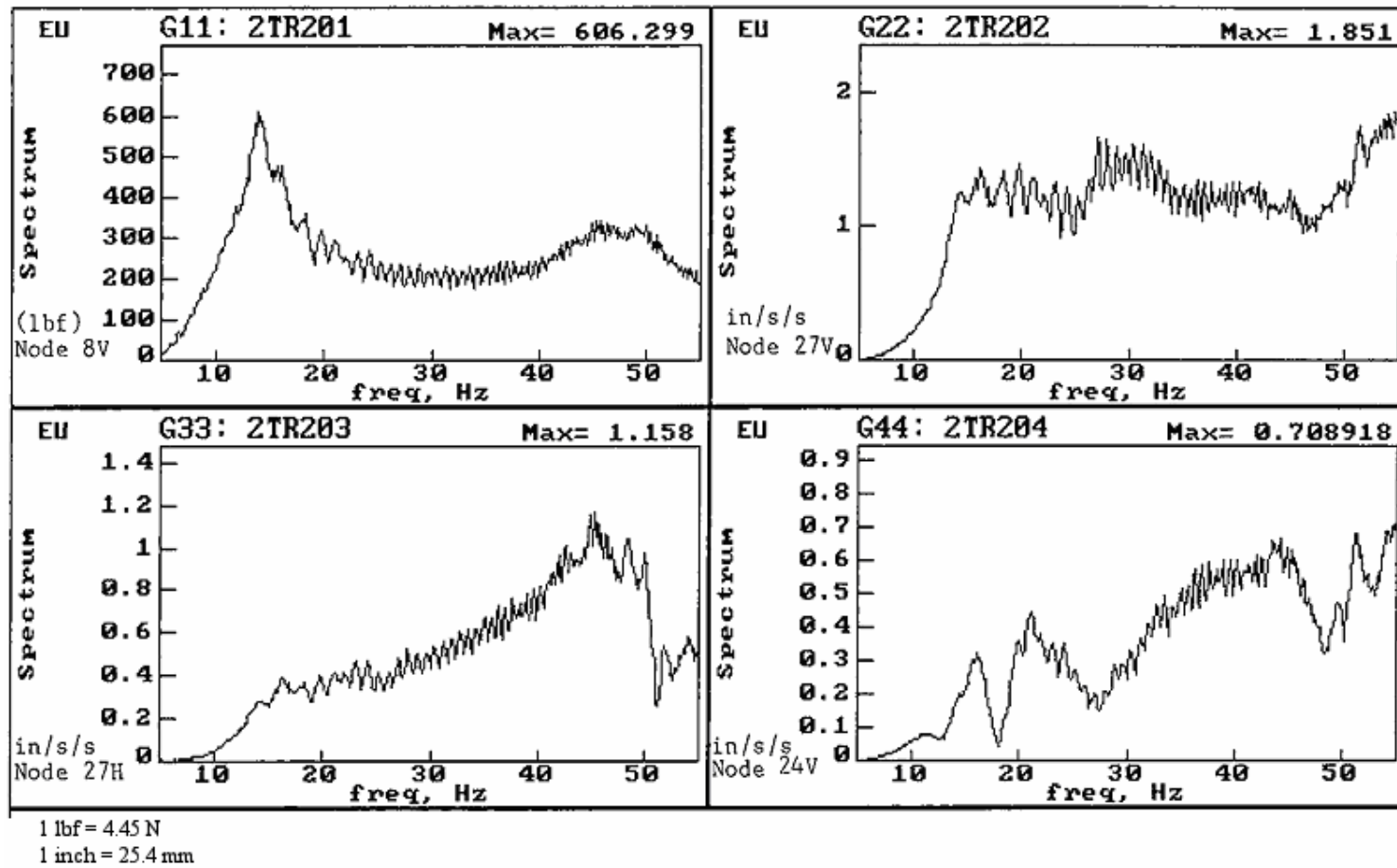


Figure 46. Graphs. Average spectra of figures 42 through 45 for bent 2.

## Transfer Function Results, Bents of Structure 4, Trinity River Relief Bridge

TFs, also known as frequency response functions, relate input force (F) and output response in terms of acceleration (A), velocity (V), or displacement (D) for linearly elastic systems as a function of frequency, as shown in figures 47, 48, and 49:

$$\frac{F(f) \times A(f)}{F(f)} = A(f),$$

Figure 47. Equation. Accelerance TF.

Where  $\frac{A(f)}{F(f)}$  is the accelerance TF.

$$\frac{F(f) \times V(f)}{F(f)} = V(f),$$

Figure 48. Equation. Mobility TF.

Where  $\frac{V(f)}{F(f)}$  is the mobility TF.

$$\frac{F(f) \times D(f)}{F(f)} = D(f),$$

Figure 49. Equation. Flexibility TF.

Where  $\frac{D(f)}{F(f)}$  is the flexibility TF.

The inverses of the mobility and flexibility TFs are mechanical impedance and stiffness, respectively.

The DP420 was used to field process the time-domain data and save and store the accelerance, mobility (integrated once from accelerance), and flexibility (integrated twice from accelerance) TFs from each test series in the research. To illustrate this, the accelerance TFs for the excitation force at node 8V and the acceleration responses at nodes 27V, 27H, and 24V are shown in figure 50 for bent 2 and the data of figures 42, 43, 44, 45, and 46. Review of this figure shows apparent resonances between 10 Hz to 20 Hz in the A/F, or  $m/s^2-N$  (inch/s<sup>2</sup>/lbf or inch/s<sup>2</sup>-lbf) accelerance plots.

Flexibility TF plots of the data from figures 42, 43, 44, 45, and 46 are shown in figure 51. The top three plots are the flexibility TF, and the bottom three plots are data coherence. A coherence greater than 0.9 is good, with most of the data exceeding this throughout the plotted frequency range of 5 Hz to 55 Hz. Coherence is related to signal-to-noise ratio, and a value of 1.0 indicates the response resulting from the input with nil contamination caused by noise. Review of the flexibility TF plots shows that the effect of frequency has been removed and the resonant peaks at about 15 Hz are more clearly apparent than in the acceleration plots (compare figures 50 and 51).

Because the flexibility (inch/lbf) TF plots showed the resonances most clearly, and they are the simplest to understand (the inverse of flexibility is stiffness (lbf/inch)), flexibility plots were chosen to compare modal test results of bent 2 (figure 51) and bent 12 (figure 52). The data for bent 12 were from nodes located on bent 12 in the same configuration as nodes on bent 2. Comparison of these two figures shows that bent 2 was more flexible than bent 12, that is, less stiff. The peak flexibility in the vertical direction for bent 2 (piles plus footing) was about  $3.42 \times 10^{-9}$  m/N (600 nanoinches/lbf (600 x  $10^{-9}$  inch/lbf)); the peak flexibility in the vertical direction for bent 12 (piles only) was about 1.71 nm/N (300 nanoinches/lbf).

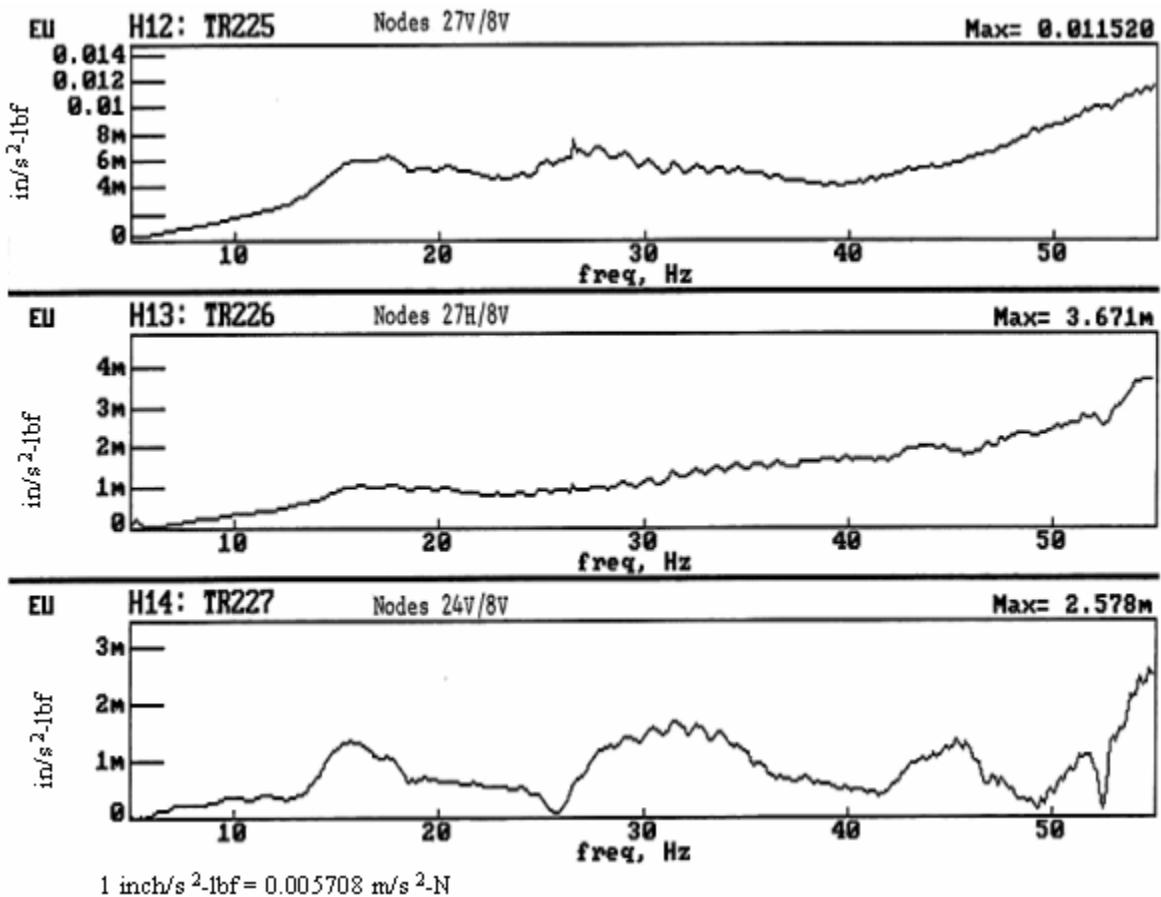
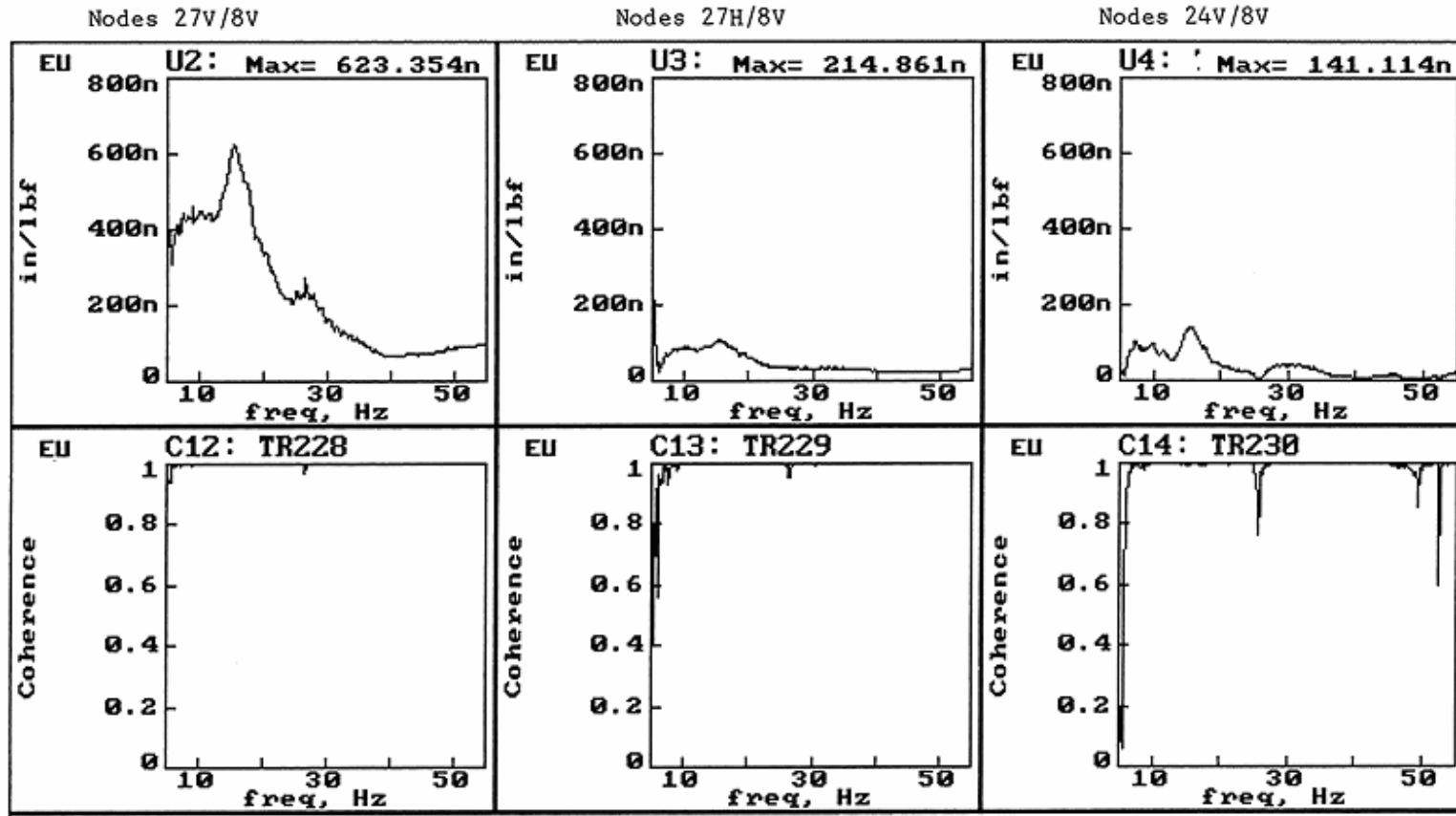
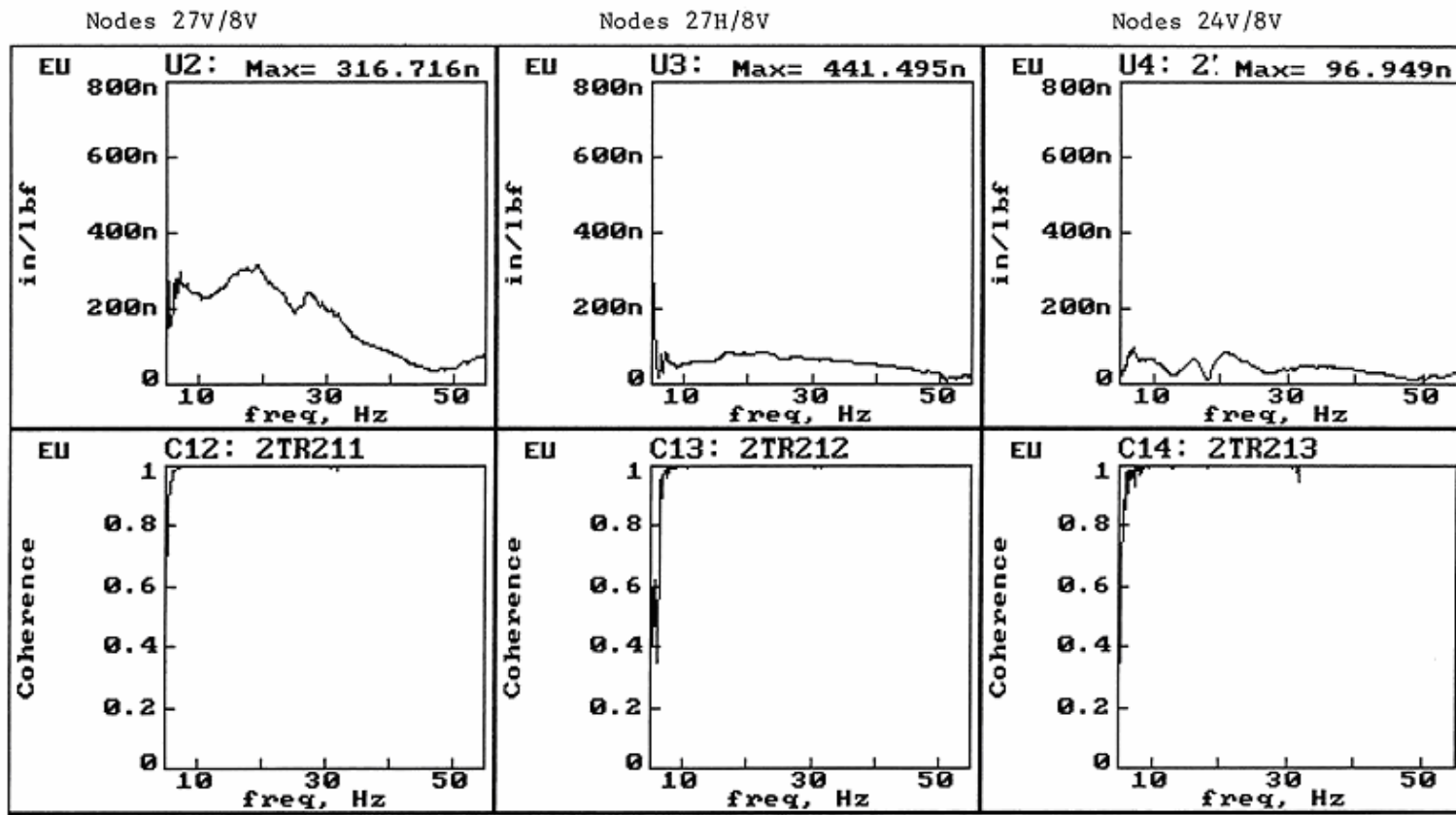


Figure 50. Graphs. Accelerance TF for figures 42 through 45 for bent 2.



1 lbf = 4.45 N  
1 inch = 25.4 mm

Figure 51. Graphs. Flexibility TFs with coherences for figures 42 through 50 for bent 2.



1 lbf = 4.45 N  
1 inch = 25.4 mm

Figure 52. Graphs. Bent 12 flexibility TFs with coherences for test configuration identical to bent 2.

## MODAL VIBRATION DATA PROCESSING

The next step in processing the field modal vibration test data was to combine the accelerance TF results of all of the test series (from a given linear force excitation level) to obtain mode shapes, resonant frequencies, and damping information for the tested bents. This was done to provide input and a basis of comparison to experimental results discussed later in this chapter in the sections on the Trinity River bents 2 and 12 and on the Woodville and Old Reliance bridge bents. The processed modal data were also used with theoretical modeling results and structural parameter estimation studies discussed in chapter 6.

The first step in the modal processing was to curve fit the accelerance data for bent 2, discussed in the following paragraphs. The derived mode shapes, resonant frequency, and damping results from curve-fitting of each bent's data are illustrated after that. A detailed discussion of modal vibration testing and analysis is found in Ewins.<sup>(29)</sup>

### Curve-Fitting of DP420 Field Modal Vibration Data

The DP420 dynamic testing data were processed by the commercial PCMODAL software. Because accelerance TFs in the PCMODAL software are derived from the power spectrum of the excitation, the power spectrum of the acceleration response, and the cross-power spectrum between the excitation and response, the recorded field data were recalled from the DP420 dynamic signal analyzer and resaved with the PCMODAL-specified data format.

After this data conversion to a PCMODAL format was accomplished, curve-fits of the PCMODAL-calculated accelerance results were conducted within fixed frequency bandwidths for each accelerometer and Vibroseis location used in a given test series. The following research curve-fitting criteria were established:

- The bandwidth should be as wide as possible.
- The same bandwidth and mode numbers should be used at different measurement locations for the same mode.
- The curve-fitting results should be evaluated when displayed in real, imaginary, magnitude, and Nyquist plots.

As a result, the curve-fitting was begun by setting the bandwidth at the valley-to-valley (negative peak-to-negative peak) positions in the magnitude plots (or the peak-to-peak positions in the imaginary plots). Next, the bandwidth was adjusted to obtain the best-looking curve fits from a visual perspective on the computer screen in all of the real, imaginary, magnitude, and Nyquist plots for all measurement combinations. If appropriate, based on all of the measurement location results, occasional efforts were made to fit two modes even if there was only one visualized peak within the bandwidth.

The modal constants, frequencies, and damping ratios were calculated during the curve-fitting and saved in the residual data files by the PCMODAL software. Examples of curve-fits are shown in figures 53 through 55 for the bent 2 accelerance TFs of figure 50.

Review of these figures shows the resulting resonant frequency values in hertz and the associated damping percentages that were derived from the curve-fitting of the experimental accelerance data using PCMODAL.

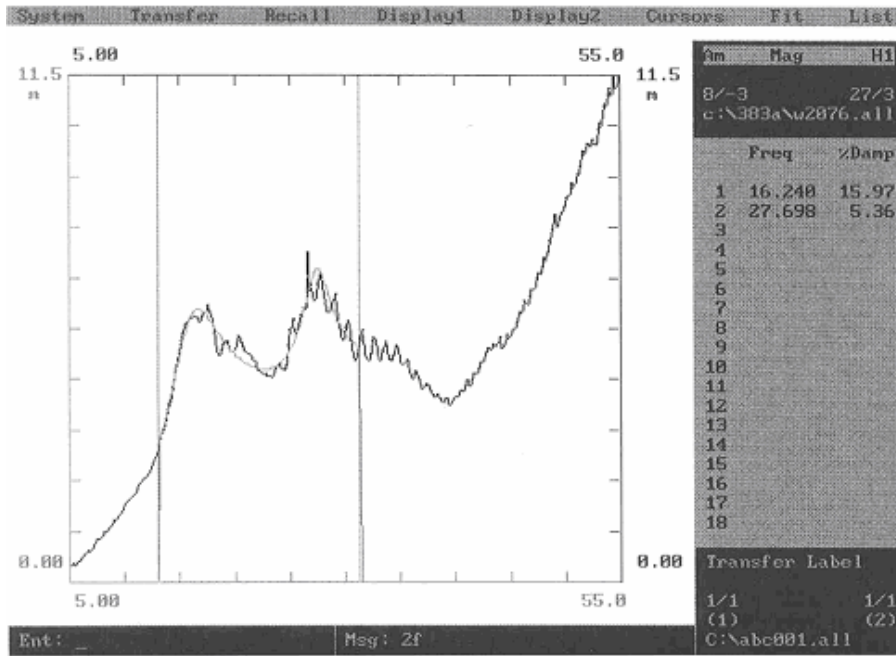


Figure 53. Graph. Curve-fit for accelerance TF, bent 2, node 27V/node 8V.

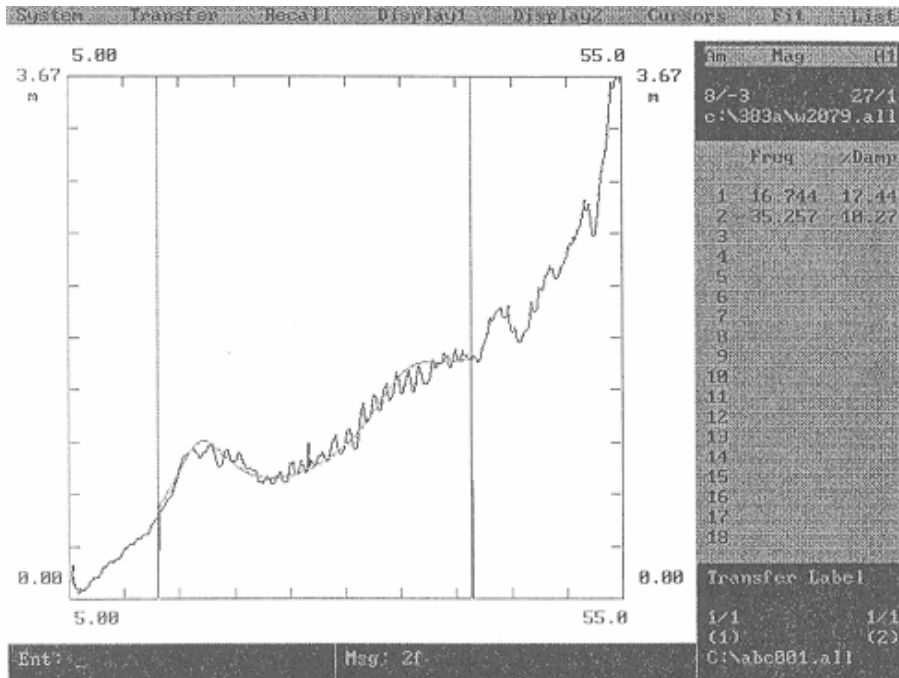


Figure 54. Graph. Curve-fit for accelerance TF, bent 2, node 27H/node 8V.

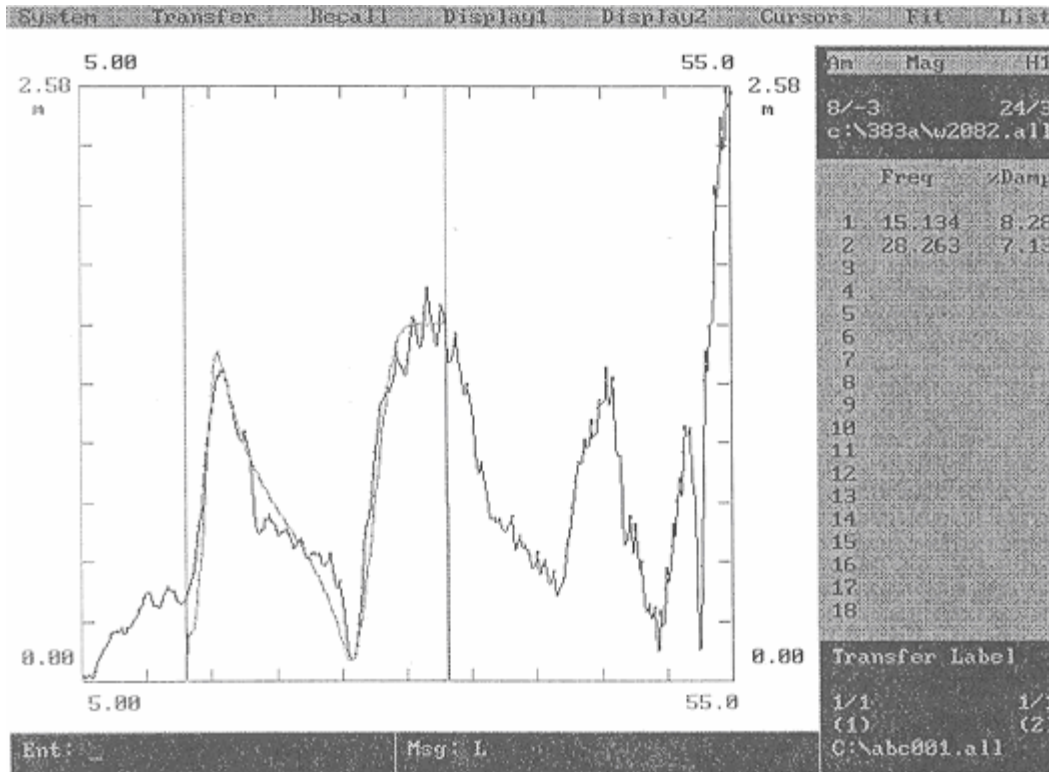


Figure 55. Graph. Curve-fit for accelerance TF, bent 2, node 24V/node 8V.

### Mode Shape Determination Using PCMODAL

After all of the accelerance TFs from a given test series were curve-fitted, PCMODAL was used to calculate mode shapes for each identified vibration mode frequency. Based on the measurement location, direction, and data quality, only one residual data file at each measurement location and direction was selected to extract the mode shapes. In general, the residual data files with the peak-to-peak forces below 176 kilonewtons (kN) (40,000 lbf) were selected. This is because higher dynamic loads would induce nonlinear behavior, especially for the soil around the concrete piles.

The selected residual data files were combined to obtain the relative magnitudes and phases of vibrations at each measurement location and direction to get the mode shape, frequency, and damping associated with the curve-fitted accelerance data. The mode shapes can be displayed in both static and dynamic fashions on the computer screen with PCMODAL. To illustrate a static mode shape display, the first mode shape from initial tests of bent 2 (piles plus footing) is shown in figure 56. Review of this figure shows the deflected mode shape for the first mode, a fundamental first mode frequency of 15.13 Hz, and damping of 0.165 (16.5 percent).

The primary curve fitting with PCMODAL and subsequent vibration mode shape, frequency, damping, magnitude, and phase were performed on the results from the more comprehensive final visit to bents 2 and 12, as discussed in the next section.

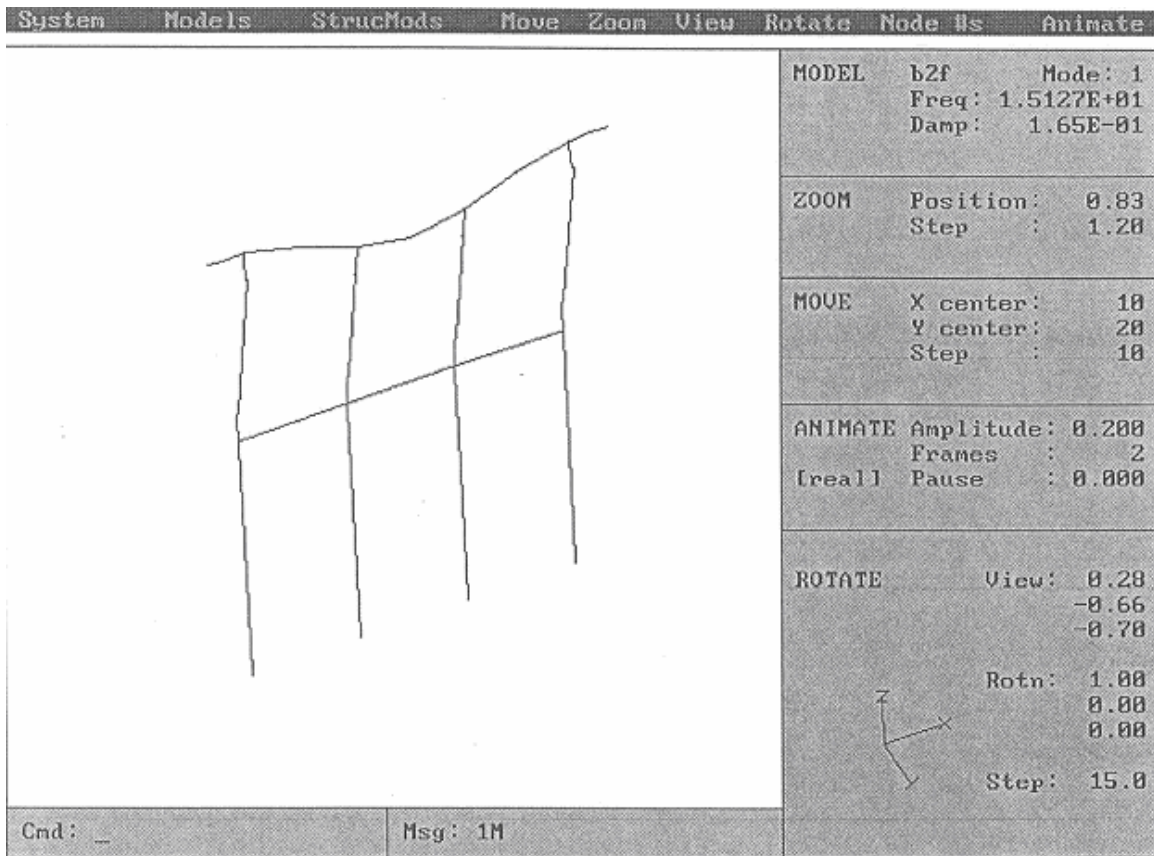


Figure 56. Diagram. First mode shape, frequency, and damping for bent 2.

### **SOUND VERSUS SIMULATED SCOUR AND EARTHQUAKE DAMAGE RESULTS, TRINITY RIVER RELIEF BRIDGE**

As discussed in chapter 4, bents 2 and 12 were tested for three cases in the final site visit:

- Case 1. Sound, undamaged condition.
- Case 2. With full to partial excavation of the south and south-center piles, respectively.
- Case 3. With the two piles excavated and the south pile broken.

The second and third cases were intended to simulate scour (excavated piles) and earthquake damage (broken piles). Two topics are covered in the following paragraphs. First, the possibility of determining damaged substructure conditions through field-obtainable flexibility TF plots is examined. Second, a more sophisticated approach involving modal curve-fitting and modal analyses is considered. The field data for the modal curve-fitting and modal analyses are from the simplest geometry of bent 12 (piles only).

### Flexibility Transfer Function Results for Bents 2 and 12

The node points and geometry of bents 2 and 12 are shown in figures 57 and 58, respectively. The node points are the same for both bents, but bent 2 has the additional strip footing around the piles at ground level. Loads were applied to the bridge deck over the pile beams of the bents at nodes 2, 4 (center point), and 6 for the first two cases and at nodes 2 and 4 for the third case. (No load was applied to node 6 because of safety concerns; a load over the broken south piles might have led to the collapse of the bridge.)

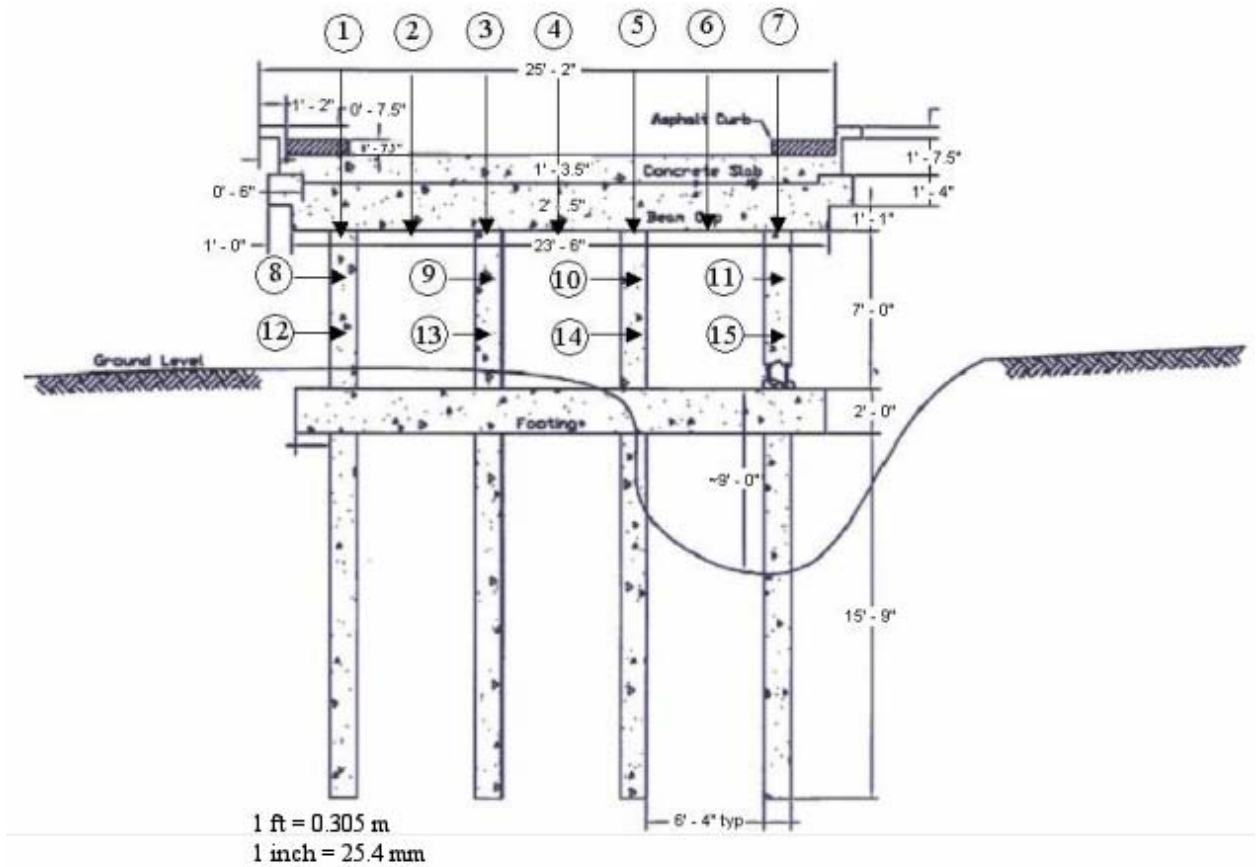


Figure 57. Diagram. Node points and geometry of bent 2.

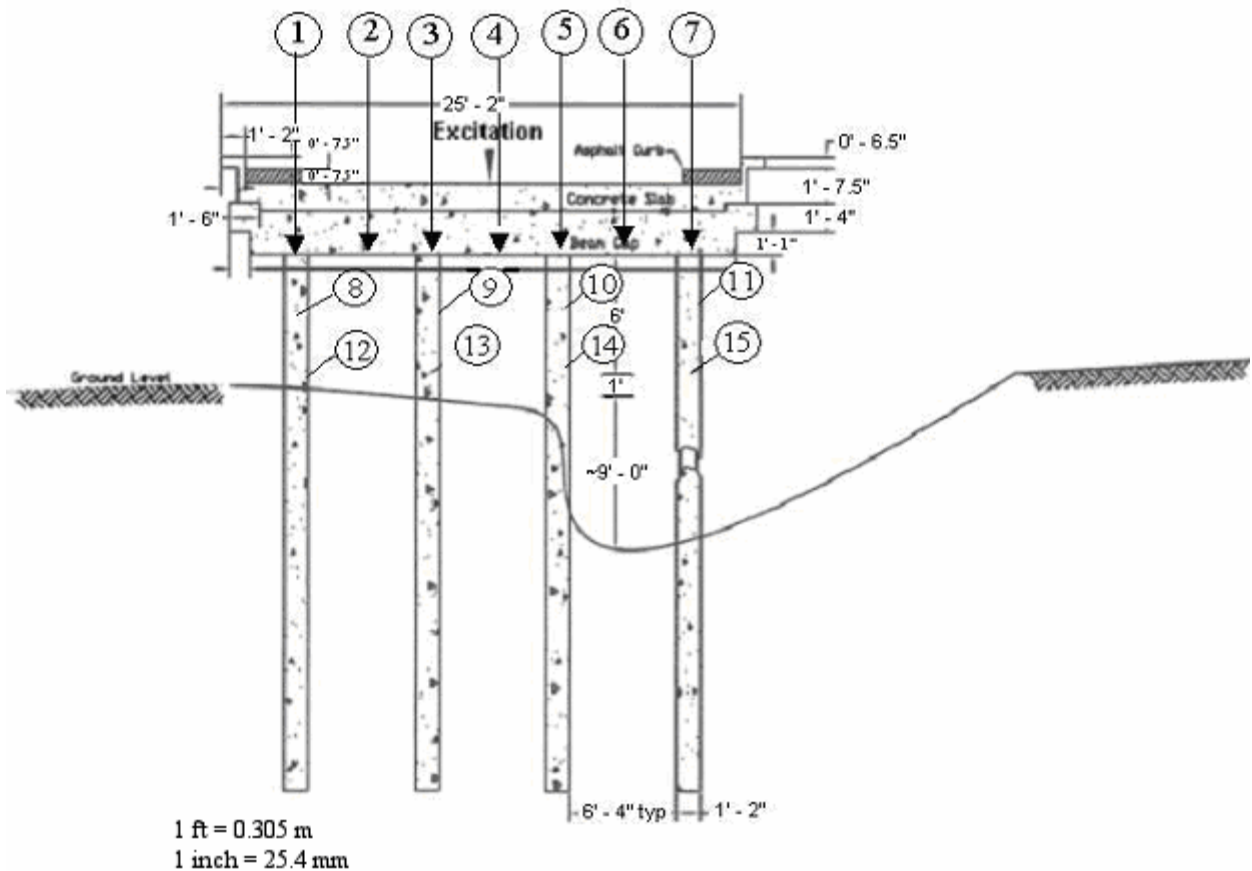


Figure 58. Diagram. Node points and geometry of bent 12.

### ***Flexibility Plot Results for Bent 12***

If flexibility plots are to indicate damage directly in the field, it would have been expected to see a shift downward in frequency of the vibration modes and an associated increase in flexibility (inches/lbf, or m/N), which means a decrease in stiffness (lbf/inch, or N/m). The frequency of the vibration modes decreases because natural frequencies decrease as stiffness decreases. It should also be noted that the closer the loading point is to the member, the greater its response is to excitation. Presumably, the flexibility TF results will be more sensitive to a locally damaged member as well. Furthermore, the simplest mode to detect and interpret in the field is the fundamental vertical mode of vibration for bridges.

To examine this, flexibility plots are shown in figures 59, 60, and 61 for the case of third-point loading of the bridge deck between each of the four piles. In figure 59, the loading is applied to the bridge deck at node 2, and the response is read from the vertical accelerometer on the underside of the pile cap at node 2. In figure 60, the loading is

applied to node 4, and the response is read from the underside of the pile cap at node 4. Three flexibility plots are presented in figures 59 and 60. The plots denote the following pile cases: i—initial undamaged, sound piles; e—excavated piles; and n—the broken south pile.

In figure 61, the loading is applied to node 6 and the responses are read from the underside of the pile cap at nodes 6, 10, and 11. In figure 61, only the case of the undamaged pile is considered. The three flexibility plots are for the responses at the three different nodes: 6, 10, and 11.

Review of figures 59 and 60 indicates there is the expected reduction in the first and second mode frequencies (about 0.8 Hz) and an increase in flexibility between the initial and excavated pile cases. There is almost no change in frequency and a smaller increase in flexibility between the excavated and broken pile cases. Comparing the results from node 2 (figure 59), which is furthest from the excavated and damaged piles, with results from node 4 (figure 60) shows that the greater flexibility increase resulting from excavating piles and breaking a pile occurred closer to the damage, as expected.

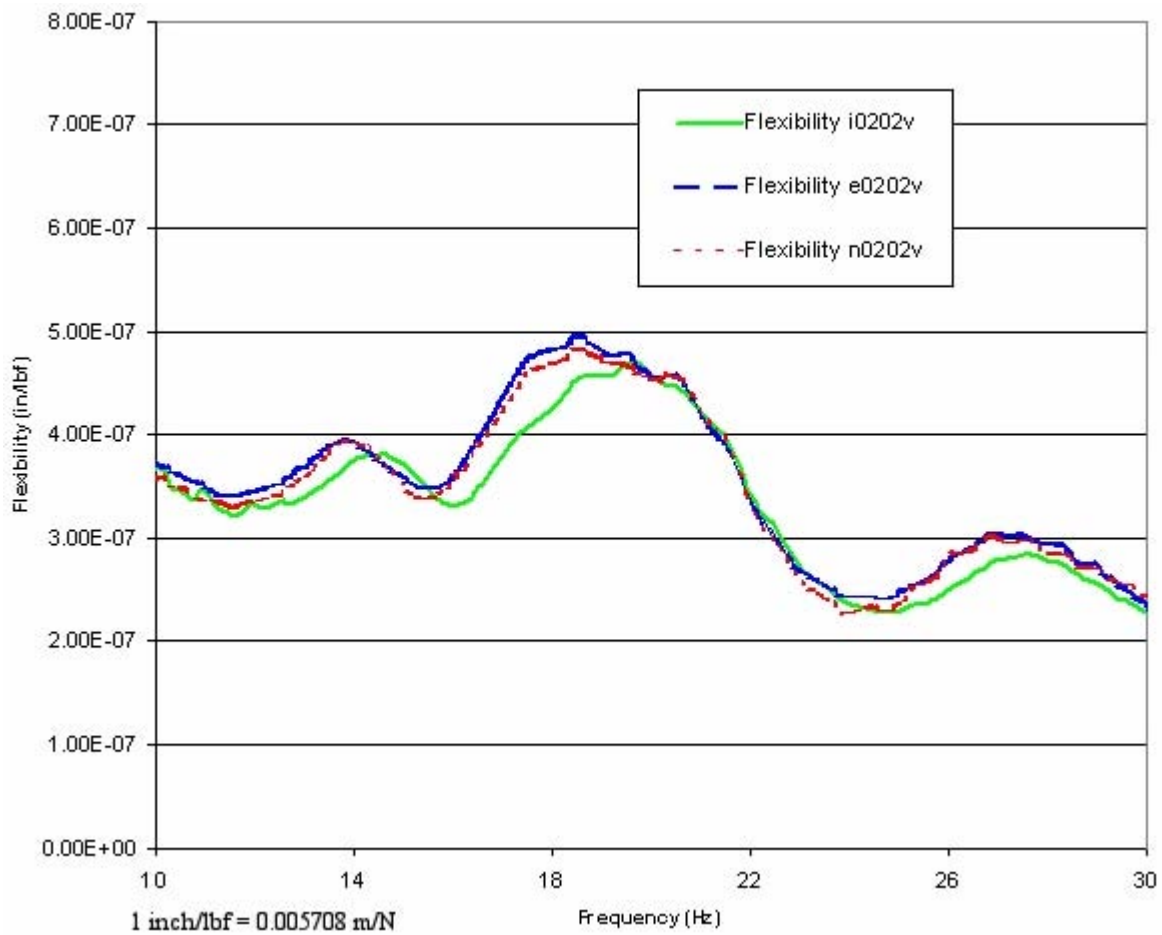


Figure 59. Graph. Bent 12 flexibility TFs at node 2 for intact (i), excavated (e), and broken (n) piles.

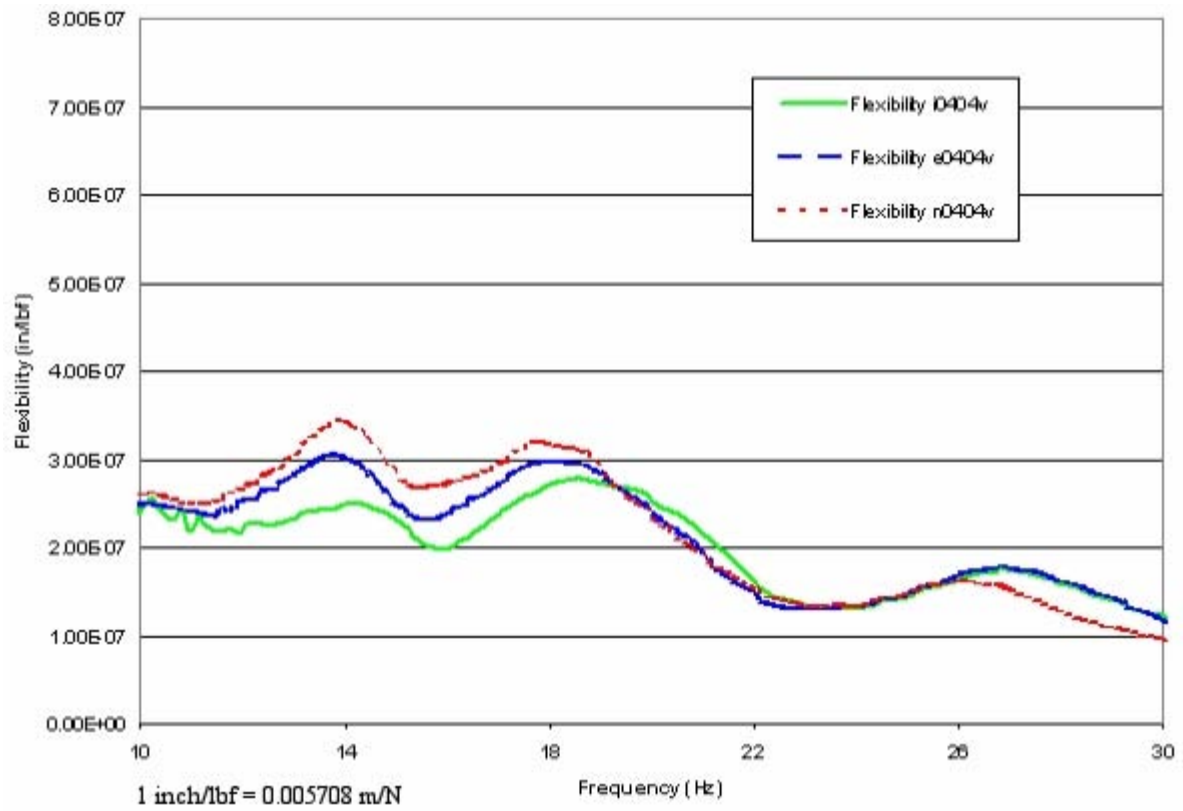


Figure 60. Graph. Bent 12 flexibility TFs at node 4 for intact (i), excavated (e), and broken (n) piles.

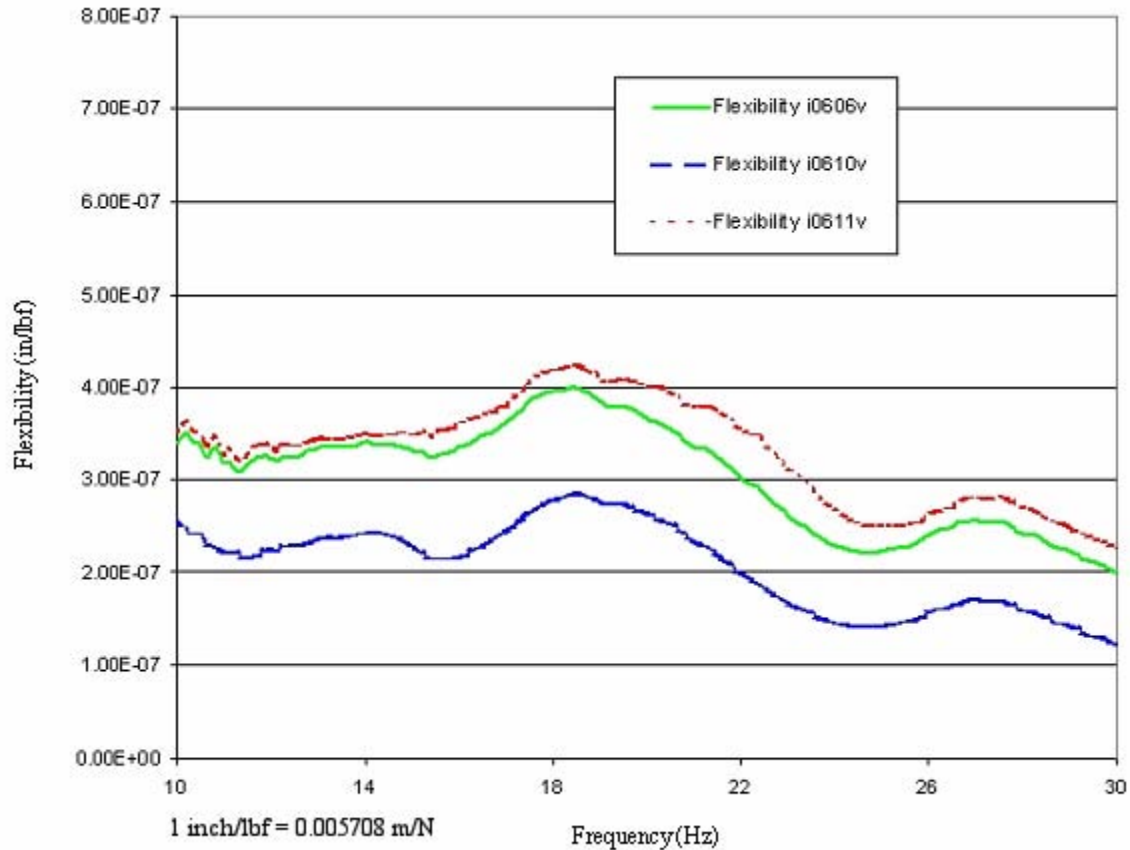


Figure 61. Graph. Bent 12 flexibility TFs at nodes 6, 10, and 11 for the intact pile.

Because the south-center and south piles are the members that were directly excavated and damaged, comparison of the flexibility results for the four piles should provide the best indication of whether field modal tests can directly indicate damaged substructure. These plots are shown in figures 62 through 65 for the cases of loading at the closest node to each pile and the vertical accelerometer response at either node 8, 9, 10, or 11, which are respectively the top receiver locations on each pile. (See figure 58 for bent 12 test geometry.) In the figure captions, the loading node, or node where the Vibroseis truck applies the force, is the denominator of the TF and the response node, which is the receiver location or node where the vertical accelerometer is read, is the numerator of the TF. Review of these figures shows that the south and north piles are the most flexible. Further review shows the first and second mode frequencies shift to a slightly lower frequency for the excavated versus initial sound pile cases, with no real shift in frequency among the excavated and broken pile cases. Of further interest is that the flexibility increases significantly between the initial, excavated, and broken cases for the south, south-center, and north-center piles, but for not the north pile, which is the farthest from the damage. The effect of the broken pile on increasing flexibility was likely somewhat muted; although the concrete was broken for the south pile, the four rebar were still intact.

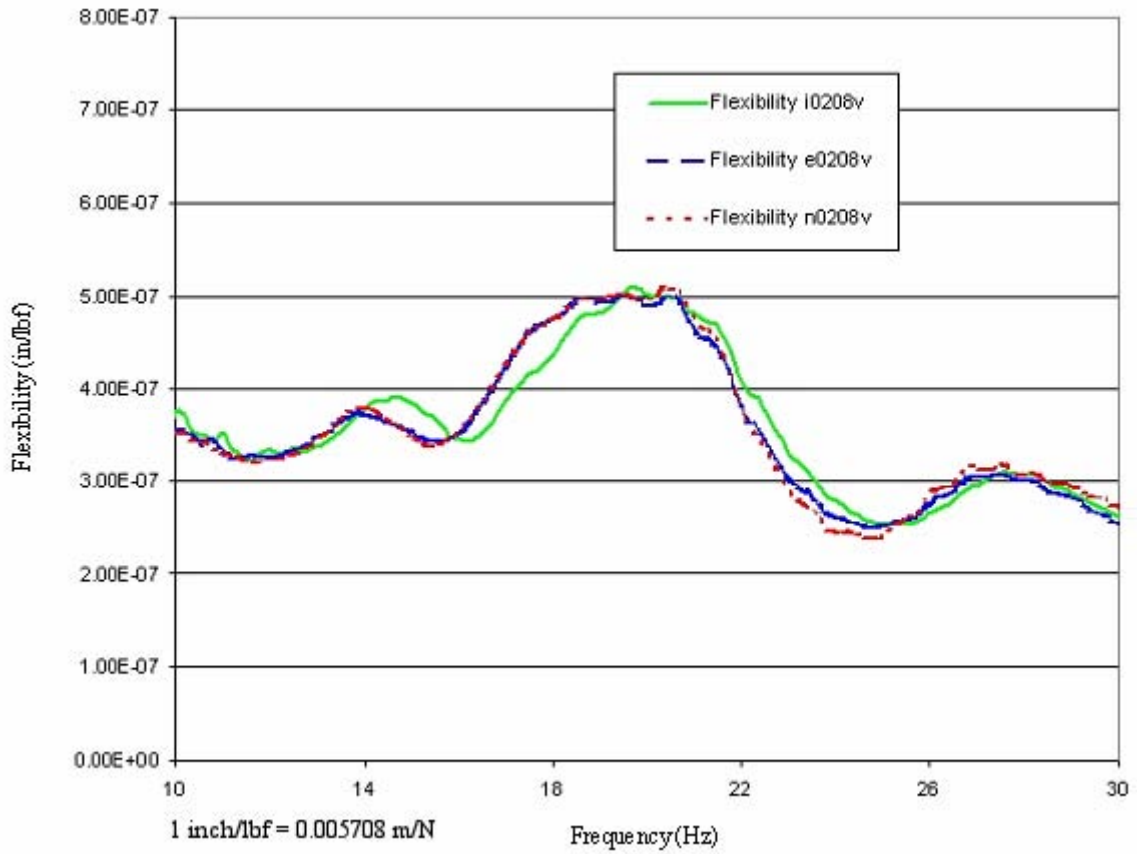


Figure 62. Graph. Bent 12 flexibility TFs for node 8/node 2 for intact (i), excavated (e), and broken (n) piles.

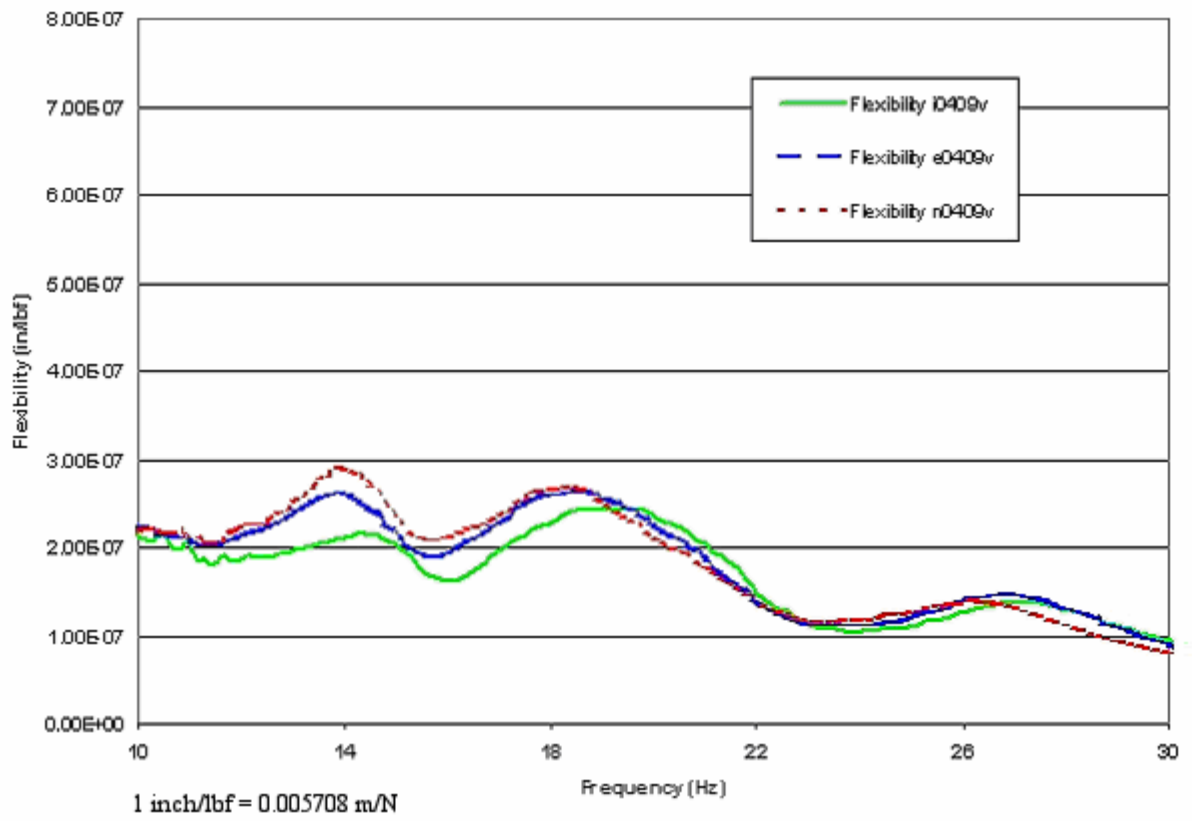


Figure 63. Graph. Bent 12 flexibility TFs for node 9/node 4 for intact (i), excavated (e), and broken (n) piles.

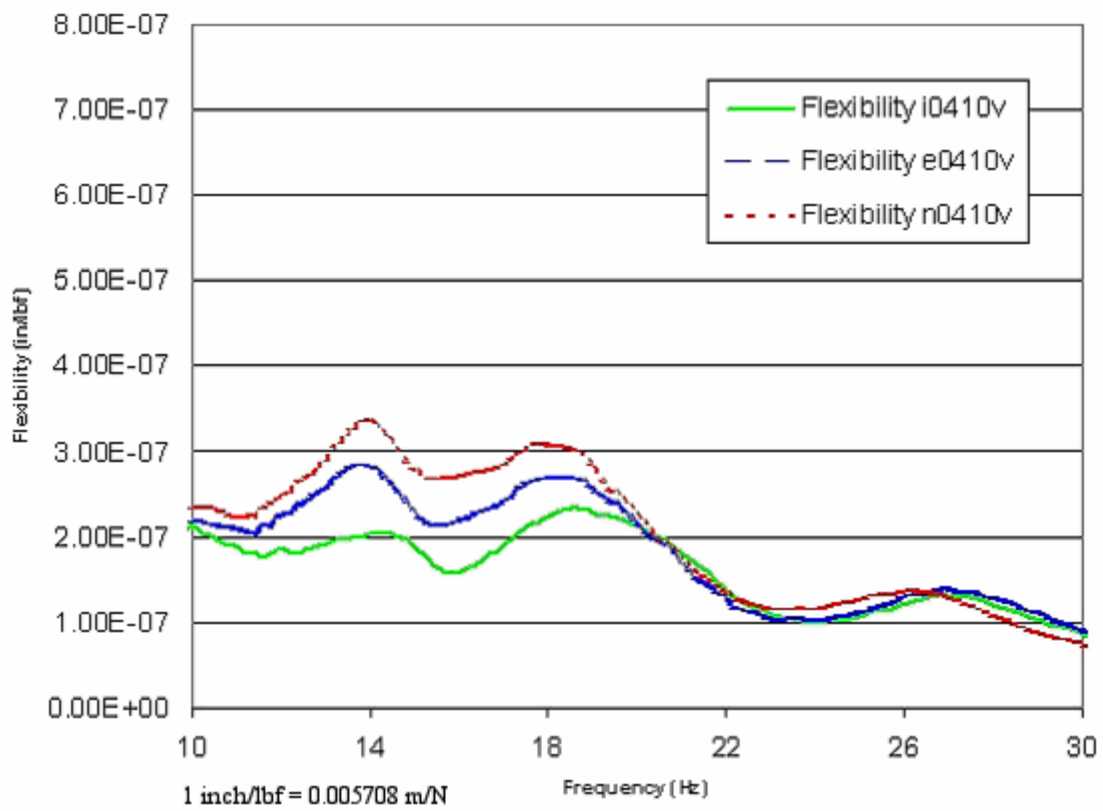


Figure 64. Graph. Bent 12 flexibility TFs for node 10/node 4 for intact (i), excavated (e), and broken (n) piles.

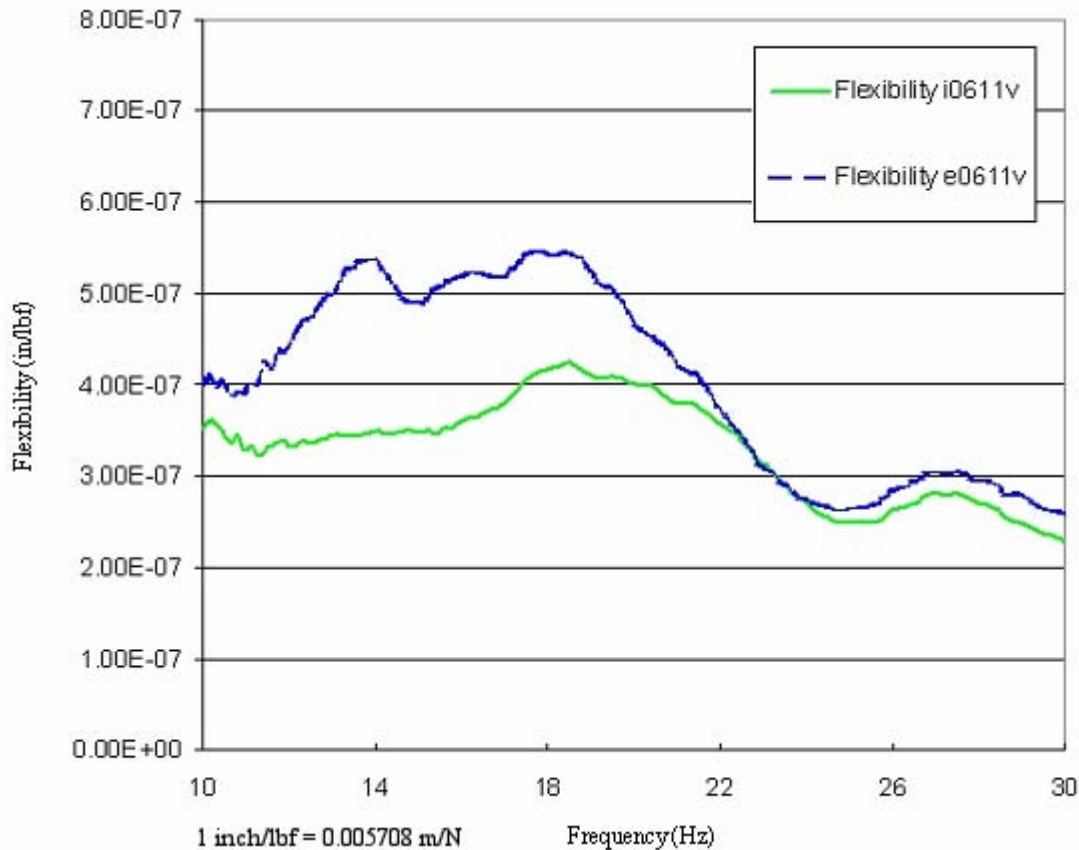


Figure 65. Graph. Bent 12 flexibility TFs for node 11/node 6 for intact (i) and excavated (e) piles.

### ***Flexibility Plot Results for Bent 2***

For bent 2, the flexibility results for the top loading and pile cap beam responses are shown in figures 66, 67, and 68. Each figure involves the loading and response at a single node: figure 66 for node 2, figure 67 for node 4, and figure 68 for node 6. The top loading to top vertical accelerometer results are shown in figures 69 through 72. In the captions to figures 69 through 72, the loading node, or node where the Vibroseis truck applies the force, is the denominator of the TF; the response node, which is the receiver location or node where the vertical accelerometer is read, is the numerator of the TF. Bent 2 flexibility plots showed similar behavior and trends as those discussed for bent 12. The frequency decrease after excavation was about 0.7 Hz. The effect of breaking the south pile resulted in a more pronounced increase in flexibility for bent 2 than for bent 12. The increase in flexibility was about 25 percent for the excavated case and 60 percent for the broken pile case as compared to the initial sound case.

### Summary of Flexibility Test Findings to Predict Damage

The flexibility results show promise for being able to directly identify substructure damage if a baseline of the sound response of a bridge has been determined above all critical members. The damage will be indicated by a small decrease in frequency and an increase in flexibility (corresponding decrease in stiffness). This result is not surprising because it is predicted theoretically, and in a sense, a flexibility modal TF test is a dynamic load test. However, it is expected that more complicated substructures where loading may or may not be close to the damaged member would not show as much of an effect in the flexibility results. The drawbacks of this flexibility TF approach are the need to put sensors on critical members and to test before damage is caused. These actions are necessary to establish a basis for judging and identifying, in future tests, the extent of damage.

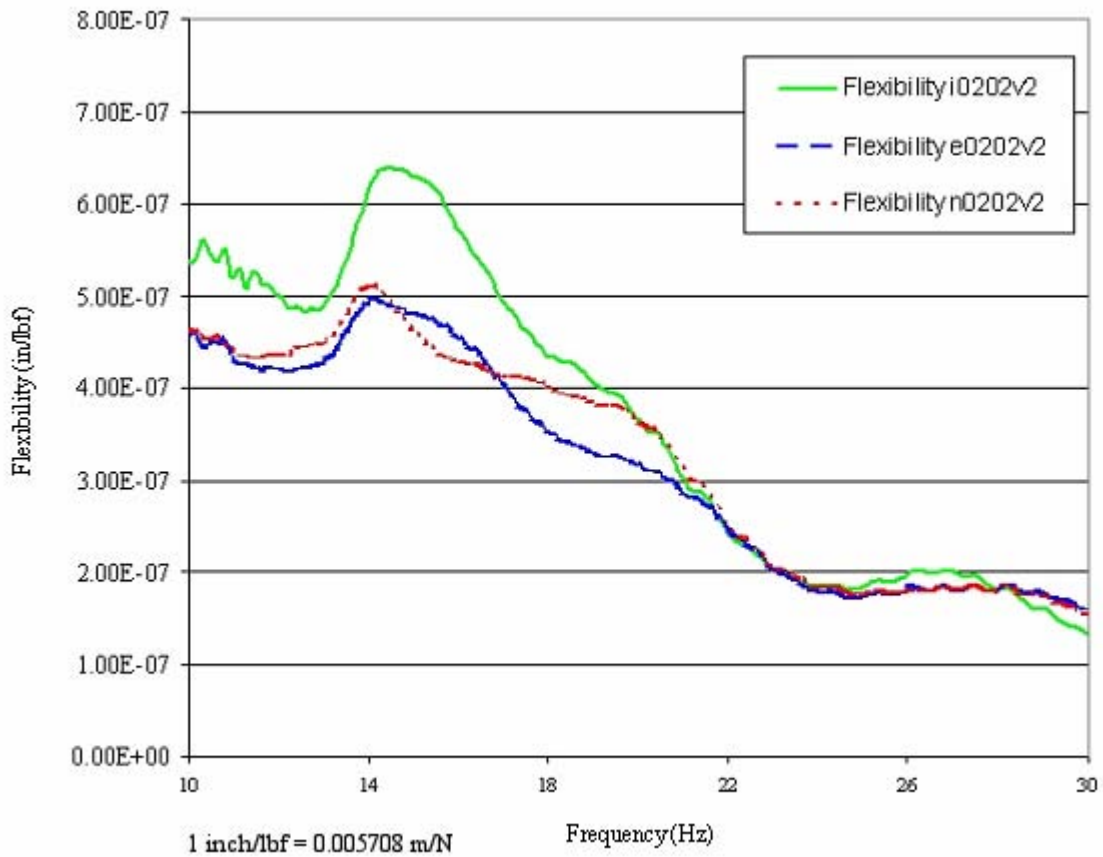


Figure 66. Graph. Bent 2 flexibility TFs at node 2 for intact (i), excavated (e), and broken (n) piles.

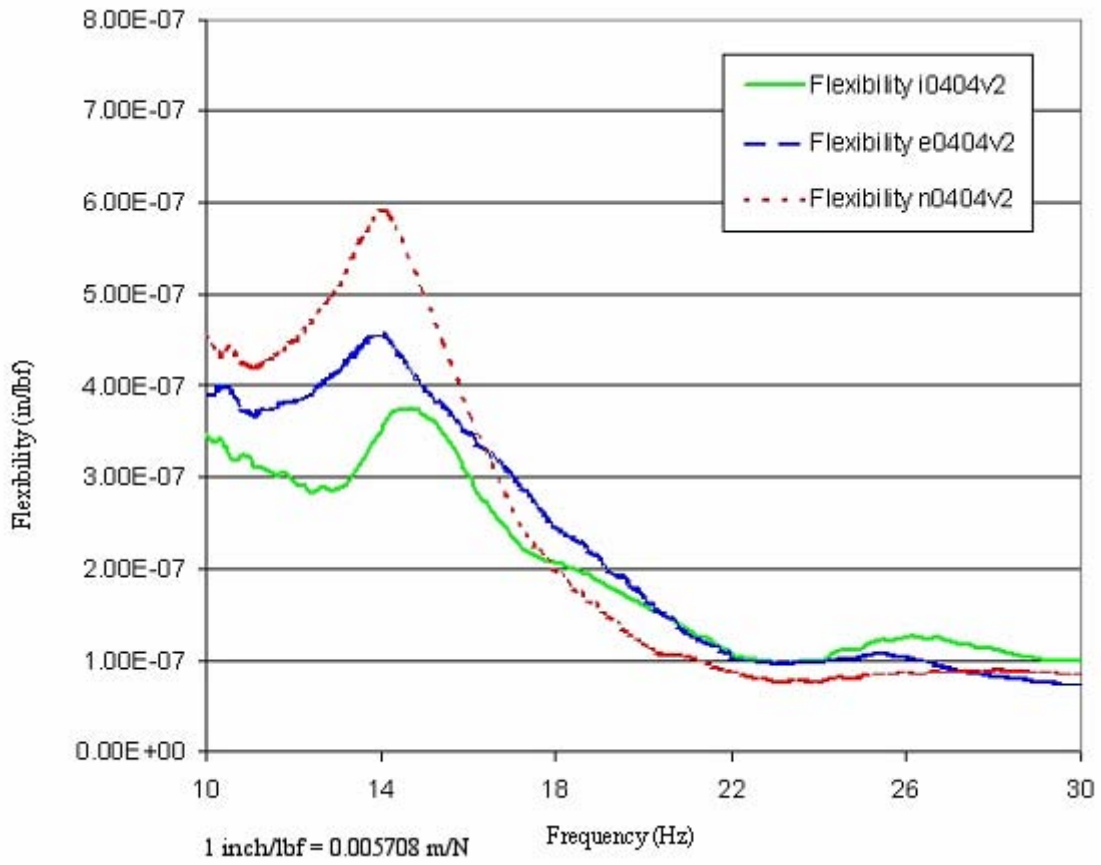


Figure 67. Graph. Bent 2 flexibility TFs at node 4 for intact (i), excavated (e), and broken (n) piles.

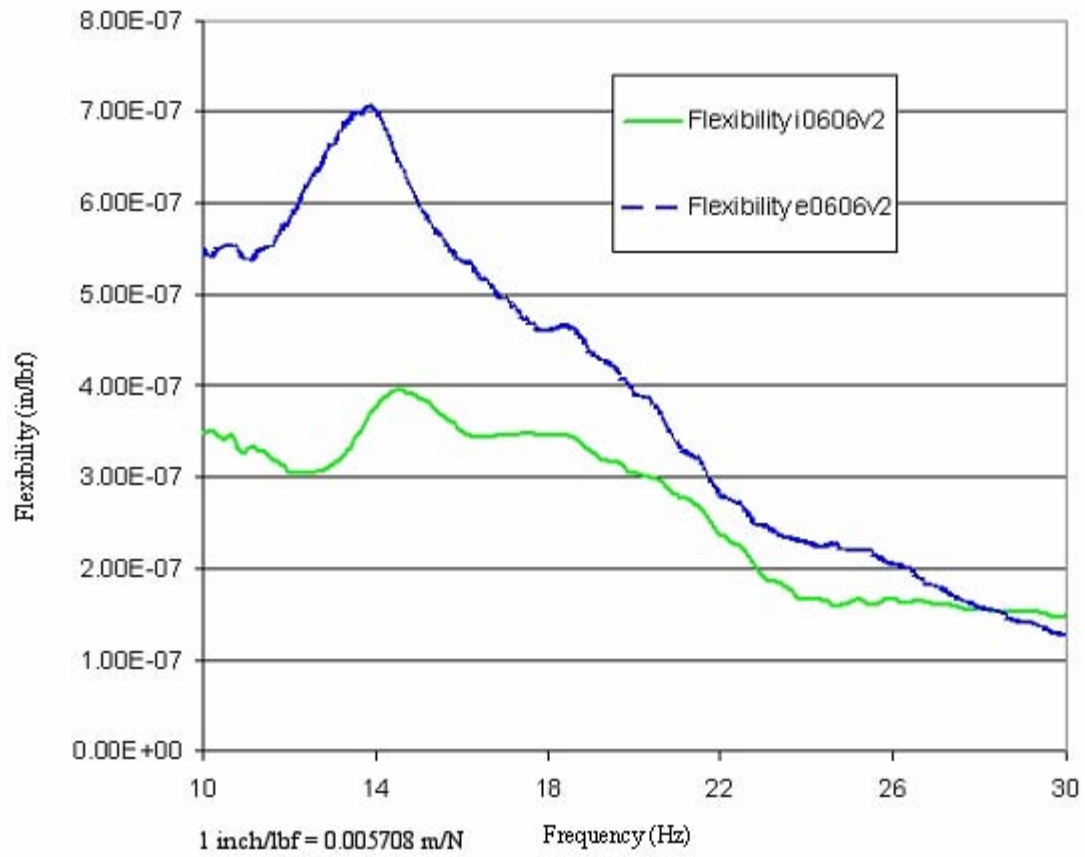


Figure 68. Graph. Bent 2 flexibility TFs at node 6 for intact (i) and excavated (e) piles.

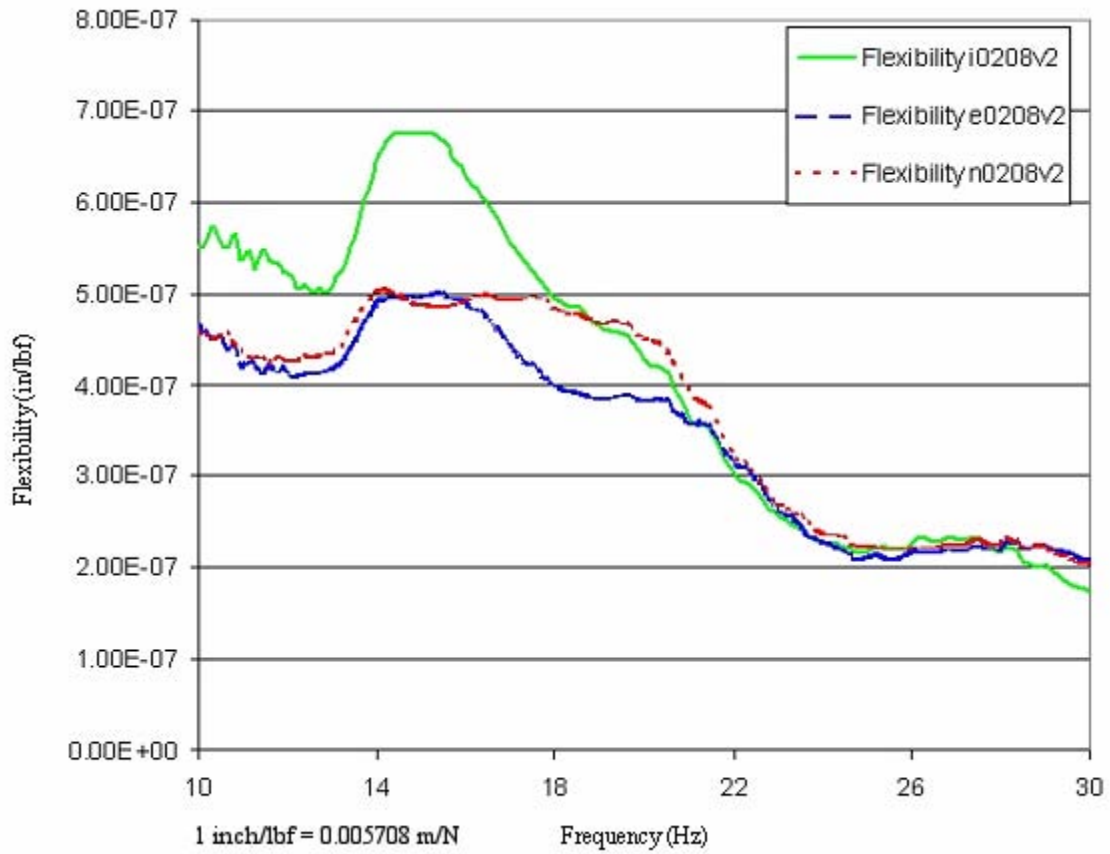


Figure 69. Graph. Bent 2 flexibility TFs for node 8/node 2 for intact (i), excavated (e), and broken (n) piles.

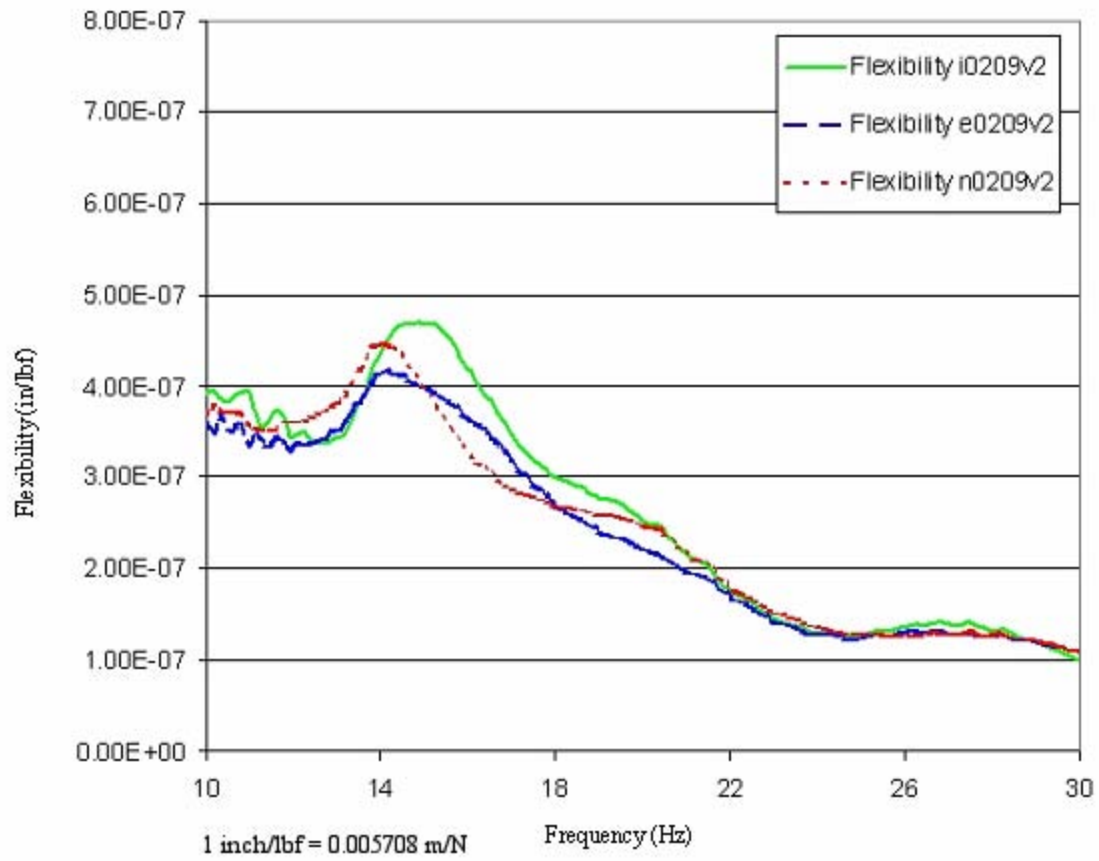


Figure 70. Graph. Bent 2 flexibility TFs for node 9/node 2 for intact (i), excavated (e), and broken (n) piles.

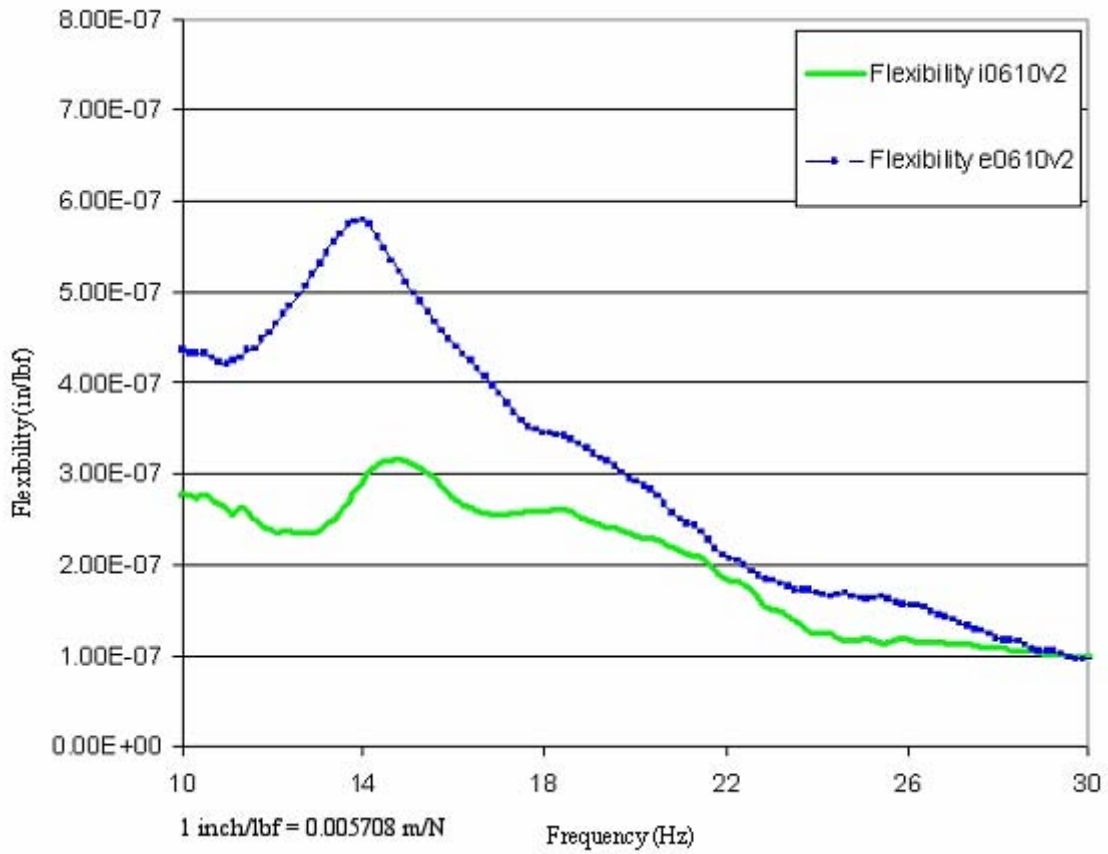


Figure 71. Graph. Bent 2 flexibility TFs for node 10/node 6 for intact (i) and excavated (e) piles.

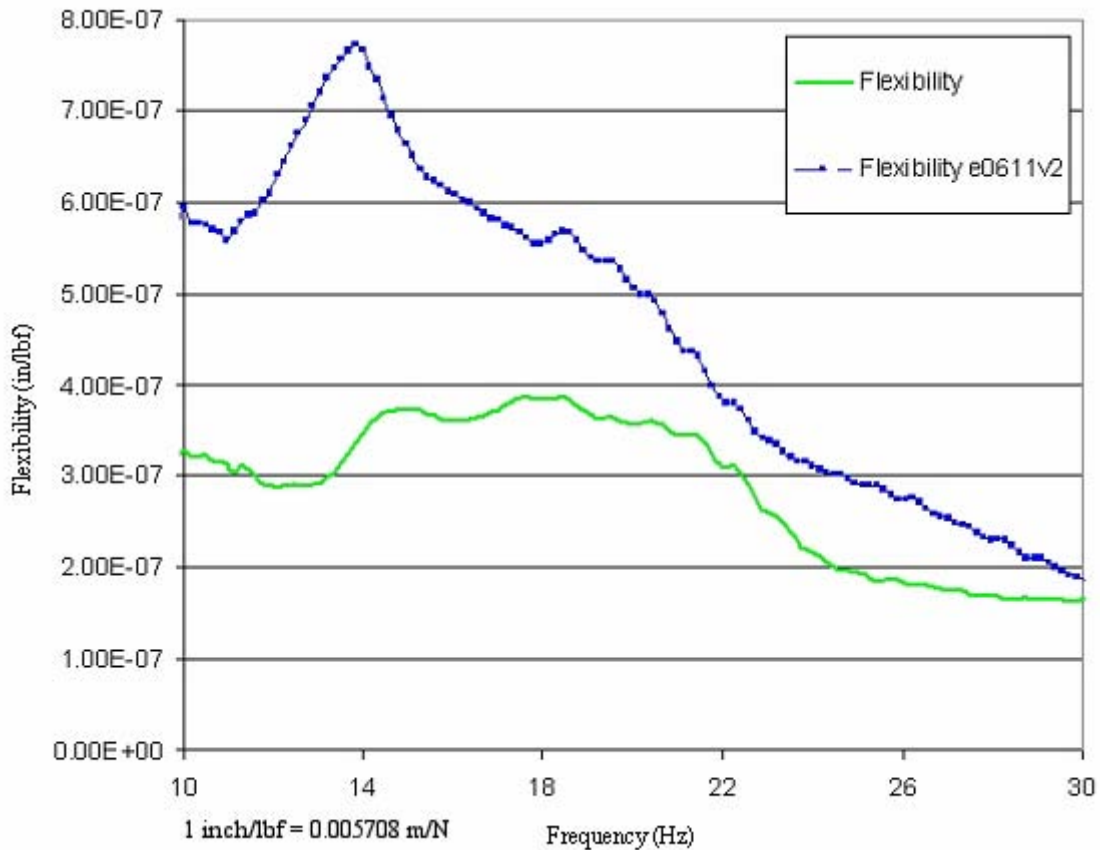


Figure 72. Graph. Bent 2 flexibility TFs for node 11/node 6 for intact (i) and excavated (e) piles.

### Modal Curve-Fitting Results for Bent 12

Because bent 12 had the simplest test geometry with piles only, it was selected for detailed modal analysis with the PCMODAL software. Three vibration modes were identified as a result of the curve-fitting analyses: Mode 1 Vertical; Mode 2 Vertical; and Mode 2 Horizontal. Tests were performed for loading at nodes 2, 4, and 6, but only results of the center, symmetrical loading at node 4 and the loading at node 2 (farthest from the damaged south piles) are presented here. Results are presented only from node 4 and node 2 to evaluate differences between the sound, excavated, and broken south piles and the sound north piles. The following paragraphs discuss the results for each of these vibration modes.

#### *Modal Analysis Results for Mode 1 Vertical*

For the first vertical mode analysis, results of the individual curve-fits of the modal vibration data for center loading at node 4 are shown in figure 73. Data are given for

nodes 2, 4, 6, and 8 through 15. For each node, three sets of values are given for, first, frequency (Hz) and second, damping (percent). The top values at each node are the readings when all piles are sound (the sound pile case). The middle values are the readings when the south and south-central piles are excavated (the excavated pile case). The bottom values are the readings when the south pile is broken (the broken or broken south pile case). For center loading at node 4, the averages of the frequencies at nodes 2, 4, 6, and 8 through 15 for the first vertical mode analysis are 14.78 Hz for the sound pile case, 13.90 Hz for the excavated pile case, and 13.90 Hz for the broken pile case; thus, comparing the sound to the excavated first mode vertical frequencies shows a decrease of about 0.9 Hz. No significant change in frequency was noted between the excavated and the broken pile cases. Probably this is because the four vertical rebars in the south pile were not broken; only the concrete was broken.

The corresponding absolute magnitudes of the mode shape (normalized to node 4) and the phases (plus or minus in degrees relative to node 4) are shown in figure 74. The mode shape magnitudes are normalized to node 4, which is assigned a value of 1.0; the phase is also relative to node 4, which is at 0 degrees (in-phase). Review of figure 74 shows fairly symmetrical responses for the sound pile case but an asymmetrical response for the excavated and broken pile cases. Responses at nodes 11 and 15 for the fully excavated and then broken south pile cases show similar increased magnitudes and out-of-phase responses versus the sound pile case.

For the sound pile case, figures 75 and 76 allow comparisons between the effects of center loading at node 4 and loading at node 2. Figure 75 gives frequency (in hertz) and damping (in percent) for nodes 4 and 2 loading. Figure 76 gives magnitude (normalized to node 4) and phase (in degrees relative to node 4) for node 4 loading and node 2 loading. For both figures, the top values at each node are the results of center loading at node 4; the bottom values are the results of loading at node 2. The average frequencies and damping for the two loading points are similar—approximately 14.8 Hz for frequency and approximately 9 percent for damping. The largest difference between the two loading points is in the phase. Reflecting the asymmetric location of node 2, the phase resulting from node 2 loading shifts approximately 150 degrees from left to right (the north pile to the south pile).

### Mode 1 (Vertical)

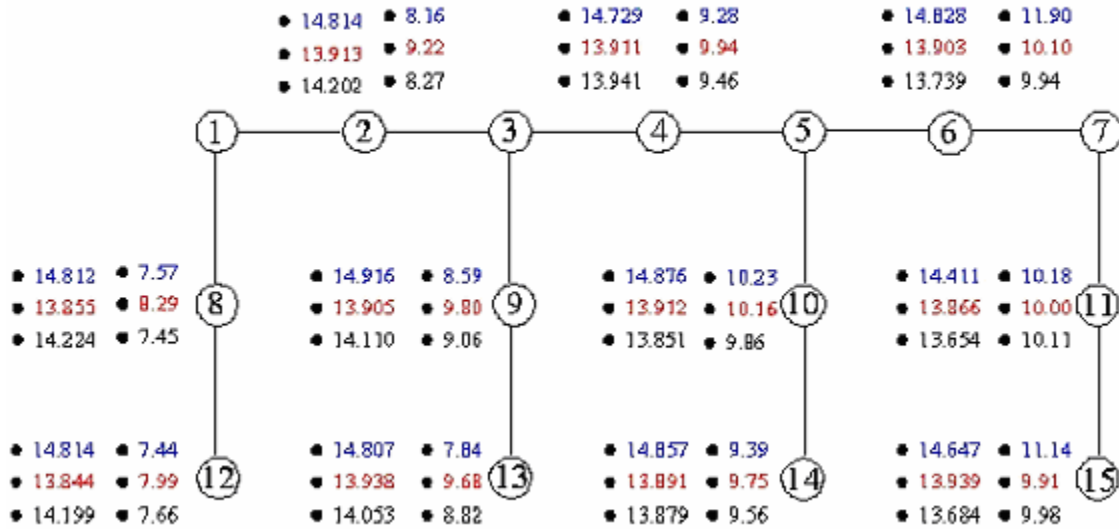


Figure 73. Diagram. Bent 12, Mode 1 Vertical, node 4 (center) loading, frequency and damping.

### Mode 1 (Vertical)

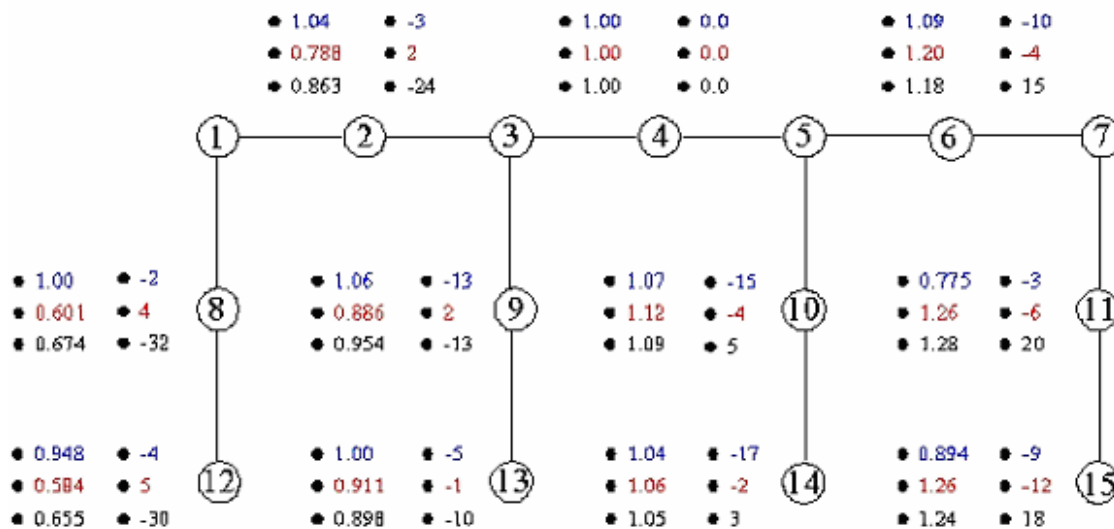


Figure 74. Diagram. Bent 12, Mode 1 Vertical, node 4 (center) loading, magnitude and phase.

### Mode 1 (Vertical)

Center Loading: 14.779 Hz 9.46%

N2 Loading: 14.782 Hz 8.38%

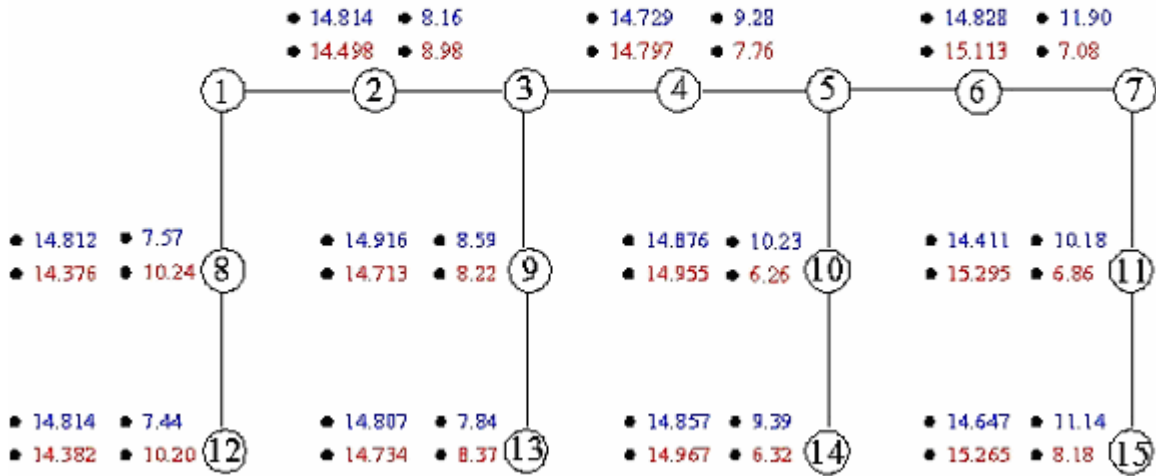


Figure 75. Diagram. Bent 12, Mode 1 Vertical, loading at nodes 2 and 4, frequency and damping.

### Mode 1 (Vertical)

Center Loading: 14.779 Hz 9.46%

N2 Loading: 14.782 Hz 8.38%

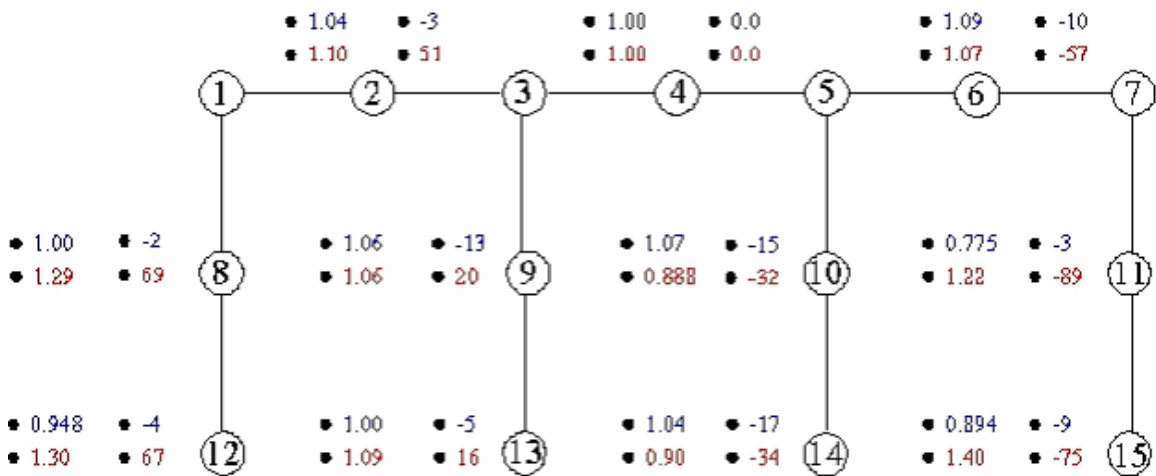


Figure 76. Diagram. Bent 12, Mode 1 Vertical, loading at nodes 2 and 4, magnitude and phase.

### ***Modal Analysis Results for Mode 2 Vertical***

For the second vertical mode, figures 77 through 80 present data corresponding to figures 73 through 76 of the first vertical mode. The average frequencies for the second vertical mode with node 4, or center, loading are 21.88 Hz for the sound pile case, 21.20 Hz for the excavated pile case, and 20.77 Hz for the broken pile case; thus, for the second vertical mode, the excavated pile case decreases about 0.7 Hz from the sound pile case. The decrease in frequency resulting from breaking the pile is about 0.4 Hz. This smaller decrease in frequency for the excavated-to-broken pile case as compared to the sound-to-excavated pile case likely results because the four vertical rebars in the south pile were not broken; only the concrete was broken.

The corresponding relative absolute magnitude of the mode shape (normalized to node 4) and the phase (plus or minus in degrees relative to node 4) are shown in figure 78. The mode shape magnitudes are normalized to node 4, which is assigned a value of 1.0, and the phase is also relative to node 4, which is at 0 degrees (in-phase). Figure 78 shows asymmetrical responses for the sound, excavated, and broken pile cases.

For the sound pile case, figures 79 and 80 allow comparisons between the effects of center loading at node 4 and loading at node 2. Figure 79 gives frequency (in hertz) and damping (in percent) for nodes 4 and 2 loading. Figure 80 gives magnitude (normalized to node 4) and phase (in degrees relative to node 4) for nodes 4 and 2 loading. In both figures, the top values at each node are the results of center loading at node 4, and the bottom values are the results of loading at node 2. The largest phase difference is found from one edge pile to the other in node 2 loading, caused by the asymmetric nature of node 2 loading.

### Mode 2 (Vertical)

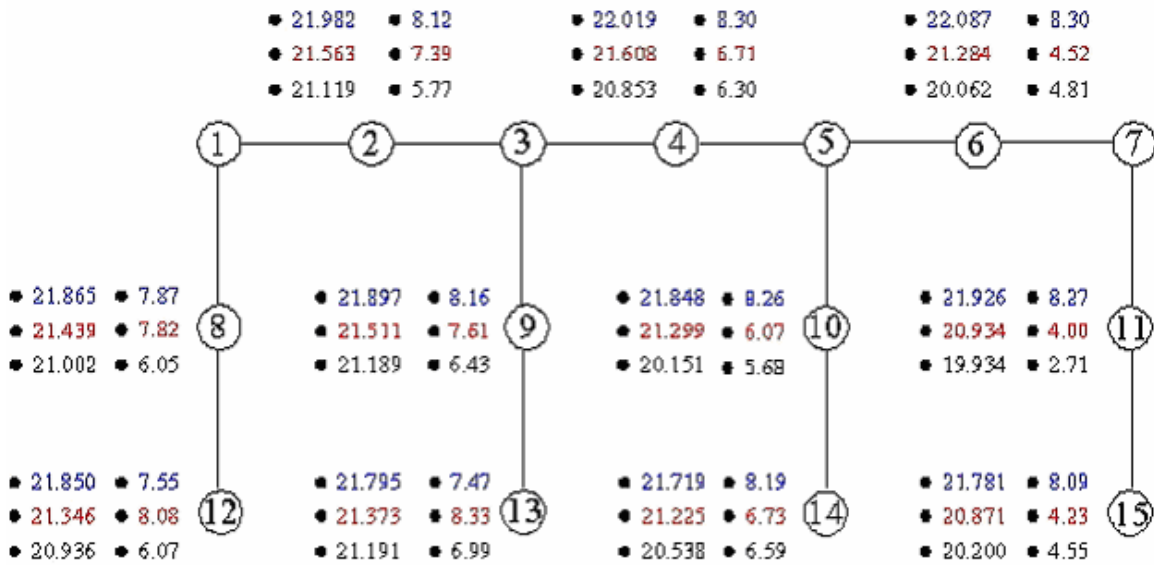


Figure 77. Diagram. Bent 12, Mode 2 Vertical, node 4 (center) loading, frequency and damping.

### Mode 2 (Vertical)

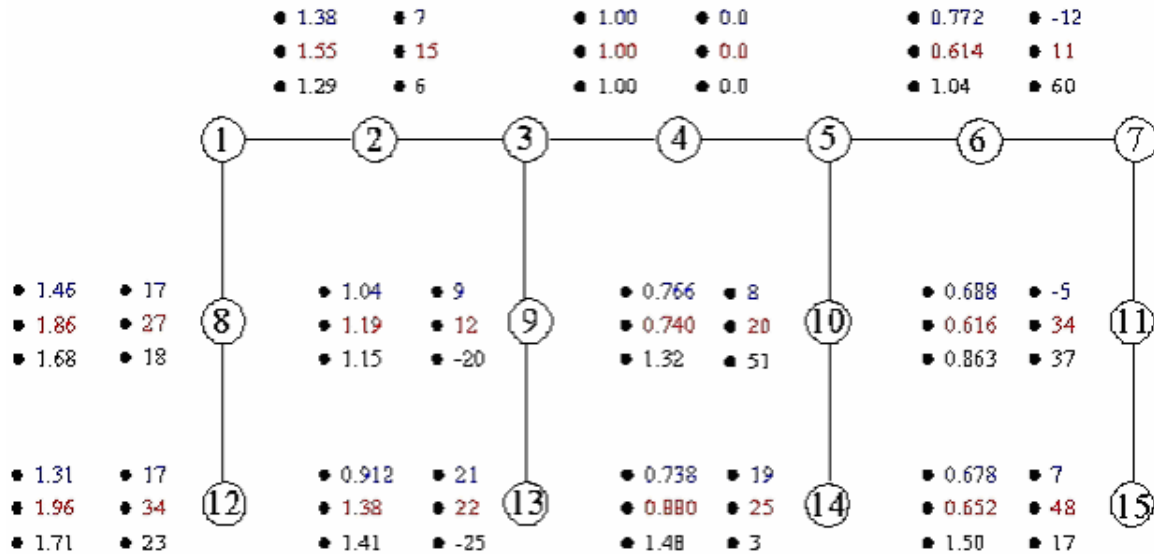


Figure 78. Diagram. Bent 12, Mode 2 Vertical, node 4 (center) loading, magnitude and phase.

### Mode 2 (Vertical)

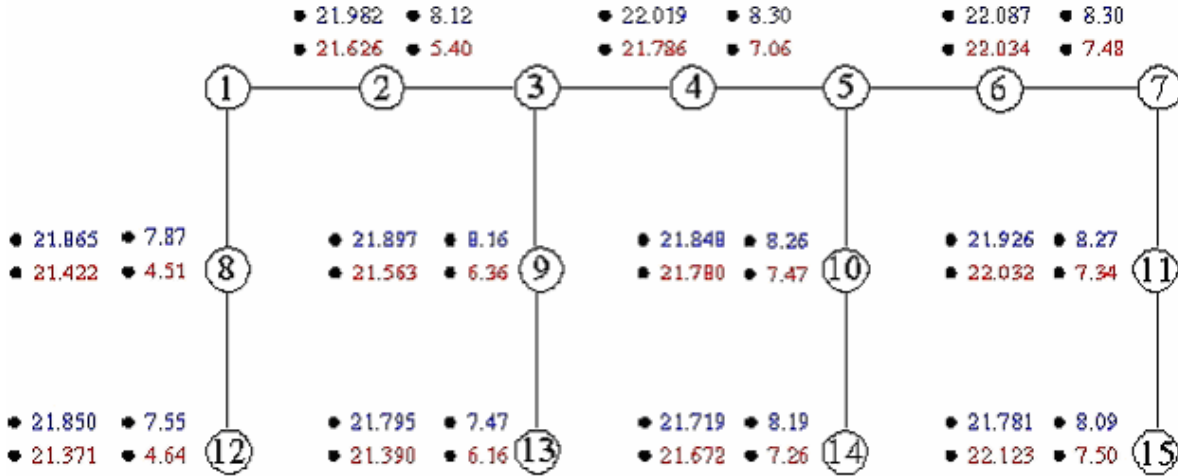


Figure 79. Diagram. Bent 12, Mode 2 Vertical, loading at nodes 2 and 4, frequency and damping.

### Mode 2 (Vertical)

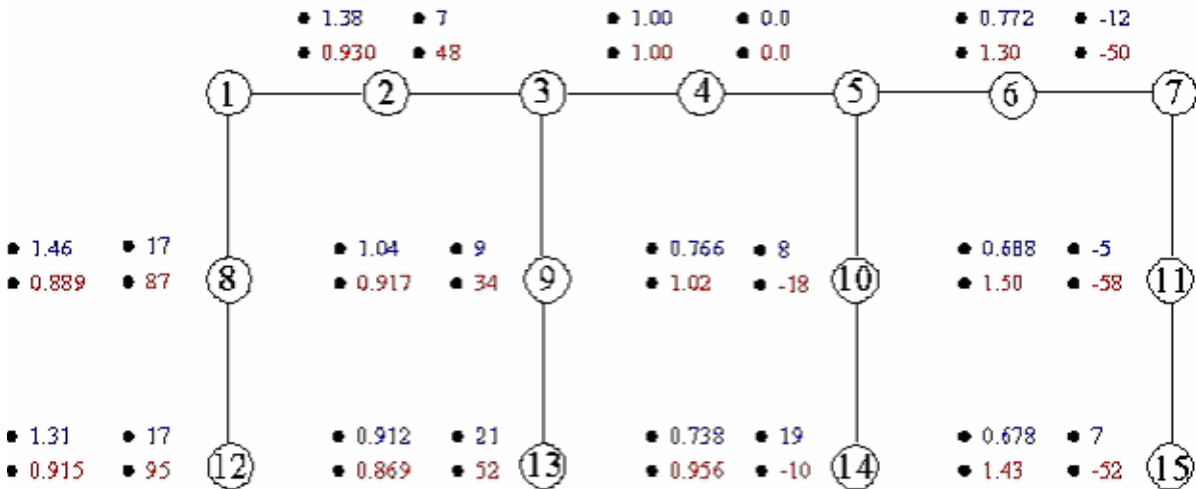


Figure 80. Diagram. Bent 12, Mode 2 Vertical, loading at nodes 2 and 4, magnitude and phase.

### ***Modal Analysis Results for Mode 2 Horizontal***

Figures 81 through 84 present data for the second horizontal mode, corresponding to figures 73 through 76 of the first vertical mode. Second horizontal mode data are calculated from horizontal accelerometers. The average frequencies for the second horizontal mode with node 4, or center, loading are 21.84 Hz for the sound pile case, 20.66 Hz for the excavated pile case, and 20.63 Hz for the broken pile case; thus, for the second horizontal mode, the excavated pile case decreases about 1.2 Hz from the sound pile case. The decrease in frequency resulting from breaking the pile is about 0.03 Hz. This smaller decrease in frequency from the excavated-to-broken pile case as compared to the sound-to-excavated pile case likely results because the four vertical rebars in the south pile were not broken; only the concrete was broken.

The corresponding relative absolute magnitude of the mode shape (normalized to node 4) and the phase (plus or minus in degrees relative to node 4) are presented in figure 82. The mode shape magnitudes are normalized to node 4, which is assigned a value of 1.0, and the phase is also relative to node 4, which is at 0 degrees (in-phase). Figure 78 shows asymmetrical responses for the sound, excavated, and broken pile cases.

For the sound pile case, figures 83 and 84 allow comparisons between the effects of center loading at node 4 and loading at node 2. Figure 83 gives frequency (in hertz) and damping (in percent) for nodes 4 and 2 loading. Figure 84 gives magnitude (normalized to node 4) and phase (in degrees relative to node 4) for nodes 4 and 2 loading. For both figures, the top values at each node are the results of center loading at node 4, and the bottom values are the results of loading at node 2. The largest phase difference is found from one edge pile to the other in node 2 loading, resulting from the asymmetric nature of node 2 loading.

### ***Summary of Modal Curve-Fitting Analysis Results***

The clearest indication of damage was provided by the decrease in frequency of the first and second vibration modes among the cases of sound, excavated, and broken piles. Changes in magnitude and phase from symmetrical to asymmetrical also indicated damage in some cases. The other analysis result of damping did not prove to be a damage indicator. Considering the additional effort required to perform the PCMODAL curve-fits, and the fact that the modal frequency peaks are apparent in the field flexibility TFs, the extra effort required to perform the curve-fits did not result in that much additional information from a substructure damage perspective.

Mode 2 (Horizontal)

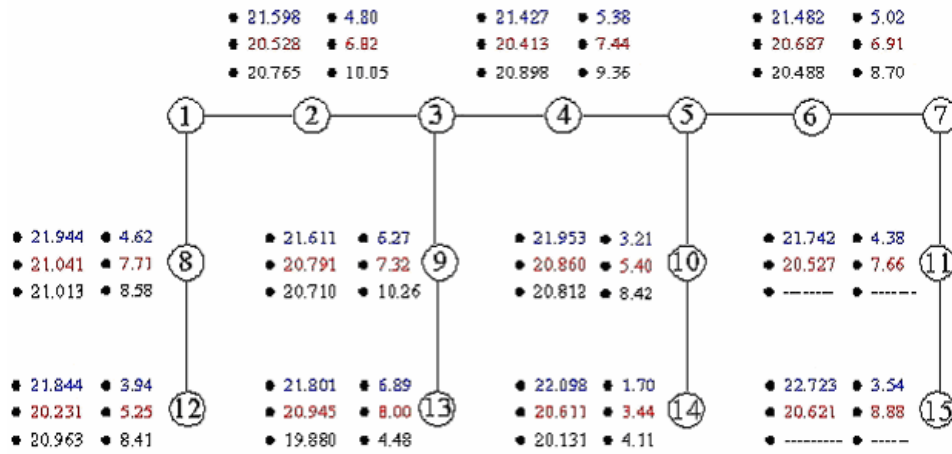


Figure 81. Diagram. Bent 12, Mode 2 Horizontal, node 4 (center) loading, frequency and damping.

Mode 2 (Horizontal)

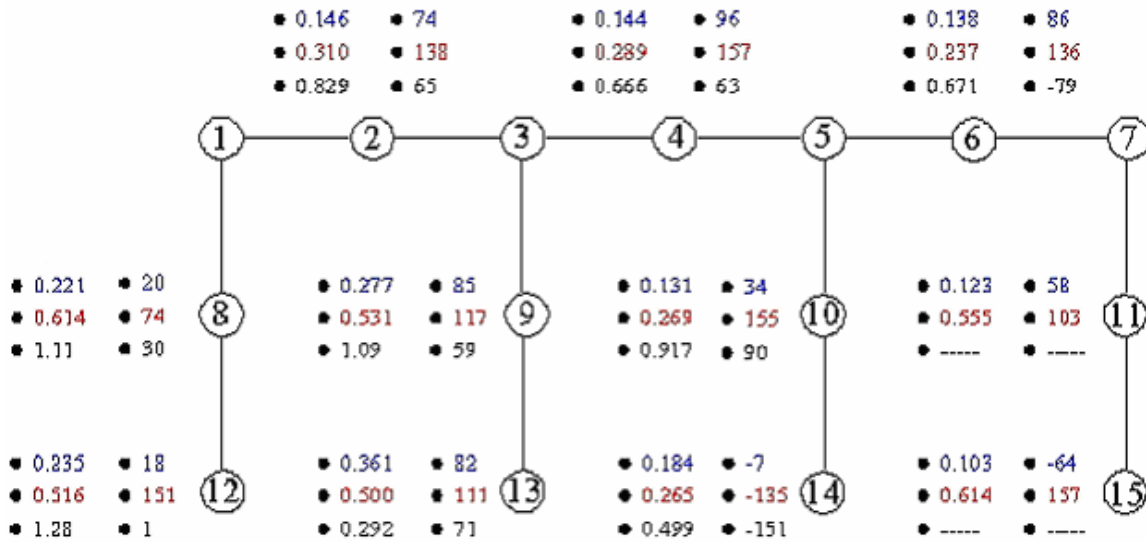


Figure 82. Diagram. Bent 12, Mode 2 Horizontal, node 4 (center) loading, magnitude and phase.

### Mode 2 (Horizontal)

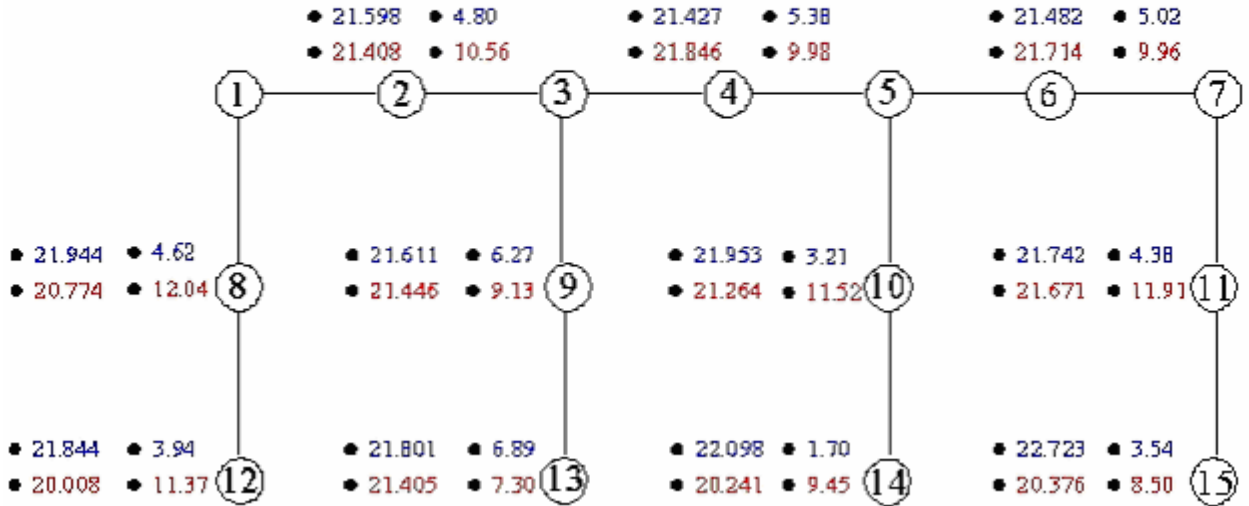


Figure 83. Diagram. Bent 12, Mode 2 Horizontal, loading at nodes 2 and 4, frequency and damping.

### Mode 2 (Horizontal)

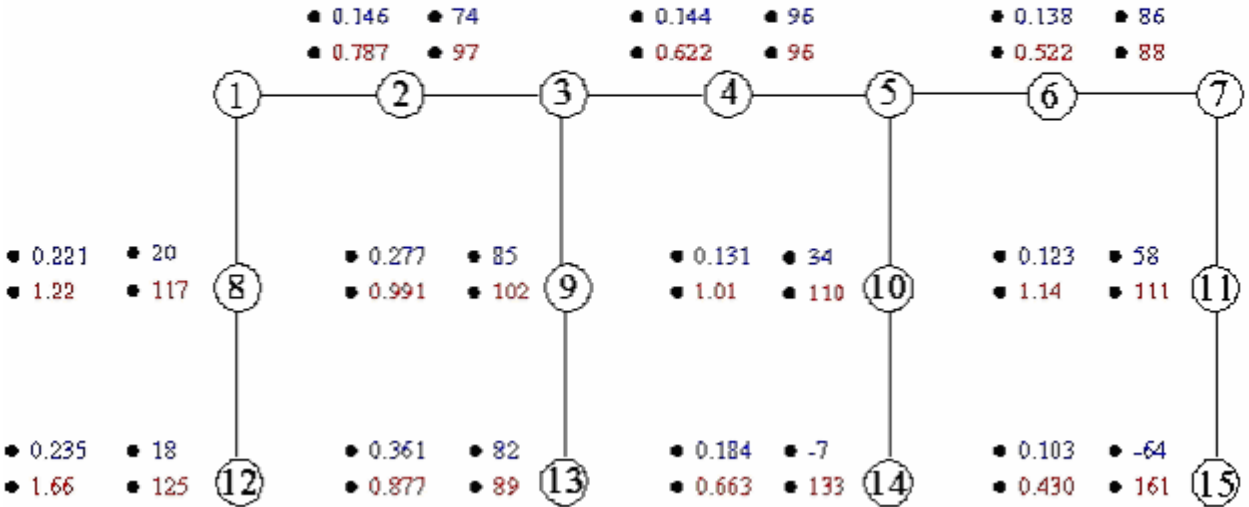


Figure 84. Diagram. Bent 12, Mode 2 Horizontal, loading at nodes 2 and 4, magnitude and phase.

## **SHALLOW VERSUS DEEP FOUNDATION IDENTIFICATION RESULTS— WOODVILLE AND OLD RELIANCE BRIDGES**

These two bridges were selected for this research because they were of similar design in similar soil conditions, except that the Woodville Road Bridge had a footing foundation, while the Old Reliance Road Bridge had a similar size pile cap footing on top of steel BP (bearing pile) piles. The modal analysis nodes and accelerometer and force excitation locations are shown in figures 34 and 39 in chapter 4 for the Woodville and Old Reliance Bridges, respectively.

A hypothesis is that different resonant frequencies and modal TF responses will be measured for bridges with shallow versus deep foundation systems even when the bridges are otherwise virtually identical. To examine this hypothesis, figures 85 and 86 present flexibility TF results for the Woodville and Old Reliance bridges. For each bridge, the Vibroseis force was applied directly over the top vertical accelerometer on each of the two bridge columns. For figure 85, the Vibroseis force was applied at node 17, and the response reading was taken at the vertical accelerometer at node 9. In figure 86, the Vibroseis force was applied at node 18, and the response reading was taken at the vertical accelerometer at node 10. The figures show that the flexibility TFs are similar for loading at nodes 17 and 18 for each bridge itself, but very different between the two bridges.

Thus, an initial conclusion might be that modal testing can differentiate between shallow versus deep foundations for otherwise similar bridges. However, the first vertical mode resonant peak, 9 Hz, for Old Reliance with the steel piles is not greater than the first vertical mode resonant peak, 10 Hz, for Woodville. Therefore, at least in the case of the Old Reliance and Woodville bridges, contrary to expectations, steel piles plus pile cap do not result in greater stiffness than footing alone. Moreover, the flexibility, and inversely the stiffness magnitudes, is similar for the two bridges. Finally, the first three resonant peaks for Old Reliance are all at lower frequencies than for Woodville. In view of these facts, modal testing might have limited capability of uniquely and clearly determining shallow versus deep foundations, unless otherwise identical bridge structures are situated in similar soils. Furthermore, at least one of the foundations tested probably should have a known shallow or deep foundation system to serve as the basis against which unknown foundation systems can be judged. Finally, modal testing to determine unknown depths of foundations for scour safety evaluation is unlikely to be successful.

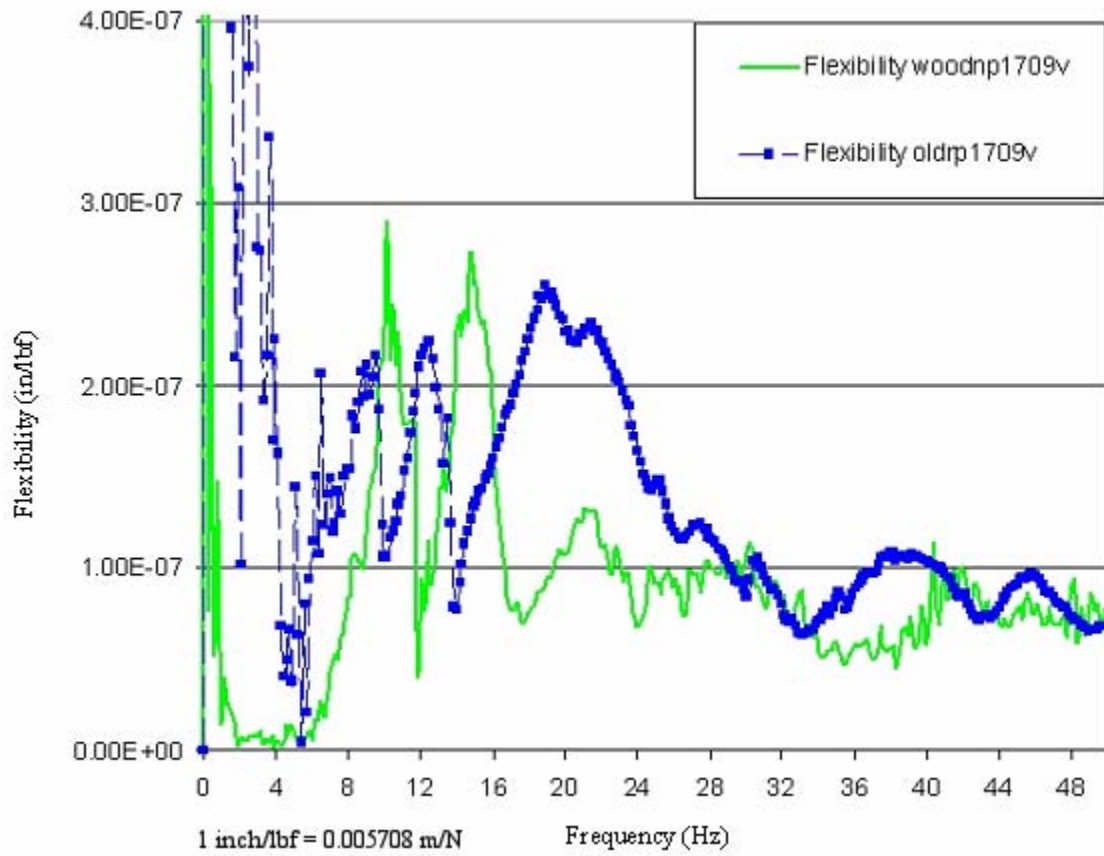


Figure 85. Graph. Woodville and Old Reliance Bridges, flexibility TFs, node 9/node 17.

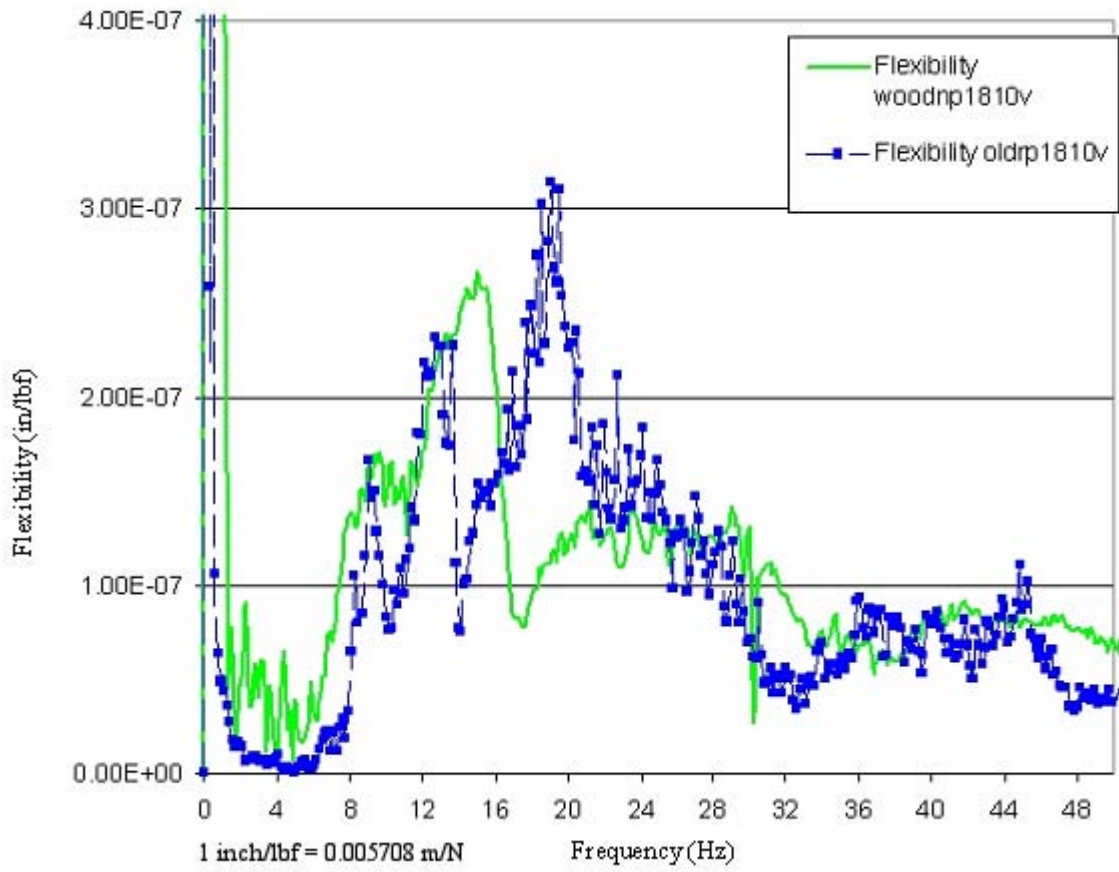


Figure 86. Graph. Woodville and Old Reliance Bridges, flexibility TFs, node 9/node 18



## CHAPTER 6. STRUCTURAL MODELING AND PARAMETER ESTIMATION

### INTRODUCTION

The overall objective of the analytic modeling in this project was to provide a means for interpretation of the field data based on the predictable dynamics of a structure. Finite element modeling provided an analytical basis for understanding the resonant frequencies and mode shapes observed in the field data. Parameter estimation provided a means for determining bridge foundation stiffness properties from the field data, which can then be used to determine bridge foundation type and condition. One of the prime purposes of the research was to evaluate the capabilities of using parameter estimation to determine bridge substructure conditions and possibly foundation type, such as shallow or deep foundation system.

3-D FEM models were formulated for each of the three tested bridges—Trinity River, Old Reliance, and Woodville Road. For the Trinity River Bridge, separate FEM models were generated for bents 2 and 12 because bent 2 had piles plus a strip footing and bent 12 had only piles. Of the other two bridges, only one bent was tested for each bridge; thus, only one FEM model per bridge was generated. The FEM models were generated using geometry from plan drawings and geometric field measurements. Construction material properties were taken as standard values except where the field data were available, such as for the elastic moduli of concrete and soil.

3-D FEM models revealed the key mode shapes and resonant frequencies associated with each of these structures. Because the field instrumentation was confined to the plane of the tested bent, it was simpler to model the tested bent as a 2-D structure, and then conduct a 2-D finite element analysis; however, it was necessary to lump the tributary mass of the superstructure (bridge deck and girders) on the cap beam of the bent. The 3-D FEM models provided a means for determining the magnitude of the lumped mass as a function for each mode of interest. The 2-D FEM models served as the basis for parameter estimation, described in detail later in this chapter. Because of issues related to the field data, 2-D finite element modeling was conducted for only the Trinity River Bridge, whose superstructure consisted of only a concrete slab.

### 3-D ANSYS MODEL

The 3-D FEM models were formulated for all three tested bridges using ANSYS<sup>®</sup>, a commercial FEM software. For each FEM model, the bridge foundation stiffness and mass were represented by soil-substructure super-elements  $K_{SSS}$  and  $M_{SSS}$ , each of which is a 6-by-6 matrix described in the equations in figures 87 and 89. The calculation of specific elements in the matrices depends on the nature of the bridge foundation—whether the bridge columns act as individual piles or are supported by either a spread footing or a pile cap supported by a pile group. The following paragraphs describe the features of the 3-D FEM model for each of the tested bridges.

$$K_{SSS} = \begin{bmatrix} K_{xx} & 0 & 0 & 0 & 0 & K_{\phi_z x} \\ 0 & K_{yy} & 0 & 0 & 0 & 0 \\ 0 & 0 & K_{zz} & K_{\phi_x z} & 0 & 0 \\ 0 & 0 & K_{z\phi_x} & K_{\phi_x \phi_x} & 0 & 0 \\ 0 & 0 & 0 & 0 & K_{\phi_y \phi_y} & 0 \\ K_{x\phi_z} & 0 & 0 & 0 & 0 & K_{\phi_z \phi_z} \end{bmatrix}$$

Figure 87. Equation.  $K_{SSS}$ .

$$M_{SSS} = \begin{bmatrix} M_{xx} & 0 & 0 & 0 & 0 & 0 \\ 0 & M_{yy} & 0 & 0 & 0 & 0 \\ 0 & 0 & M_{zz} & 0 & 0 & 0 \\ 0 & 0 & 0 & M_{\phi_x \phi_x} & 0 & 0 \\ 0 & 0 & 0 & 0 & M_{\phi_y \phi_y} & 0 \\ 0 & 0 & 0 & 0 & 0 & M_{\phi_z \phi_z} \end{bmatrix}$$

Figure 88. Equation.  $M_{SSS}$ .

### Descriptions of 3-D FEM Modeling

The bents on the Trinity River, Old Reliance Road, and Woodville Road bridges tested in this research were all modeled with 3-D FEM techniques.

### ***Trinity River Bridge (Bents 2 and 12)***

For the Trinity River Bridge, shell elements were used to capture the out-of-plane bending of the bridge deck; beam elements were used to model the cap beam and concrete columns of the bent. Because the neutral axis of the bridge deck element is 0.508 m (20 inches) above the neutral axis of the cap beam, coupling was introduced numerically to model this connection. Because the bridge deck was supported simply by the bent, the corresponding bridge deck and bent elements were coupled in translation, but they were free to rotate with respect to each other. The cap beam has rigid connections with the concrete columns of the bent. The cross-sectional and material properties were calculated using standard strength of material techniques. The low-strain maximum Young's modulus for the concrete in the bent was computed from the ultrasonic pulse velocity field data and estimated values of Poisson's ratio and concrete density. The shear modulus of the soil was calculated from the SASW velocity data collected at the site and estimated values of Poisson's ratio and soil density. The bridge foundations were modeled using lumped stiffness ( $K_{SSS}$ ) and mass ( $M_{SSS}$ ) matrices, as explained by Santini.<sup>(134)</sup>

FEM models reflecting different locations of the Vibroseis truck were created for each tested bent of the Trinity River Relief Bridge. A lumped mass element was used to represent the mass of the Vibroseis truck. The truck mass was distributed as follows: 15,890 kg (35,000 lb) at the loading point; 2,724 kg (6,000 lb) at the position of the front wheels; and 3,178 kg (7,000 lb) at the position of the rear wheels. A 3-D FEM model for bent 2 consisted of 1,400 elements and 8,353 DOFs, while a 3-D FEM model for bent 12 consisted of 1,349 elements and 8,215 DOFs. Santini discusses in detail the calculations used to produce the 3-D FEM models for bents 2 and 12 of the Trinity River Bridge.<sup>(134)</sup>

### ***Old Reliance Road and Woodville Road Bridges***

Shell elements were used to model the bridge deck and girders because of the height-to-thickness ratio of the girders—1.37 m-to-0.381 m (4.6 ft-to-1.25 ft). The use of the shell elements for the girders also provides a means for modeling the vertical offset between the bridge deck and the cap beam. The cap beam and columns, modeled as beam elements, were rigidly connected to each other. The cross-sectional and material properties were calculated using standard strength of material techniques. Santini made the detailed calculations for the elements in the lumped stiffness ( $K_{SSS}$ ) and mass ( $M_{SSS}$ ) matrices.<sup>(134)</sup> The resulting 3-D FEM model for the Old Reliance Road Bridge consisted of 4,639 elements and 29,298 DOFs; the 3-D FEM model for the Woodville Road Bridge consisted of 5,255 elements and 31,380 DOFs.

Only two loading locations of the Vibroseis truck were designated for these two bridges. Because of the large tributary mass of the bridge deck compared with the truck mass, the truck mass was ignored in the FEM modeling. Santini provides a detailed account of the calculations used to produce the 3-D FEM models for the Old Reliance Road and the Woodville Road bridges.<sup>(134)</sup>

## Results of 3-D FEM Modeling

After each model was completed, a modal analysis was run in ANSYS, and subspace iteration was used. Only the first 60 modes were requested. The first 15 resonant frequencies for each model are shown in table 4, and Santini describes the mode shapes.<sup>(134)</sup>

Table 4. First 15 resonant frequencies in hertz for 3-D ANSYS FEM models.

Mode	Trinity River Bridge, Bent 12 (side loading)	Trinity River Bridge, Bent 12 (center loading)	Trinity River Bridge, Bent 2 (side loading)	Trinity River Bridge, Bent 2 (center loading)	Old Reliance Road Bridge	Woodville Road Bridge
1	11.066	11.660	10.546	11.033	2.0748	2.457
2	14.345	14.815	13.406	13.680	2.8910	3.470
3	14.810	15.066	13.678	14.072	3.3675	3.873
4	16.668	16.142	15.074	14.648	3.8730	4.353
5	18.746	18.822	16.287	16.287	4.2182	4.473
6	22.470	23.605	16.288	16.288	4.3035	5.018
7	23.584	23.811	16.288	16.288	4.6305	5.155
8	26.767	25.593	17.276	17.327	4.7763	5.656
9	27.298	26.771	20.357	21.284	5.9227	5.956
10	32.542	31.557	25.286	23.598	6.6892	6.703
11	33.001	33.558	26.044	25.292	6.7339	6.985
12	35.266	35.233	28.083	25.572	8.5283	7.136
13	37.056	39.391	28.092	28.083	8.9415	9.257
14	39.352	39.580	28.116	28.092	10.335	9.752
15	40.260	40.086	30.809	30.999	11.078	10.265

### *Trinity River Bridge Bent 12*

Because the mass of the Vibroseis truck is part of the FEM model, the location of the truck affects the model; therefore, table 4 reports resonant frequencies from both side and center loading—the Vibroseis truck in different locations for each. These resonant frequencies range from 11 Hz to 40 Hz. Generally, the resonant frequencies excited by the center loading closely track those excited by the side loading. According to Santini, the mode shapes of the first 4 modes and 8 of the remaining 11 reported modes show motion only in the plane of the bent.<sup>(134)</sup> This behavior suggests that a 2-D FEM model would capture the significant behavior of the bent as measured in the field. Judging from the plotted mode shapes, the primary motion at the bridge foundations is vertical, which is the expected response with vertical excitation. Certain modes reveal horizontal motion, such as the eighth mode at 26.7 Hz for the side loading of bent 12. However, these modes are not revealed in the field data.

### ***Trinity River Bridge Bent 2***

For both side and center loading, the first 15 resonant frequencies ranged from 10.5 Hz to 30.8 Hz; therefore, one effect of the strip footing appears to be a lowering of the higher resonant frequencies. As with bent 12, the first four modes from both side and center loading show motion only in the plane of the bent; however, fewer of the remaining 11 reported modes show motion only in the plane of the bent, indicating that the strip footing appears to induce more out-of-plane motion. This behavior suggests that a 2-D FEM model may not capture the significant behavior of the bent in this frequency range. For the first four modes, the predominant motion at the bridge foundation is vertical.

### ***Old Reliance Road Bridge***

Table 4 shows that the first 15 resonant frequencies ranged from 2.1 Hz to 11.1 Hz. Unlike the Trinity River Bridge, where mostly vertical motion occurred for the lower modes, the lower modes of the Old Reliance Road Bridge show considerable lateral movement both in and out of the plane of the bent. For example, the first and second modes are sideways in the plane of the bent, and the third and fourth modes combine this sideways movement with rocking in the direction of the roadway. This behavior difference may result from several factors—increased vertical stiffness of the bridge foundation used in the FEM model, exclusion of the truck mass, longer spans with different lengths leading to higher lateral frequencies, or a combination of these factors. Also, the height-to-width ratio for this bridge is greater than that for the Trinity River Bridge, making this bridge more prone to the observed motion.

### ***Woodville Road Bridge***

Table 4 shows the first 15 resonant frequencies ranging between 2.5 Hz and 10.3 Hz, which is similar to that of the Old Reliance Road Bridge. Although this bridge has no skew, the observed modes show the motion both in and out of the plane of the bent. As with the Old Reliance Road, the predominant motion in the lower modes is horizontal. In fact, vertical motion begins to appear only in the eleventh and twelfth modes. The eleventh mode of this bridge is equivalent in motion to the first mode, and the twelfth mode is equivalent to the third mode under the center loading for bents 2 and 12 of the Trinity River Bridge.

## **2-D ANSYS MODELS**

2-D FEM models serve as the baselines for the parameter estimation software. The parameter estimations were conducted only on bents 2 and 12 of the Trinity River Bridge. These estimations were conducted because of either the slightly poorer quality field data or the inability of the parameter estimation software to deal with variability in field data, or both.

In 2-D FEM models, the cap beam and columns of the bent, modeled with beam elements, were rigidly connected to each other. Because the bridge deck is not included in the 2-D FEM model, its mass and stiffness effects must be lumped onto the cap beam so that the resulting dynamic behavior of the bent is equivalent to what would be

observed with the 3-D FEM model. However, the stiffness of the bridge deck does not appear to be significant in the lower modes of interest; thus, it is ignored here. Note that the absence of the third dimension causes certain modes representing out-of-plane motion in the 3-D FEM model not to appear in the 2-D FEM model.

For each 2-D FEM model, the bridge foundation stiffness and mass were also represented by soil-substructure super-elements  $K_{SSS}$  and  $M_{SSS}$ , each of which is a 3-by-3 matrix, described in the equations in figures 89 and 90.

$$K_{SSS} = \begin{bmatrix} K_{xx} & 0 & K_{\phi x} \\ 0 & K_{yy} & 0 \\ K_{x\phi} & 0 & K_{\phi\phi} \end{bmatrix}$$

Figure 89. Equation.  $K_{SSS}$  (3-by-3 matrix).

$$M_{SSS} = \begin{bmatrix} M_{xx} & 0 & 0 \\ 0 & M_{yy} & 0 \\ 0 & 0 & M_{\phi\phi} \end{bmatrix}$$

Figure 90. Equation.  $M_{SSS}$  (3-by-3 matrix).

The Rayleigh-Ritz method is used to determine the tributary deck mass to be lumped onto the cap beam. This energy-based method allows practitioners to select locations of the lumped masses and determine the equivalent masses that produce the same resonant frequencies as the structure with the distributed mass. In this project, the 3-D FEM models represent the structures with the distributed mass, and the 2-D FEM models have the equivalent lumped masses. Assuming that the tributary deck mass is  $M$ , the factor of alpha for each 2-D mode is determined so that when alpha  $M$  is placed on the cap beam, the resonant frequency of each 2-D mode equals that of the corresponding 3-D mode. The calculation of alpha is detailed in the following paragraphs.

### Rayleigh-Ritz Method

The Rayleigh-Ritz method is an energy-based method to estimate the resonant frequency of a structure given the approximate mode shape. The maximum kinetic energy ( $KE_{max}$ ) and the maximum potential or strain energy ( $SE_{max}$ ) of a structure are calculated using the known mode shape or the estimated mode shape from the known static-deformed shape. For a structure with distributed mass and stiffness,  $KE_{max}$  and  $SE_{max}$  can be formulated as

shown in the equations in figures 91 and 92, respectively, where  $\Phi_n$  is the mode shape associated with the resonant frequency of  $\omega_n$ , and  $m(x)$  and  $EI(x)$  are the distributed mass and stiffness properties, respectively.

$$KE_{max} = 1/2 \omega_n^2 \int_0^l m(x) \{\Phi_n\}^2$$

Figure 91. Equation.  $KE_{max}$  (distributed properties).

$$SE_{max} = 1/2 \int_0^l EI(x) \{\Phi_n\}^2$$

Figure 92. Equation.  $SE_{max}$  (distributed properties).

For a structure with lumped mass and distributed stiffness,  $KE_{max}$  and  $SE_{max}$  can be modified as in the equations in figures 93 and 94, respectively, where  $M$  is the number of lumped mass and  $\Phi_i$  is the displacement at the location of the lumped mass at  $i$ , or ( $M_i$ ). It should be mentioned that the equation in figure 92 is the same as the equation in figure 94, because both structures are assumed to have the same distributed stiffness properties,  $EI(x)$ , and the same mode shapes,  $\Phi_n$ .

$$KE_{max} = 1/2 \omega_n^2 \sum_{i=1}^m M_i \{\Phi_i\}^2$$

Figure 93. Equation.  $KE_{max}$  (lumped properties).

$$SE_{max} = 1/2 \int_0^l EI(x) \{\Phi_n\}^2$$

Figure 94. Equation.  $SE_{max}$  (lumped properties).

It is apparent that the effective amount of the lumped mass,  $M$ , can be found by equating the equations in figures 91 and 93, assuming that each lumped mass,  $M_i$ , has the same effective amount,  $M$ . Because the maximum kinetic energy,  $KE_{max}$ , and the maximum strain energy,  $SE_{max}$ , of a structure should be equal, the resonant frequency of  $\Phi_n$  can be estimated by setting the equation in figure 91 equal to the equation in figure 92 or the equation in figure 93 equal to the equation in figure 94. The applications of the Rayleigh-Ritz method to both a simply supported and a cantilever beam demonstrated that the effective amount of the lumped mass depends on the structure type, the location of the lumped mass, and the specified mode shape.

## Description of 2-D FEM Modeling

The 2-D FEM models for bents 2 and 12 of the Trinity River Bridge were created in both ANSYS and PARIS<sup>©</sup>, a static and dynamic PARAmeter Identification System program for a linear-elastic structure.<sup>1</sup> The 2-D FEM models were created using the same cross section and material properties as in the 3-D ANSYS models except for the material densities of the beam elements. Taking into consideration the tributary mass of the bridge deck, the densities of the beam elements in the 2-D FEM models were multiplied by the alpha factors for each mode.

The initial 2-D FEM models using ANSYS were created assuming the tributary mass of the bridge deck from midspan to midspan. The resulting mode shapes and resonant frequencies from the initial 2-D FEM models were compared with those from the 3-D ANSYS models. Based on the Rayleigh-Ritz method, the resonant frequencies should be the same if the mode shapes from the two FEM ANSYS models are identical. Consequently, the alpha factors can be obtained easily by matching the resonant frequencies for the identical mode shapes from the 2-D and 3-D ANSYS models, as shown in the equation in figure 95.

$$\alpha_n = \left\{ \frac{\omega_{n(2D)}}{\omega_{n(3D)}} \right\}^2$$

Figure 95. Equation.  $\alpha_n$ .

It can be proven that the alpha factors obtained from the ratio of the resonant frequencies in the equation in figure 95 are the same as those from the procedure described earlier. After the alpha factors are determined for each mode, the 2-D FEM models using both ANSYS and PARIS are created with adjusted mass densities of the beam elements.

## Results of 2-D FEM Modeling

The 2-D FEM models had 80 elements and 213 DOFs for bent 2, and 63 elements and 167 DOFs for bent 12. The elements and DOFs for bent 2 were higher because of the additional strip footing of bent 2. Each mode in each 2-D FEM model had a separate and unique alpha factor. Santini discusses the selected alpha factors and resonant frequencies based on the suitable field data.<sup>(134)</sup>

---

<sup>1</sup> PARIS, Parameters Identification Systems, is a copyrighted software developed by Professor Masoud Sanayei, Ph.D. and Tufts University, Department of Civil and Environmental Engineering, Medford, MA.

## PARAMETER ESTIMATION WITH PARIS PROGRAM

Parameter estimations were conducted using the PARIS system and software. Parameter estimation in this project is a procedure for determining unknown bridge foundation stiffness from selected frequency measurements and incomplete mode shapes. It represents an inverse problem, similar to those solved in geophysics for evaluating unknown geology and in pavements for backcalculating pavement layer moduli. Typical structural analysis is a forward-calculated problem, where the structure is considered known and the displacements, natural frequencies, and mode shapes are calculated for given loading conditions. Although the structure may be linear—that is, display linear elastic behavior and react with only small displacements—for the forward model, the inverse model of the same structure is algebraically nonlinear. Likewise, the results may be unique for the forward model, but the results may not be unique in solving the inverse problem. Following is a list of the basic steps of parameter estimation used in this project:

1. Identify the unknown structural parameters.
2. Develop a structural FEM model.
3. Assume the initial values for the unknown structural parameters.
4. Calculate natural frequencies and mode shapes using steps 2 and 3 or 7.
5. Develop an error function based on the calculated and measured data.
6. Minimize the error function for the unknown structural parameters.
7. Update the values for the unknown structural parameters.
8. Repeat steps 4 to 7 until convergence.

The solution for the updated values of the unknown structural parameters involves a set of linear equations defined by a sensitivity matrix. The condition of the sensitivity matrix determines the ability to solve for the unknown structural parameters. If the sensitivity matrix is singular or ill-conditioned, then a solution may not be found. At this point, the alternative for a given set of field measurements is to reduce the number of unknown structural parameters, which may lead to a solvable set of equations, but it involves assuming properties for certain structural parameters that are unknown. A second alternative is to anticipate the behavior of the sensitivity matrix before field measurements are made, which allows for the selection of field measurements that will lead to a better-conditioned set of equations.

As an inverse problem, small errors in the field measurements may be magnified in the solution process to produce much larger errors in the calculated unknown structural parameters; therefore, the influence of this measurement error must be evaluated and understood. Parameter estimation using a structural model before field data collection can be used to select the set of field measurements that are most error tolerant. Artificial errors may be added to the error-free simulated measurements from the structural FEM model, then PARIS is run with the contaminated simulated measurements to calculate the unknown structural parameters. By comparing the calculated values of the unknown structural parameters with those used in the structural FEM model, the sensitivities of the unknown structural parameters to different sets of simulated measurements are evaluated to determine the most error-tolerant sets of field measurements.

An underlying assumption in this project for parameter estimation is that structural parameters not identified as “unknown” actually are known. This is a grey area; some structural parameters may be better known than others, but they could differ significantly from actual values. For example, the foundation stiffness coefficients might be considered unknown and the column section properties known; however, the actual column section properties could be 25 to 50 percent different from the assumed values. The influence of this modeling error can be unacceptably magnified in the parameter estimation process. The influence of modeling error can be evaluated by simulation in a manner similar to the approach used for measurement error. If the influence of modeling error of a particular component is considered unacceptable, then that component may also be considered unknown. If it is found that the influence of modeling error is acceptably small, then the parameters estimation is successful.

### Error Functions in PARIS

PARIS has both stiffness-based and flexibility-based modal error functions to detect deviations in each parameter from the original FEM model. This is done by using a selected number of resonant frequencies and associated mode shapes measured sparsely at certain DOFs. After this has been checked, the structural stiffness and mass parameters of the FEM model are updated at the element level to match the measured resonant frequencies and mode shapes. The stiffness-based modal error function was developed by Sanayei and Santini,<sup>(135)</sup> the flexibility-based modal error function was developed and programmed by Sanayei and Arya.<sup>(136)</sup>

Figure 96 is the equation for motion of an undamped free vibration. The equation can be partitioned, as shown in the equation in figure 97, for mode shapes at measured and unmeasured DOFs for each measured resonant frequency.

$$[K]\{\Phi\}_i = \omega_i^2 [M]\{\Phi\}_i$$

Figure 96. Equation. Matrix K times vector  $\Phi$ .

$$\begin{bmatrix} K_{aa} & K_{ab} \\ K_{ba} & K_{bb} \end{bmatrix} \begin{Bmatrix} \Phi_a \\ \Phi_b \end{Bmatrix}_i = \omega_i^2 \begin{bmatrix} M_{aa} & M_{ab} \\ M_{ba} & M_{bb} \end{bmatrix} \begin{Bmatrix} \Phi_a \\ \Phi_b \end{Bmatrix}_i$$

Figure 97. Equation. Matrix K times vector  $\Phi$  (partitioned).

$[K]$  and  $[M]$  are the stiffness and mass matrices of the structure.  $\Phi_i$  and  $\omega_i$  represent the mode shape at  $i$  and corresponding resonant frequency. The subscripts  $a$  and  $b$  denote the measured and unmeasured DOFs, respectively. By condensing out the unmeasured mode shapes  $\Phi_b$ , the stiffness-based residual modal error function  $\{e_s(p)\}_i$  can be expressed as the equation in figure 98, where  $(p)$  is the vector of the unknown parameters. The stiffness-based modal error function  $\{E_s(p)\}$  can be derived by vertically appending the

residual modal error function  $\{e_s(p)\}_i$ . The resulting  $\{E_s(p)\}$  is a  $1 \times a$  vector, where  $a$  is the number of the measured mode shapes.

$$\{e_s(p)\}_i = \left( \left( [K_{aa}] - \omega_i^2 [M_{aa}] \right) - \left( [K_{ab}] - \omega_i^2 [M_{ab}] \right) \right. \\ \left. \left( [K_{bb}] - \omega_i^2 [M_{bb}] \right)^{-1} \left( [K_{ba}] - \omega_i^2 [M_{ba}] \right) \right) \{\Phi_a\}_i$$

Figure 98. Equation. Stiffness-based residual modal error function.

The equation in figure 99 is the flexibility-based residual modal error function  $\{e_f(p)\}$  expressed in a form similar to the stiffness-based residual modal error function of the equation in figure 98.

$$\{e_f(p)\}_i = \left( \omega_i^2 \left( [F_{aa}] [M_{aa}] + [F_{ab}] [M_{ba}] \right) \right. \\ \left. + \omega_i^4 \left( [F_{aa}] [M_{ab}] + [F_{ab}] [M_{bb}] \right) \right. \\ \left. \left( [I] - \omega_i^2 \left( [F_{ba}] [M_{ab}] + [F_{bb}] [M_{bb}] \right) \right)^{-1} \right. \\ \left. \left( [F_{ba}] [M_{aa}] + [F_{bb}] [M_{ba}] \right) - [I] \right) \{\Phi_a\}_i$$

Figure 99. Equation. Flexibility-based residual modal error function.

The flexibility-based error function  $\{E_f(p)\}$  also can be derived by vertically appending the residual modal error function  $\{e_f(p)\}_i$ .

Both stiffness-based and flexibility-based residual error functions contain inverses of the stiffness matrices; therefore, they are algebraically nonlinear with respect to the unknown parameter vector ( $p$ ).

### Minimization of Modal Error Functions in PARIS

After it is established, the stiffness-based or flexibility-based error function  $\{E(p)\}$ , or both, can be approximated linearly, using Taylor Series expansion as shown in the equation in figure 100.

$$\{E(p + \Delta p)\} \cong \{E(p)\} + [S(p)]\{\Delta p\}$$

Figure 100. Equation. Error function approximation.

The sensitivity matrix  $[S(p)]$  is the partial derivative of  $\{E(p)\}$  with respect to each of the unknown parameters. Furthermore, in the equation in figure 101, an objective function  $J$  is defined as the Euclidean norm of the modal error functions  $\{E(p)\}$ .

$$J(p + \Delta p) = \{E(p + \Delta p)\}^t \{E(p + \Delta p)\}$$

Figure 101. Equation. Objective function  $J$ .

By minimizing the objective function  $J$  with respect to each unknown parameter, the change in each unknown parameter is determined by the Gauss-Newton formulation, as shown in the equation in figure 102.

$$\{\Delta p\} = -\left([S(p)]^T [S(p)]\right)^{-1} [S(p)]^T \{E(p)\}$$

Figure 102. Equation. Change in parameter vector.

The updated values of the unknown parameters are calculated in the equation in figure 103, and they are used as the initial values for the next iteration until convergence is achieved.

$$\{p\}_{k+1} = \{p\}_k + \{\Delta p\}_k$$

Figure 103. Equation. Parameter iteration.

## PARAMETER ESTIMATION USING SIMULATED FIELD DATA

Before using the real field data in PARIS, parameter studies using the computer-simulated field data were carried out for Trinity River Bridge bent 12 to evaluate the capacity of PARIS for bridge foundation stiffness estimation and the effects of measurement and modeling errors. There were four stages of parameter studies with simulated data:

1. Feasibility of bridge foundation stiffness estimations.
2. Feasibility of bridge foundation stiffness estimations adding beam and column properties as unknown parameters.
3. Effect of measurement errors.
4. Effect of modeling errors.

Based on the real field data from the final site visit, the first four modes at 11 receiver locations were extracted from the 2-D FEM PARIS model for bent 12. The first mode from the computer simulations was considered a pseudo-mode because the lateral stiffness of the bridge deck was not included in the 2-D FEM model; thus only the second, third, and fourth modes were used in the parameter studies. Also, only the stiffness-based modal error function was used in stages 1 and 2, while both stiffness-based and flexibility-based modal error functions were used in stages 3 and 4.

### Feasibility Study for Bridge Foundation Stiffness Estimation (Stage 1)

Table 5 summarizes the results of the parameter studies in stage 1.  $K_{SSS}$  represents a fully populated bridge foundation stiffness matrix with six unknowns.  $K^{**}$  represents the one with four nonzero unknowns,  $K_{xx}$ ,  $K_{yy}$ ,  $K_{\phi\phi}$ , and  $K_{y\phi}$ , and  $K^{***}$  represents the one with three nonzero diagonal unknowns,  $K_{xx}$ ,  $K_{yy}$ , and  $K_{\phi\phi}$ . “NA” in the column, “Number of Iterations,” means insufficient rank given the number of unknown parameters.

Table 5. Feasibility study for bridge foundation stiffness estimations.

Loading Location	Measured Modes	Modal DOF	Total DOF	Unknown Parameters	Number of Unknown Parameters	Rank	Number of Iterations
Side	2,3,4	22	66	$4 \times (K_{SSS})$	24	24	4
Side	2,4	22	44	$4 \times (K_{SSS})$	24	20	NA
Side	2,4	22	44	$4 \times (K^{**})$	16	16	4
Side	2	22	22	$4 \times (K^{**})$	16	12	NA
Side	2	22	22	$4 \times (K^{***})$	12	12	4
Side	2	22	22	$4 \times (K_{yy})$	4	4	3
Center	2,3,4	22	66	$4 \times (K_{SSS})$	24	24	5
Center	2,4	22	44	$4 \times (K_{SSS})$	24	20	NA
Center	2,4	22	44	$4 \times (K^{**})$	16	16	4
Center	2	22	22	$4 \times (K^{**})$	16	12	NA
Center	2	22	22	$4 \times (K^{***})$	12	12	4
Center	2	22	22	$4 \times (K_{yy})$	4	4	3

The following conclusions can be drawn based purely on the ability to solve the equations, without regard to error in either the measurements or the modeling, or both:

- A minimum of three modes is required to calculate all six unknown parameters of bridge foundation stiffness.
- If only two modes are available, then two modes of the off-diagonal bridge foundation stiffness cannot be calculated.
- If only one mode is available, then only the diagonal bridge foundation stiffness can be evaluated.
- No significant differences exist between the side and center loading.

### **Feasibility Study for Bridge Foundation Stiffness Estimation with Unknown Beam and Column Parameters (Stage 2)**

The moments of inertia of the concrete beam and columns were identified as additional unknown parameters in stage 2 because of their uncertainties and significant effects in PARIS. Only the successful cases in table 5 were run with PARIS in stage 2. The parameter studies showed that an error of 10 percent in the moments of inertia of the concrete beam and columns would produce errors of up to 60 percent in the resulting bridge foundation stiffness. In addition, the uncertainties in the moments of inertia may result in either singular sensitivity matrices or dispersed cases; therefore, two additional unknown parameters were added in the PARIS runs to represent the moments of inertia of the beam cap ( $I_b$ ) and columns ( $I_c$ ), assuming all columns have the same moments of inertia. Table 6 summarizes the results of the parameter studies in stage 2, and it shows that all of the successful cases in table 5 also converged with unknown  $I_b$  and  $I_c$  in table 6.

Table 6. Bridge foundation stiffness estimations with unknown concrete beam and column moments of inertia.

Loading Location	Measured Modes	Modal DOF	Total DOF	Unknown Parameters	Number of Unknown Parameters	Rank	Number of Iterations
Side	2,3,4	22	66	$4 \times (K_{sss}), I_b, I_c$	26	26	6
Side	2,4	22	44	$4 \times (K^{**}), I_b, I_c$	18	18	6
Side	2	22	22	$4 \times (K^{***}), I_b, I_c$	14	14	4
Side	2	22	22	$4 \times (K_{yy}), I_b, I_c$	6	6	4
Center	2,3,4	22	66	$4 \times (K_{sss}), I_b, I_c$	26	26	6
Center	2,4	22	44	$4 \times (K^{**}), I_b, I_c$	18	18	6
Center	2	22	22	$4 \times (K^{***}), I_b, I_c$	14	14	5
Center	2	22	22	$4 \times (K_{yy}), I_b, I_c$	6	6	4

### Effect of Measurement Errors (Stage 3)

Effects of measurement errors on the PARIS runs have been studied by contaminating the computer-simulated resonant frequencies and corresponding mode shapes. PARIS has an option to assume the artificial errors to be uniform or normal distribution errors, using its user-defined internal functions. The artificial errors can be either proportional to the maximum values of the measurements or absolute values regardless of the magnitudes of the measurements. In this project, the corrupted computer-simulated field measurements with absolute uniform distributed errors were generated as shown in the equations in figures 104 and 105 to evaluate the error sensitivity of both stiffness-based and flexibility-based modal error functions.

$$\{\omega_m\} = \{\omega_c\} + [e_\omega] \{R_\omega\}$$

Figure 104. Equation. Resonant frequency with artificial errors.

$$[\Phi_m] = [\Phi_c] + [e_\Phi] [R_\Phi]$$

Figure 105. Equation. Mode shape with artificial errors.

The terms  $\{\omega_c\}$  and  $[\Phi_c]$  are, respectively, a pure computer-simulated resonant frequency vector and mode shape matrix from a 2-D PARIS model.  $[R_\omega]$  and  $[R_\phi]$  are fully populated with uniform distributed random numbers between  $-1$  and  $+1$ . The measurement errors with the prescribed level,  $[e_\omega]$  and  $[e_\phi]$ , are multiplied by, respectively, the random numbers in  $[R_\omega]$  and  $[R_\phi]$ , and then added to the pure computer-simulated field measurements  $\{\omega_c\}$  and  $[\Phi_c]$ .

Because the random numbers in  $[R_\omega]$  and  $[R_\phi]$  are used, a Monte Carlo analysis is conducted to produce meaningful results. Although 100 to 1,000 observations normally are considered in a Monte Carlo analysis to gain a comprehensive understanding of the statistical properties of the output variables, only 10 observations are used for each of the prescribed measurement-error levels because of the relative small size and minimum complexity of 2-D PARIS models in this project.

Assuming that the percentage error for the  $j$ th unknown parameter estimated in the  $i$ th observation is  $PE_j^i$ , the grand mean percentage error ( $GPE$ ) and the grand standard deviation percentage error ( $GSD$ )<sup>(89)</sup> can be defined as in the equations in figures 106 and 107.

$$GPE = \frac{1}{NUP \times NOBS} \sum_{i=1}^{NOBS} \sum_{j=1}^{NUP} PE_j^i$$

Figure 106. Equation. Grand mean percentage error.

$$GSD = \sqrt{\frac{1}{NUP \times NOBS} \sum_{i=1}^{NOBS} \sum_{j=1}^{NUP} (PE_j^i - GPE)^2}$$

Figure 107. Equation. Grand standard deviation percentage error.

$NUP$  is the number of unknown parameters, and  $NOBS$  is the number of observations.  $P_j^i$  can be calculated as the deviation of the estimated value  $P_j^i$  from the true value  $P_j^t$ , as in the equation in figure 108.

$$PE_j^i = \frac{P_j^i - P_j^t}{P_j^t} \times 100$$

Figure 108. Equation. Percentage error.

*GPE* and *GSD* can be used to compare the overall behaviors of the 2-D PARIS models to different levels of the input errors for all unknown parameters estimated in PARIS with several Monte Carlo experiments. When *GSD* is relatively small and *GPE* approaches zero for a prescribed measurement error level, the sensitivity of the 2-D PARIS models to the prescribed measurement error level can be determined. *GPE* will decrease as *NOBS* increases. In addition, the maximum value of  $PE_j^i$  in each unknown parameter for any observation,  $MAX PE_j$ , and the maximum value of  $PE_j^i$  in any unknown parameter for any observation,  $MAX PE_j^i$ , are examined to provide the vital insight into the unknown parameters that are overly sensitive to the measurement errors

Only one-mode cases in table 6 were considered in stage 3 because of the real field-data issues, which appeared to provide adequate data for one mode only. The objective of stage 3 was to ascertain which case was most measurement-error tolerant. Tables 7 and 8 summarize the results for the measurement-error analysis, showing that in general, very small measurement errors produced very large errors in the unknown parameters estimated in PARIS. For example, the most measurement-error-tolerant case was for center loading with Case Type II. For a 0.01 percent measurement error, the errors in the estimated  $K_{yy}$  ranged from 1.4 percent to 1.9 percent, and 4.2 percent and 4.8 percent for  $I_b$  and  $I_c$ , respectively. This represents an error magnification of 140 to 190 times for the bridge foundation stiffness estimations. Case Type I in tables 7 and 8 is the case with the unknown parameters of  $4 \times (K^{***})$ ,  $I_b$ , and  $I_c$ , while Case Type II is the case with the unknown parameters of  $4 \times (K_{yy})$ ,  $I_b$ , and  $I_c$ .

Table 7. Effects of measurement errors (stiffness-based modal error function) using one-mode simulated field data.

Case Type	Error (%)	GPE	GSD	MAX PE <sub>j</sub> <sup>i</sup>	MAX PE <sub>j</sub>													
					I <sub>b</sub>	I <sub>c</sub>	K <sup>1</sup> <sub>xx</sub>	K <sup>1</sup> <sub>yy</sub>	K <sup>1</sup> <sub>φφ</sub>	K <sup>2</sup> <sub>xx</sub>	K <sup>2</sup> <sub>yy</sub>	K <sup>2</sup> <sub>φφ</sub>	K <sup>3</sup> <sub>xx</sub>	K <sup>3</sup> <sub>yy</sub>	K <sup>3</sup> <sub>φφ</sub>	K <sup>4</sup> <sub>xx</sub>	K <sup>4</sup> <sub>yy</sub>	K <sup>4</sup> <sub>φφ</sub>
Side																		
I	0.001	-7.5	485.0	6653.0	1.6	8.3	4.8	1.0	5.8	3.3	2.3	14.0	3.1	4.4	12.0	4.7	6E3	9.8
I	0.01	-50.0	869.0	1.2E4	18.0	252.0	51.0	17.0	554.0	41.0	23.0	162.0	38.0	44.0	264.0	31.0	1E4	315.0
II	0.001	-0.9	3.9	59.0	1.8	4.9	NA	1.7	NA	NA	2.3	NA	NA	4.9	NA	NA	59.0	NA
II	0.01	-16.0	43.0	567.0	20.0	107.0	NA	17.0	NA	NA	23.0	NA	NA	48.0	NA	NA	567	NA
II	0.1	NA	NA	NA	NA	NA	NA	NA	NA	NA	NA	NA	NA	NA	NA	NA	NA	NA
Center																		
I	0.001	-0.6	6.6	39.0	10.0	1.7	8.0	3.1	36.0	6.6	2.1	23.0	7.4	1.8	18.0	5.1	3.5	39.0
I	0.01	8.3	51.0	208.0	17.0	127.0	30.0	23.0	208.0	56.0	20.0	197.0	28.0	21.0	129.0	31.0	31.0	179.0
II	0.001	-0.6	2.9	7.8	1.8	7.8	NA	3.1	NA	NA	1.1	NA	NA	2.1	NA	NA	3.4	NA
II	0.01	-9.7	29.0	83.0	18.0	83.0	NA	31.0	NA	NA	20.0	NA	NA	21.0	NA	NA	34.0	NA
II	0.1	NA	NA	NA	NA	NA	NA	NA	NA	NA	NA	NA	NA	NA	NA	NA	NA	NA

Table 8. Effects of measurement errors (flexibility-based modal error function) using one-mode simulated field data.

Case Type	Error (%)	GPE	GSD	MAX PE <sub>j</sub> <sup>i</sup>	MAX PE <sub>j</sub>													
					I <sub>b</sub>	I <sub>c</sub>	K <sup>1</sup> <sub>xx</sub>	K <sup>1</sup> <sub>yy</sub>	K <sup>1</sup> <sub>φφ</sub>	K <sup>2</sup> <sub>xx</sub>	K <sup>2</sup> <sub>yy</sub>	K <sup>2</sup> <sub>φφ</sub>	K <sup>3</sup> <sub>xx</sub>	K <sup>3</sup> <sub>yy</sub>	K <sup>3</sup> <sub>φφ</sub>	K <sup>4</sup> <sub>xx</sub>	K <sup>4</sup> <sub>yy</sub>	K <sup>4</sup> <sub>φφ</sub>
Side																		
I	0.001	4.1	61	919	3.3	0.6	1.2	0.1	4.8	0.8	0.3	5.0	1.6	0.6	6.3	1.7	919.0	9.2
I	0.01	12.0	151	2,151.0	4.5	11.0	7.9	0.4	56.0	7.6	2.8	48.0	7.6	4.9	27.0	5.9	2E3	43.0
II	0.001	0.02	0.2	1.9	0.4	0.2	NA	0.06	NA	NA	0.2	NA	NA	0.5	NA	NA	1.9	NA
II	0.01	0.2	2.5	19.0	4.1	1.6	NA	0.6	NA	NA	2.3	NA	NA	5.1	NA	NA	18.0	NA
II	0.1	-0.4	17	160.0	30.0	17.0	NA	4.4	NA	NA	17.0	NA	NA	35	NA	NA	160.0	NA
Center																		
I	0.001	NA	NA	NA	NA	NA	NA	NA	NA	NA	NA	NA	NA	NA	NA	NA	NA	NA
I	0.01	NA	NA	NA	NA	NA	NA	NA	NA	NA	NA	NA	NA	NA	NA	NA	NA	NA
II	0.001	-0.2	0.2	0.5	0.4	0.5	NA	0.2	NA	NA	0.2	NA	NA	0.1	NA	NA	0.2	NA
II	0.01	-1.6	2.7	4.8	4.2	4.8	NA	1.6	NA	NA	1.9	NA	NA	1.4	NA	NA	1.5	NA
II	0.1	-16.0	29	100.0	30.0	99.0	NA	16.0	NA	NA	15.0	NA	NA	11.0	NA	NA	14.0	NA

Review of  $MAX PE_j$  reveals that the rotational stiffness,  $K_{\phi\phi}$ , is the most measurement-error-sensitive parameter because only vertical and horizontal, not rotational, mode shapes are measured in this project. Therefore,  $K_{\phi\phi}$  is eliminated from the list of unknown parameters. In addition, the horizontal stiffness,  $K_{xx}$ , and one of the vertical stiffnesses,  $K_{yy}^A$ , for the side-loading cases are considered as known parameters because of their high measurement-error sensitivities. The resulting most-measurement-error-tolerance cases are 4  $K_{yy}$  plus  $I_b$  and  $I_c$  for the center-loading cases, and 3  $K_{yy}$  plus  $I_b$  and  $I_c$  for the side-loading cases.

#### **Effect of Modeling Errors (Stage 4)**

The measurement error analysis suggests that only vertical bridge foundation stiffness,  $K_{yy}$ , can be estimated using one-mode field data from vertical excitations used in this project. This means that the values of the other unknown bridge foundation stiffness variables must be assumed. Uncertainty of the assumed values causes modeling errors, and its effects on PARIS have been studied by manually changing the assumed values up to  $\pm 10$  to 30 percent for each of the assumed parameters and their combinations. Only the two most measurement-error tolerance cases in stage 3 were used in the modeling-error analysis. Table 9 summarizes the results of the modeling-error analysis for the center-loading cases only, since the results for the side-loading cases are similar to those for the center-loading cases. Note that the elements with the initial value of zero in the soil-substructure super-elements  $K_{sss}$  in the equation in figure 87, such as  $K_{y\phi}$ ,  $K_{xz}$ , and  $K_{xy}$  are also considered in the modeling-error analysis.

Table 9. Effects of modeling errors for the most measurement error tolerance case (center loading).

Modeling Error Combinations	Modal Error Function	MAX MPEj					
		$I_b$	$I_b$	$K^1_{yy}$	$K^2_{yy}$	$K^3_{yy}$	$K^4_{yy}$
-20% in ( $K_{xx}$ , $K_{\phi\phi}$ , $K_{x\phi}$ ) and +20% in ( $K_{y\phi}$ , $K_{xz}$ )	Stiffness-based	9.2	85.0	0.4	1.0	3.1	4.5
	Flexibility-based	11.0	296.0	35.0	25.0	33.0	56.0
-20% in ( $K_{xx}$ , $K_{\phi\phi}$ , $K_{y\phi}$ , $K_{xz}$ ) and +20% in ( $K_{x\phi}$ )	Stiffness-based	7.8	83.0	4.8	3.1	0.7	0.05
	Flexibility-based	21.0	313.0	68.0	41.0	29.0	40.0
-20% in ( $K_{xy}$ ), -15% in ( $K_{xx}$ , $K_{y\phi}$ ), -10% in ( $K_{\phi\phi}$ ), and +30% in ( $K_{x\phi}$ )	Stiffness-based	7.5	80.0	4.8	3.1	0.7	1.3
	Flexibility-based	20.0	319.0	70.0	42.0	30.0	41.0
-20% in ( $K_{\phi\phi}$ , $K_{x\phi}$ , $K_{xz}$ ) and +20% in ( $K_{xx}$ , $K_{y\phi}$ )	Stiffness-based	8.1	68.0	3.5	2.5	0.8	0.2
	Flexibility-based	14.0	71.0	13.0	13.0	2.9	15.0
-20% in ( $K^1_{xx}$ , $K^1_{\phi\phi}$ , $K^1_{x\phi}$ , $K^2_{xx}$ , $K^2_{\phi\phi}$ , $K^2_{y\phi}$ , $K^2_{xz}$ , $K^3_{xy}$ , $K^4_{\phi\phi}$ , $K^4_{x\phi}$ , $K^4_{xz}$ ), -15% in ( $K^3_{xx}$ , $K^3_{y\phi}$ ), -10% in ( $K^3_{\phi\phi}$ ), +20% in ( $K^1_{y\phi}$ , $K^1_{xz}$ , $K^2_{x\phi}$ , $K^4_{xx}$ , $K^4_{y\phi}$ ), and +30% in ( $K^3_{x\phi}$ )	Stiffness-based	1.9	48.0	0.1	3.2	0.9	0.4
	Flexibility-based	59.0	267.0	58.0	52.0	23.0	39.0

Review of table 9 shows that  $MAX PE_j$  for all estimated  $K_{yy}$ , using the stiffness-based modal-error function, is less than 5 percent, which is small relative to the assumed modeling errors of up to 30 percent. Table 9 also shows that the flexibility-based modal error function is much more sensitive to the modeling errors than the stiffness-based modal error function. Therefore, because neither of them stands out as the optimum choice of both measurement errors and modeling errors, both stiffness-based and flexibility-based modal error functions were selected for analysis in the final PARIS runs with the real field data.

## **PARAMETER ESTIMATION USING REAL FIELD DATA**

Parameter estimations using the real field data were performed for the two most error-tolerant cases on bents 2 and 12 of the Trinity River Bridge. Before doing this, it was necessary to match the experimental mode shapes and natural frequencies with those from 2-D FEM models. An exact match of the measured and analytical mode shapes is not likely, and it typically was not achieved. The possibility that the measured field mode shapes would be a combination of more than one natural mode severely affects the usefulness of these measurements in PARIS. Also, the measured mode shapes are assumed to be the 2-D response of the bridge pier only to the loading cases (center loading or side loading), but this is not necessarily the case.

The measured horizontal accelerations either were unreadable or unreliable because only vertical loading could be used in this project; therefore, only one up-down mode with little lateral motion was selected for the final PARIS runs, and only the vertical bridge foundation stiffness of each bent could be estimated. For bent 2, the up-down mode at the frequency of 14.6 Hz was selected for the center-loading case only. For bent 12, the up-down modes at the frequencies of 20.44 Hz and 20.40 Hz were selected for the side-loading and center-loading cases, respectively. Each of the measured mode shapes is assumed to contain only one mode, not a combination of two or more modes. The experimental mode results also indicated that the bridge foundations were asymmetrical.

### **Variations of Mode Shapes Extracted from Real Field Data**

Variations of the mode shapes extracted from the real field data have been observed when using different bandwidths to process the same sets of the real field data. A bandwidth is defined as a frequency window in a transfer-function plot selected to extract a particular mode shape and its frequency. For a particular mode, different bandwidths produce the different mode shapes and frequencies with a maximum difference of up to 5 percent in terms of the resulting resonant frequency. All of the selected bandwidths were within the reasonable limits for a seasoned user of the PCMODAL curve-fitting software. The maximum difference of up to 5 percent certainly exceeds the most measurement-error tolerance of the analytical simulated field data study, which was usually less than 1 percent, as described in the following paragraphs on stage 3.

### **PARIS Runs Using Real Field Data for Bent 2**

PARIS runs using only one suitable mode extracted from the real field data on bent 2 were conducted for the center-loading cases. This up-down mode has a resonant frequency of 14.6 Hz. Although both stiffness-based and flexibility-based modal-error functions were used in the PARIS runs, only the stiffness-based modal-error function produced acceptable values for the

bridge foundation stiffness estimations for each of the four piles with a strip footing as shown in table 10. The initial values of the estimated vertical stiffness  $K_{yy}$  in PARIS runs are also presented in table 10, using analytical models of Novak et al.<sup>(137)</sup> and Poulos and Davis,<sup>(138)</sup> respectively. In fact, PARIS does not require accurate initial values for successful and meaningful parameter estimation. Even if the initial values are increased or decreased by 50 percent, the PARIS runs converged at exactly the same values, indicating the PARIS results were based on the global minimums instead of the local minimum of the stiffness-based modal error function.

Table 10. Initial and resulting  $K_{yy}$  in PARIS runs with real field data for bent 2.

	$K_{yy}^1$ $\times 10^6 \text{ kg/m}$ $(\times 10^6 \text{ lb/inch})$	$K_{yy}^2$ $\times 10^6 \text{ kg/m}$ $(\times 10^6 \text{ lb/inch})$	$K_{yy}^3$ $\times 10^6 \text{ kg/m}$ $(\times 10^6 \text{ lb/inch})$	$K_{yy}^4$ $\times 10^6 \text{ kg/m}$ $(\times 10^6 \text{ lb/inch})$
PARIS (center loading)	21.4 (1.2)	21.4 (1.2)	8.93 (0.5)	44.65 (2.5)
Novak model	89.3 (5.0)	89.3 (5.0)	89.3 (5.0)	89.3 (5.0)
Poulos and Davis model	10.7 (0.6)	10.7 (0.6)	10.7 (0.6)	10.7 (0.6)

Note: Reference Novak et al.<sup>(137)</sup> and Poulos and Davis.<sup>(138)</sup>

The resulting vertical  $K_{yy}$  were used in the 2-D ANSYS model for bent 2 to compare the resulting mode shapes and frequencies with the ones extracted from the real field data. As shown in table 11, the resonant frequencies from the 2-D ANSYS models (11.3 Hz and 14.7 Hz) do not match the resonant frequency from the real field data (20.0 Hz). This indicates that the resulting  $K_{yy}$  from the PARIS runs are not real, and the parameter estimation with PARIS using the real field data was unsuccessful for the center-loading cases of bent 2 (piles plus footing).

Table 11. Resonant frequencies from 2-D ANSYS models and real field data for the center-loading cases of bent 2 with an alpha of 1.056.

Mode Number	2-D ANSYS Model with the Theoretical $K_{yy}$	2-D ANSYS Model with the Resulting $K_{yy}$ from PARIS Runs	Real Field Data
1	3.94	3.98	NA
2	11.3	14.7	20.0
3	13.7	20.4	NA
4	25.9	29.2	NA

## PARIS Runs Using Real Field Data for Bent 12

For bent 12, PARIS runs using the real field data were carried out for both the center- and side-loading cases. The up-down vertical modes at the frequencies of 20.44 Hz and 20.40 Hz were extracted from the real field data for the side- and center-loading cases of bent 12, respectively. Like the case with bent 2, even though both stiffness- and flexibility-based modal error functions were run with PARIS, only the stiffness-based modal error function produced acceptable values for the bridge foundation stiffness estimations, as shown in table 12.

Table 12. Initial and resulting  $K_{yy}$  in PARIS runs with real field data for bent 12.

	$K^1_{yy}$ $\times 10^6 \text{ kg/m}$ ( $\times 10^6 \text{ lb/inch}$ )	$K^2_{yy}$ $\times 10^6 \text{ kg/m}$ ( $\times 10^6 \text{ lb/inch}$ )	$K^3_{yy}$ $\times 10^6 \text{ kg/m}$ ( $\times 10^6 \text{ lb/inch}$ )	$K^4_{yy}$ $\times 10^6 \text{ kg/m}$ ( $\times 10^6 \text{ lb/inch}$ )
PARIS (side loading)	35.7 (2.0)	32.1 (1.8)	25.0 (1.4)	K <sup>a</sup>
PARIS (center loading)	28.6 (1.6)	12.5 (0.7)	16.1 (0.9)	16.1 (0.9)
Novak model	89.3 (5.0)	89.3 (5.0)	89.3 (5.0)	89.3 (5.0)
Poulos and Davis model	10.7 (0.6)	10.7 (0.6)	10.7 (0.6)	10.7 (0.6)

Note: Reference Novak et al.<sup>(137)</sup> and Poulos and Davis.<sup>(138)</sup>

<sup>a</sup>  $K^4_{yy}$  must be assumed as known, denoted by “K,” to achieve reasonable convergence.

Just as for bent 2, the resulting  $K_{yy}$  were used in the 2-D ANSYS model for bent 12 to compare the mode shapes and frequencies with the ones extracted from the real field data. As shown in table 13, the resonant frequencies for the side-loading cases are relatively close for the visually matching mode shapes from the 2-D ANSYS models (14.5 Hz and 18.5 Hz) and the real field data (20.4 Hz); however, table 14 shows the resonant frequencies for the center-loading cases are not close for those from the 2-D ANSYS models (11.8 Hz and 13.8 Hz) and the real field data (20.0 Hz). The results in table 14 indicate that the  $K_{yy}$  vertical stiffness values for the four pile foundations from PARIS runs are not real for the center-loading of bent 12.

Table 13. Resonant frequencies from 2-D ANSYS models and real field data for the side-loading cases of bent 12 with an alpha of 1.035.

Mode Number	2-D ANSYS Model with the Theoretical $K_{yy}$	2-D ANSYS Model with the Resulting $K_{yy}$ from PARIS Runs	Real Field Data
1	3.94	4.03	NA
2	11.2	16.0	14.8
3	14.5	18.5	20.4
4	21.6	26.2	27.7

Table 14. Resonant frequencies from 2-D ANSYS models and real field data for the center-loading cases of bent 12 with an alpha of 1.055.

<b>Mode Number</b>	<b>2-D ANSYS Model with the Theoretical <math>K_{yy}</math></b>	<b>2-D ANSYS Model with the Resulting <math>K_{yy}</math> from PARIS Runs</b>	<b>Real Field Data</b>
1	3.92	4.01	15.0
2	11.8	13.8	20.0
3	14.5	18.5	27.4
4	19.2	23.3	NA



## CHAPTER 7. USING THE HILBERT-HUANG TRANSFORM FOR SUBSTRUCTURE DAMAGE EVALUATION

### BACKGROUND

Because of the failure of the structural parameter estimation approach to identify substructure damage, the completion of this research project was delayed to conduct a preliminary evaluation of the capabilities of a comparatively new technique, the HHT. The premise of this research is that identifying certain vibration patterns (or signature recognition) by data analysis of vibration records can reveal structural dynamic characteristics such as natural frequencies and modes. This approach in structural engineering already has broad-based applications such as structural model validation and updating, condition assessment and monitoring, and damage diagnosis and detection. Traditional modal analysis generally has been found lacking in identifying damage in structures until failure was imminent. This is caused by the redundancy present in most structures and the difficulty in identifying the change in response to lower frequencies and less damping of an individual member without directly exciting and monitoring the member. In other words, the shift from a linearly elastic response to a nonlinear, damaged response generally is not apparent in the modal vibration measurements and analyses until failure is just about to occur or has occurred.

The HHT technique has the potential to address this problem because it was researched and developed to use modal vibration measurement data to identify nonlinear, damaged response of members. In this research, the HHT technique was applied to bents 12 and 2 of structure 4 of the Trinity River Relief Bridge as an alternative to the signature recognition of modal vibration analyses used with Fourier-based or wavelet data processing. This chapter reports the results of a preliminary evaluation of the HHT method to identify substructure damage signature from vibration data. In particular, HHT analyses were performed on the intact, excavated, and damaged pile foundations of bents 12 and 2.

The interpretation of the HHT analysis for the vibration records is based on the following observations, assumptions, and theories of vibration and HHT:

- Structural vibration to a given excitation should reveal its proper frequency content, which includes driving frequencies, natural frequencies of the whole structure or local members, or both, and noise frequencies.
- When a member of the structure is damaged, its stiffness is reduced in comparison with its undamaged state; therefore, vibration recorded at the damaged member could show larger vibration amplitude at lower frequency than the vibration at the same member without damage.
- Even though the damage, or the stiffness reduction, to the local structural member is large with respect to the member, it still might be small in comparison with the whole structural stiffness. Consequently, vibration recorded on the other members might not be sensitive to such a localized damage. In other words, for damaged or undamaged structures, vibrations at

a member other than the to-be-damaged or damaged member will show almost the same vibration amplitude at almost the same natural frequencies.

- Because the HHT method can identify the instantaneous frequency of measured vibrations through the Hilbert spectrum, the frequency of vibration for a damaged member could be observably less than the frequency on other members. This leads to identifying the damaged structural member.

The HHT analyses of the testing data on bents 12 and 2 were found to support these assertions.

As a prelude to the use of the HHT technique, the following paragraphs review the current nondestructive techniques and give an overview of the limitations of current vibration-based signature-recognition techniques. Following that is a discussion of the limitations of the modal vibration analysis approach described in chapter 5. Further discussion describes the HHT method and its application to bents 12 and 2. This chapter concludes with the proposed approach for further research and application of the HHT to dynamic evaluation of bridge substructures.

## **CURRENT APPROACHES IN NONDESTRUCTIVE CONDITION ASSESSMENT**

Regular condition assessment inspections are essential for reliable performance of aging and deteriorating civil structures and infrastructure, as described by Mori and Ellingwood<sup>(139,140)</sup> and Olson and Wright.<sup>(141)</sup> Currently, bridge engineers and inspectors must visually examine each visible major member and certify its safety, particularly after natural hazards such as an earthquake. Such a visual inspection approach is limited to surface conditions; it is neither totally objective nor reliable because of the great uncertainty in identifying the existence, location, and degree of internal damage, as described by Doebling et al.<sup>(50,142,143)</sup> This costly and ineffective approach stimulated recent research and development in new technologies for the NDE of civil infrastructures, described by Chang<sup>(144)</sup> and Chase and Washer.<sup>(145)</sup> These new technologies are in the areas of infrared thermography, ground-penetrating radar, acoustic emission monitoring, and eddy current detection. While these technologies are feasible technically, they probably are used most efficiently when the locations of damage are first identified. For a complicated structure, locating the damage is difficult. Some members are physically unreachable or invisible, or both; a large number of sensors are required; and a large instrumentation system is costly, requires frequent recalibration, and involves extensive data analysis. The foundation elements of bridge substructures are not visible at all; consequently, visual inspection is not useful unless a failure also affects the visible bridge elements.

Using only stress-wave and vibration-based measurements is sometimes a simpler, less costly technique, as described by Olson and Wright,<sup>(141)</sup> Farrar et al.,<sup>(33,146)</sup> Farrar and Doebling,<sup>(147)</sup> Salawu and Williams,<sup>(42,148)</sup> Salawu,<sup>(149)</sup> Caicedo et al.,<sup>(150)</sup> and Chang.<sup>(151)</sup> These techniques, however, can lead to large, costly instrumentation systems. Moreover, without appropriate data analysis methods, they will not identify damage precisely, and access must be gained to each of the critical members, also costly and time consuming.

## CURRENT VIBRATION-BASED SIGNATURE-RECOGNITION TECHNIQUES

Identification of certain vibration patterns (or signature recognition) from vibration records can reveal structural dynamic characteristics such as natural frequencies and modes. This ability to identify vibration patterns is of paramount importance to broad-based applications in structural engineering such as structural model validation and updating, condition assessment and monitoring, and damage diagnosis and detection. With a few exceptions, two sets of large-array vibration data recorded at multiple points (pre- and post-damage) are usually required. Analysis and comparison of these two data sets can reveal different dynamic characteristics in the structure, and thus lead to the identification of damage location and severity. This kind of approach builds on the incorporation of the experimental data process with simplified structural modal models, described by Caicedo et al.,<sup>(150)</sup> Chang,<sup>(151)</sup> Aktan et al.,<sup>(152)</sup> Hou et al.,<sup>(153)</sup> Kim and Stubbs,<sup>(154)</sup> Park et al.,<sup>(155)</sup> Shi et al.,<sup>(156,157)</sup> Shah et al.,<sup>(158)</sup> Smyth et al.,<sup>(159)</sup> Vanik et al.,<sup>(160)</sup> Sohn et al.,<sup>(161)</sup> Vestroni and Capecchi,<sup>(162)</sup> and Yun et al.<sup>(163)</sup> The currently used signature-recognition methods can be improved upon in three respects, which are covered in the following subsections.

### Experimental Vibration Data Processing Analysis Approaches

Traditional data processing such as Fourier-based provides distorted or indirect information of nonstationary data of measured vibrations (such as from traffic) that are also nonlinear for a damaged structure. This can mask real effects of the damage and mislead those using the data for signature recognition.

For example, the Fourier spectral analysis approach used in this study is one of the most widely used methods for vibration data analysis. It is valid, however, only for processing linear, stationary data. The Fourier spectrum defines harmonic components globally. That is, it yields average characteristics over the entire time duration of the data; however, some characteristics of vibration data such as the dominant frequencies may change significantly over different portions of the duration. Also, because Fourier spectral analysis explains data in terms of a linear superposition of harmonic functions, it typically needs higher frequency harmonics to simulate nonlinear, nonstationary data. In short, Fourier spectral analysis distorts information from data by spreading the energy over a wide frequency range and losing the locality of energy distribution, that is, the location of the damaged members.

To improve the Fourier approach, windowed Fourier spectral analysis can be used. In this approach, Fourier spectral analysis is performed over restricted windows centered on specific features of interest in the data. The analysis provides information on frequency content locally in the data, thus reducing the problem of nonstationary data, although still not solving for the nonlinear issue. The window technique reduces frequency resolution as the length of the window shortens, thus requiring a tradeoff: the shorter the window, the better the locality of the Fourier spectrum, but the poorer the frequency resolution. In addition, selection of window length is primarily visual and subjective.

Wavelet analysis has been used in past decades to recover more accurate local information from nonstationary data. It has found applications in, for example, earthquake data processing,<sup>(164, 165,166)</sup> system identification,<sup>(153,167)</sup> and random field representation.<sup>(168,169)</sup> According to Daubechies, among many others, wavelet analysis can provide a sound tool in situations where better time resolution at high frequencies rather than at low frequencies is desirable.<sup>(170)</sup> On one hand, the wavelet analysis can characterize time-dependent high-frequency signals effectively from a vibration record. This feature is particularly useful to single out, from a time-vibration record, abnormal high-frequency signals that are likely related to one type of structural damage, such as cracks during a severe earthquake.<sup>(153)</sup>

On the other hand, wavelet analysis does not result in any essential improvements over conventional or windowed Fourier spectral analysis to characterize low-frequency signals from a record, because the largest scale in the wavelet transform (related to the frequency resolution) should be less than one-half of the length of the entire time series.<sup>(171)</sup> The difference in low-frequency signals of the vibration records in a damaged structure from those in the undamaged structure may indicate another type of structural damage such as continuous degradation of a structure from corrosion and other deterioration mechanisms. Wavelet transform is strongly conditional on the selected mother wavelet; consequently, the physical interpretation of each wavelet decomposition and spectrum is indirectly related to the underlying physical process that the data exposes through the different mother wavelets, explained in an example later.

### **Signature of Damaged Structural Members**

Modal analysis often is used with data processing of in situ vibration responses for structural identification or signature recognition. Such an approach is neither efficient nor sensitive when identifying the change of local dynamic properties of a structure from vibration records.

The modal analysis builds on multiple DOF modeling of the whole structure as discussed in chapter 6. The signature of local dynamic properties can be identified only through higher modes. Determining the shape of higher modes requires a large number of sensors, which makes data collection not only costly, but also complicated (for example, in issues on optimal locations of sensors). Typically, the number of response measurement locations is significantly less than the number of DOFs in a structural model, although this is not as much a problem in simpler substructures. This mismatch often makes it difficult to precisely identify the local dynamic properties. Even with the detailed data from large sensory systems, sensitivity is still low for identifying local dynamic properties from vibration records. The reasons are the ubiquitous noise problem and the intrinsic drawback of traditional data-analysis methods for nonlinear, nonstationary data processing.

From the perspective of damage detection, most existing signature-recognition techniques require a priori data. In other words, vibrations need to be measured from the same structure in its undamaged state. Both a priori (healthy) and damaged structure data are analyzed by using one of the traditional data processes. The two sets of data are then compared to determine the change in natural frequencies, amplitudes, and vibration modes to locate the damage and estimate its severity. Obtaining a priori data, however, is not economically practical for most existing structures.

Even if a priori data could be obtained for important structures such as large bridges, hospitals, and communication centers, the change in natural frequencies, amplitudes, and modes in a structure's different health or damage conditions often is inconsequential, making the identification ineffective. Moreover, because the modal models are inherently linear and time invariant, the structure to be identified must conform to those assumptions as well. Consequently, the modal-based techniques cannot efficiently reveal the nonlinear structural features caused by damage.

### ***In Situ Vibration Data***

For real structures, the practical amount of high-strain modal vibration testing with controlled excitation and associated damage is small. In situ vibration typically is limited to a low-strain response regime because of difficulties with controlled exciting at higher strain levels. It is difficult, if not impossible, to validate the accuracy, sensitivity, and effectiveness of signature-recognition techniques that are developed primarily on the basis of laboratory experiments and computer models.

For example, ambient vibration data often are used in signature recognition. Because ambient excitation is not measured, however, it is unknown if this excitation source provides input at the frequencies of interest or if the input is uniform over a particular frequency range. Similarly, seismic data often are used to identify the dynamic properties of damaged structures to locate the damage and estimate the severity. Because the degree of seismic-induced structural damage is primarily visual, and thus difficult to quantify precisely, pertinent assumptions must be made in the approach. These and other factors can increase significantly the uncertainties for the use of traditional signature-recognition techniques for broad-based applications in general and identified dynamic properties in particular. The problem is a lack of high-strain, even destructive, tests of a real structure with controlled excitation and damage. These destructive tests cannot be replaced with laboratory experiments and computer models because there are always inherent differences between the models and the as-built structure. These differences arise from simplifications of the boundary and support conditions, connectivity between various structural elements, unknown material properties and constitutive relationships (particularly those associated with soil and concrete), and energy-dissipation (damping) mechanisms.

## **LIMITATIONS OF MODAL VIBRATION APPROACH FOR BENT 12**

This discussion focuses on the limitations of traditional modal vibration analysis approaches for signature recognition in vibration records for bent 12 of the Trinity River Relief Bridge, which was the simplest bridge substructure tested. Both Fourier spectra and wavelet analysis techniques are applied.

### **Review of Field Test Conditions for Structure 4 of the Trinity River Relief Bridge**

This bridge had a 6.1-m (20-ft)-wide roadway consisting of 151 concrete panels directly supported by 66 concrete pile bents with a span of 5.49 m (18 ft). The nominal thickness of the concrete slab panels between the bents was 40.64 cm (16 inches). These concrete slabs were reinforced with number 7 steel bars at a spacing of 14.6 cm (5.75 inches) longitudinally and number 4 steel bars at a spacing of less than 0.61 m (2 ft) transversely. The concrete panels had

one fixed end and an expansion end, resulting in both fixed and roller-pin connections supported by each intermediate bridge bent. The asphalt topping had been removed to the concrete slab level at the time of field tests. Bent 2 and bent 12 were tested because they had the same superstructures with different foundation types of footing plus piles and piles only, respectively. This review is limited to the simplest substructure case, bent 12, which was supported by four concrete piles.

Figure 109 shows the structural configuration of bent 12 in its damaged pile state under an excitation from the Vibroseis in the middle of the deck. As shown in the figure, bent 12 comprised a concrete beam cap supported by four driven concrete piles. The beam cap was 7.17 by 0.61 by 0.61 m (23.5 by 2 by 2 ft) (length by width by height). The piles had a 0.356-by-0.356-m (14-by-14-inch)-square cross section. The beam cap was reinforced longitudinally with seven number 7 steel bars. There were number 4 steel stirrups at a spacing of 0.458 m (1.5 ft) transversely. The concrete beam spanned 1.93 m (6.33 ft) symmetrically between the piles. Each pile had four number 8 steel bars at four corners of its cross section with number 2 steel hoops at variable spacing from 50.8 to 152.4 cm (2 to 6 inches) along the pile. The pile length between the top of the concrete strip footing and the ground surface was 2.14 m (7 ft). Following is a list of the three tested structural states of bent 12:

- Intact: the column with accelerometer 15 (the right-most south pile) was not broken and soil around the pile had the same height as the soil around the pile with accelerometer 13 (second to the left-most pile, or the north-center pile).
- Excavated damage: the south pile with accelerometer 15 was not broken, but soil around the pile was fully excavated and the south, east, and west faces of the south-center pile also were excavated.
- Damaged (also called broken) pile: about 0.305 m (1 ft) of concrete of the south pile with accelerometer 15 was broken out with the vertical steel bars left in place, and soil around the south and south-center piles was as in the excavated damage state.

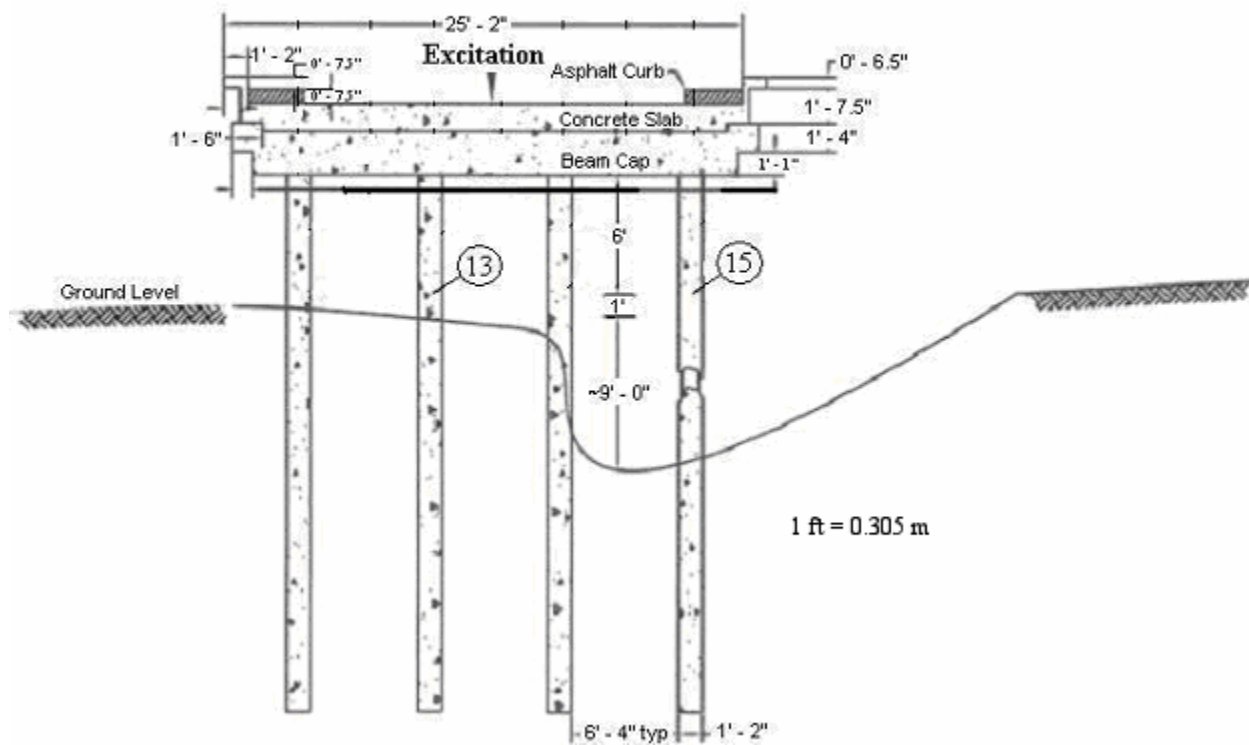


Figure 109. Diagram. Vibration tests of bent 12 of the Trinity River Relief Bridge.

### Fourier and Wavelet Analysis Limitations for Dynamic Properties of Bent 12

Both Fourier and wavelet analysis techniques were applied to bent 12. Following is a description of the results.

#### *Global Modal Properties from Fourier Analysis*

The most widely used method to identify global structural dynamic properties such as fundamental natural frequency and mode of a structure is Fourier spectral analysis of vibration data measured at limited locations. Figure 110 shows the time histories of vertical excitation (or forcing function) and its corresponding vertical (along-column) acceleration-vibration response at accelerometer 15 with bent 12 in its intact state. Both time histories are highly nonstationary, with the frequency increasing almost linearly from 5 Hz at 0.5 s to 75 Hz at 5.5 s. The Fourier spectra corresponding to the time-domain traces of figure 110 are shown in figure 111. The ratio of the Fourier spectrum of vibration in the middle graph of figure 111 to the Fourier spectrum of the forcing function in the top graph is the normalized Fourier spectrum, or the accelerance TF, of the bottom graph. The normalized Fourier spectrum shows the resonances clearly.

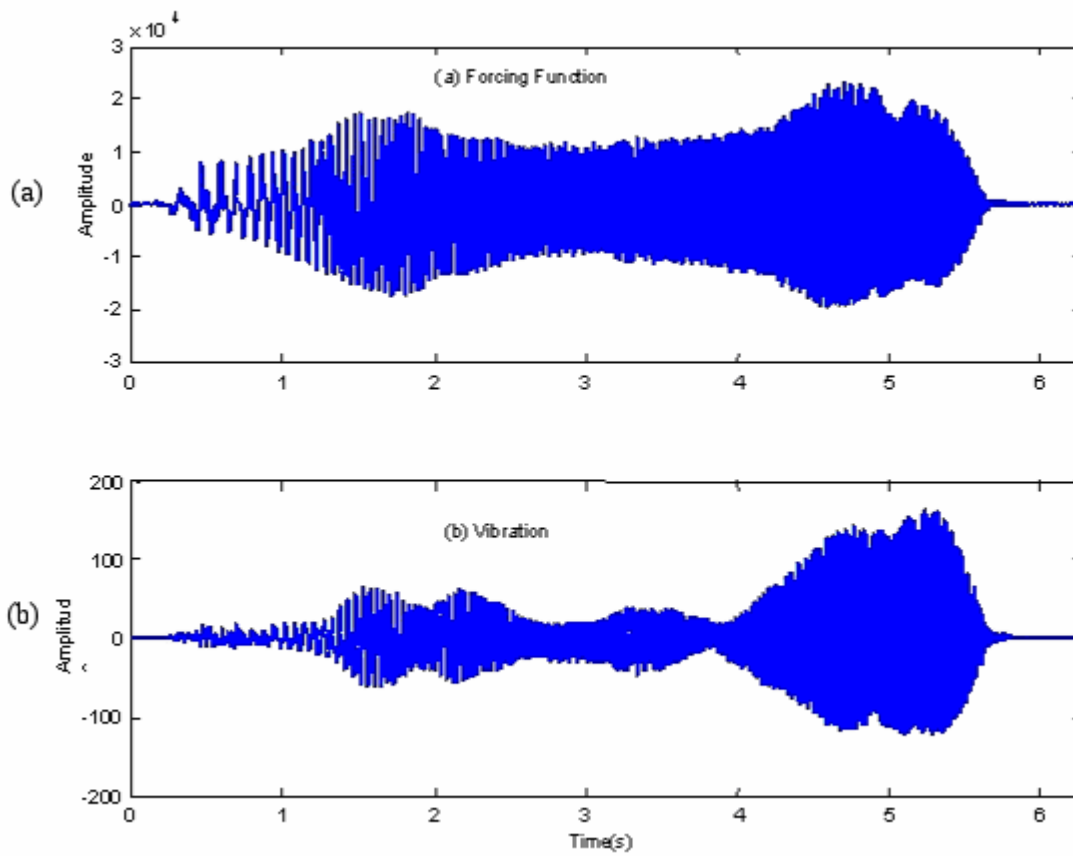


Figure 110. Graphs. (a) Vibroseis chirp forcing function in poundforce at center of bent 2.  
(b) Accelerometer 15 response in inches/seconds squared.

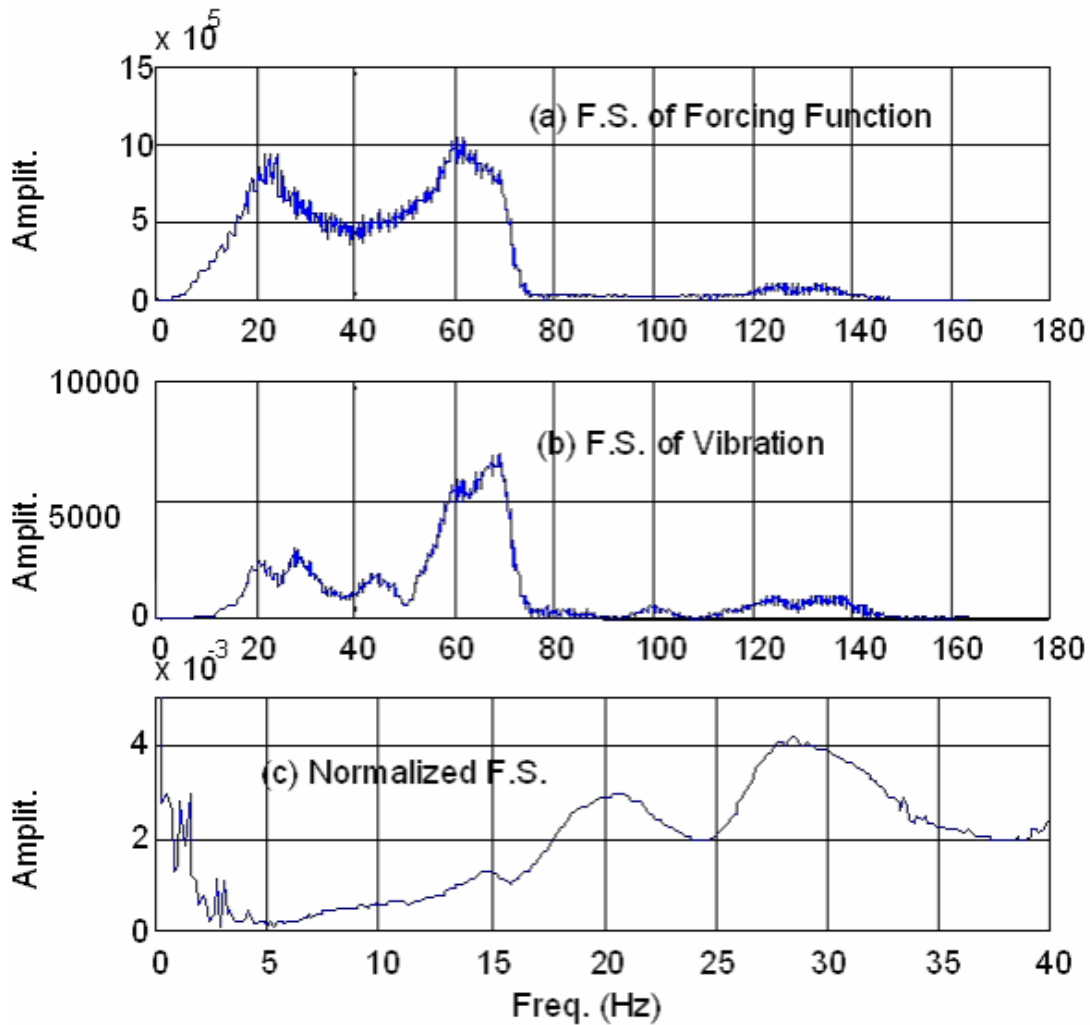


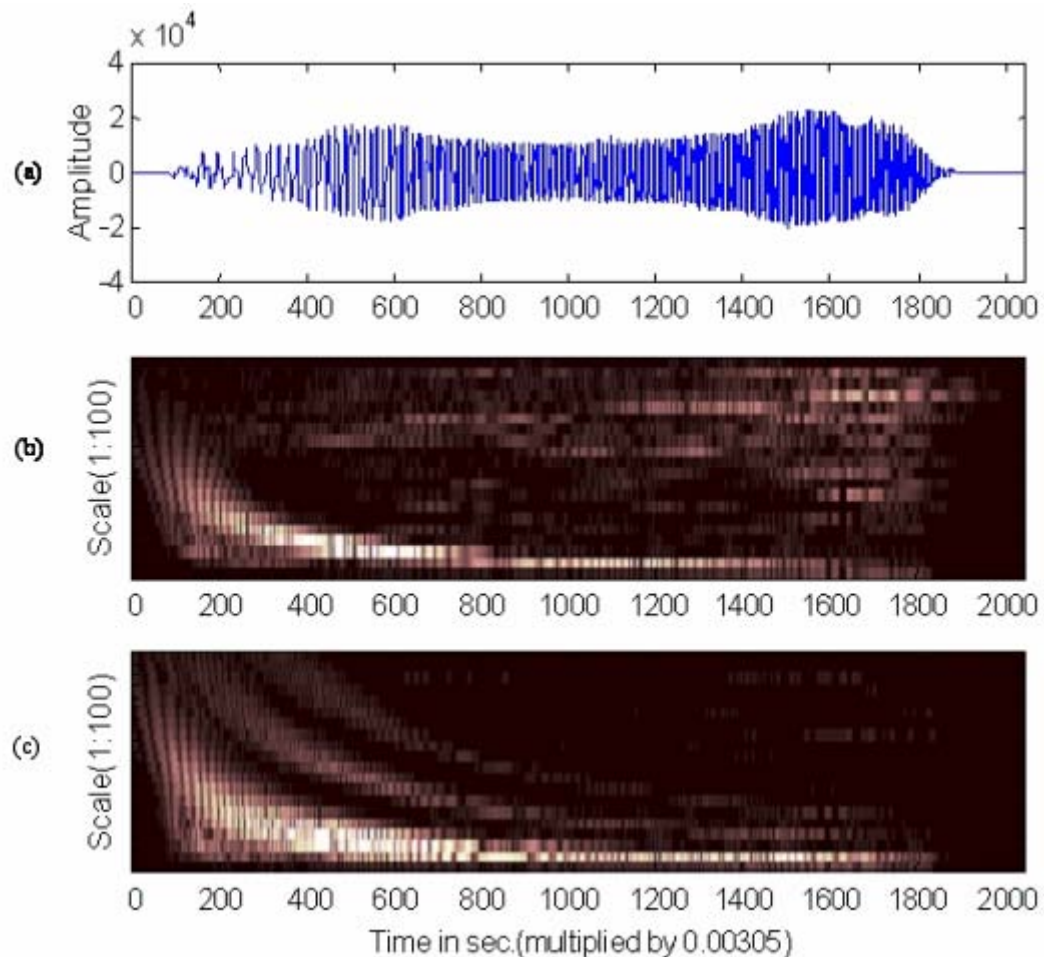
Figure 111. Graphs. Fourier spectra (F.S.) of figure 110 data.

For example, the fundamental natural frequency of the structure is obtained by identifying the first peak location in the Fourier spectrum of vibration acceleration normalized by the Fourier spectrum of forcing function (this is the acceleration TF discussed in chapter 5), which is 14.8 Hz, as shown in figure 111. Note that the identified fundamental natural frequency (14.8 Hz) is close to the driving frequency content of the excitation time history during 1 to 2 s in figure 110a. Because the vibration time history between 1 and 2 s in figure 110b should contain a mixed content of both the driving and natural frequencies, among others, such a phenomenon exists only locally in 1 to 2 s, not globally in 0 to 6 s in the vibration time history. Therefore, the natural frequencies identified from the global-based (or time-independent) Fourier spectra may not distinguish the mixed frequency content well. The fundamental problem with this approach is the inability of the TF to clearly resolve, from the overall structural response, nonlinear responses at resonance associated with an individual damaged member.

Windowed Fourier spectral analysis could find window-length-dependent frequencies; however, windowed Fourier spectral analysis would not help with the dilemma of time-frequency resolution, that is, getting accurate low-frequency information at the cost of sacrificing the local time information and vice versa, as discussed earlier. Primarily because of this, no windowed Fourier spectral analyses were done.

### ***Global Modal Properties from Wavelet Analysis***

Alternatively, wavelet analysis could be used to analyze the bent 12 data and thus recover time-dependent information from the data, especially through the temporal-frequency energy distribution of vibration or simply the wavelet spectrum. Figure 112 center and bottom, respectively, present the wavelet spectra of the forcing function in figure 110 (replotted in figure 112 top) created with the use of mother wavelets described by Morlet<sup>(172)</sup> and Daubechies.<sup>(170)</sup> The latter characterizes his procedure as the creation of Db5 wavelets. These results clearly indicate that each of the wavelet spectra depends on the selected mother wavelet. For example, there exists only one dominant scale-decreasing trend of high-energy (white color in figure 112 center) as time increases from 0 s to 1,000 s in the Morlet<sup>(172)</sup> wavelet spectrum. This implies that the forcing function has a dominant frequency increasing from that time period because the frequency is inversely proportional to the scale. In the same period, there are three such trends in the Db5 wavelet spectra in figure 112 bottom. A similar phenomenon is also observed at the time period between 1,400 s to 1,800 s. More important, Morlet and Db5 mother wavelets have their own frequency band in the conventional frequency sense, that is, Fourier-based.<sup>(172)</sup> Therefore, the scale factor in the wavelet spectrum will no longer be simply (or inversely) related to the conventional Fourier-based frequency. Converting the scale in wavelet spectrum to the conventional Fourier-based frequency content requires much detailed analysis, and it is inefficient. This dependency on the wavelet selection is problematic for this study.



Note: the lighter the color in graphs (b) and (c), the larger the energy in the wavelet spectra.

Figure 112. Graphs. Morlet (graph b) and Db5 (graph c) wavelet spectra of the forcing function (graph a).

### ***Local Properties***

In response to an excitation or driving force, vibration measured at any point on a structure should reveal certain frequency information such as driving frequency content, natural frequency content of the whole structure and its members, and noise frequency content. If one structural member has been damaged—for example, the south pile only out of the four piles of bent 12 (see figure 109)—the stiffness and thus the natural frequencies, proportionally to the degree of the damage of the member, are reduced in comparison to those without damage. The vibration recorded on the damaged member could show larger vibration amplitude at lower frequency than the vibration at the same member without damage, as reported in chapter 5. That is the signature of damaged structures in vibration records collected near the damaged element. Damage may reduce the stiffness of a single member in a large structure; however, damage might not affect

the stiffness of the whole structure significantly. Consequently, vibration measured on members other than the damaged one might not be sensitive to a small amount of localized damage in the damaged one; therefore, while the intact, excavated, and damaged pile states of bent 12 should produce three explicitly different signatures of local dynamic properties from vibration data taken at accelerometer location 15 on the damaged pile, corresponding data for the three states taken at accelerometer location 13 on an undamaged pile should produce three similar signatures.

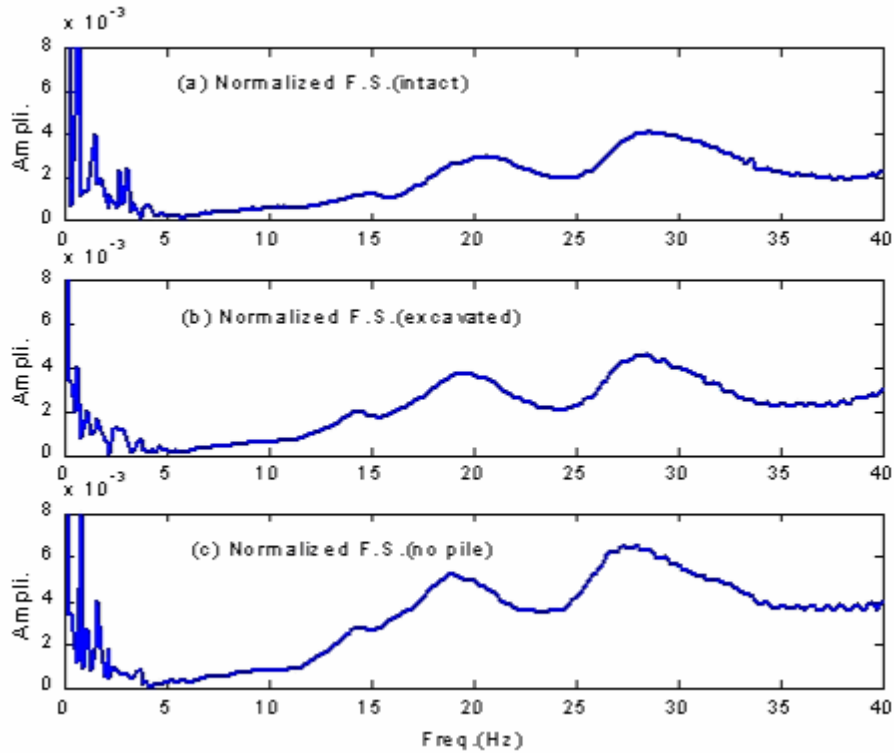


Figure 113. Graphs. Accelerance TFs for intact, excavated, and broken pile states.

Figure 113 shows the accelerance TFs at accelerometer 15 for the intact, excavated, and broken pile states. The fundamental natural frequencies measured at accelerometer 15 in the excavated- and broken-pile states are only 6 percent and 9 percent lower than the natural frequency in the intact state. This probably can be explained by considering the difference between localized and global effects. The fundamental natural frequencies measured are of a global nature. Because the damage of bent 12 was localized, the global properties, even though measured at the damaged pile, were not changed much. Considering the difficulty of isolating local and global effects, it may be difficult in practice to tell if the change in a TF response is caused by structural damage, measurement error, or other reason such as temperature change, until a comprehensive database is developed.

## HILBERT-HUANG TRANSFORM ANALYSES OF VIBRATION DATA FROM BENTS 12 AND 2

Recently, because of its uniqueness in faithfully representing nonlinear, nonstationary data, the HHT method has found many different and diverse applications, including use in blood-pressure variation, earthquake engineering, seismology, earthquake data analysis, building structural identification, building damage detection, and bridge system identification, among others. (See references 173, 174, 175, 176, 177, 178, 179, 180, 181, 182, 183, 184, and 185.) The following paragraphs discuss HHT fundamentals, followed by HHT analysis results for bents 12 and 2.

### Fundamentals of HHT Method

The HHT method consists of empirical mode decomposition (EMD) and Hilbert spectral analysis (HSA), which are summarized from Huang et al.<sup>(5,186)</sup>

#### *Empirical Mode Decomposition*

Contrary to almost all existing methods of vibration data frequency analysis, EMD is based on the simple assumption that any data set consists of different, simple, intrinsic modes of oscillation that need not be sinusoidal. The nonsinusoidal character of each mode of oscillation is derived from the data. At any given time, the data may have many different coexisting modes of oscillation. The superposition of all these modes is the original data record. Each of these oscillatory modes, called an intrinsic mode function (IMF), is defined by the following conditions:

- Over the entire data set, the number of extrema and the number of zero-crossings must be equal or differ at most by one.
- At any point, the mean value of the envelope defined by the local maxima and the envelope defined by the local minima is zero.

An IMF represents a simple oscillatory mode similar to a component in the Fourier-based simple harmonic function, but it is more general. Any data can be decomposed as follows: First, identify all the local extrema; next, connect all the local maxima by a cubic spline to produce the upper envelope; and repeat the procedure for the local minima to produce the lower envelope. In this sifting process, the upper and lower envelopes should encompass all the data between them. Their mean can then be found as a function of time. The difference between the data and the mean is the first IMF component, which contains the finest scale or the shortest period component of the signal. This sifting process might be repeated a couple of times in practice. The first IMF component then can be removed from the data to obtain the residue, which is treated as the new data and subjected to the same sifting process as described above. This procedure can be repeated to obtain all the IMF components. The sifting process can be terminated if either the last IMF component or the residue is less than a predetermined value of consequence, or if the residue becomes a monotonic function from which no more IMF can be extracted. If the data have a trend, the final residue should be that trend. Mathematically, the data  $X$  can be given by the equation in figure 114.

$$X(t) = \sum_{j=1}^{\mathcal{N}} c_j(t) + r_{\mathcal{N}}(t)$$

Figure 114. Equation.  $X(t)$ .

Where  $C_j$  is the  $j$ th component,  $r_n$  is the residue, and  $(t)$  is time.

### Hilbert Spectral Analysis

Data  $C(t)$  and its Hilbert transform  $Y(t)$  can be combined to form the analytical signal  $Z(t)$ , as in the equation in figure 115.

$$Z(t) = C(t) + iY(t) = a(t)e^{i\theta(t)}$$

Figure 115. Equation.  $Z(t)$ .

Where  $a(t) = \sqrt{C^2(t) + Y^2(t)}$  is the time-dependent amplitude and  $i\theta(t) = \arctan[Y(t)/C(t)]$  is the phase.

Applying the Hilbert transform to the  $n$  IMF components, the original data  $X(t)$  can be written in the form of the equation in figure 116.

$$X(t) = \Re \sum_{j=1}^n a_j(t) e^{i \int \omega_j(t) dt}$$

Figure 116. Equation.  $X(t)$  in Hilbert transform form.

Where  $\Re$  denotes the real part of the value to be calculated and  $\omega_j(t) = d\theta_j(t)/dt$  is the instantaneous frequency of the  $j$ th IMF component.

The residue  $r_n$  is not included in the equation in figure 116 because of its monotonic properties. The equation in figure 116 gives both amplitude and instantaneous frequency as functions of time. This equation is qualitatively different than the Fourier series representation in the equation in figure 117, which uses time-independent amplitude and phase.

$$X(t) = \Re \sum_{j=1}^n A_j e^{i\Omega_j t}$$

Figure 117. Equation.  $X(t)$  in Fourier series representation.

Where  $\Re$  denotes the real part of the value to be calculated and  $A_j$  is the Fourier transform of  $X(t)$ ;  $\Omega_j$  is time-independent frequency.

A comparison of the equations in figures 116 and 117 suggests that the HHT represents a generalized Fourier expansion. Note that the windowed Fourier representation cannot give an instantaneous frequency because the smallest window length is governed by the data-sampling rate and the uncertainty principle. The time-dependent amplitude and instantaneous frequency in the equation in figure 116 not only improve the flexibility of the expansion but also enable the expansion to accommodate nonstationary data. The frequency-time distribution of the amplitude  $a_j(t)$  is designated as the Hilbert amplitude spectrum  $H(w,t)$ , or simply Hilbert spectrum. Its square reveals the evolutionary energy distribution or energy density.

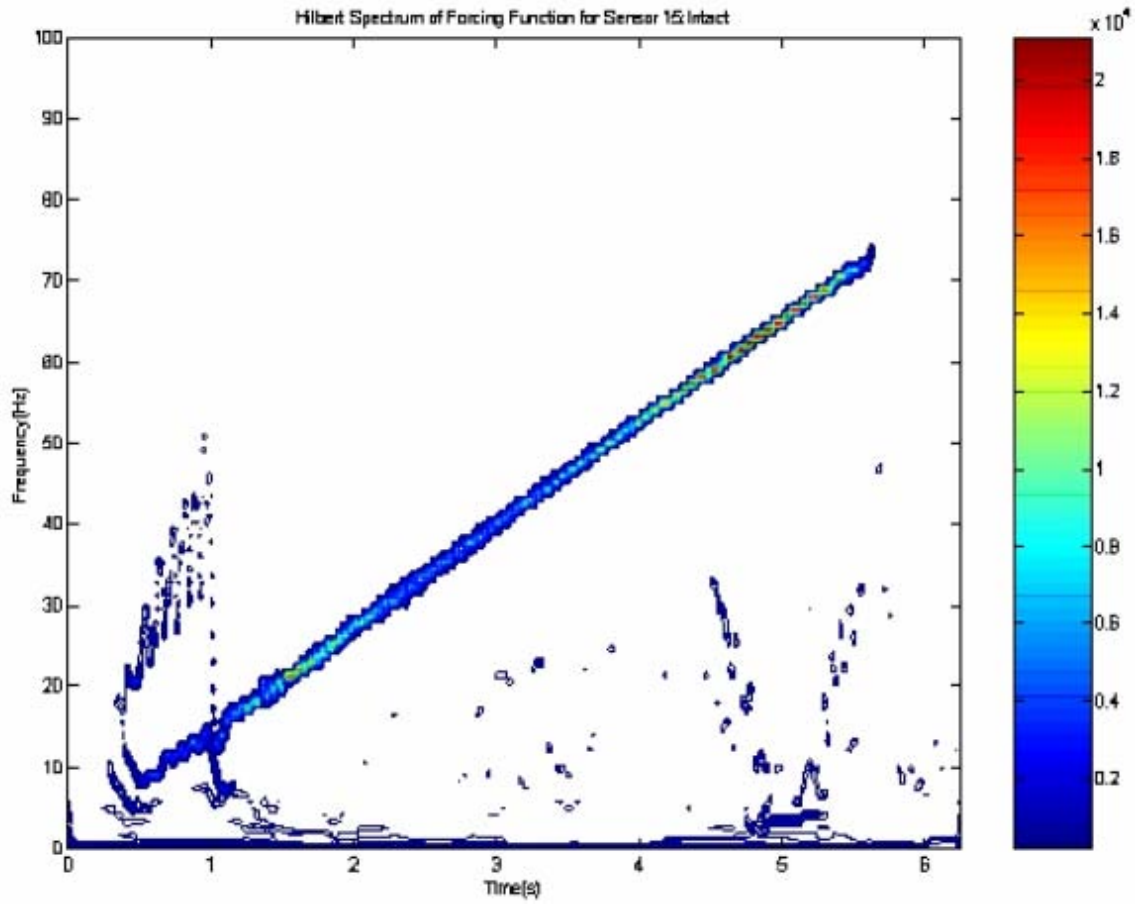
Any complicated data set can be decomposed through EMD into a finite and often small number of IMFs that admits a well-behaved Hilbert transform. The EMD is based on the local characteristic time scale of the data; thus, it is adaptive to nonstationary data processes. The HSA defines an instantaneous or time-dependent frequency of the data through the Hilbert transform on each IMF component. The two steps of data processing discussed above, EMD and HSA, which combined are HHT analysis, show a generalized version of Fourier expansion. These two unique properties also enable the HHT analysis to reveal, as an alternative to Fourier-based or wavelet components and spectra, a possible physical meaning of each EMD-based IMF component and HSA-based Hilbert spectrum. The details of the method can be seen in Huang et al.<sup>(5,186)</sup>

## HHT Analysis of Data from Bent 12

The HHT analysis was first applied to the data from bent 12 because this bent had the simplest substructure geometry. Figures 118 and 119 depict contour plots for the HHT spectrum of the excitation and vibration time histories shown in figures 110a and 110b. The plots show the temporal-frequency energy distribution of the excitation and vibration signals. The darker colors in the figures indicate greater energy at that frequency and time. Figure 118 shows that the chirp excitation from the Vibroseis, which was applied at the center loading point, has a dominant energy band the frequency of which increases with time—at 0.5 s, the energy band is at 5 Hz; at 5.5 s, the energy band is at 75 Hz. The dominant frequency content is referred to in this paper as

the dominant increasing driving frequency, or DIDF. The excitation also has energy at additional time-frequency combinations. Probably most notable, a grouping of frequencies ranging from approximately 20 Hz to 45 Hz is found between 0.5 and 1 s. This grouping can be inferred from the excitation time history shown in figure 110a.

According to vibration theory, the frequency content of the vibration response should contain primarily both the driving frequencies, such as shown in figure 118, and the natural frequencies of the structure. This assertion appears verified by figure 119, which shows the energy of the vibration response at accelerometer 15 for the intact bent. The main frequency content increases linearly with time, which corresponds to the behavior of the DIDF in figure 118. In addition to the energy that tracks the DIDF, figure 119 includes other energy concentrations, including a prominent grouping in the frequency range of 10 to 20 Hz between 1 and 2 s. These energy concentrations can be interpreted as the energy contributed from the structural vibration modes at various natural frequencies. Collectively, these natural frequencies constitute the signature of the structure. The prominent energy grouping in the frequency range of 10 to 20 Hz between 1 and 2 s was likely the result of the low frequencies of the driving force between 0.5 and 1 s. As time increased beyond 2 s, lower natural frequencies died down because of damping or energy levels too small in comparison with the strong DIDF energy to register in the analysis.



Note: the darker the color, the larger the energy in the spectra.

Figure 118. Graph. HHT spectrum of forcing function, bent 12, intact state.

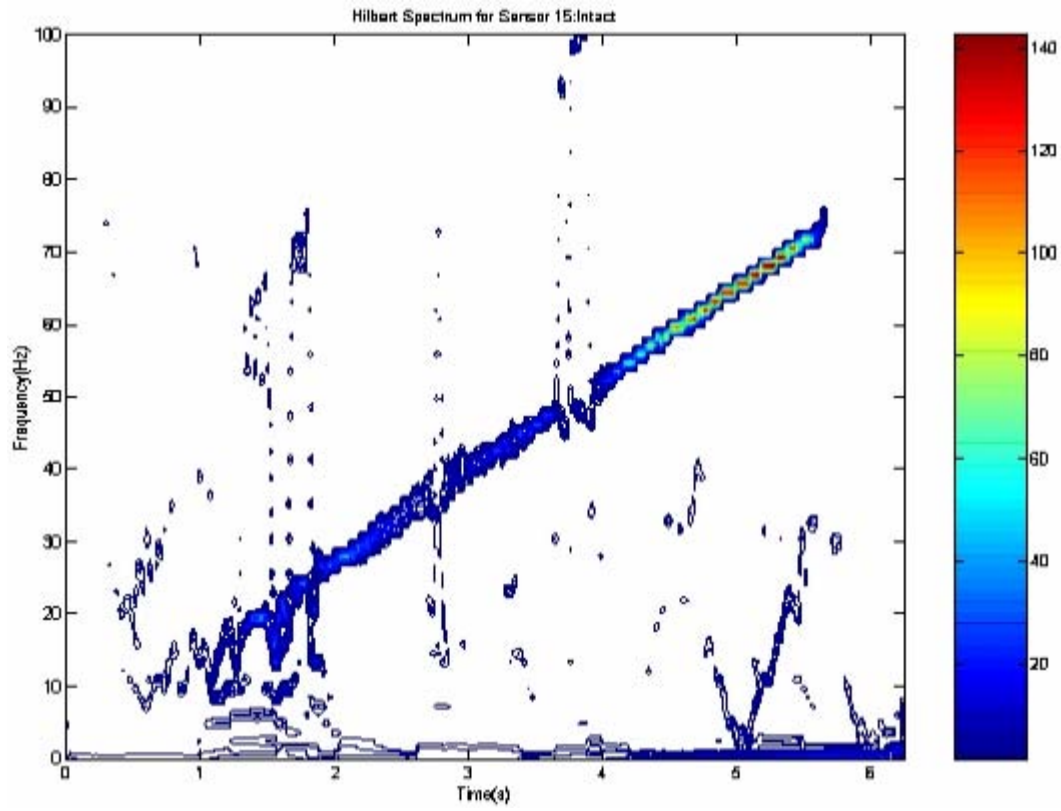


Figure 119. Graph. HHT spectrum of vibration, accelerometer 15, bent 12, intact state.

To further demonstrate this point, examine the IMF components extracted from the vibration response and their corresponding Fourier spectra, shown respectively in figures 120 and 121. As seen from these figures, the first two or three IMF components are dominant because their amplitudes are much larger than other IMF components. The first IMF component contains the vibration with a frequency content linearly increasing with time, which could be explained as the vibration component primarily inherited from the Vibroseis excitation at the DIDF. The temporal-frequency energy distribution (the HHT spectrum) of the first IMF component in figure 122 further supports this clarification. The second and third IMF components contain relatively low frequency content, implying that they likely are the results of a couple of low-frequency vibration modes. Their Fourier-based dominant frequencies (around 16 and 10 Hz) shown in figure 121 also partially support such a hypothesis. It appears that the fundamental natural frequency can be found from the HHT spectrum of the second or third IMF component, particularly around the time between 1 and 2 s. Figure 123 shows the HHT spectrum of the second IMF component, and it reveals that the lowest frequency of high energy in the time between 1 and 2 s is around 10 Hz.

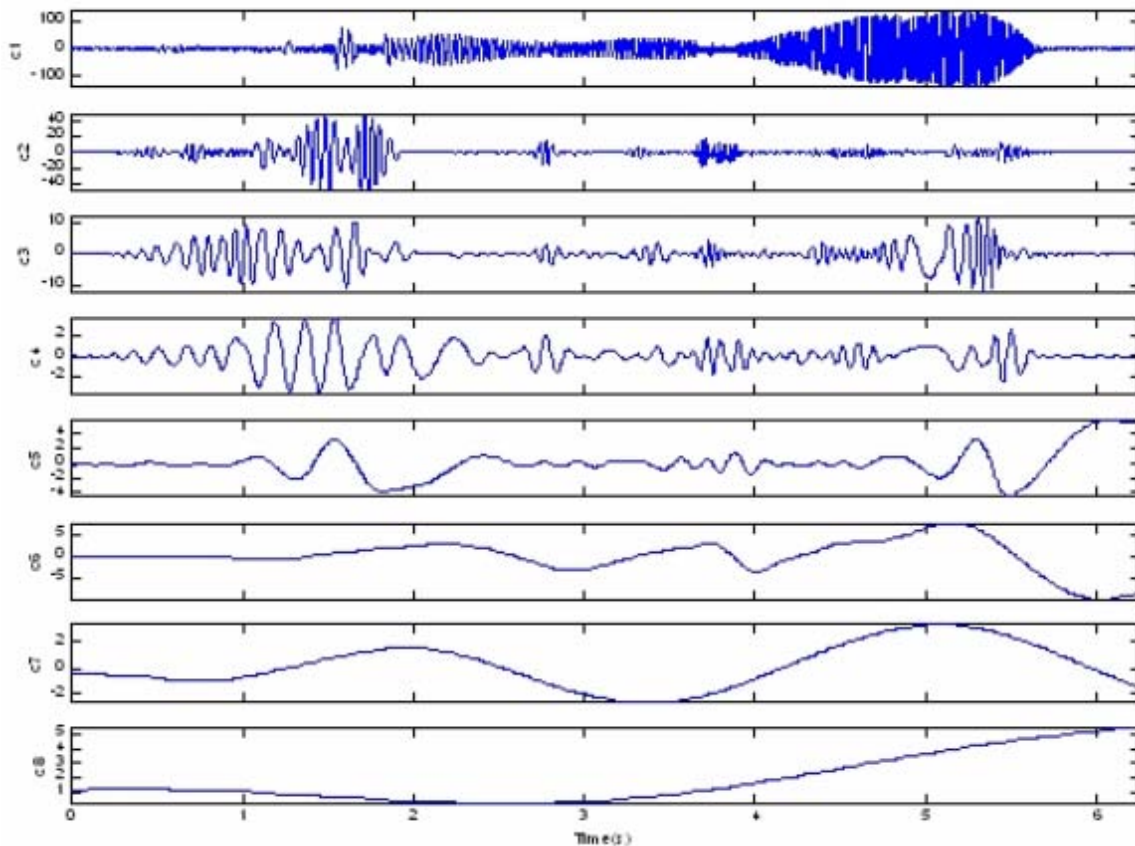


Figure 120. Graphs. EMD with the eight IMF components of vibration, accelerometer 15, bent 12, intact state.

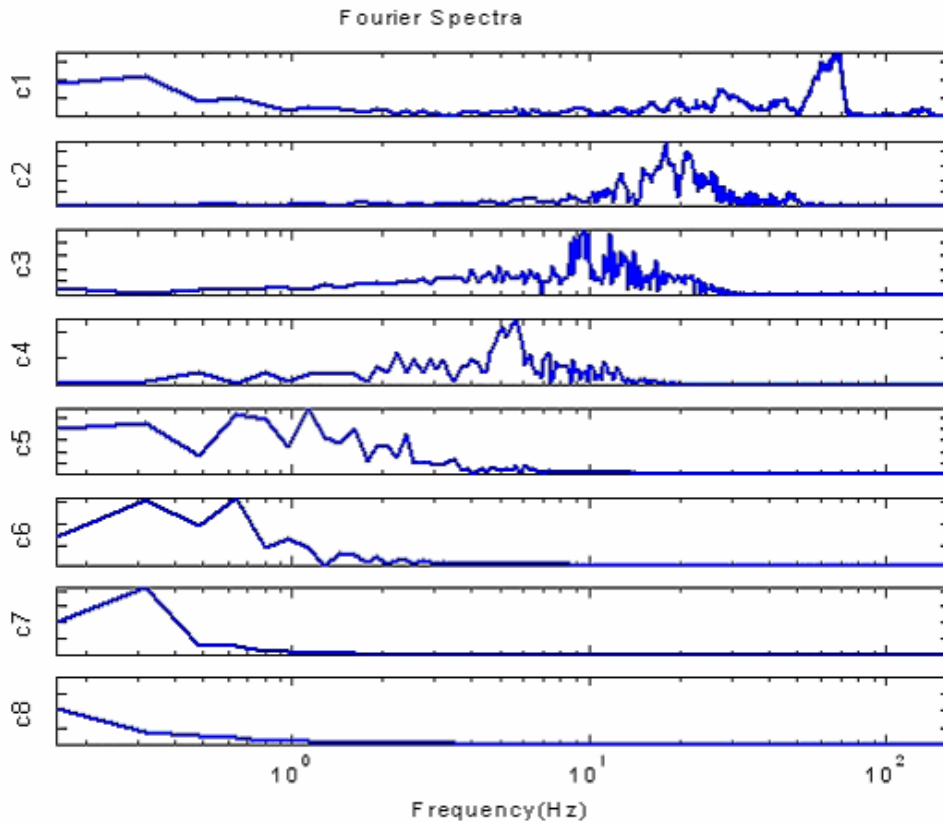


Figure 121. Graphs. Fourier spectra of IMF components in figure 120.

HHT theory and software have the issue of mode mixture in IMF components. This is observed in the first and second IMF components in figures 123 and 124, in which part of the motion in the second IMF component should belong to the first component and vice versa. This issue can be partially, if not completely (because of its complex nature), solved by using the intermittency criterion or check in the HHT software. With the proper use of the intermittency check, all the modes can be separated with more IMF components generated. Such a sifting process with intermittency check will not significantly affect the whole temporal-frequency HHT spectrum. As a matter of fact, great progress recently has been made in refining the HHT in theoretical maturity and numerical accuracy in general and in unique decomposition of the data into IMF components in particular.<sup>(187)</sup> These refinements can overcome some drawbacks exposed in the early version of HHT software. Because identifying frequency content from HHT spectrum is of sole interest for the problem at hand, the intermittency check was not used at this stage of the study. The sifting process with intermittency check, however, is a possibility for examining in greater detail each IMF component.<sup>(182)</sup>

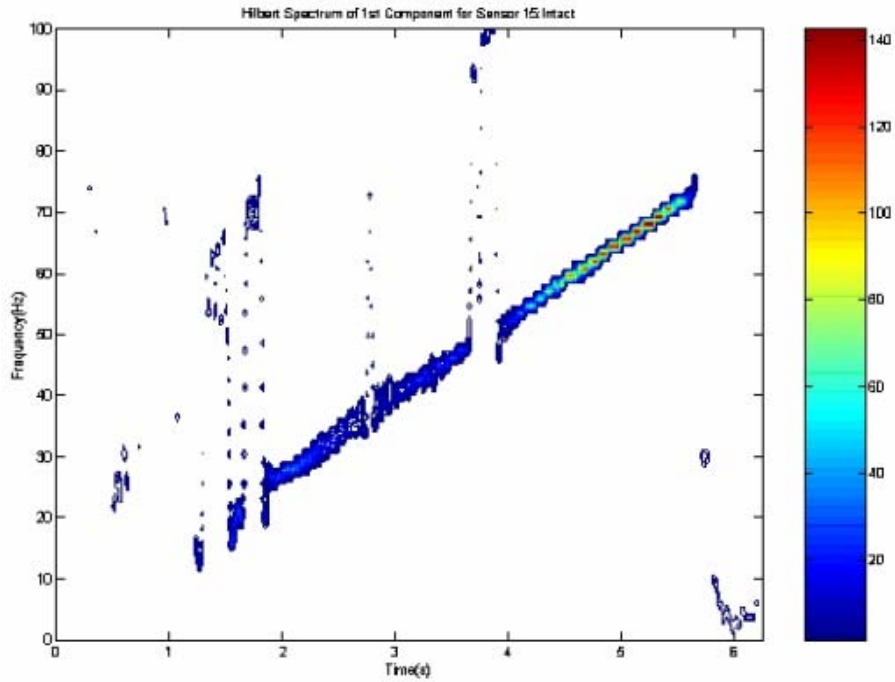


Figure 122. Graph. HHT spectrum of first IMF component of vibration, accelerometer 15, bent 12, intact state.

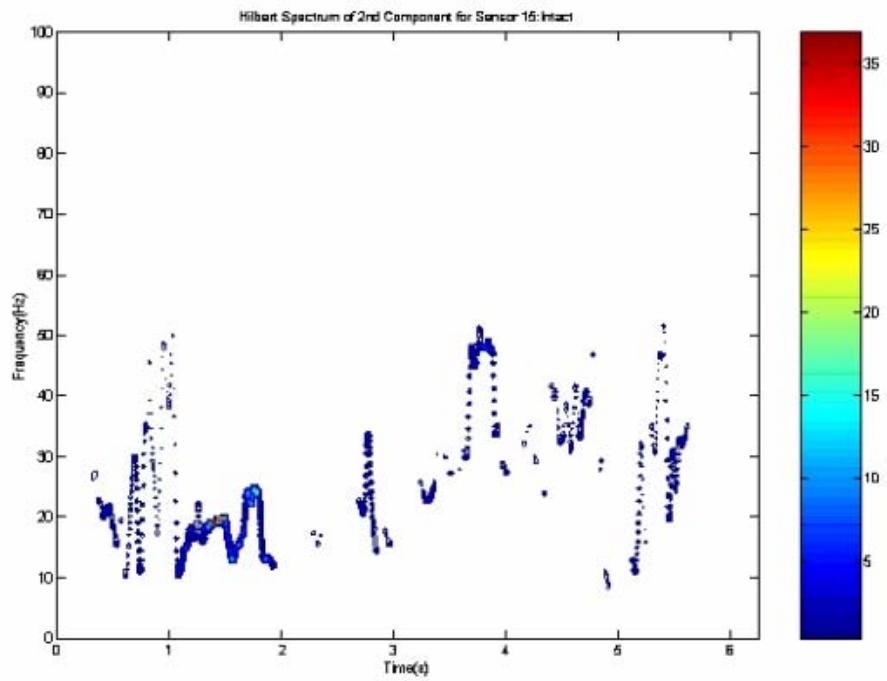


Figure 123. Graph. HHT spectrum of second IMF component of vibration, accelerometer 15, bent 12, intact state.

Identifying the fundamental natural frequencies of the structure from the vibrations during the time between 1 and 2 s is of primary interest; consequently, most of the remaining figures containing the HHT spectrum are presented with times of less than 3 s and frequencies less than 40 Hz. Figure 124 enlarges the HHT spectrum of vibration response at accelerometer 15 with the structure in its sound state. Except for the DIDF, the energy concentration shown in figure 124 is attributed primarily to the structure itself. Because the accelerance TF shows a resonance of about 15 Hz, examination of the energy at frequencies up to 15 Hz during the first 1 to 2 s may be useful. The energy below roughly 10 Hz (light lines or dots) is much less than that above 10 Hz (dark lines or dots). This response energy is believed to be generated by the DIDF during the time between 0.5 and 1 s and the driving frequency of 6 to 15 Hz at around 1+ s, as shown in figure 118. If the fundamental natural frequency falls in the driving frequency range of 5 to 15 Hz, the response energy at the fundamental natural frequency should be much stronger than at lower frequencies, but not necessarily stronger than at higher frequencies because of the existence of second and higher natural frequencies. The dark area of 14 to 15 Hz at 1.5 s in figure 124 suggests that the fundamental natural frequency is approximately 14 to 15 Hz; but also, considerable energy is found from 12 to 20 Hz in the 1 to 2 s timeframe.

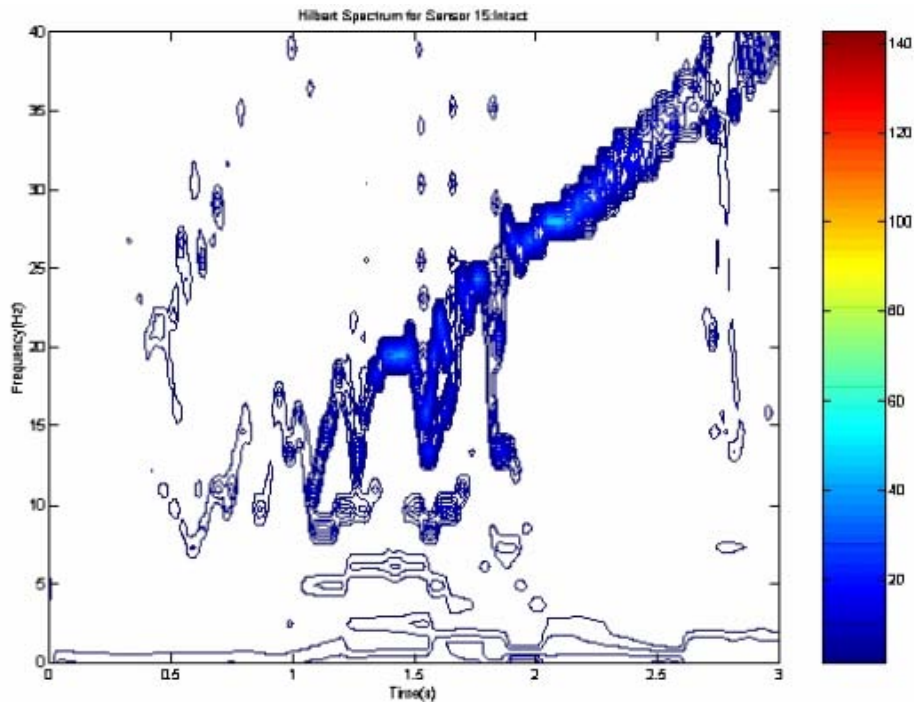


Figure 124. Graph. HHT spectrum of vibration, accelerometer 15, bent 12, intact state.

Figure 125 shows the HHT spectrum of vibration response at accelerometer 15 with the structure in its excavated damage state. In addition to the DIDF, an energy concentration is found at approximately 7 Hz at approximately 1.4 s. This concentration corresponds to the concentration found at 14 to 15 Hz at 1.5 s in figure 122 for the intact pile. The decrease from 14 to 15 Hz in the intact state to 7 Hz in the excavated damage state could be related to the mixed natural frequency of the pile and pier because the vibration at accelerometer 15 should reflect the dynamic characteristics of both the whole structure and the local member. The excavated soil reduces the stiffness of the south pile and south-center pile, and thus the fundamental natural frequency of bent 12. This is the signature of local damage in the vibration records, damage that was not as clearly shown in traditional modal vibration data analysis. Such an explanation is further supported by figure 126, which shows the HHT spectrum of vibration response at accelerometer 15 with the south pile broken, and thus the structure in its broken state. The frequency concentration has further decreased to 3 Hz at 1.7 s.

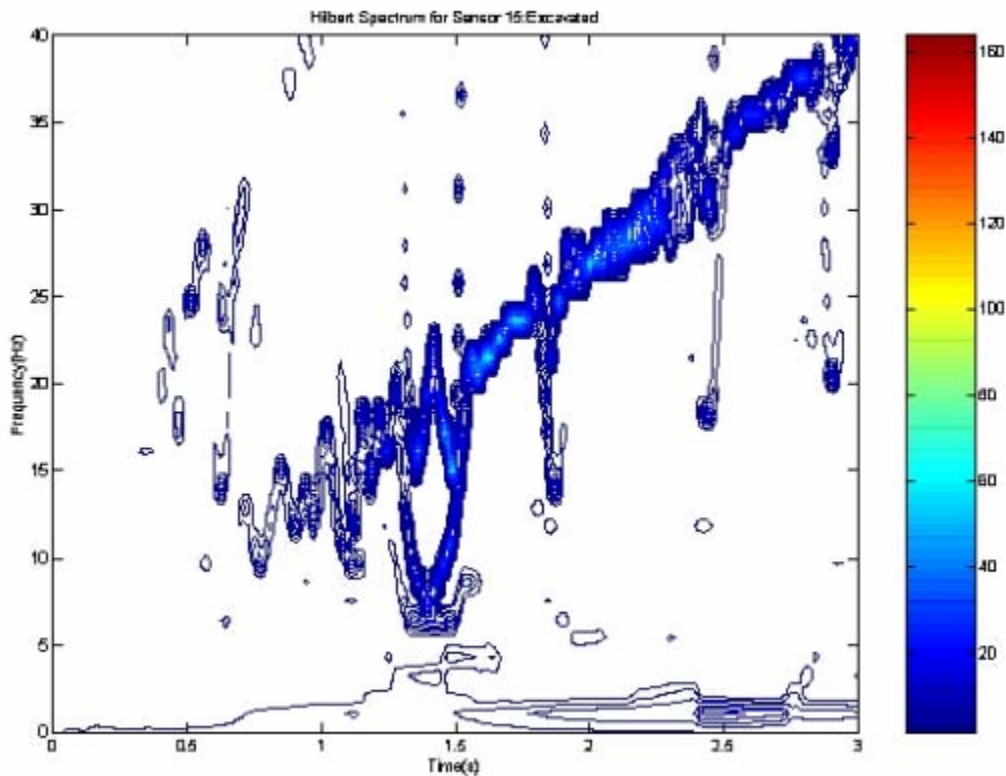


Figure 125. Graph. HHT spectrum of vibration, accelerometer 15, bent 12, excavated state.

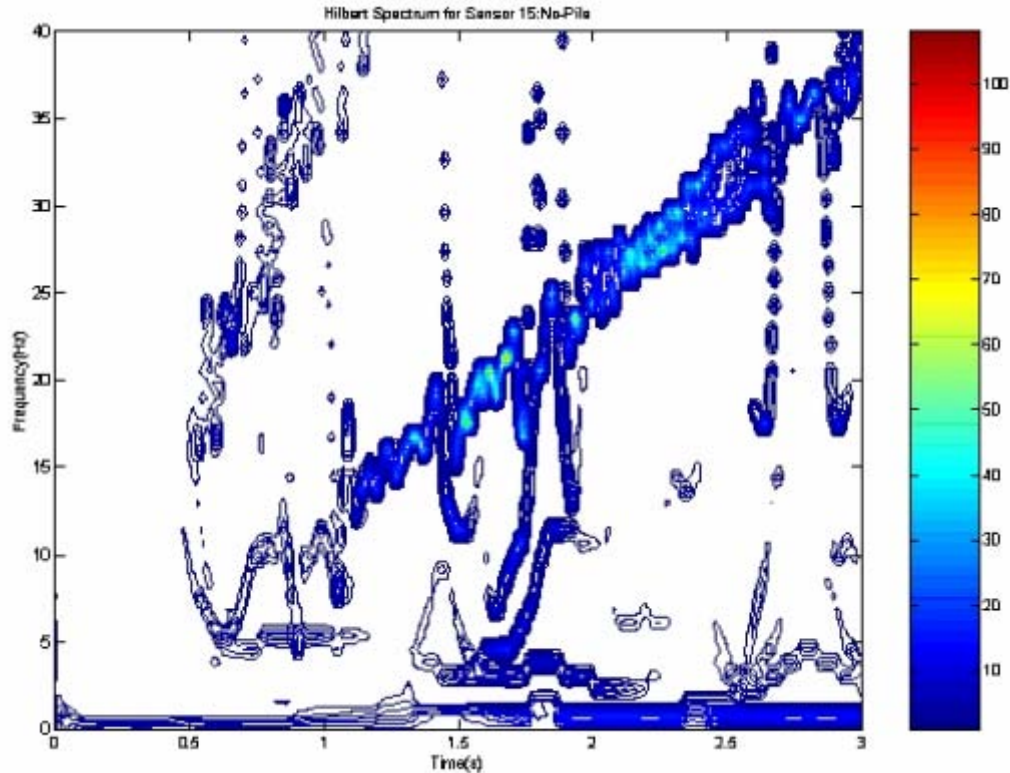


Figure 126. Graph. HHT spectrum of vibration, accelerometer 15, bent 12, broken state.

The preceding discussion is based on the HHT-analyzed data observations with the aid of vibration theory. Further model-based validation is the subject of a continuing study. Following is a simple, rough argument about the validity of the preceding discussion.

Accelerometer 15 is mounted on the pile/column with one end connected to the beam and the other end buried in the soil; thus, the dominant vibration recorded should more likely contain the dynamic features of the column itself. To examine the change of fundamental natural frequency of the column in three damage states, one can roughly model the column with different boundary conditions and lengths. In particular, the boundary conditions are approximated as fixed-fixed with a length of 2.14 m (7 ft) for the pile/column in the intact state, fixed-fixed with a length of 4.88 m (16 ft) in the excavated damage state, and fixed-free with a length of 2.14 m (7 ft) in the broken pile/severe damage state. These boundary conditions were chosen not only because they crudely model the real vibration of the column but also because they have simple exact solutions for the fundamental natural frequency. This simple theoretical model shows that the relative reduction of the fundamental natural frequency for the excavated and broken pile states with respect to that in the intact state is 56 and 68 percent, respectively. In comparison, the pertinent relative change with the use of the observed fundamental natural frequency is 50 and 70 percent. The detailed comparison is given in table 15. The observed results are close to the theoretical ones. While this comparison is not proof that this discussion is a correct approach to analyzing the data, it does provide substantial support for the approach. Further research and solid validation are needed.

Table 15. Comparison of fundamental natural frequencies of a column in three states.

State	Boundary Condition with Length	Theoretical Frequency (F)	Observed Frequencies (HHT Analysis) (f)	Relative Change of Frequency with Respect to Frequency at Intact Stage		Figure
Intact	Fixed-fixed with $l = 2.1$ m (7 ft)	$F_i = \frac{1}{2l} \sqrt{\frac{E}{\rho}}$	$f_i = 10$ Hz	N/A		127
Minor damage	Fixed-fixed with $l = 4.9$ m (16 ft)	$F_m = \frac{1}{2l} \sqrt{\frac{E}{\rho}}$	$f_m = 5$ Hz	$(F_i - F_m)/F_i = 56\%$	$(f_i - f_m)/f_i = 50\%$	128
Severe damage	Fixed-free with $l = 3.4$ m (11 ft)	$F_s = \frac{1}{2l} \sqrt{\frac{E}{\rho}}$	$f_s = 3$ Hz	$(F_i - F_s)/F_i = 68\%$	$(f_i - f_s)/f_i = 70\%$	129

The HHT analysis of the three states of vibration at accelerometer 15 on bent 12 shows that the HHT method might provide a means to recognize clearly, in terms of the natural frequency as determined from vibration records, the signature difference of sequential damage in a structural member. As a comparison, an HHT analysis of corresponding vibration at accelerometer 13 on the north-center pile, which is well-removed from the damage location at the south pile, is now presented.

Figures 127, 128, and 129 show the HHT spectrum of vibration data at accelerometer 13 for the structure in its intact, excavated, and broken or damaged pile states, respectively. The figures show that the lowest dominant frequency of structural vibration is approximately 10 Hz between 1 and 2 s. These data not only confirm that the fundamental natural frequency of the whole structure and its members likely can be distinguished from the driving frequency by HHT analysis, but they also suggest that HHT analysis is sensitive to changes in vibration characteristics caused by local damage.

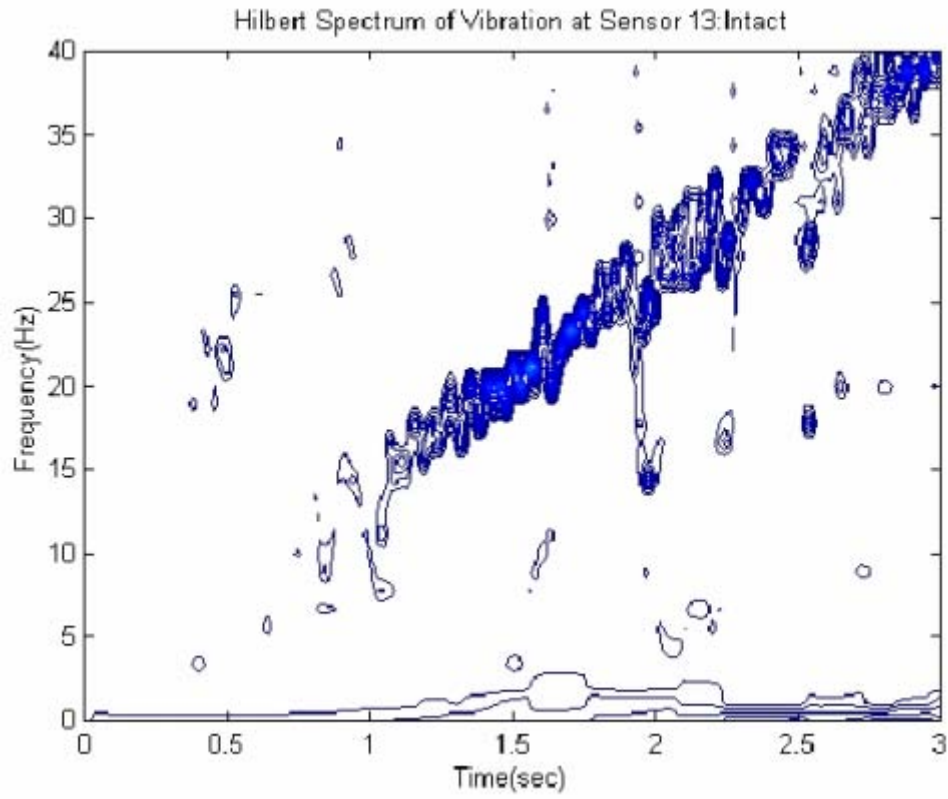


Figure 127. Graph. HHT spectrum of vibration, accelerometer 13, bent 12, intact state.

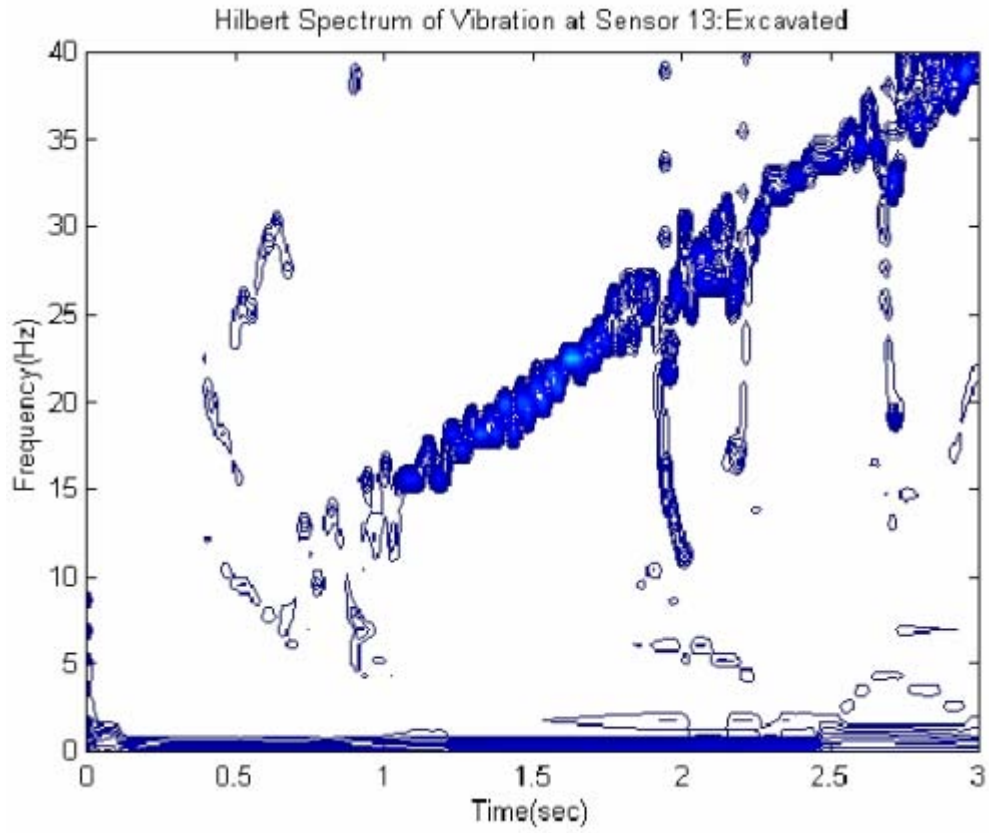


Figure 128. Graph. HHT spectrum of vibration, accelerometer 13, bent 12, excavated state.

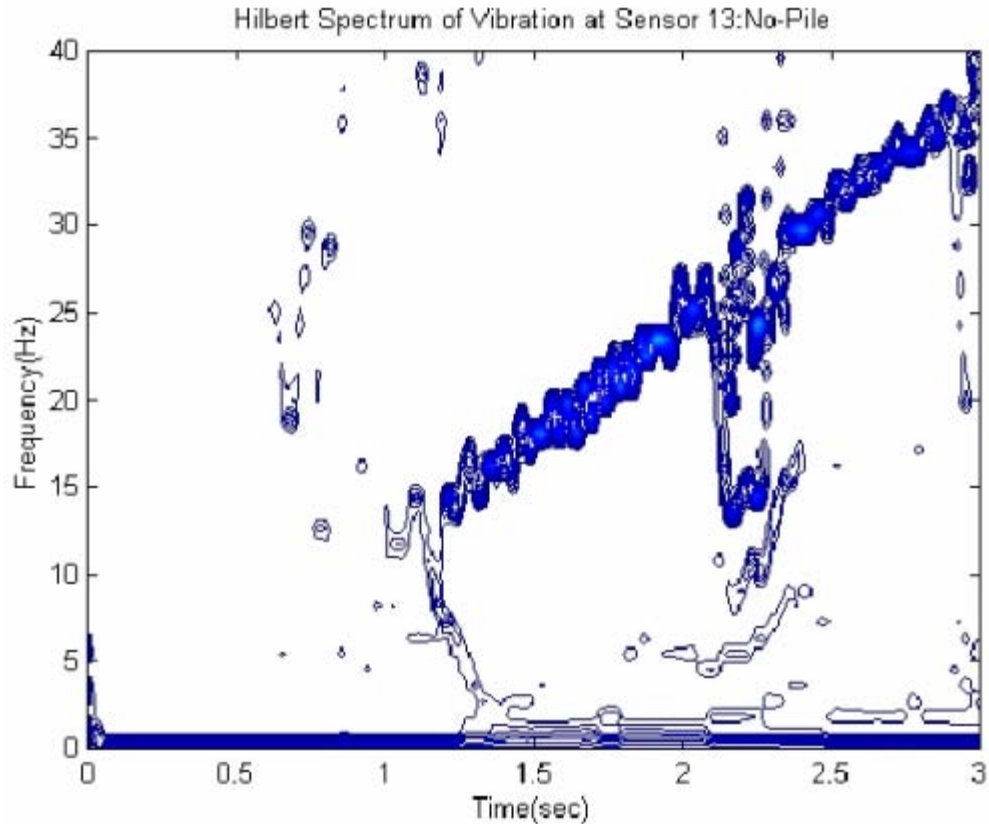


Figure 129. Graph. HHT spectrum of vibration, accelerometer 13, bent 12, broken state.

The second and third IMF components of vibration, or at least the second, are most related to the structural fundamental frequency of vibration. The HHT spectra of second IMF components of vibrations at accelerometers 15 and 13 with the structure in its intact, excavated, and damaged pile states are shown in figures 130 through 135. The mode mixture of IMF components is observed (which results in the mixture of driving and natural frequencies). The figures also show the response differences between accelerometer 15 on the excavated and then broken south pile and accelerometer 13 on the sound north pile as the south pile goes from the intact, to the excavated, to the broken state. At accelerometer 15, the fundamental frequency appears to decrease from 10 Hz, to 7 Hz, to 5 Hz. In contrast, the fundamental frequency at accelerometer 13 shows little movement.

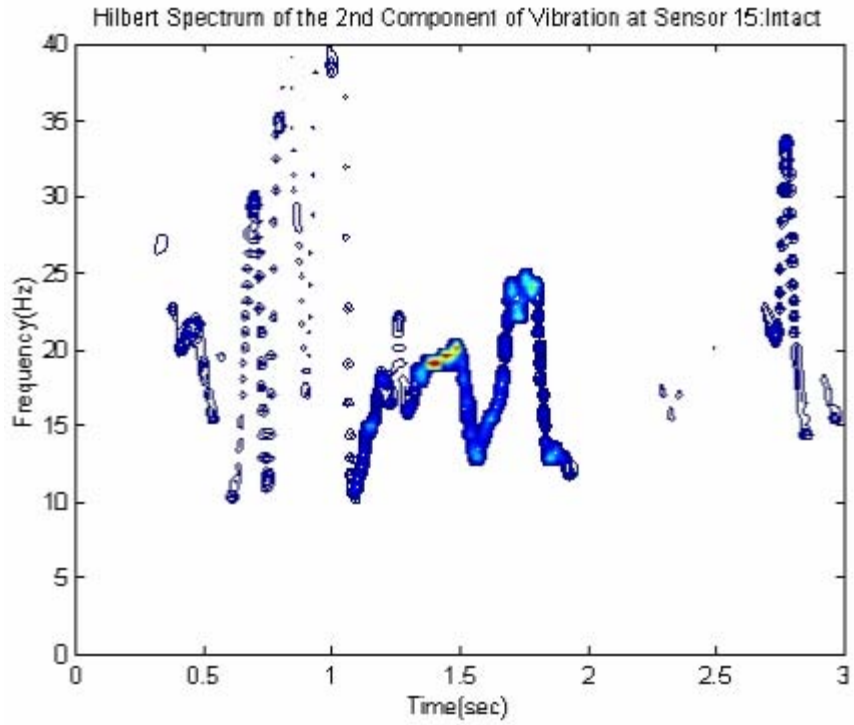


Figure 130. Graph. HHT spectrum, second component of vibration, accelerometer 15, bent 12, intact state.

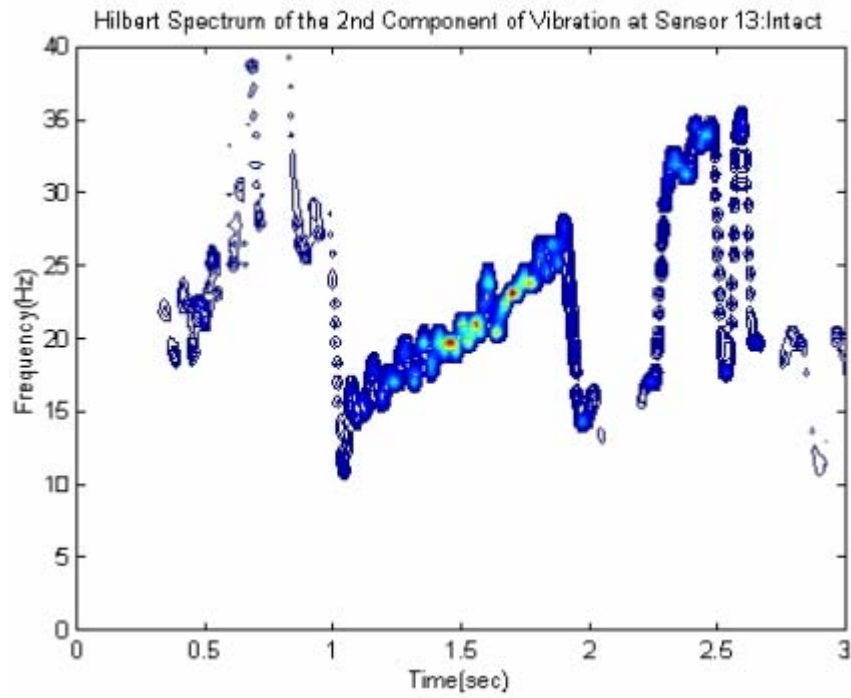


Figure 131. Graph. HHT spectrum, second component of vibration, accelerometer 13, bent 12, intact state.

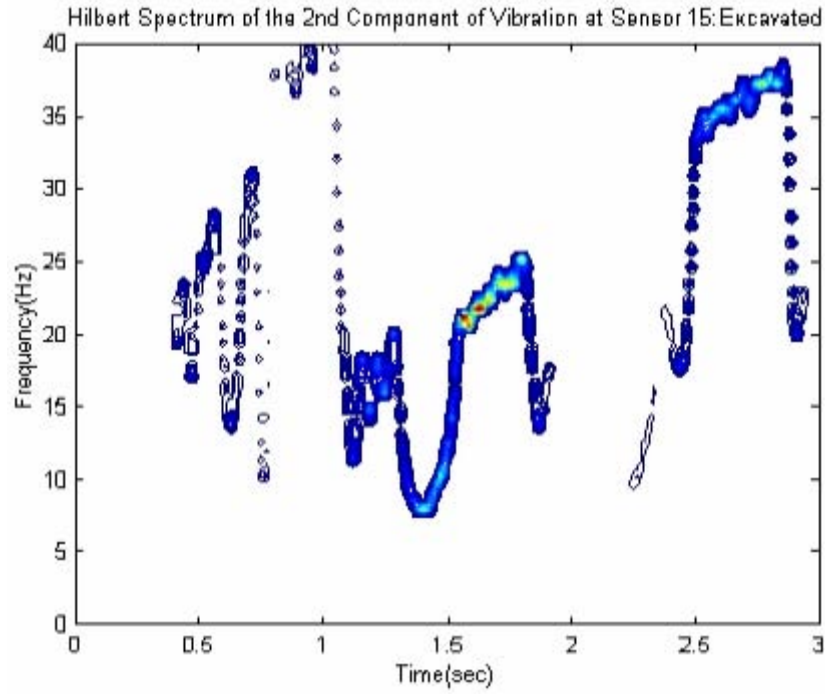


Figure 132. Graph. HHT spectrum, second component of vibration, accelerometer 15, bent 12, excavated state.

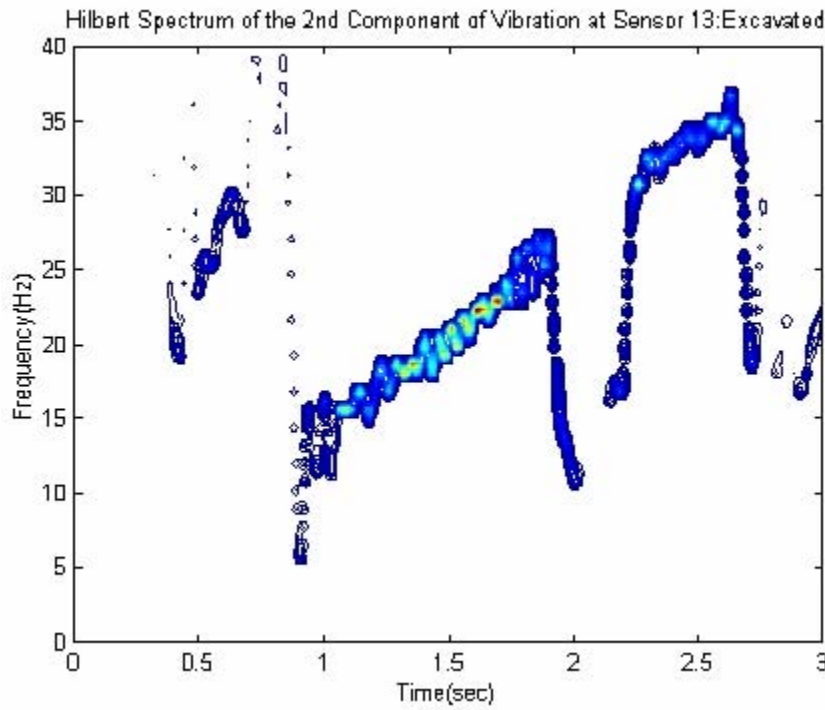


Figure 133. Graph. HHT spectrum, second component of vibration, accelerometer 13, bent 12, excavated state.

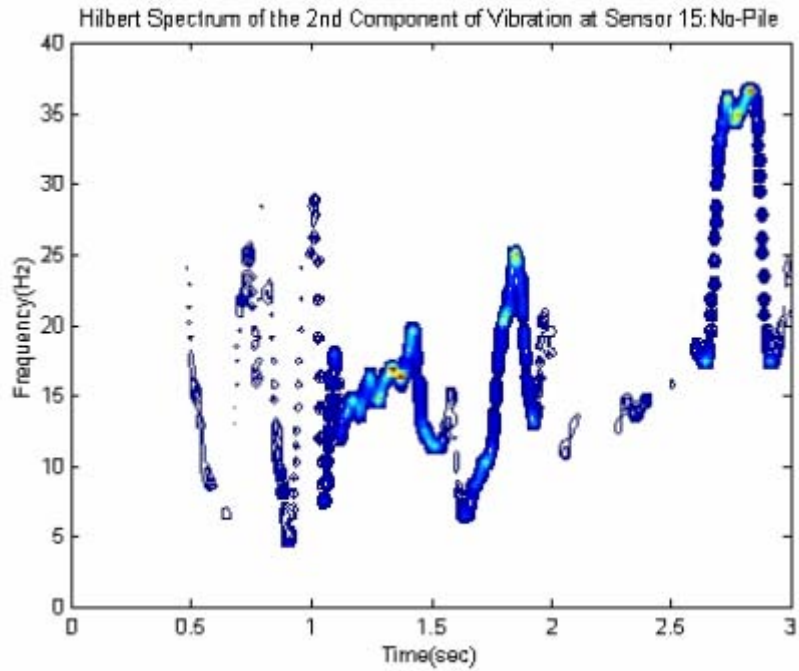


Figure 134. Graph. HHT spectrum, second component of vibration, accelerometer 15, bent 12, broken state.

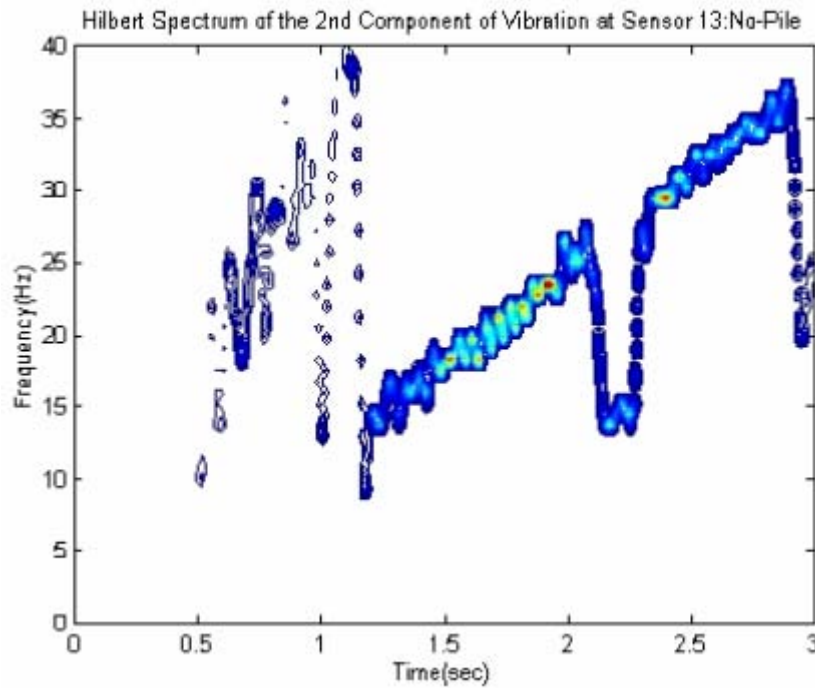


Figure 135. Graph. HHT spectrum, second component of vibration, accelerometer 13, bent 12, broken state.

## HHT Analysis of Data from Bent 2

The following paragraphs discuss the HHT analysis of the data from bent 2. The focus is on the potential of HHT analysis for recognizing damage. Figure 136 shows the structural configuration of bent 2 in its broken pile state. The Vibroseis excitation was in the middle of the deck. Bent 2 differs from bent 12 because bent 2 had a ground-level shallow footing surrounding the four piles of the bent. Other pier and test conditions, including the field test setup, data collection procedures, and states of damage, were similar to the conditions in the testing of bent 12. The modal vibration test data were analyzed from accelerometers 11 and 9 on two of the four bent 2 piles, shown in figure 136. The accelerometers were located somewhat higher on the piles than accelerometers 15 and 13 on the piles of bent 12.

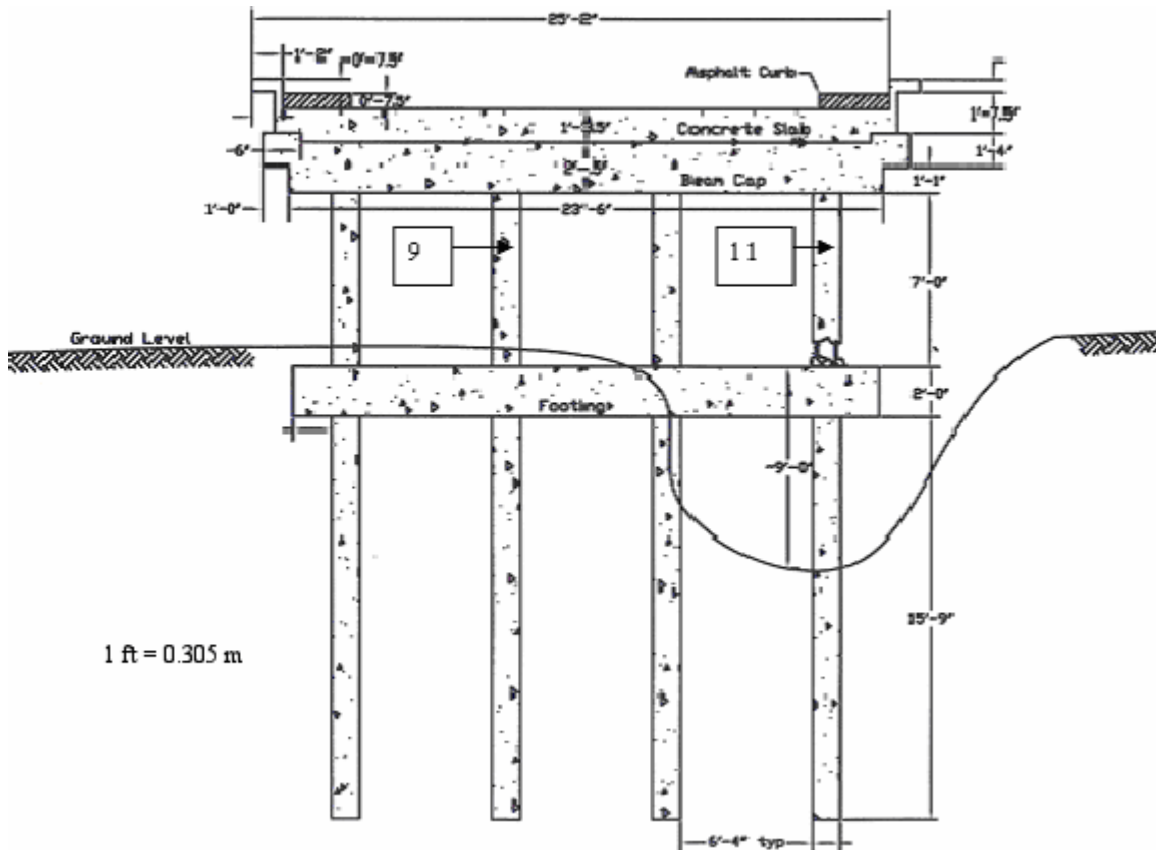


Figure 136. Diagram. Locations of accelerometers 9 and 11 on bent 2.

Figures 137, 138, and 139 show the HHT spectra of the vibration response at accelerometer 11 on the damaged pile with the structure in its intact, excavated, and damaged pile states. Figures 140, 141, and 142 show the HHT spectra of the vibration response at accelerometer 9, which is on a sound pile. Both sets of results are similar to the spectra of bent 12.

Between 1 and 1.5 s at the damaged pile, the vibration frequencies measured by accelerometer 11 drop from 10 Hz in the intact state to less than 5 Hz in the damaged state. Over the same time range at the undamaged pile, the vibration frequencies measured by

accelerometer 9 show a slight increase in frequencies. These results tract those of the bent 12 case and support the conclusion that an HHT spectra from a damaged location is more sensitive to the damage than a spectra from a more remote location.

Thus the HHT method appears to provide a means to diagnose a damaged structural member through the examination of vibration signatures contained in a limited number of vibration records. It also appears that sensors need to be fairly close to or on a damaged member to monitor changes.

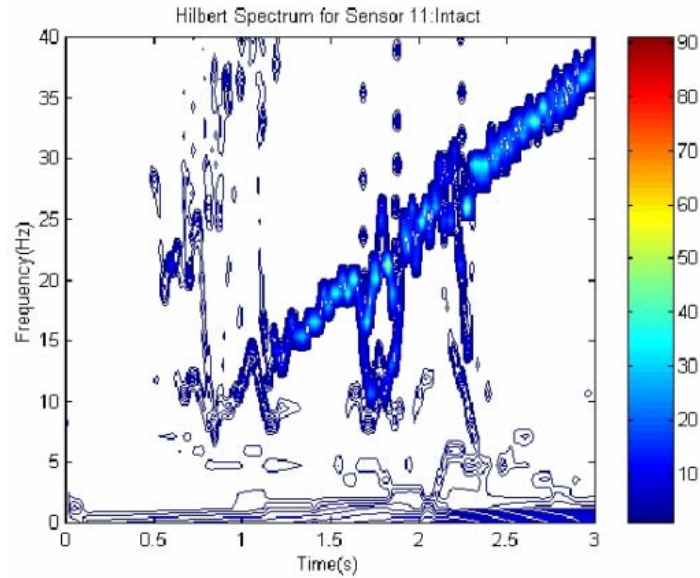


Figure 137. Graph. HHT spectrum of vibration, accelerometer 11, bent 2, intact state.

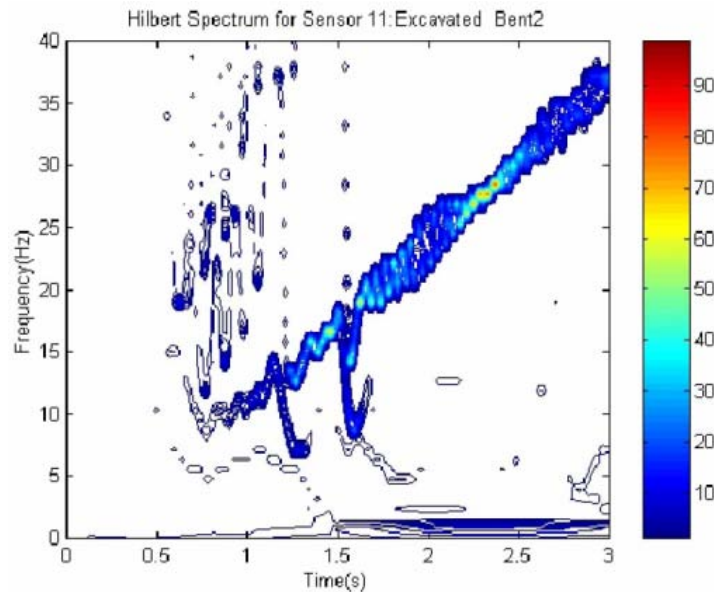


Figure 138. Graph. HHT spectrum of vibration, accelerometer 11, bent 2, excavated state.

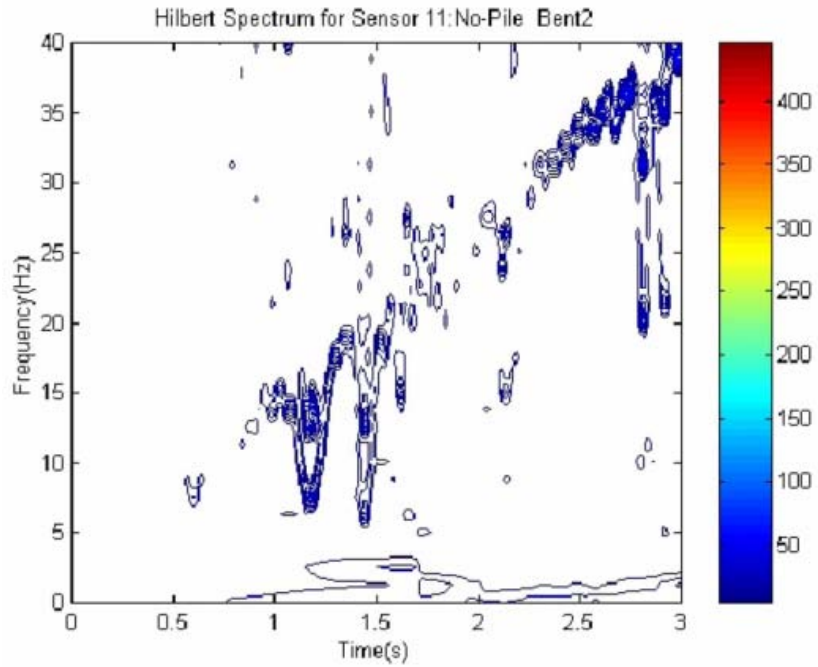


Figure 139. Graph. HHT spectrum of vibration, accelerometer 11, bent 2, broken state.

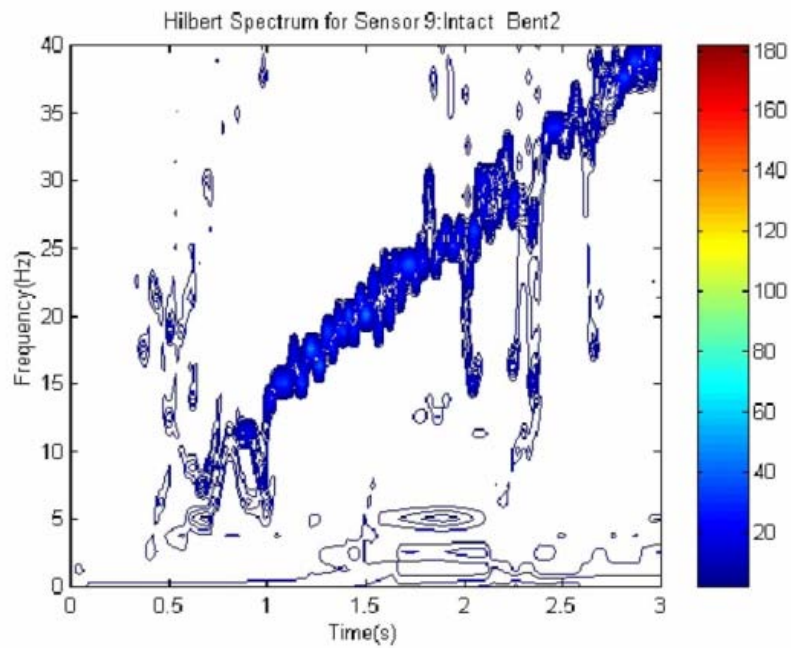


Figure 140. Graph. HHT spectrum of vibration, accelerometer 9, bent 2, intact state.

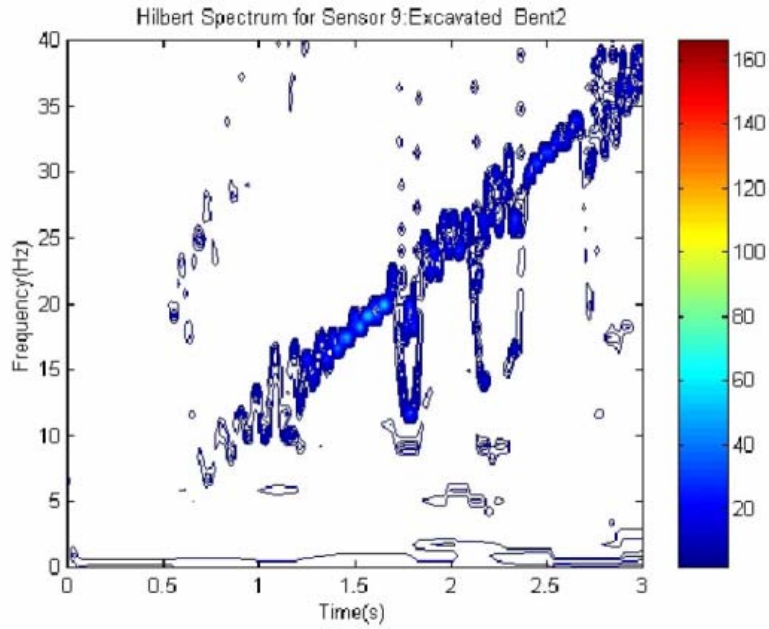


Figure 141. Graph. HHT spectrum of vibration, accelerometer 9, bent 2, excavated state.

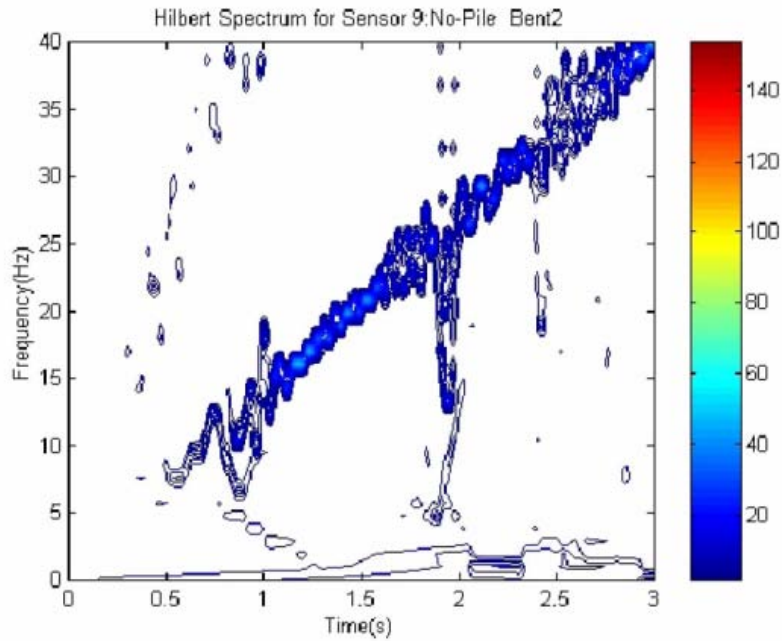


Figure 142. Graph. HHT spectrum of vibration, accelerometer 9, bent 2, broken state.

## Force Excitation Normalized HHT Spectra for Bent 12

HHT analysis appears to be very useful in identifying the frequency content of linear and nonlinear signals. To investigate its usefulness further, a normalization approach was applied to the HHT analysis of bent 12 data, more specifically to readings at accelerometer 15 on the damaged pile on bent 12. This analysis was presented earlier. The normalization approach was similar to the modal accelerance TF analysis in that the HHT spectrum of the accelerometer response readings at accelerometer 15 were divided by the HHT spectrum of the Vibroseis chirp excitation force. In other words, the HHT accelerometer response readings were normalized to the HHT input force. The input force was the average amplitude at each digital time step over the 6-s measurement range. The input force, or chirp excitation force, was not constant with time, so normalization was an attempt to remove the effect in the response data of the time varying aspect of the input force. The hope was that normalization would make resonant frequency peaks and shifts more apparent. A further hope was that the readily apparent vertical resonance frequencies obtained from the modal vibration measurements and TF analyses discussed in chapter 5 and shown in figure 113 would have corresponding resonances in the normalized HHT spectrum.

Figure 118 was the source of the HHT-processed data for the averaging of the amplitudes of the input force. For the intact state case, figure 119 was the source of the HHT-processed response readings at accelerometer 15. Other figures provided the HHT-processed response readings for the excavated and broken pile cases.

The resulting HHT spectrum plots of the normalized vibration at accelerometer 15 for the intact, excavated, and broken pile cases are given in figures 143, 144, and 145, respectively. The average amplitudes of the input force—the dominant, linear chirp force—that was used to normalize the corresponding HHT spectra for the intact, excavated, and broken pile states are shown versus time in figures 146, 147, and 148, respectively. Over the 6-s time window, these HHT amplitude plots show considerable variation. The responses at accelerometer 15 should vary in amplitude with the excitation or input force except when the structural resonant frequencies are excited by the chirp, and dynamic amplification of the response occurs, indicating a resonant peak frequency. Figure 143 shows high amplitudes at 20 Hz and 28 Hz that correspond closely to the modal vibration peaks in figure 113 for the intact case of bent 12. The weaker modal resonance peak at 15 Hz, however, does not stand out in the normalized HHT spectrum in figure 143. The integration of the acceleration data to velocity and displacement data in the time domain before HHT analyses might have made the 15 Hz resonance more apparent. Agreement between the modal and normalized HHT resonances—the latter are in figures 145 and 147—is not apparent for the excavated and broken pile cases, possibly because of the damage and nonlinear effects.

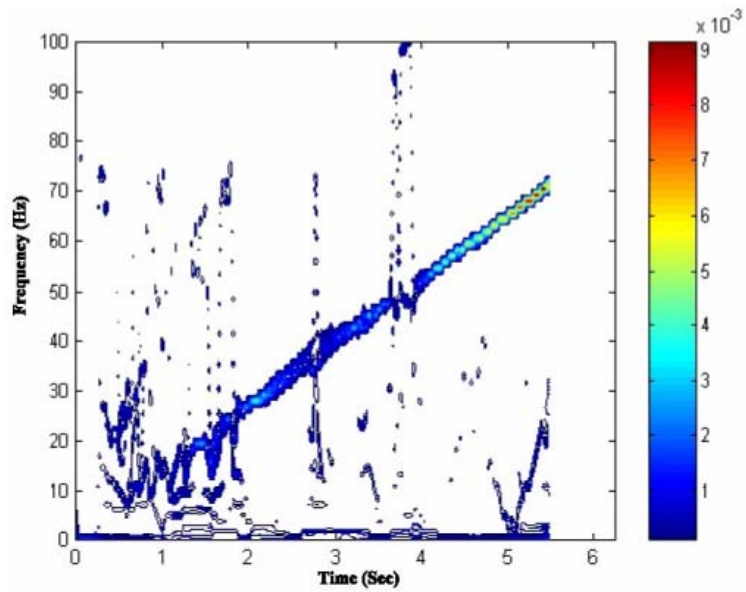


Figure 143. Graph. Normalized HHT spectrum of vibration, accelerometer 15, bent 12, intact state.

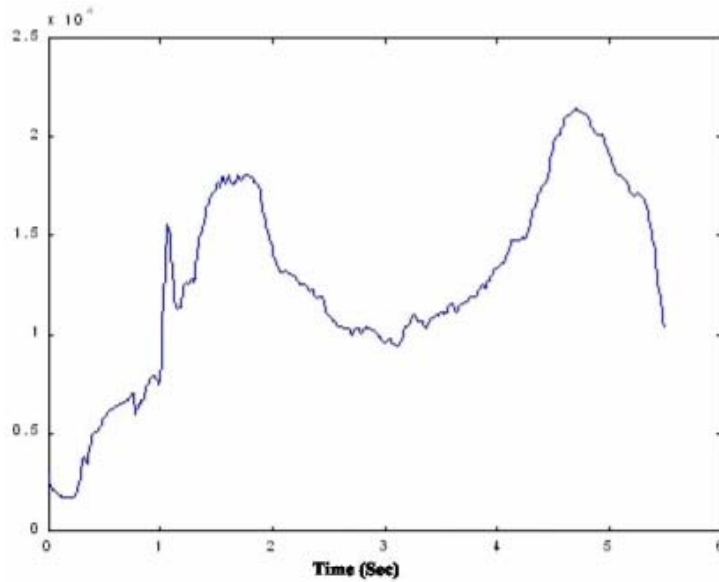


Figure 144. Graph. Amplitude of force applied to bent 12, intact state.

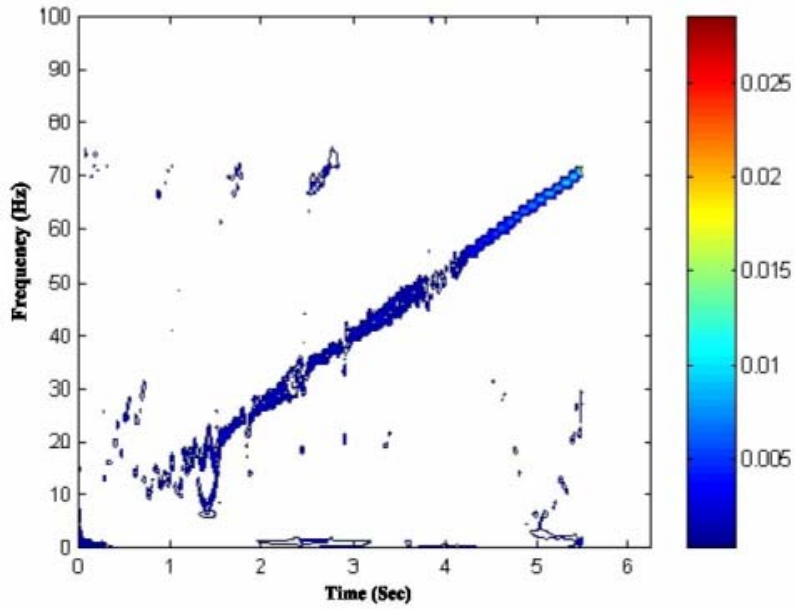


Figure 145. Graph. Normalized HHT spectrum of vibration, accelerometer 15, bent 12, excavated state.

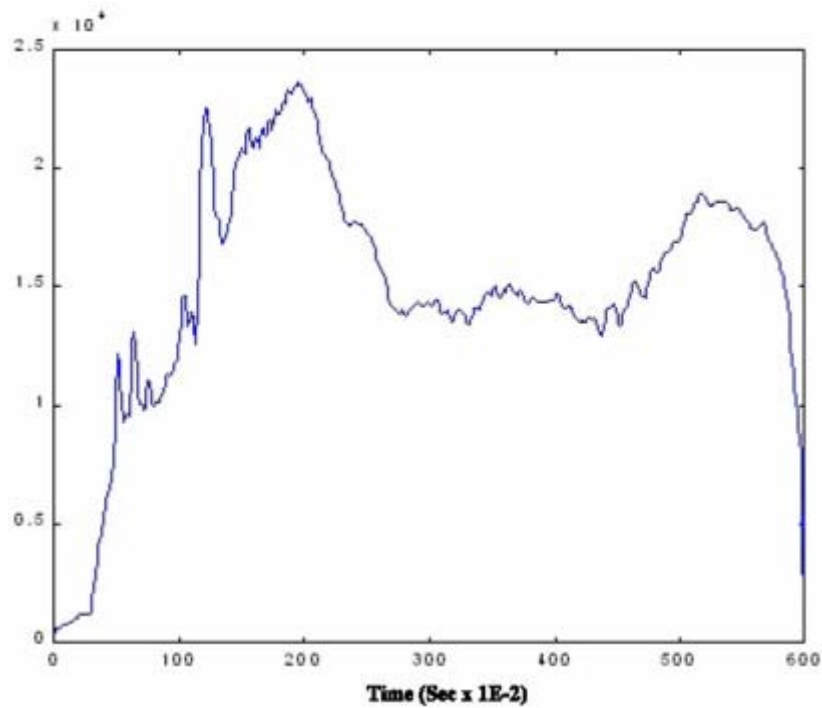


Figure 146. Graph. Amplitude of force applied to bent 12, excavated state.

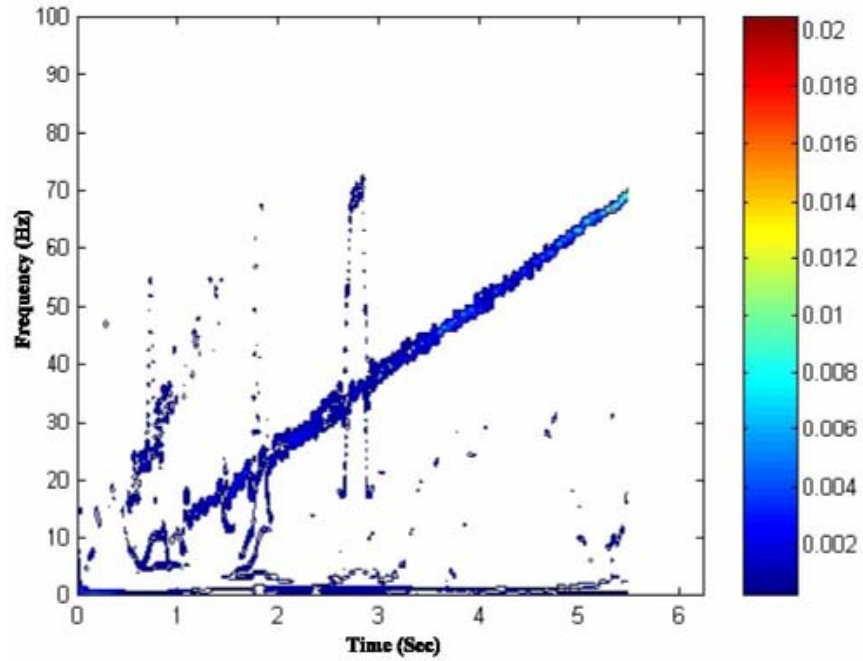


Figure 147. Graph. Normalized HHT spectrum of vibration, accelerometer 15, bent 12, broken state.

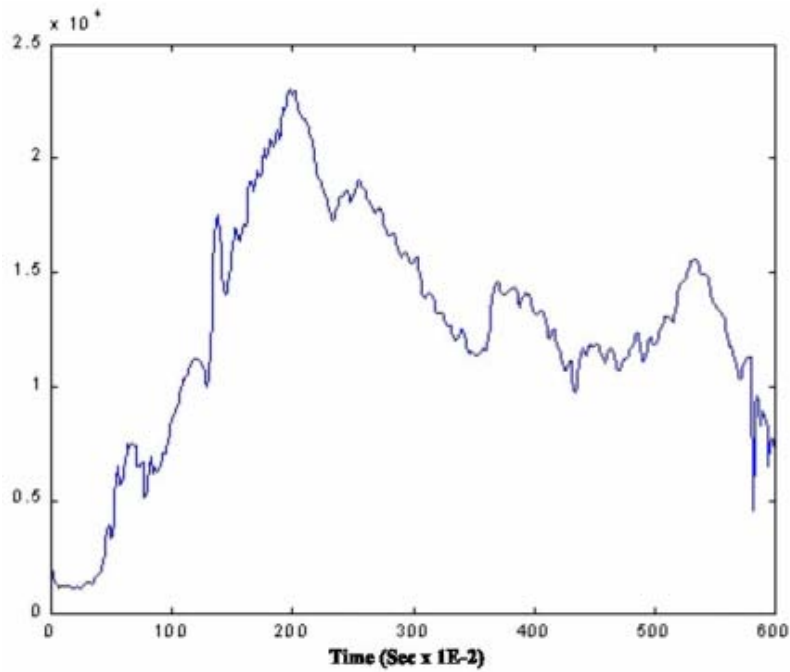


Figure 148. Graph. Amplitude of force applied to bent 12, broken state.

## Model-Based Validation for Bent 12

To further investigate both the modeling approach covered in chapter 6 and the use of HHT analysis in determining damage characteristics, an HHT analysis was performed with simulated vibration data and ANSYS-based 2-D FEMs for bent 12 in its intact and severe-damage states. It should be noted that there are always inherent differences between the FEMs and the real structure. These differences arise from simplifications of boundary and support conditions, the connectivities between various structural elements, unknown material properties and constitutive relationships (particularly those associated with soil and concrete), and energy dissipation (damping) mechanisms. Only certain aspects of the HHT-based signature-recognition features were investigated with the model-based approach.

### *ANSYS Model for Bent 12*

The ANSYS-based 2-D FEM is shown in figure 150 for bent 12 in its intact state. The model was built on design specifications and pertinent information by Sanayei and Santini.<sup>(135)</sup> This 2-D model is also consistent with a 3-D FEM in terms of dynamic characteristics of the bent in the vertical direction.<sup>(135)</sup> Vibration in the vertical direction is the sole interest in this study, so the 2-D model instead of 3-D model was used for simplicity. In the 2-D modeling for bent 12, the cap beams and columns of the bent were modeled with beam elements and rigidly connected to each other. The mass and stiffness of the bridge deck were lumped onto the cap beam. The four piles were simply supported on the ground. Nodes 53 and 37 correspond to the locations of nodes 15 and 13 in figure 109. In the study, the 2-D model was extended from the intact state to the severe-damage state by releasing boundary restrictions at the ground end of the south pile (pile 15) in figure 150.

Table 16 shows the first 10 undamped natural frequencies of the intact and severe-damage states of the 2-D model of bent 12. The first, second, and third natural frequencies in the vertical direction are also indicated. To simulate the damping effects, Rayleigh damping was used in the modeling. The resulting equation is given in figure 149. The damping matrix  $[C]$  is expressed in terms of the matrices of mass  $[M]$  and stiffness  $[K]$ .<sup>(188)</sup>

$$[C] = a_0[M] + a_1[K]$$

Figure 149. Equation. Damping matrix  $[C]$ .

Where  $a_0$  and  $a_1$  are the constant coefficients; for simplicity,  $a_0 = a_1 = d$  was used in the simulations.

The first three natural frequencies in the vertical direction in table 16 are neither consistent with those of the Fourier-based analysis nor with those of the HHT analysis. Moreover, the damping in the model might differ significantly from the damping experienced by the actual bridge. Nevertheless, the 2-D model is used to verify whether the observations and assertions for the HHT method is a way to identify the downward shift in instantaneous frequency associated with the excavated and broken pile states.

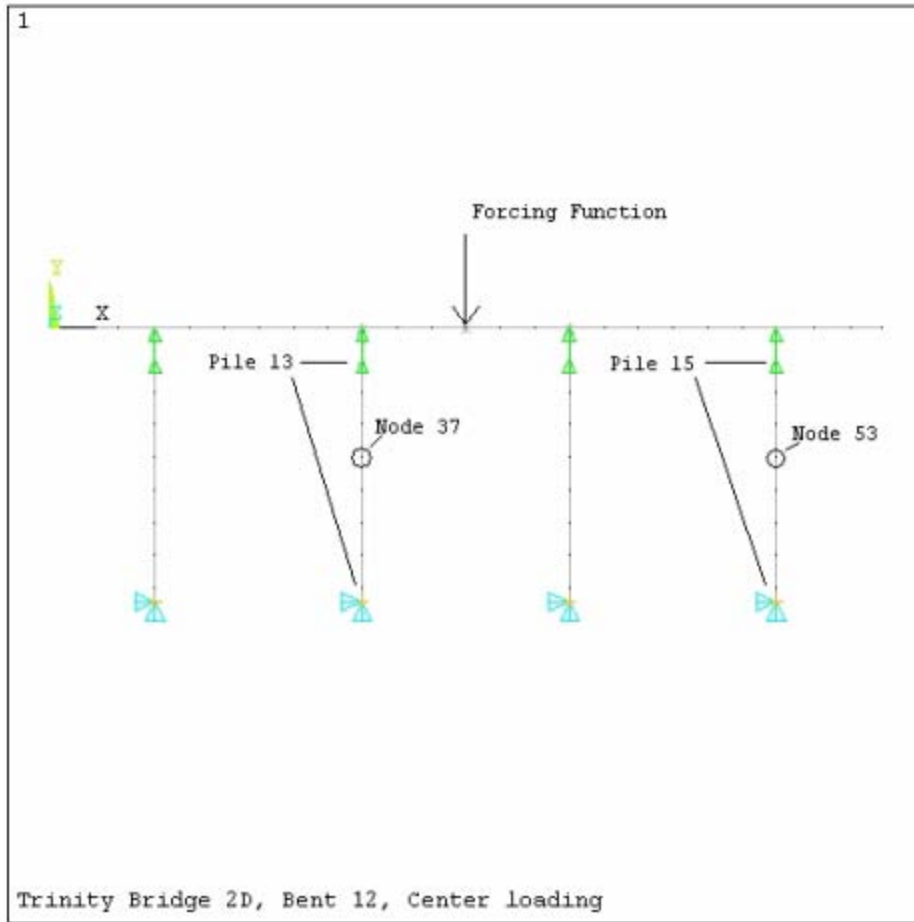


Figure 150. Diagram. ANSYS model for bent 12.

Table 16. Fundamental natural frequencies of bent 12.

<b>Natural Frequencies (Comments)</b>	<b>Intact (Hz)</b>	<b>Severe Damage (Hz) (Percent Decrease with Respect to Intact)</b>
1st	3.99	3.29
2nd (1st vertical natural frequency)	11.98	6.95 (41.98%)
3rd	14.84	12.47
4th (2nd vertical natural frequency)	19.68	18.08 (8.13%)
5th	44.01	39.19
6th (3rd vertical natural frequency)	69.22	52.50 (24.15%)
7th	93.88	72.50
8th	104.45	95.00
9th	106.37	105.82
10th	108.49	108.17

### ***HHT Analysis of Simulated Data***

The forcing function graphed in figure 110a was used to excite the 2-D model of figure 153 to calculate the vibration responses at nodes 53 and 37. Figures 151, 152, and 153 show the Hilbert amplitude spectrum of the theoretical model response at node 37 of the bent in the intact bent state with no damping,  $d = 0$ . The response energy is focused in frequency bands centered primarily around 12.0 Hz, 19.7 Hz, and 69.2 Hz. These are, respectively, the first three theoretical natural frequencies in the vertical direction, as shown in table 16. The marginal amplitude spectrum in figures 154, 155, and 156 clearly show the three resonant frequencies for the undamped case of  $d = 0$ .

Without damping, the bent is fully excited at the theoretical natural frequencies; therefore, the vibration energy at natural frequencies typically is higher than the driving excitation-inherited energy (with the natural frequency effects of the vibrator) at the chirp frequency. Consequently, with the exception of the strong energy band from 40 to 70 Hz between 3.5 and 5 s, the energy inherited from the excitation at chirp frequency is not clearly shown in figures 151, 152, and 153.

With increasing damping, the relative intensities of the energy from the structure and excitation should be affected, which arguably is discernable in the Hilbert amplitude spectra in figures 152 and 153 for  $d = 0.00198$  and  $0.05305$ , respectively.

The theoretical marginal amplitude spectrum in figure 155 suggests that the first damped fundamental natural frequency in the vertical direction might be around 11.5 Hz, which is correctly at a lower resonance than for the undamped theoretical case at 11.98 Hz. (See table 16.) This result is consistent with vibration theory. Because of the large damping used in the theoretical calculations and the strong excitation at much of the chirp frequency range, the vibration energy at natural frequencies appears greatly suppressed, as seen in figures 151 and 152. The first mode vibration energy at 11.5 Hz in figure 155 might be comparable to the chirp energy at other frequencies.

Figures 153 and 156 show the largest theoretical damping. The vibration energy at 10 Hz appears to occur primarily at 1.4 s. Because the  $d = 0.05305$  damping here is extremely high, the theoretically calculated damped fundamental natural frequency is greatly downshifted from the undamped value of 11.98 to 10 Hz. It should be noted that with damping of  $d = 0.05305$ , the ANSYS model in figure 150 generated time history responses similar to those of figure 110b. This implies that real damping of bent 12 in the vertical direction is comparatively high.

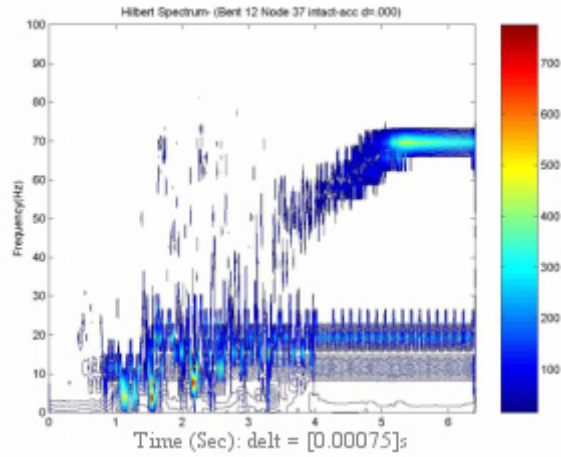


Figure 151. Graph. HHT spectra of vibration of 2-D FEM, node 37, bent 12, intact state,  $d = 0$ .

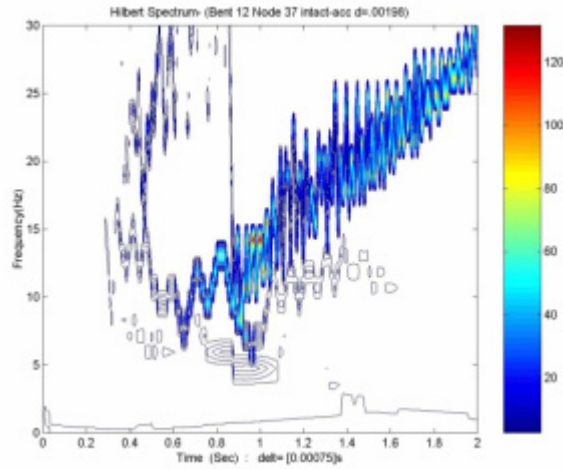


Figure 152. Graph. HHT spectra of vibration of 2-D FEM, node 37, bent 12, intact state,  $d = 0.00198$ .

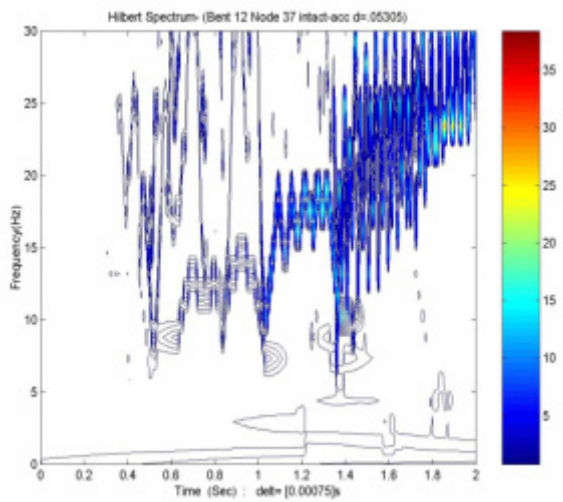


Figure 153. Graph. HHT spectra of vibration of 2-D FEM, node 37, bent 12, intact state,  $d = 0.05305$ .

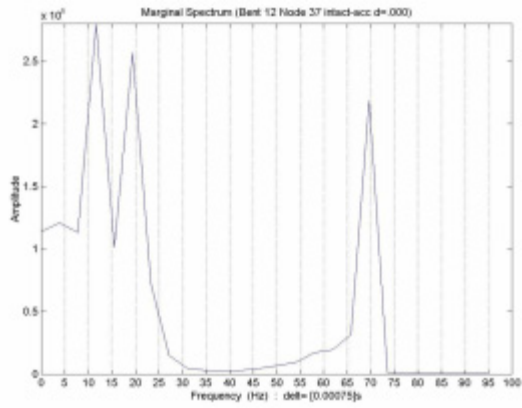


Figure 154. Graph. Spectra of marginal amplitude, node 37, bent 12, intact state,  $d = 0$ .

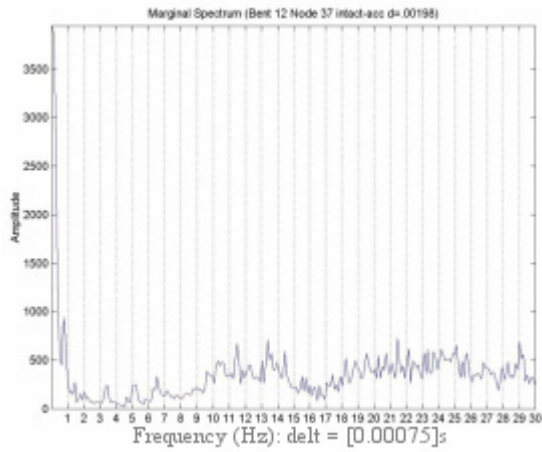


Figure 155. Graph. Spectra of marginal amplitude, node 37, bent 12, intact state,  $d = 0.00198$ .

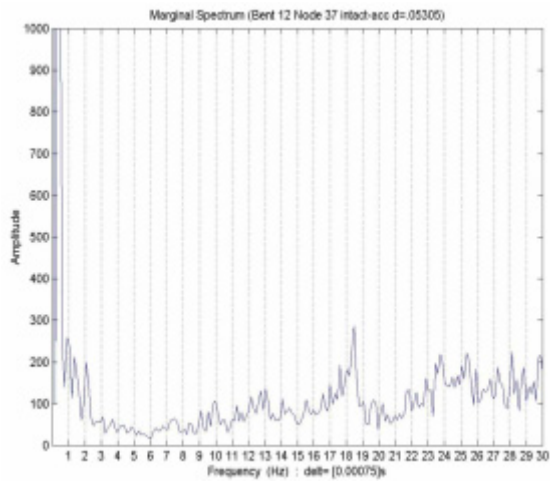


Figure 156. Graph. Spectra of marginal amplitude, node 37, bent 12, intact state,  $d = 0.05305$ .

To examine theoretical results for the broken pile state, the Hilbert amplitude spectra of the response at node 37 on the sound pile and at node 53 on the broken pile are presented in figures 157 and 158 for the broken pile state and for  $d = 0.003979$ . In other words, the pile of node 53 in the model of bent 12 was theoretically broken, and readings were taken at node 53 on the broken pile and node 37 on the sound pile. The node 53 readings in figure 158 show the vibration energy concentrated at 7 Hz from 0.5 to 1.2 s, which is the fundamental natural frequency of the theoretical broken pile case in table 16. In contrast, the dominant resonant vibration energy at node 37—figure 157—is approximately 12 Hz between 0.6 and 1 s; a minor resonant peak is found at 7 Hz at just over 1 s.

The marginal amplitude spectra for the sound and broken piles are presented in figures 159 and 160, respectively.

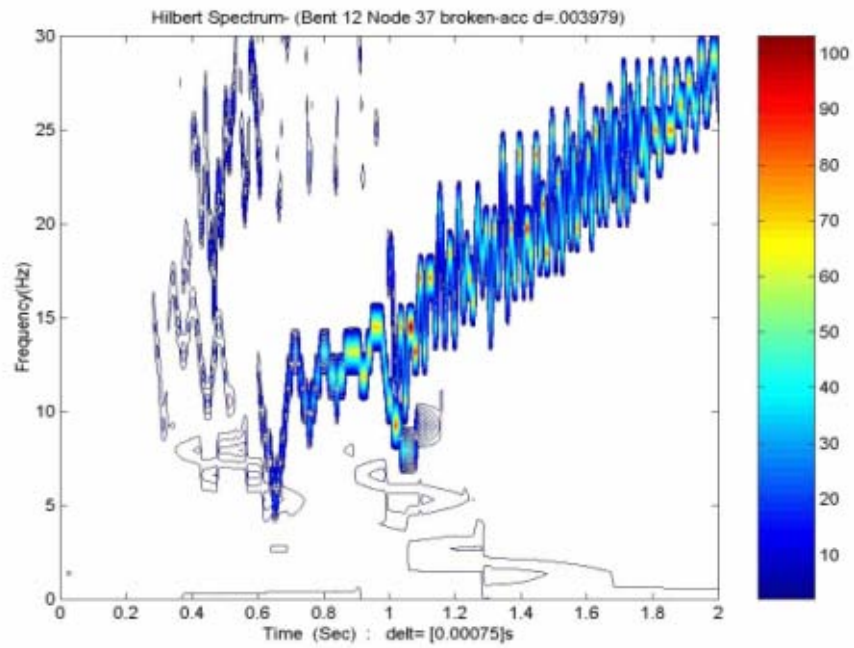


Figure 157. Graph. HHT spectra of vibration of 2-D FEM,  $d = 0.003979$ , bent 12, broken state, node 37.

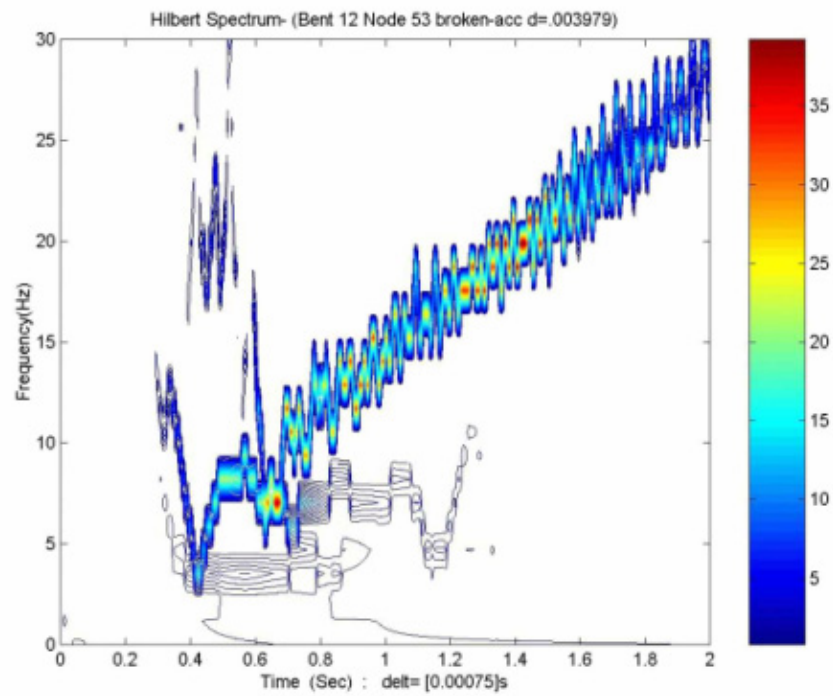


Figure 158. Graph. HHT spectra of vibration of 2-D FEM,  $d = 0.003979$ , bent 12, broken state, node 53.

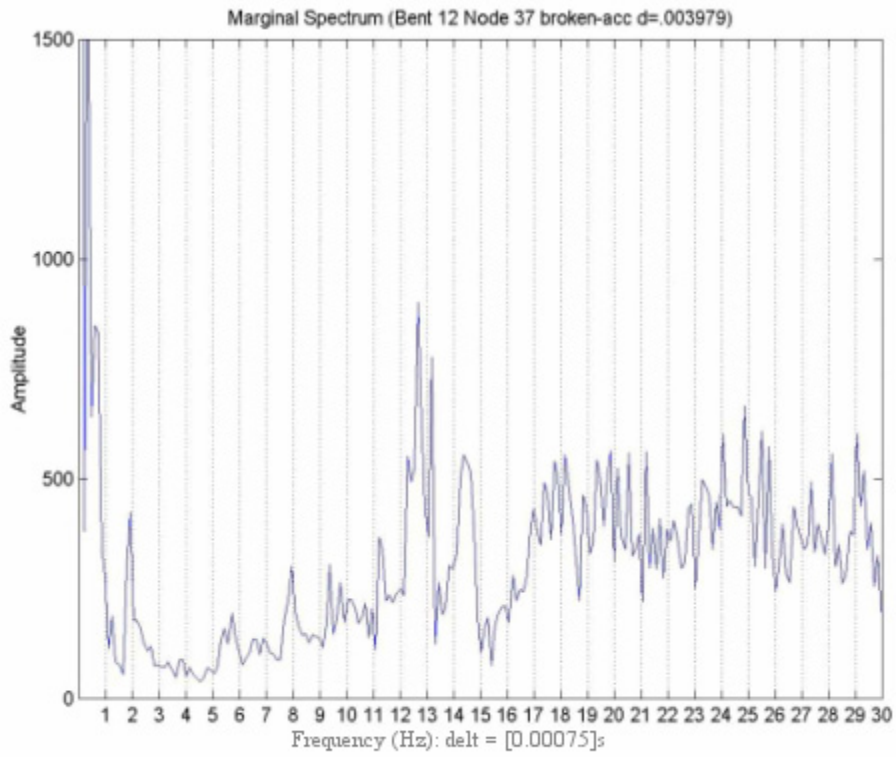


Figure 159. Graph. Spectra of marginal amplitude,  $d = 0.003979$ , bent 12, broken state, node 37.

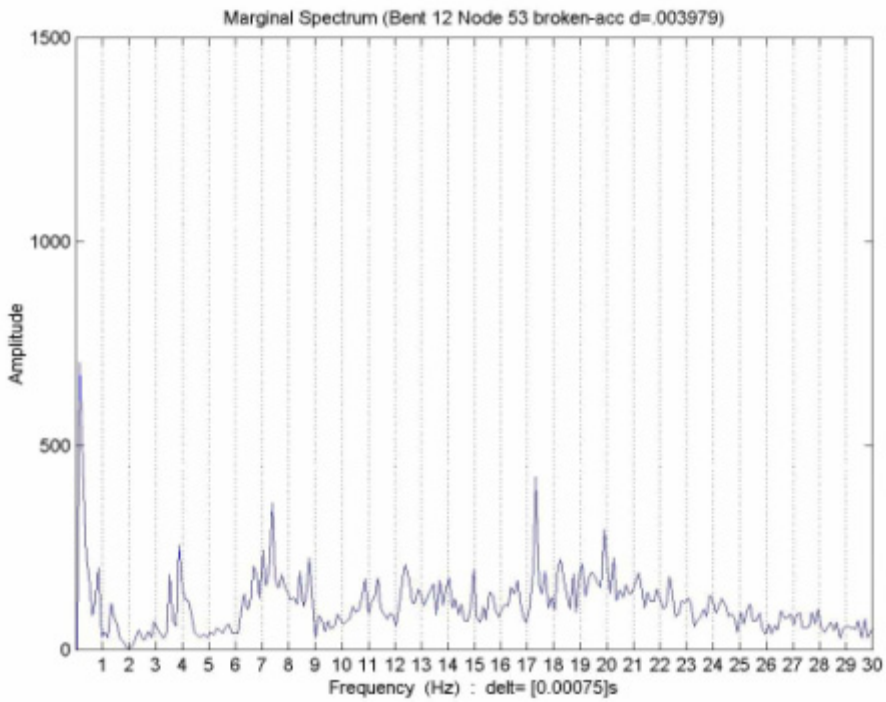


Figure 160. Graph. Spectra of marginal amplitude,  $d = 0.003979$ , bent 12, broken state, node 53.

## **SUMMARY OF HILBERT-HUANG TRANSFORM RESULTS**

The preliminary, initial study discussed in this chapter compares the HHT view of vibration records of bridge structures in their intact, excavated, and damaged (broken) pile states with traditional modal vibration analyses. The comparison shows that HHT-based signature recognition might be a means of identifying local dynamic properties. In addition, HHT analysis might be a means of determining differences in the signatures of local structural members. The HHT approach appears to identify local, nonlinear, and lower frequency responses of structural members to damage. A new concept of normalizing HHT response spectrum data to HHT force excitation data was shown to have possibilities for revealing modal vibration resonances and removing the effects of varying force excitation. Finally, a comparatively simple FEM showed theoretically that the HHT method identified natural frequencies of undamped systems readily, and the damped theoretical result was similar to actual experimental data. Further validation of HHT analysis is necessary, but if the approach proves successful, the need for a priori data for damage diagnosis could be reduced or even eliminated.



## CHAPTER 8. INTEGRATION OF DYNAMIC TESTING RESULTS TO BRIDGE MANAGEMENT SYSTEMS

### INTRODUCTION

A bridge management system must have a comprehensive bridge inventory that contains the number, type, size, and condition of each of the elements, the cost of maintenance and repair activities, and predictions for the future bridge conditions. Commonly used bridge management systems such as Pontis™ rely on subjective visual ratings to determine bridge element conditions. Recent research suggests that integrating NDE with visual ratings provide more consistent and richer bridge condition data.

Exploration of dynamic bridge substructure evaluation and monitoring systems has shown that bridge foundation vertical stiffness is an appropriate indicator for the bridge condition evaluation, and it can be used to support BMSs in three ways:

- Inventory: Identification of the type of bridge foundation as either pile, pile with cap, or spread footing is possible based on bridge foundation vertical stiffness.
- Condition evaluation and monitoring: Changes in bridge foundation vertical stiffness over time and after major events such as earthquakes, floods, and ship impacts can be tied to the need for corrective action or closing or posting the bridge to protect users. This would generally require a baseline signature for comparison, although the HHT method shows promise to identify differences on a comparative basis alone.
- Deterioration modeling: Historical data for a variety of bridge types help to assess the future costs and estimate the remaining service life of a bridge.

It is important to remember that a BMS is not a complete repository of bridge inspection-related data; however, it is valuable to think of a BMS as a framework that can be used to obtain the results. Hearn and Shim propose integrating NDE data with visual condition ratings to form an integrated condition state.<sup>(189)</sup> A hypothetical integrated condition state for a reinforced concrete bridge substructure is shown in table 17, which demonstrates the potential role of dynamic testing results in BMSs for assessments of bridge safety, scouring, and condition.

Table 17. Hypothetical integrated condition state for reinforced concrete substructure.

<b>Item/State</b>	<b>1 Protected</b>	<b>2 Exposed</b>	<b>3 Vulnerable</b>	<b>4 Attacked</b>	<b>5 Damaged</b>
Change in vertical stiffness	<10%		10% to 30%	30% to 50%	>50%
Foundation scour	Not present			Some	Significant
Foundation movement	Not present			Some	Significant
Corrosion	No activity		Possible corrosion	Corrosion activity	Loss of rebar section
Fracture	No activity		Some cracking	Cracking and delamination	Spalls
Action	No action		Observe	Post load limit, reinforce, replace	Close bridge, rehabilitation, replace

## THE ROLE OF NDE IN A BMS

Because a BMS relies on bridge condition ratings to develop optimal decisions for repair, maintenance, and rehabilitation, NDE results can be used for BMS in two strategies. The first is to modify a BMS to account for the additional information from NDE data. The second is to use NDE data to either determine or modify the bridge condition rating before it is input into a BMS. Using either strategy requires careful consideration of the quality and reliability of NDE results, and the different types of information that NDE and visual ratings provide. In general, NDE data require interpretation before becoming information that can be used to make decisions.<sup>(145)</sup>

Hearn and Shim have developed a strategy for integrating NDE data into or with condition ratings instead of modifying a BMS to account for additional information from NDE data.<sup>(189)</sup> By reducing the reliance on visual inspection, the integrated condition ratings reflect the presence of aggressive agents, the stage in the deterioration process, and the existence of damage. The proposed condition ratings are integrated with a focus on the condition states that are mutually exclusive, detectable, defined by multiple attributes, correspond to maintenance repair actions, and indicative of severity but not extent of damage. Table 18 shows an example of the integrated condition states approach for a reinforced concrete element.

Table 18. Integrated condition states for a reinforced concrete element, modified from Hearn and Shim.<sup>(189)</sup>

		<b>1 Protected</b>	<b>2 Exposed</b>	<b>3 Vulnerable</b>	<b>4 Attacked</b>	<b>5 Damaged</b>
<b>Attributes</b>	Exposure/condition state	No ingress of chloride (Cl) ions	Cl ion ingress, concentration below threshold	Cl ion ingress, concentration at threshold	–	–
	Corrosion activity level	–	No corrosion activity	Possible corrosion activity	Corrosion activity	–
	Rebar damage	–	–	–	No loss in rebar area	Loss of rebar section
	Concrete damage	–	–	–	Delaminations and minor spalls	Large spalls
<b>NDE Measure</b>	Electrical resistance	High	Low			
	Specific ion probe	Low Cl		High Cl		
	Corrosion current	Low			High	
	Impact echo, radar, sounding	No damage				Damage

Similarly, Hadavi suggests the use of NDE results to quantitatively measure condition states, which can be compared with a standard that uniquely determines the repair or maintenance strategy.<sup>(127)</sup>

### THE ROLE OF DYNAMIC TESTING RESULTS IN A BMS

Dynamic bridge substructure evaluation and monitoring provide bulk properties of the bridge substructure in terms of stiffness or flexibility, and they measure downward natural frequency shifts associated with damage.<sup>(4)</sup> The bridge foundation vertical stiffness could be used in the future at an aggregate level for monitoring the changes of the bridge foundation conditions such

as stiffness or flexibility versus a baseline signature. Knowledge of the bridge foundation type and depth to a large extent may be obtained with surface and borehole NDE methods.<sup>(27)</sup>

Based on the identification of the bridge foundation type and depth and evaluation of the bridge foundation condition as sound or damaged with reduced capacity, the inventory of the bridges, particularly of those with unknown foundations, can be completed to assist in better decisions on overall bridge management strategy. Currently, Pontis does not differentiate between pile caps and footings, but it does distinguish pile caps and piles as well as footings and piles.

Changes in bridge foundation vertical stiffness from the baseline condition indicating either substructure damage or loss of bearing capacity, or both, should be an effective indicator for repairs or other actions, such as the posting of weight restrictions.<sup>(189)</sup> Experience with the limited set of bridges in this project and experience gained on drilled shaft foundations suggest that when the changes in bridge foundation vertical stiffness are greater than the threshold values to be determined in the future (hypothetical data shown in table 19), the appropriate actions should be taken. The suggested hypothetical threshold values are based on limited research data, and further investigation is needed to determine their appropriateness. Furthermore, research is needed on the HHT frequency shifts that indicate damage. The suggested threshold values most likely are conservative. The use of threshold values is applicable to both long-term monitoring and short-term evaluation after an event such as an earthquake, barge collision, or huge flood. Consequently, catastrophic failure could be avoided. Prevention of catastrophic failure means saving lives, saving time by avoiding detours and reconstruction, and preserving the existing investment in the bridges.

Table 19. Hypothetical thresholds for action.

<b>Foundation State and Change in Bridge Foundation Vertical Stiffness from Baseline</b>	<b>Action</b>
Sound < 10%	None
Questionable 10% to 20%	Regular observation/continuous monitoring
Poor/Damage > 20%	Action required ranging from reinforcement/repair to immediate action such as closing bridge depending on the severity of the vertical foundation stiffness reduction

## INTEGRATION OF DYNAMIC TESTING RESULTS INTO A BMS

Before dynamic bridge substructure evaluations can be widely adopted, additional experimentation and evaluation are required. Several practical issues also must be addressed and a data-collection strategy must be developed.

### Experimentation

Additional experimentation is required to further develop the correlation between NDE attributes and bridge substructure conditions and explore field data quality. The NDE attributes are not necessarily direct measures of the bridge substructure conditions. Instead, the NDE attributes are simply indicators of performance of the tested structures.<sup>(190)</sup> The limited experimental results of this research suggest that the use of bridge foundation vertical stiffness and possibly the HHT method to identify frequency shifts are appropriate measures of performance of the bridge substructure; additional experimentation is required to confirm the relationships among bridge foundation vertical stiffness, HHT spectrum results, and bridge substructure load-carrying capacity, element condition, and remaining life. Because no other objective and quantitative measures of bridge substructure conditions exist, expert judgment is required. The HHT method may offer more accurate identification of weakened and damaged bridge foundations than the stiffness approach if the HHT method can be implemented on a comparative basis without having a sound bridge signature for comparison.

The limited sample of bridges used in this project did not permit any evaluation of field data quality. Hearn and Shim point out the need to explore accuracy and variability (repeatability) when using NDE.<sup>(189)</sup> Because bridge foundation vertical stiffness will not be monitored continuously, change must be distinguished from inherent variability. Recognizing that a change in bridge foundation vertical stiffness is a realization of a random variable, one may assume that different probability density functions are applicable to damaged and undamaged substructures, as shown in figure 161.

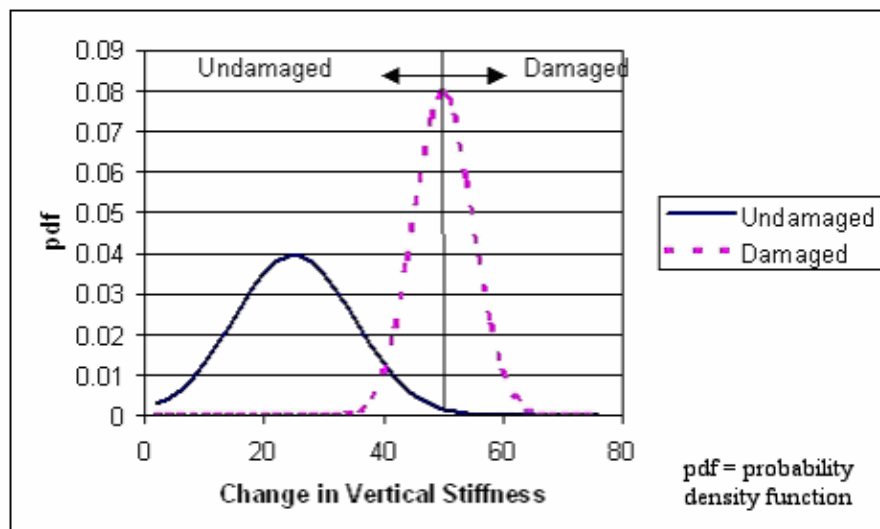


Figure 161. Graph. Hypothetical probability density functions for percent change in vertical stiffness.

## Evaluation of NDE Methods

Cost/benefit analysis of an NDE method requires understanding the value of information obtained from the NDE method and the cost of the NDE data collection. This also involves developing strategies to select an NDE method to identify vulnerable bridges. Other important issues are the role of complementary versus competing data and opportunities for sensor fusion. One technique for evaluation of an NDE method is to use an influence diagram for the expected life cycle cost for the bridge with and without the NDE data.<sup>(191)</sup> While this is not easy, it does provide some important insights into the value of an NDE. Prine identifies the need to address several practical issues:<sup>(192)</sup>

- **Accessibility.** The size and configuration of a bridge mean that not all parts of the bridge are physically accessible and the field data cannot necessarily be collected at the most desirable locations because of disruption to traffic and safety issues.
- **Environment.** Field environments can be very harsh. Changes in temperature, vibration, and noise can all have significant effect on field data-collection efforts that may not be identified in the laboratory.
- **Training of operators.** The correct operation of equipment is critical to the success of the field data-collection effort. This can be accomplished through training and certification of operators, including ongoing education.

## Developing Data-Collection Strategy

Federal mandates require visual inspection of all bridges on the Federal-aid system every 2 years. Because NDE is not mandated, a recommended data-collection frequency must be determined. This provides an opportunity to design a data-collection strategy that reflects the need for NDE data. The strategy will identify the following information:

- Bridges to be inspected (on the basis of type of bridge, age, or vulnerability).
- Frequency of dynamic testing (on the basis of the expected rate of progression of deterioration or the occurrence of major events).
- Other types of testing that may complement the dynamic testing.
- Relationship to visual inspection and other NDE.<sup>(193)</sup>

## SUMMARY

Dynamic bridge substructure evaluation and monitoring provide some important opportunities for improving bridge management systems and enhancing the current state of the art in bridge evaluation and monitoring. Specifically, measures of dynamic bridge foundation vertical stiffness or HHT results, or both, that identify downward frequency shifts indicating damage show promise in the following applications:

- Monitoring bridge substructure conditions and assessing the remaining life of a bridge.
- Assessing the effect of major events such as barge collisions, floods, and earthquakes on bridge substructure integrity.
- Aiding the development of deterioration models for bridge substructures.

In conclusion, recent research on the role of NDE in BMSs suggests the desirability of integrating dynamic testing results, including HHT results, with visual ratings data.



## **CHAPTER 9. CONCLUSIONS AND RECOMMENDATIONS**

### **FIELD MODAL VIBRATION DYNAMIC TESTING FOR DAMAGE**

The results of flexibility TF measurements of Trinity Relief Bridge bent 12 (piles only) and bent 2 (piles plus footing pile cap) are discussed in chapter 5 for intact, excavated (simulated flood scour damage), and broken (simulated earthquake damage) pile cases. The TF results showed distinct and clear increases in flexibility and lower natural first vertical mode fundamental resonant frequencies with increasing damage. Because flexibility is the inverse of stiffness, increases in flexibility of more than 50 percent correspond to greater than 50 percent reductions in stiffness.

The flexibility results show promise for helping directly identify substructure damage if a baseline of the sound response of a bridge has been determined above all critical members. The damage will be indicated by a comparatively small decrease in natural frequency and a larger increase in flexibility (corresponding decrease in stiffness) using traditional modal testing and analysis techniques. This result is not surprising—it is theoretically predicted, and in a sense a flexibility modal TF test is a dynamic load test. It is expected that more complicated substructures where loading cannot be close to the damaged member would not show as much of an effect in the flexibility results. The drawbacks of this flexibility TF approach are the need to put sensors on critical members and test before damage to obtain a basis of comparison by which to judge and identify the extent of damage in future tests. This method does seem to show real promise for determination of damage if before-and-after modal vibration measurements can be performed.

### **FIELD MODAL VIBRATION DYNAMIC TESTING FOR SHALLOW VERSUS DEEP FOUNDATION DETERMINATION**

As discussed in chapter 5, dynamic tests were conducted on the Woodville Road Bridge (shallow footing foundations) and Old Reliance Road Bridge (footing pile cap on steel BP piles) to investigate whether modal vibration testing could differentiate between shallow and deep foundation systems for otherwise almost identical bridges. Although the two bridges had similar modal response signatures, their modal resonant frequencies were substantially different; however, the first vertical mode resonant peak for Old Reliance Bridge with the steel piles was not at a significantly higher frequency (9 Hz) than the first vertical mode resonant peak for Woodville Road Bridge (10 Hz). This result was contrary to the expected results—that the Old Reliance Road Bridge with the steel piles plus pile cap would show greater stiffness, and therefore a higher frequency for the peak of the first vertical mode.

It is interesting that the flexibilities, and inversely, the stiffness magnitudes, were similar for the two bridges. The first three resonant peaks for Old Reliance Road Bridge were all at lower frequencies than the corresponding resonant peaks for the Woodville Road Bridge. Considering these initial results, it appears doubtful that modal testing could uniquely and clearly determine shallow versus deep foundations without having otherwise identical bridge structures situated in similar soils. It further appears that at least one of the foundations tested should have a known shallow or deep foundation system to serve as the basis against which unknown foundation

systems could be judged. It is extremely unlikely that modal testing could determine unknown depths of foundations for scour safety evaluation.

## **STRUCTURAL MODELING AND PARAMETER ESTIMATION**

As discussed in chapter 6, considerable effort was devoted to determining changes in foundation stiffness through structural modeling and parameter estimation. Unfortunately, the structural parameter estimation approach did not find a consistent, correct solution to the intact versus excavated versus broken pile cases. The modal vibration data quality was as high as could reasonably be expected, but the parameter estimation ultimately was unable to resolve the basic case of the first vertical mode of vibration. Considering the effort required and complexity of this approach, it does not seem suitable for bridge substructure damage detection at this time. The fundamental problem may be that the effects of the foundation damage are too small for parameter estimation, and they are buried in the overall modal response of the structure.

## **HILBERT-HUANG TRANSFORM FOR EVALUATION OF BRIDGE SUBSTRUCTURE DAMAGE**

The completion of this research was delayed in part to evaluate the potential of the HHT to indicate the presence of damaged substructure foundations. Specifically, HHT analysis was used to identify, by decreases in frequencies, nonlinear responses that indicate damage. HHT analysis shows promise in being able to identify damage comparatively in conjunction with modal vibration testing without a structure having been tested before the damage occurs. The HHT results and comparisons with the traditional modal and wavelet analysis method suggest the following findings:

- Conventional methods in structural damage diagnosis are found to be both less effective and sensitive than the HHT method is for signature recognition of certain types of structural damage such as the excavated and broken piles used in the study. While this conclusion needs further validation, the HHT results showed the expected decrease in frequency associated with damaged foundation states. Furthermore, normalization of the Hilbert spectrum of the accelerometer response by the Vibroseis excitation force showed the larger amplitudes at the stronger second and third vertical mode resonant frequencies identified by the modal vibration tests. The weak first vertical mode resonant frequency in the acceleration TFs was not apparent in the HHT results. Integration of the acceleration data to velocity or displacement data in the time domain likely would have made the first mode resonance more apparent in the force-normalized HHT Hilbert spectrum.
- Based on these promising results, an HHT-based method for structural damage diagnosis is proposed. If the effectiveness of the proposed HHT method is further confirmed, the method would have at least two unique features:
  - Only a few sensors (two in general) and no a priori data from an undamaged structure would be needed, which would make data collection simple and cost effective.

- Because the HHT method reveals the temporal-frequency energy of various intrinsic oscillation modes, a damage diagnosis would be sensitive to the local damage associated with intrinsic oscillation modes.

The following novel signature recognition technique based on modal vibration testing with HHT analysis is proposed for structural health monitoring and damage detection:

1. Two or more similar structural members such as two of four bridge piles with the same size, cross-section, and materials are selected for a nondestructive vibration test. A sensor (an accelerometer) is mounted on each pile. The piles are subjected to a dynamic excitation acting at a location close to, but not on, the piles. A computer data acquisition system digitizes and stores the sensors' response to the excitation. This results in two sets of data and either modal or spectral data from which to determine resonant frequencies with traditional methods to aid in interpreting the HHT results.
2. For the HHT analysis, the two data sets are decomposed in the EMD process into a number of IMF components, which are used to compute the Hilbert spectrum. The driving frequency, natural frequency, and other frequency contents can be identified partially, if not completely, by analyzing the Hilbert spectra and the IMF components.
3. If the natural frequencies of the two members are different, the member with the lower frequency has damage while the other is comparatively sound, or the former has more severe damage than the latter. On the other hand, if the frequencies are the same, both members are either undamaged or damaged to the same degree. For the result of identical frequencies, the testing will be repeated with a third member involved. It is always better to have a priori data from testing the same structure before a damaging event (such as flooding or an earthquake) to use as a baseline.
4. After identifying the damaged member and if access permits, the excitation is exerted at different locations on the damaged member and a series of vibration data sets are recorded at one sensor location.
5. The data from step 4 are analyzed as in step 2.
6. If one of the data sets shows the lowest natural frequency of the member, the location of the pertinent excitation is at or close to the damaged location.

The first three steps were explained in chapter 7 in the analysis of the in situ data from the bents of the Trinity River Relief Bridge. The reasons for the last three steps are given in this paragraph. When the excitation is acting directly on the damaged location, the effect on the structure at that location will be the strongest. Even if the load is small and well within the design range, the damaged member could have nonlinear responses, that is, responses characterized by lower natural frequencies resulting from local damage. On the other hand, if the excitation acts neither directly on nor close to the damaged spot, the vibration responses of the structure could remain elastic and linear. Because HHT analysis can identify the instantaneous frequency of data, the damaged location can be found by identifying the lowest natural frequency of vibration from the series of data sets.

## **IMPLEMENTING DYNAMIC TESTING RESULTS IN BRIDGE MANAGEMENT SYSTEMS**

As discussed in chapter 8, dynamic bridge substructure evaluation and monitoring provides important opportunities for improving a BMS and enhancing the current state of the art in bridge evaluation and monitoring. Specifically, measures of dynamic bridge foundation vertical stiffness or HHT results, or both, that identify downward frequency shifts indicating damage show considerable promise for the following uses:

- Monitoring bridge substructure conditions and assessing the remaining life of a bridge.
- Assessing the effect of major events such as barge collisions, floods, and earthquakes on bridge substructure integrity.
- Aiding the development of deterioration models for bridge substructures.

In conclusion, recent research on the role of NDE in BMSs suggests the desirability of integrating dynamic testing results, including HHT results, with visual ratings data.

### **RECOMMENDATIONS FOR RESEARCH**

In the research described in this paper, modal vibration testing and the HHT approach appear to have successfully identified the effects of damage to concrete pile and concrete pile plus pile cap deep foundations; however, particularly for the HHT method, it must be emphasized that only limited studies have been performed to date and further research is necessary to understand, validate, and apply the combined approach of modal or spectral vibration testing (or both) and the HHT method. Because it appears capable of identifying local, short-duration, lower frequency responses indicative of nonlinear and nonstationary damage to local structural members, the HHT method has real potential for detecting damage to bridge structures and substructures after catastrophic events such as floods, earthquakes, and collisions. Future research also should address the issue of how the vibration and HHT approach could be implemented in a BMS.

## REFERENCES

1. Lagasse, P.F., P.L. Thompson, and S.A. Sabol (1995) "Guarding Against Scour," *Civil Engineering Magazine*, 65(6), 56–59.
2. Egri, R., G. Henderson, A. Lichtenstein, S. Madanat, and K. Maser (1995) "Development of a Wireless Global Bridge Evaluation and Monitoring System: Literature Review," FHWA Contract No. DTFH61-94-C-00217.
3. Aktan, A.E., C. Chuntavan, K.L. Lee, and T. Toksoy (1993) "Structural Identification of a Steel-Stringer Bridge for Nondestructive Evaluation," *Transportation Research Record*, Number 1393, 1–36.
4. Olson, L.D., F. Jalinoos, and M.F. Aouad (1995) "Determination of Unknown Subsurface Bridge Foundations," Research Report NCHRP 21–5.
5. Huang, N.E., Z. Shen, S.R. Long, M.C. Wu, H.S. Shih, Q. Zheng, N-C. Yen, C.C. Tung, and H.H. Liu (1998) "The Empirical Mode Decomposition and Hilbert Spectrum for Nonlinear and Non-Stationary Time Series Analysis," *Proceedings of the Royal Society of London, A* 454, 903–995.
6. Bay, J.A., K.H. Stokoe II, and J.D. Jackson (1995) "Development of a Rolling Dynamic Deflectometer," *Transportation Research Record*, Number 1473, 43–54.
7. Chase, S.B. (1995) "FHWA NDE Contract Research, an Overview," Presentation at North American Workshop on Instrumentation and Vibration Analysis of Highway Bridges, Cincinnati, OH.
8. FHWA (2004) *Performance and Accomplishments Report*, Pub. No. FHWA-HPL-05-009, Washington, DC.
9. Cantieni, R. (1992) "Dynamic Behavior of Highway Bridges Under the Passage of Heavy Vehicles," Swiss Federal Laboratories for Materials Testing and Research, Dübendorf, Switzerland.
10. Richardson, E.V., and S.R. Davis (1995) *Evaluating Scour at Bridges*, Pub. No. FHWA-IP-90-017, Hydraulic Engineering Circular Number 18.
11. Chang, F.M. (1973) "A Statistical Summary of the Cause and Cost of Bridge Failures," FHWA-RD-75-87, FHWA, NTIS Number PB 224091, September.
12. Lagasse, P.F., C.F. Nordin, G.V. Sabol, and J.D. Schall (1991) "Scour Monitoring Devices for Bridges," *Transportation Research Record*, Number 1290, 281–294.
13. Meadowcroft, I.C., and J.E. Whitbread (1993) "Assessment and Monitoring of Bridges for Scour," *Proceedings of the Bridge Management 2nd International Conference*, Guildford, UK.

14. International Association for Bridge and Structural Engineering (IABSE) (1983) "Ship Collision with Bridges and Offshore Structures," Preliminary Report, IABSE Colloquium, Copenhagen, Denmark.
15. Subcommittee on Coast Guard and Navigation, U.S. House of Representatives (1993) "On the Safety of the Inland Tug and Barge Industry and Investigate the Circumstances Surrounding Two Fatal Bridge Accidents Involving this Industry," 103rd Congress.
16. Roeder, C., and S. Moorty (1992) "Thermal Movements in Bridges," *Transportation Research Record*, Number 1290, Transportation Research Board, National Research Council, Washington, DC, 135–143.
17. Raghavendrachar, M., and A.E. Aktan (1992) "Flexibility by Multi-Reference Impact Testing for Bridge Diagnostics," *Journal of Structural Engineering*, American Society of Civil Engineers (ASCE), 2186–2203.
18. Aktan, A.E., and A.J. Helmicki (1995) "Instrumentation, Testing, and Monitoring of Reinforced Deck-on-Steel Girder Bridges: Mid-Term Project Report," Report No. UC-CII94, FHWA/ODOT Contract No. 7665, College of Engineering, University of Cincinnati, OH.
19. Shelley, S.J., K.L. Lee, T. Aksel, and A.E. Aktan (1995) "Active Control and Forced Vibration Studies on a Highway Bridge," *Journal of Structural Engineering*, ASCE, 121(9), 1306–1312.
20. Warren, G.E., and L.J. Malvar (1993) "Structural Assessment of Reinforced Concrete Piers Using the Impact Load Method," Proceedings of the International Conference on Nondestructive Testing of Concrete in the Infrastructure, Dearborn, MI, 378–390.
21. Eberhard, M.O., G. Hjartarson, J.A. MacLardy, and M.L. Marsh (1993) *Lateral-Load Response of a Reinforced Concrete Bridge*, WA-RD 305.2. Final Report, U.S. Department of Transportation, Washington, DC.
22. Pierce, C.E., and C.H. Dowding (1995) *Long-Term Monitoring of Bridge Pier Integrity with Time Domain Reflectometry Cables*, Northwestern University, Evanston, IL.
23. Sandford, T.C., and M. Elgaaly (1993) "Skew Effects on Backfill Pressures at Frame Bridge Abutments," *Transportation Research Record*, Number 1415, Transportation Research Board, Washington, DC, 1–11.
24. Hussein, M., G. Likins, and G.G. Goble (1993) "Determination of Pile Lengths Under Existing Structures," Deep Foundations Institutes' 17th Annual Members Conference, New Orleans, LA.
25. Finno, J.R., and J.P. Prommer (1994) *Evaluation of Inaccessible Drilled Shafts Using the Impulse Response Method*, ITI Technical Report #3, Northwestern University, Evanston, IL.

26. Chen, S., and Y.R. Kim (1996) "Condition Assessment of Marine Timber Piles Using Stress Wave Method," *Building an International Community of Structural Engineers*, Proceedings of the Structures Congress XIV, 2, 853–860.
27. Olson, L.D., and M.F. Aouad (2001) *Unknown Subsurface Bridge Foundation Testing*, NCHRP 21-5(2), Final Report.
28. Halling, M.W., I. Muhammad, and K.C. Womack (2001) "Dynamic Field Testing for Condition Assessment of Bridge Bents," *Journal of Structural Engineering*, Vol. 127(2), 161–167.
29. Ewins, D.J. (1985) *Modal Testing: Theory and Practice*, John Wiley, NY.
30. Bakht, B., and L. Jaeger (1990) "Bridge Testing—A Surprise Every Time," *Journal of Structural Engineering*, ASCE, 116(5), 1370–1383.
31. Aktan, A.E., R. Miller, B. Shahrooz, M. Zwick, M. Heckenmueller, I. Ho, W. Hrinko, and T. Toksoy (1992) *Nondestructive and Destructive Testing of a Reinforced Concrete Slab Bridge and Associated Analytical Studies*, Report No. FHWA/OH-93/017 and UC-CII 92/02. ODOT Contract No.14482, College of Engineering, University of Cincinnati, Cincinnati, OH.
32. Woodward, C., J. Minor, K. White, and R. Idriss (1994) "Nondestructive Evaluation of Fracture Critical Bridge," *Structural Materials Technology*, Proceedings of the Nondestructive Testing Conference, Atlantic City, NJ.
33. Farrar, C.R., W.B. Baker, T.M. Bell, K.M. Cone, T.W. Darling, T.A. Duffey, A. Eklund, and A. Migliori (1994) *Dynamic Characterization and Damage Detection in the I-40 Bridge over the Rio Grande*, Los Alamos Report LA-12767-MS UC-906, Los Alamos, NM.
34. Salane, H.J., J.W. Baldwin, and R. Duffield (1981) "Dynamics Approach for Monitoring Bridge Deterioration," *Transportation Research Record*, Number 832, 21–28.
35. Cawley, P., and R.D. Adams (1979) "The Location of Defects in Structures from Measurements of Natural Frequencies," *Journal of Strain Analysis*, 4(2), 49-57.
36. Manning, D.G. (1985) "Detecting Defects and Deterioration in Highway Structures," *NCHRP Synthesis of Practice No. 118*.
37. DeWolf, J., D.A. Bagdasarian, and P.N. O'Leary (1992) "Bridge Condition Assessment Using Signatures," *Nondestructive Evaluation of Civil Structures and Materials*, Conference sponsored by the FHWA and the National Science Foundation, Boulder, CO, 171-179.
38. Huston, D., and M.G. Gardner-Morse (1993) "Modal Identification of Cable-Stayed Pedestrian Bridge," *Journal of Structural Engineering*, ASCE, 119(11), 3384-04.

39. Gregory, A.E., N.C. Yang, and R.C.Y. Young (1985) "Bridge Inspection by Dynamic Loading Technique," Proceedings of the ASCE National Convention, Denver, CO.
40. Mazurek, D., and J. DeWolf (1990) "Experimental Study of Bridge Monitoring Technique," *Journal of Structural Engineering*, ASCE, 116(9), 2532-49.
41. Biswas, M., A.K. Pandey, and M.M. Samman (1990) "Diagnostic Experimental Spectral/Model Analysis of a Highway Bridge," *International Journal of Analytical and Experimental Modal Analysis*, 5, 33-42.
42. Salawu, O.S., and C. Williams (1995a) "Bridge Assessment Using Forced-Vibration Testing," *Journal of Structural Engineering*, ASCE, 121(2), 161-173.
43. Alampalli, S., and G. Fu (1994) "Instrumentation of Remote and Continuous Monitoring of Structure Conditions," Transportation Research Board preprint No. 94-0261.
44. Baumgartner, W., and H. Waubke (1993) "Service Life Estimation of Bridges," Proceedings of the Bridge Management 2nd International Conference, Guildford, UK.
45. Hart, G.C., and J.T.P. Yao, (1977) "System Identification in Structural Dynamics," *Journal of Engineering Mechanics Division*, ASCE, 103(EM6), 1089-104.
46. Liu, S.C., and J.T.P. Yao (1978) "Structural Identification Concept," *Journal of Structural Division*, ASCE, 104(ST12), 1845-858.
47. Mottershead, J.E., and M.I. Friswell (1993) "Model Updating in Structural Dynamics: A Survey," *Journal of Sound and Vibration*, 167(2), 347-75.
48. Ghanem, R., and M. Shinozuka (1995) "Structural-System Identification. I: Theory," *Journal of Engineering Mechanics*, ASCE, 121(2), 255-264.
49. Shinozuka, M., and R. Ghanem (1995) "Structural System Identification. II: Experimental Verification," *Journal of Engineering Mechanics*, ASCE, 121(2), 265-273.
50. Doebling, S.W., C. R. Farrar, M.B. Prime, and D.W. Shevitz, (1996) *Damage Identification and Health Monitoring of Structural and Mechanical Systems from Changes in their Vibration Characteristics: A Literature Review*, Report LA: I3070-MS, Los Alamos National Laboratory, Los Alamos, NM.
51. Sanayei, M., and R.B. Nelson (1986) "Identification of Structural Element Stiffnesses From Incomplete Static Test Data," Society of Automotive Engineers Technical Paper Series, SAE-861793, 7.1248-7.1248.
52. Sanayei, M., and O. Onipede (1991) "Damage Assessment of Structures Using Static Test Data," *American Institute of Aeronautics and Astronautics Journal*, 29(7), 1174-1179.

53. Hajela, P., and F.J. Soeiro (1990b) "Structural Damage Detection Based on Static and Modal Analysis," *American Institute of Aeronautics and Astronautics Journal*, 28(9), 1110–1115.
54. Banan, Mo.R., and K.D. Hjelmstad (1993) *Identification of Structural Systems from Measured Response*, Report No. SRS 579, UILU-ENG-93-2002, University of Illinois at Urbana-Champaign, Urbana, IL.
55. Banan, Mo.R., Ma.R. Banan, and K.D. Hjelmstad, (1994a) "Parameter Estimation of Structures from Static Response, Part I: Computational Aspects," *Journal of Structural Engineering*, ASCE, 120(11), 3243–3258.
56. Banan, Mo.R., Ma.R. Banan, and K.D. Hjelmstad (1994b) "Parameter Estimation of Structures from Static Response, Part II: Numerical Simulation Studies," *Journal of Structural Engineering*, ASCE, 120(11), 3259–3283.
57. Bruno, R.J. (1994) "Identification of Nonlinear Joints in a Truss Structure," Proceedings of the American Institute of Aeronautics and Astronautics (AIAA)/American Society of Mechanical Engineers (ASME) Adaptive Structures Forum, Hilton Head, SC, 402–410.
58. Warren, G.E., and L.J. Malvar (1995) "Evaluation of Permanent Monitoring Sensors on Navy Piers," Proceedings of the ASCE Structures Congress XIII, Boston, MA, 28–43.
59. Sanayei, M., and M.J. Saletnik, (1996a) "Parameter Estimation of Structures from Static Strain Measurements; I: Formulation," *Journal of Structural Engineering*, ASCE, 122(5), 555–562.
60. Ibrahim, S.R., and E.C. Mikulcik (1977) "A Method for the Direct Identification of Vibration Parameters from the Free Response," *Shock and Vibration Bulletin*, Number 47, Part 4, 183–198.
61. Ibrahim, S.R., and R.S. Pappa (1982) "Large Modal Survey Testing Using the Ibrahim Time Domain Identification Technique," *Journal of Spacecraft*, 19(5), 459–465.
62. Seibold, S., and C.P. Fritzen (1991) "Recursive Identification of Nonlinear Systems by Means of the Extended Kalman Filter," Proceedings of the 9th International Modal Analysis Conference, Florence, Italy, 802–809.
63. Hjelmstad, K.D., Mo.R. Banan, and Ma.R. Banan (1995) "Time-Domain Parameter Estimation Algorithm for Structures I: Computational Aspects," *Journal of Engineering Mechanics*, ASCE, 121(3), 424–434.
64. Goodwin, G.C., and R.L. Payne (1977) *Dynamic System Identification: Expert Design and Data Analysis*, Academic Press, Inc., New York, NY.
65. Baruch, M. (1982) "Optimal Correction of Mass and Stiffness Matrices Using Measured Modes," *American Institute of Aeronautics and Astronautics Journal*, 20(11), 1623–1626.

66. Berman, A., and E.J. Nagy (1982) "Improvements of a Large Analytical Model Using Test Data," *American Institute of Aeronautics and Astronautics Journal*, 21(8), 1168–1173.
67. Chen, J.C., J.A. Garba, and L.F. Pertti (1987) "Spacecraft Structural Model Improvement by Modal Test Results," *Journal of Spacecraft and Rockets*, 24(1), 90–94.
68. Collins, J.D., G.C. Hart, T.K. Hasselman, and B. Kennedy (1974) "Statistical Identification of Structures," *American Institute of Aeronautics and Astronautics Journal*, 12(2), 185–190.
69. Kabe, A.M. (1985) "Stiffness Matrix Adjustment Using Mode Data," *American Institute of Aeronautics and Astronautics Journal*, 23(9), 1431–1436.
70. Beck, J.L., and P.C. Jennings (1980) "Structural Identification Using Linear Models and Earthquake Records," *Earthquake Engineering and Structural Dynamics*, 8, 145–160.
71. Natke, H.G., and J.T.P. Yao, eds (1988) *Structural Safety Evaluation Based on System Identification Approaches*, Friedrick Vieweg & Son, Wiesbaden, Germany.
72. Stubbs, N., and R. Osegueda (1990a) "Global Non-Destructive Damage Evaluation in Solids," *International Journal of Analytical and Experimental Modal Analysis*, 5(2), 67–79.
73. Stubbs, N., and R. Osegueda (1990b) "Global Damage Detection in Solids—Experimental Verification," *International Journal of Analytical and Experimental Modal Analysis*, 5(2), 81–97.
74. Kim, J.T., and N. Stubbs (1995) "Damage Detection in Offshore Jacket Structures from Limited Modal Information," *International Journal of Offshore and Polar Engineers*, 5(1), 58–66.
75. Dascotte, E. (1991) "Applications of Finite Element Tuning Using Experimental Modal Data," *Journal of Sound and Vibration*, 25(6), 22–26.
76. Smith, S.W., and C.A. Beattie (1991) "Optimal Identification Using Modal Data," Proceedings of the SDM Conference, American Institute of Aeronautics and Astronautics-91-0948-CP, 2319–2324.
77. Chen, G.S., and B.J. Lurie (1992) "Active Member Bridge Feedback Control for Damping Augmentation," *Journal of Guidance, Control, and Dynamics*, 15(5), 1155–1160.
78. Fritzen, C.P., and S. Zhu (1991) "Updating the Finite Element Models by Means of Measured Information," *Computers & Structures*, Vol. 40(2), 475–486.
79. Gornshteyn, I. (1992) "Parameter Identification of Structures Using Selected Modal Measurements," M.S. Thesis No. 4340, Tufts University, Medford, MA.

80. Liu, P.L. (1995) "Identification and Damage Detection of Trusses Using Modal Data," *Journal of Structural Engineering*, ASCE, 121(4), 599–608.
81. Farrar, C.R., T.A. Duffey, P.A. Goldman, D.V. Jauregui, and J.S. Vigil (1996) *Finite Element Analysis of the I-40 Bridge over the Rio Grande*, Los Alamos National Laboratory, LA-12979-MS, Los Alamos, NM.
82. Yao, G.C., K.C. Chang, and G.C. Lee (1992) "Damage Diagnosis of Steel Frames Using Vibrational Signature Analysis," *Journal of Engineering Mechanics*, ASCE, 118(9), 1949–1961.
83. Li, D., H. Zhung, and B. Wang (1989) "The Principle and Technique of Experimental Strain Modal Analysis," Proceedings of the 7th International Modal Analysis Conference (IMAC), Society for Experimental Mechanics (SEM), 1285–1289.
84. Wu, X., J. Ghaboussi, and J.H. Garrett, Jr. (1992) "Use of Neural Networks in Detection of Structural Damage," *Computers and Structures*, 42(4), 649–659.
85. Masri, S.F., T.K. Caughey, and A.G. Chassiakos (1993) "Identification of Nonlinear Dynamic Systems Using Neural Networks," *Journal of Applied Mechanics, Transactions*, ASME, 60(1), 123–133.
86. Shinozuka, M., E. Samaras, and A. Tsurui (1985) "ARMA Representation of Random Processes," *Journal of Engineering Mechanics*, ASCE, 111(3), 449–461.
87. Stubbs, N., J.T. Kim, and C.R. Farrar (1995) "Field Verification of a Nondestructive Localization and Severity Estimation Algorithm," Proceedings of the 13th International Modal Analysis Conference, Nashville, TN, 210–218.
88. Ross, T.J., H.C. Sorensen, S.J. Savage, and J.M. Carson (1990) "DAPS: Expert System for Structural Damage Assessment," *Journal of Computing in Civil Engineering*, ASCE, 4(4), 327–347.
89. Sanayei, M., and M.J. Saletnik (1996b) "Parameter Estimation of Structures from Static Strain Measurements; II: Error Sensitivity Analysis," *Journal of Structural Engineering*, ASCE, 122(5), 563–572.
90. Banan, Mo.R., Ma.R. Banan, and K.D. Hjelmstad (1995) "Time-Domain Parameter Estimation Algorithm for Structures. II: Numerical Simulation Studies," *Journal of Engineering Mechanics*, ASCE, 121(3), 435–447.
91. Haftka, R.T., and H.M. Adelman (1985) "Selection of Actuator Locations for Static Shape Control of Large Space Structures by Heuristic Integer Programming," *Computers & Structures*, 20(1–3), 575–582.
92. DeLorenzo, M.L. (1990) "Sensor and Actuator Selection for Large Space Structure Control," *Journal of Guidance*, 13(2), 249–257.

93. Hajela, P., and F.J. Soeiro (1990a) "Recent Developments in Damage Detection Based on System Identification Methods," *Structural Optimization*, 2, 1–10.
94. Kammer, D.C. (1991) "Sensor Placement for On-orbit Modal Identification and Correlation of Large Space Structures," *American Institute of Aeronautics and Astronautics Journal*, 14(2), 251–259.
95. Holnicki-Szulc, J., F. Lopez-Almansa, and J. Rodellar (1993) "Optimal Location of Actuators for Active Damping of Vibration," *American Institute of Aeronautics and Astronautics Journal*, 31(7), 1274–1279.
96. Lim, T.W. (1991) "Structural Damage Detection Using Modal Test Data," *American Institute of Aeronautics and Astronautics Journal*, 29(12), 2271–2274.
97. Sanayei, M., O. Onipede, and S.R. Babu, (1992) "Selection of Noisy Measurement Locations for Error Reduction in Static Parameter Identification," *American Institute of Aeronautics and Astronautics Journal*, 30(9), 2299–2309.
98. Sanayei, M., and M.J. Saletnik (1995) "Design of Nondestructive Tests for Health Monitoring of Structures," Proceedings of the ASCE Structures Congress XIII, ASCE, Boston, MA, 684–687.
99. Brown, C.B. (1987) "Jaynes, Bayes and Fuzzy Identification," *Civil Engineering Systems*, September, Vol. 4, 142–146.
100. Beck, J.L. (1989) "Statistical System Identification of Structures," Proceedings of the 5th International Conference on Structural Safety and Reliability, 1395–1402.
101. Gangadharan, S.N., R.T. Haftka, and E. Nikolaidis (1991) "Probabilistic System Identification of Two Flexible Joint Models," *American Institute of Aeronautics and Astronautics Journal*, 29(8), 1319–1326.
102. Newmark, N.M., and E. Rosenblueth (1971) *Fundamentals of Earthquake Engineering*, Prentice-Hall, New Jersey.
103. Bertero, V.V., and B. Bresler (1971) *Developing Methodologies for Evaluating the Earthquake Safety of Existing Buildings*, Report No. UCB 71-13, University of California, Berkeley, CA.
104. Banon, H., and D. Veneziano (1982) "Seismic Safety of Reinforced Concrete Members and Structures," *Earthquake Engineering and Structural Dynamics*, Vol. 10, 170–193.
105. Park, Y.J., and A.H.S. Ang (1985) "Mechanistic Seismic Damage Model for Reinforced Concrete," *Journal of Structural Engineering*, ASCE, 111(4), 740–757.
106. Stephens, J.E., and J.T. Yao (1987) "Damage Assessment Using Response Measurements," *Journal of Structural Engineering*, ASCE, 113(4), 787–801.

107. Yao, J.T.P., and W.H. Munse, (1962) "Low-Cycle Fatigue Behavior of Mild Steel," Special Technical Publication Number 338, American Society for Testing and Materials, Philadelphia, PA.
108. Chung, Y.S., C. Meyer, and M. Shinozuka (1988) "Damage Model for Reinforced Concrete, Seismic Engineering Research and Practice," Proceedings of the 1989 ASCE Structures Congress, San Francisco, CA, 478–487.
109. DiPasquale, E., J.W. Ju, A. Askar, and A.S. Cakmak (1990) "Relation Between Global Damage Indices and Local Stiffness Degradation," *Journal of Structural Engineering*, ASCE, 116(5), 1440–1456.
110. Pandey, P.C., and S.V. Barai (1994) "Sensitivity-Based Weighted-Average in Structural Damage Assessment," *Journal of Performance of Constructed Facilities*, 8(4), 243–263.
111. Farrar, C.R., and K.M. Cone (1995) "Vibration Testing of the I-40 Bridge Before and After the Introduction of Damage," Proceedings of the 13th International Modal Analysis Conference, Nashville, TN. Published in cooperation with SPIE, Vol. 2460, 203–209.
112. Mayes, R.L. (1995) "An Experimental Algorithm for Detecting Damage Applied to the I-40 Bridge over the Rio Grande," Proceedings of the 13th International Modal Analysis Conference, Nashville, TN, 219–225.
113. Reese, L.C., and K.H. Stokoe II, (1988) "Instrumentation for Tests of Piles Subjected to Axial Loading," *Transportation Research Record*, 1169, 33–42.
114. Richart, Jr., F.E. and R.V. Whitman (1967) "Comparison of Footing Vibration Tests with Theory," *Journal of the Soil Mechanics Division*, ASCE, 93(SM6), 143–165.
115. Samtani, N.C., J. Wang, F. Pepe, and M.J. Abrahams (1994) "Horizontal and Vertical Movements of Bridge Piers Subjected to Ship Impact," Proceedings of the Vertical and Horizontal Deformations of Foundations and Embankments, ASCE, College Station, TX, 245–257.
116. Norman, A., I. Cannon, and L. Asch (1989) "The History and Future of Safety Monitoring in Liquid Rocket Engines," AIAA Technical Paper, 89–2410.
117. Pau, L.F. (1989), *Failure Diagnosis and Performance Monitoring*, Marcel Dekker, Inc., New York, NY.
118. Patton, R., P. Frank, and R. Clark (1989) *Fault Diagnosis in Dynamic Systems*, Prentice-Hall, Englewood Cliffs, NJ.
119. Willsky, A.S. (1976) "A Survey of Design Methods for Failure Detection in Dynamic Systems," *Automatica*, 12, 601–611.
120. "Pontis, Version 2.0 Technical Manual," FHWA (1994) Report No. SA-94-031.

121. Czepiel, E. (1995) "Bridge Management Systems Literature Review and Search," ITI Technical Report No. 11, Northwestern University, Evanston, IL.
122. FHWA (2004), *Milepost 2004*, Pub. No. FHWA-HPL-05-012, Washington, DC.
123. Public Law 104-59 (1995) "National Highway System Designation Act of 1995," Section 205.
124. FHWA (1993) "Federal Register, Management and Monitoring Systems Interim Final Rule," 58(229), 63442.
125. Ismart, D. (1994) "State Management System," *TR News*, Number 173.
126. FHWA (1996) Pontis, Release 3.1, User's Manual.
127. Hadavi, A. (1998) "Incorporation of Non-Destructive Evaluation in Pontis Bridge Management System," Proceedings of 1998 SMT III: A Non-Destructive Testing Conference, San Antonio, TX, March, 464-471.
128. McNeil, S. (1995) "Management Systems Data Requirements: Boon or Burden," Proceedings of the ASCE Transportation Congress, San Diego, CA.
129. Ellingwood, B.R. (1995) "Engineering Reliability and Risk Analysis for Water Resources Investments: Role of Structural Degradation in Time-Dependent Reliability Analysis," Final Report to U.S. Army Corps of Engineers, Contract Number ITL-95-3, Waterways Experiment Station, Vicksburg, MS.
130. Sanford, K. (1995) "Data Integration: Leveraging Data Collection Efforts for Infrastructure Management," PhD Proposal, Department of Civil and Environmental Engineering, Carnegie Mellon University, Pittsburgh, PA.
131. Adams, T. (1989) "RETAIN: An Integrated Knowledge-Based Expert System for Retaining-Wall Rehabilitation Design," Ph.D. Thesis, Department of Civil Engineering, Carnegie Mellon University, Pittsburgh, PA.
132. ACI 228.2R-98 (1998) "Nondestructive Test Methods for Evaluation of Concrete in Structures," *American Concrete Institute (ACI) Manual of Concrete Practice, Part 2*, Farmington Hills, MI.
133. American Institute of Steel Construction, Inc. (2002) *LRFD Manual of Steel Construction*, Chicago, IL.
134. Santini, E.M. (1998) "Bridge Foundation Stiffness Estimation Using Dynamic Non-Destructive Test Data," Master of Science in Civil and Environmental Engineering, Thesis, Tufts University, Medford, MA; Advisor: Masoud Sanayei.

135. Sanayei, M., and E.M. Santini (1998) "Dynamic Bridge Substructure Evaluation and Monitoring System," Report of subcontract to Tufts University from FHWA grant to Olson Engineering, Wheat Ridge, CO.
136. Sanayei, M., and B. Arya (1998) unpublished work.
137. Novak, M., H. El-Marsafawi, and Y.C. Han (1992) "Dynamic Experiments on Two Pile Groups," *Journal of Geotechnical Engineering*, ASCE, 118(4), 576-592.
138. Poulos, H.G., and E.H. Davis (1980) *Pile Foundation Analysis and Design*, John Wiley, New York, NY.
139. Mori, Y., and B.R. Ellingwood (1994a) "Maintaining Reliability of Concrete Structures. 1. Role of Inspection Repair," *Journal of Structural Engineering*, ASCE, 120(3), 824–845.
140. Mori, Y., and B.R. Ellingwood (1994b) "Maintaining Reliability of Concrete Structures. 2. Optimum Inspection Repair," *Journal of Structural Engineering*, ASCE, 120(3), 846–862.
141. Olson, L.D., and C.C. Wright (1990) "Nondestructive Testing for Repair and Rehabilitation," *Concrete International: Design & Construction*, March, 58–64.
142. Doebling, S.W., C. Farrar, F.M. Hemez, and L.D. Peterson (1997) "Improved Damage Location Accuracy Using Strain Energy-Based Mode Selection Criteria," *American Institute of Aeronautics and Astronautics Journal*, Vol. 35(4), 693–699.
143. Doebling, S.W., C.R. Farrar, M.B. Prime, and D.W. Shevitz (1998) "A Review of Damage Identification Methods That Examine Changes in Dynamic Properties," *Shock and Vibration Digest*, 30(2), 91–105.
144. Chang, F.K. (1998) *Structural Health Monitoring: Current Status and Perspectives*, CRC Press, Lancaster, PA.
145. Chase, S.B., and G. Washer (1997) "Nondestructive Evaluation for Bridge Management in the Next Century," FHWA, *Public Roads*, July/August, 16–25.
146. Farrar, C.R., S.W. Doebling, and D.A. Nix (2001) "Vibration-Based Structural Damage Identification," *Philosophical Transactions of the Royal Society: Mathematical, Physical & Engineering Sciences*, 359(1778), 131–149.
147. Farrar, C.R., and S.W. Doebling (1997) "Lessons Learned from Applications of Vibration Based Damage Identification Methods to Large Bridge Structure," *Structural Health Monitoring: Current Status and Perspectives*, (F.K. Chang, ed.) CRC Press, Lancaster, PA., 351–370
148. Salawu, O.S., and C. Williams (1995b) "Review of Full-Scale Dynamic Testing of Bridge Structures," *Engineering Structures*, 17(2), 113–121.

149. Salawu, O.S. (1997) "Detection of Structural Damage Through Changes in Frequency: A Review," *Engineering Structures*, 19(9), 718–723.
150. Caicedo, J., S.J. Dyke, and E.A. Johnson (2000) "Health Monitoring Based on Component Transfer Functions," *Advances in Structural Dynamics*, (J.M. Ko and Y.L. Xu, eds.) Vol. II, 997–1004.
151. Chang, F.K. (1999) *Structural Health Monitoring 2000*, CRC Press, Lancaster, PA.
152. Aktan, A.E., F.N. Catbas, K.A. Grimmelsman, and C.J. Tsikos (2000) "Issues in Infrastructure Health Monitoring for Management," *ASCE Journal of Engineering Mechanics*, 126(7), 677–683.
153. Hou, Z., M. Noori and R. St. Amand (2000) "Wavelet-Based Approach for Structural Damage Detection," *Journal of Engineering Mechanics*, ASCE, 126(7), 677–683.
154. Kim, J.T., and N. Stubbs (2000) "Nondestructive Crack Detection Model and Vibration-Based System Identification in Structures," Eighth ASCE Specialty Conference on Probabilistic Mechanics and Structural Reliability, Notre Dame, IN, July 24–26, 2000, CD-ROM.
155. Park, G., H.H. Cudney, and D.J. Inman (2000) "Impedance-Based Health Monitoring of Civil Structural Components," *Journal of Infrastructure*, ASCE, 6(4), 153–160.
156. Shi, Z.Y., S.S. Law and L.M. Zhang (2000a) "Optimum Sensor Placement for Structural Damage Detection," *Journal of Engineering Mechanics*, ASCE, 126(11), 1173–1179.
157. Shi, Z.Y., S.S. Law and L.M. Zhang (2000b) "Structural Damage Detection from Modal Strain Energy Change," *Journal of Engineering Mechanics*, ASCE, 126(12), 1216–1223.
158. Shah, S.P., J.S. Popovics, K.V. Subramaniam and C-M. Aldea (2000) "New Directions in Concrete Health Monitoring Technology," *Journal of Engineering Mechanics*, ASCE, 126(7), 754–760.
159. Smyth, A.W., S.F. Masri, T.K. Caughey, and N.F. Hunter (2000) "Surveillance of Mechanical Systems on the Basis of Vibration Signature Analysis," *Journal of Applied Mechanics*, ASME, 67, 540–551.
160. Vanik, M.W., J.L. Beck, and S.K. Au (2000) "Bayesian Probabilistic Approach to Structural Health Monitoring," *Journal of Engineering Mechanics*, ASCE, 126(7), 738–745.
161. Sohn, H., J.A. Czarnecki, and C.R. Farrar (2000) "Structural Health Monitoring Using Statistical Process Control," *Journal of Structural Engineering*, ASCE, 126(11), 1356–1363.

162. Vestroni, F., and D. Capecchi (2000) "Damage Detection in Beam Structures Based on Measurements of Natural Frequencies," *Journal of Engineering Mechanics*, ASCE, 126(7), 761–768.
163. Yun, C.B., J. H. Yi, J. M. Shim, J.W. Lee, and J. Kim (2000) "Damage Estimation for Bridge Model Under Traffic Loading," Eighth ASCE Specialty Conference on Probabilistic Mechanics and Structural Reliability, Notre Dame, IN, July 24–26, 2000, CD-ROM.
164. Onsay, T., and A.G. Haddow (1994) "Wavelet Transform Analysis of Transient Wave Propagation in a Dispersive Medium," *Journal of the Acoustical Society of America*, 95(3), 1441–1449.
165. Chakraborty, A., and D. Okaya (1995) "Frequency-Time Decomposition of Seismic Data Using Wavelet-Based Methods," *Geophysics*, 60(6), 1906–1916.
166. Gurley, K. and A. Kareem (1999) "Applications of Wavelet Transforms in Earthquake, Wind, and Ocean Engineering," *Engineering Structures*, Vol. 21, 149–167.
167. Ghanem, R., and F. Romeo (2001) "A Wavelet-Based Approach for Model and Parameter Identification of Non-Linear Systems," *International Journal of Non-Linear Mechanics*, 36(5), 835–859.
168. Zeldin, B.A., and P.D. Spanos (1996) "Random Field Representation and Synthesis Using Wavelet Bases," *Journal of Applied Mechanics*, ASME, 63, 946–952.
169. Spanos, P.D., and V.R.S. Rao (2001) "Random Field Representation in a Biorthogonal Wavelet Basis," *Journal of Engineering Mechanics*, ASCE, 127(2), 194–205.
170. Daubechies, I. (1990) "The Wavelet Transform, Time-Frequency Localization and Signal Analysis," *IEEE Transaction on Information Theory*, Vol. 36, No. 5, 961–1005.
171. Daubechies, I. (1992) "Ten Lectures on Wavelets," Society for Industrial and Applied Mathematics, Philadelphia, PA.
172. Morlet, J., and A. Grossmann (1984) "Decomposition of Hardy Functions into Square Integrable Wavelets of Constant Shape," *SIAM Journal on Mathematical Analysis*, 15, 723-736.
173. Huang, W., Y.C. Fung, N.E. Huang, and Z. Shen (1998) "Engineering Analysis of Biological Variables: An Example of Blood Pressure over 1 Day," Proceedings of the National Academy of Science, 4816–4821.
174. Huang, N.E. (2000) "A new view of earthquake ground motion data: The Hilbert spectral analysis," Proceedings of International Workshop on Annual Commemoration of Chi-Chi Earthquake (C.H. Loh and W.I. Liao, eds.), Vol. II, 64–75.

175. Zhang, R., and S. Ma (2000) "HHT Analysis of Earthquake Motion Recordings and Its Implications to Simulation of Ground Motion," Monte Carlo Simulation (G.I. Schueller and P.D. Spanos, eds.), 483–490.
176. Zhang, R., S. Ma, E. Safak, and S. Hartzell (2003) "Hilbert-Huang Transform Analysis of Dynamic and Earthquake Motion Recordings," *Journal of Engineering Mechanics*, ASCE, 129, 861–875.
177. Zhang, R. (2001a) "Features of HHT-Based, Low-Frequency Earthquake Recordings," Proceedings of 8th International Conference on Structural Safety and Reliability (M. Shinozuka, G.I. Schueller, and R. Corotis, eds.), Newport Beach, CA, June 17–22, 2001, CD-ROM.
178. Zhang, R. (2001b) "The Role of Hilbert-Huang Transform in Earthquake Engineering," Fifth World Multiconference on Systemics, Cybernetics, and Informatics, Orlando, FL, July 22–25, CD-ROM.
179. Ma, S., and R. Zhang (2001) "Empirical Mode Decomposition of the 1994 Northridge Earthquake and Its Interpretation for Seismic Source Mechanism," 10th International Conference on Soil Dynamics and Earthquake Engineering, Philadelphia, PA, October 7–10.
180. Zhang, R., R. King, and L. Olson (2001) "An HHT-Based Structural Damage Diagnosis," The First Asia-Pacific Workshop on Smart Materials, Nanjing, China, May 28–29.
181. Yang, J.N., P.K. Kahoo, and Y. Lei, (2000) "Parametric Identification of Tall Buildings Using Ambient Wind Vibration Data," Eighth ASCE Specialty Conference on Probabilistic Mechanics and Structural Reliability, Notre Dame, IN, July 24–26, CD-ROM.
182. Yang, J.N., and Y. Lei (2000) "Identification of Tall Buildings Using Ambient Noisy Wind Vibration Data," *Advances in Structural Dynamics*, (J.M. Ko and Y.L. Xu, eds.) Vol. II, 1093–1100.
183. Vincent, H.T., S.L.J. Flu, and Z. Hou (2000) "Damage Detection Using Empirical Mode Decomposition Method and a Comparison with Wavelet Analysis," in *Structural Health Monitoring 2000* (F.K Chang, ed.), Technomic Publishing, 891–900.
184. Loh, C.H., N.E. Huang, and T.S. Wu (2000) "Application of EMD+HHT method to seismic response data of building structure," Proceedings of International Workshop on Annual Commemoration of Chi-Chi Earthquake, (C.H. Loh and W.I. Liao, eds.), Vol. II, 270–281.
185. Loh, C.H. (2000) "Seismic Response Measurement and System Identification of Bridges," Proceedings of Workshop on Mitigation on Earthquake Disaster by Advanced Technologies, Los Angeles, CA, March 2–3, 2000.

186. Huang, N.E., R.S. Long, and Z. Shen (1999) “A New View of Nonlinear Water Waves—Hilbert Spectrum,” *Annual Review of Fluid Mechanics*, 31, 417–457.
187. Huang, K. (2001) “A Nondestructive Instrument Bridge Safety Inspection System Using a Transient Load,” U.S. Patent Application Number 09/210.693; patent allowed April 2001.
188. Clough, R.W., and J. Penzien (1993) *Dynamics of Structures*, McGraw Hill.
189. Hearn, B., and H. Shim (1998) “Integration of Bridge Management Systems and Nondestructive Evaluation,” *Journal of Infrastructure Systems*, 5(2), June 1998, 49–55.
190. Ben-Akiva, M. and R. Ramaswamy (1993) “Approach for Predicting Latent Infrastructure Facility Deterioration,” *Transportation Science*, Vol. 27(2) (May), 174–193.
191. Sanford, K. (1997) “Improving Condition Assessment; Data Requirement for Bridge Management,” PhD Thesis, Department of Civil and Environmental Engineering, Carnegie Mellon University, Pittsburgh, PA.
192. Prine, D.W. (1998) “Problems Associated with Nondestructive Evaluation of Bridges,” Northwestern University, Infrastructure Technology Institute, <http://iti.acns.nwu.edu/pubs/index.html>, accessed December 1998.
193. Aktan, A.E., V. Dalal, D. Farhey, A. Helmicki, V. Hunt, and S. Shelley, (1996) “Condition and Reliability Evaluation for Bridge Management,” *Journal of Infrastructure Systems*, 2(3), 108–117.



## BIBLIOGRAPHY

- Holzhausen, G. (1992) "Tiltmeter Monitoring of Three Unique Bridges: Golden Gate, Seattle Swing and Parrotts Ferry," IBC-92-23, Pittsburgh, PA.
- Huang, N.E. (2000) "Recent development on the HHT," informal lecture for the group who participated in the first invited session "The HHT technique at work" during 5th World Multiconference on Systemics, Cybernetics and Informatics, July 22–25, 2001, Orlando, FL.
- Kenley, R.M. and C.J. Dodds (1980) "West Sole WE Platform: Detection of Damage Using Structural Response Measurements," Technical Report 3866, Proceedings of the Offshore Technology Conference, Houston, TX.
- Lichtenstein, A. (1993) "Bridge Rating Through Nondestructive Load Testing," National Cooperative Highway Research Program (NCHRP), *Manual For Bridge Rating through Load Testing, Final Draft*, 12–28(13).
- Liu, S.C. (2000) "Natural Hazard Mitigation: Exploring the Technological Frontiers," Structural Health Monitoring 2000 (F.K. Chang, ed.), Technomic Publishing, 36–55.
- NCHRP (1994) "BRIDGIT: Bridge Management System Software, Technical Manual," NCHRP Project 12–28 (2) A.
- VanDiver, J.K. (1978) *Detection of Structural Failure on Fixed Platforms by Measurement of Dynamic Response*, Technical Report 78-10, Department of Ocean Engineering, Massachusetts Institute of Technology, Cambridge, MA.
- Wipf, T. (1991) "Use of Tilt Sensing Equipment for Monitoring Long-Term Bridge Movement," *Canadian Journal of Civil Engineering*, 18, 1033–1046.